INFORMATION TO USERS

This manuscript has been reproduced from the microfilm master. UMI films the text directly from the original or copy submitted. Thus, some thesis and dissertation copies are in typewriter face, while others may be from any type of computer printer.

The quality of this reproduction is dependent upon the quality of the copy submitted. Broken or indistinct print, colored or poor quality illustrations and photographs, print bleedthrough, substandard margins, and improper alignment can adversely affect reproduction.

In the unlikely event that the author did not send UMI a complete manuscript and there are missing pages, these will be noted. Also, if unauthorized copyright material had to be removed, a note will indicate the deletion.

Oversize materials (e.g., maps, drawings, charts) are reproduced by sectioning the original, beginning at the upper left-hand corner and continuing from left to right in equal sections with small overlaps.

Photographs included in the original manuscript have been reproduced xerographically in this copy. Higher quality 6" x 9" black and white photographic prints are available for any photographs or illustrations appearing in this copy for an additional charge. Contact UMI directly to order.

Bell & Howell Information and Learning
300 North Zeeb Road, Ann Arbor, MI 48106-1346 USA

UMI®
800-521-0600

DIFFUSION INDUCED LIQUID FILM MIGRATION IN THE ALUMINUM - COPPER SYSTEM

SIMON WILLIAM BARKER
B.Sc. Applied Science (Queen's)

A Thesis
Submitted to the School of Graduate Studies
in Partial Fulfillment of the Requirements
for the Degree
Doctorate of Philosophy in Engineering

McMaster University

BARKER, S.W.

DIFFUSION INDUCED LIQUID FILM MIGRATION IN THE AL-CU SYSTEM

Ph.D. in Engineering

DOCTOR OF PHILOSOPHY (1997)
(Materials Science and Engineering)

McMASTER UNIVERSITY
Hamilton, Ontario

TITLE:	Diffusion Induced Liquid Film Migration In the Aluminum - Copper System
AUTHOR:	Simon William Barker
	B.Sc. Applied Science Queen's University, Kingston
SUPERVISOR:	Professor G.R. Purdy
NUMBER OF PAGES:	xxix, 228

ABSTRACT

An investigation of liquid film migration (LFM) in the aluminum - copper system is presented in this thesis. Experimental and numerical modelling results are discussed for the migration of liquid lenses, formed on melting of grain-boundary θ precipitates in Al-3.4 wt% Cu alloys which had been previously equilibrated at 400°C. Liquid films of comparable thickness, formed upon the melting of intragranular Widmanstätten precipitates were found not to migrate. Volume fraction studies indicate that after the initial liquation of the θ precipitates, the liquid phase undergoes an isothermal solidification. Three-dimensional reconstructions of LFM events were created using a combined SEM / microindenting / polishing method. The results indicate the difficulty in obtaining reasonable measurements of migration distances from two-dimensional cross-sections; a method was developed to obtain appropriate two-dimensional measurements based upon these results. The modelling studies are based on the hypothesis that the leading and trailing solid-liquid interfaces are each characterized by a constrained local equilibrium, as determined by chemical, coherency and capillary terms, and that the process is driven by the liquid concentration gradient resulting from different equilibrium concentrations at the two interfaces. The model is utilized to explore the sensitivity of the process to variations in physico-chemical parameters, and ultimately as an aid in the understanding of LFM and its subsequent cessation. It is determined that the capillary term has a strong influence on the migration process, even for liquid pool dimensions of several microns. From model simulations and an analysis of coherency loss in the leading solid it is concluded that the migration of liquid films in the Al-Cu system is driven by coherency strain energy in the early stages of the process. As migration continues, the increasing energy due to curvature is sufficient to decrease the overall driving force to a point where the film slows down and coherency is lost. The liquid films become immobile (no reversal of migration) once loss of coherency occurs.

ACKNOWLEDGEMENTS

I would like to thank Dr. G.R. Purdy for his assistance and support throughout this study. His encouragement and enthusiasm have been greatly appreciated. I would also like to thank committee members Dr. G.C. Weatherly and Dr. A.P. Hitchcock for their time and guidance. I would finally like to thank my wife Patricia for her encouragement and (almost) infinite patience.

TABLE OF CONTENTS

CHAPTER 3: EXPERIMENTAL DESIGN 43

CHAPTER 4: EXPERIMENTAL RESULTS AND DISCUSSION 69

GLOSSARY OF TERMS AND SYMBOLS

a	Lattice parameter of the parent solid phase (m)
a_S	Stress free lattice parameter of the thin layer (m)
a_0	Stress free lattice parameter of the substrate (*i.e.*, parent phase)
$a_{(C_S)}$	Stress free lattice parameter of an aluminum - copper alloy with composition C_S (m)
$a_{(C_0)}$	Stress free lattice parameter of an aluminum - copper alloy with composition C_0 (m)
A	Hypothetical pure element
b	Magnitude of the Burger's vector (m)
B	Hypothetical pure element
$B_1(X_1,Z_1)$	Point on the circumference of the sphere used to estimate the radius of curvature of the solid - liquid interface
$B_2(X_2,Z_2)$	Point on the circumference of the sphere used to estimate the radius of curvature of the solid - liquid interface
$B_3(X_3,Z_3)$	Point on the circumference of the sphere used to estimate the radius of curvature of the solid - liquid interface
$C(X_C,Z_C)$	Centre point of the sphere used to estimate the radius of curvature of the solid - liquid interface
(Al)	Aluminum rich solid phase in the aluminum - copper system
$A(t)$	Modelling parameter
C	Solute concentration
C_{Cu}	Copper concentration
C_L	Equilibrium solute concentration in the liquid phase
$C_{L,EQ}$	Calculated equilibrium solute concentration in the liquid phase
C_L'	Solute concentration in the liquid phase in local equilibrium with the coherently strained solid phase
$C_L^{A'}$	Solute concentration in the liquid phase in local equilibrium with the

	coherently strained solid grain A
$C_L^{B\prime}$	Solute concentration in the liquid phase in local equilibrium the coherently strained solid grain B
$C_{L,TRAIL}$	Concentration of solute in the liquid phase adjacent to the trailing solid - liquid interface
$C_{L,TRAIL}^{i}$	Concentration of solute in the liquid phase adjacent to the trailing solid - liquid interface, calculated in the i'th iteration of the model algorithm
C_S	Equilibrium solute concentration in the solid phase
$C_{S,EQ}$	Calculated equilibrium solute concentration in the solid phase
C_S'	Solute concentration in the coherent layer adjacent to the liquid phase
C_{S1}	Concentration of solute species 1 in the coherently stressed solid phase
C_{S2}	Concentration of solute species 2 in the coherently stressed solid phase
$C_{S,TRAIL}$	Concentration of solute in the solid phase at the trailing solid - liquid interface
$C_{S,TRAIL}^{i}$	Concentration of solute in the solid phase adjacent to the trailing interface, calculated in the i'th iteration of the model algorithm
C_0	Solute concentration in the parent solid phase
C_0^A	Initial solute concentration in grain A
C_0^B	Initial solute concentration in grain B
C_{01}	Concentration of solute species 1 in the parent solid
C_{02}	Concentration of solute species 2 in the parent solid
ΔC	Difference in solute concentration across the liquid film
$\Delta C(t)$	Difference in solute concentration across the liquid film after time t
$(\Delta C)_0$	Difference in solute concentration across the liquid film at the start of the migration process
ΔC^i	Difference in solute concentration across the liquid film, calculated in the i'th iteration of the model algorithm
∇C	Gradient in solute concentration across the liquid film
$c_{11}\ c_{12}\ c_{44}$	Stiffness coefficients (J m^{-3})
D	Diffusion coefficient at temperature T ($m^2\ s^{-1}$)

D_0	Empirical constant ($m^2\,s^{-1}$)
D_L	Diffusion coefficient of copper in liquid aluminum ($m^2\,s^{-1}$)
D_S	Diffusion coefficient of copper in a dilute solid aluminum - copper alloy ($m^2\,s^{-1}$)
D_S/v	Effective solute penetration distance (m)
$(D_S/v)_{CRIT,STEP}$	Critical solute penetration distance for the case of a step change in concentration (m)
$(D_S/v)_{CRIT}$	Critical solute penetration distance assuming a concentration gradient (m)
D_1	Width of micro-indent before polishing (m)
D_2	Width of micro-indent after polishing (m)
DIGM	Diffusion induced grain boundary migration
DP	Discontinuous precipitation
E	Young's modulus (J m^{-3})
E_ϵ	Energy associated with the elastic strain (ϵ) (J m^{-2})
E_d	Energy per unit length of a single edge dislocation lying in the interface between two crystals (J m^{-1})
E_{grid}	Energy per unit area of a square grid of two non-interacting, perpendicular edge dislocation arrays (J m^{-2})
f	Misfit between the substrate and the thin film
f_{EL}	Coefficient of strain energy
$f_{EL}{}^A$	Coefficient of strain energy in grain A
$f_{EL}{}^B$	Coefficient of strain energy in grain B
f_{MS}	Coefficient of free energy of mixing of the solid
f_{ML}	Coefficient of free energy of mixing of the liquid
F	Helmholtz free energy (J mol^{-1})
F^α	Free energy of the α-phase (J mol^{-1})
F^β	Free energy of the β-phase (J mol^{-1})
F^{ALLOY}	Free energy of a two-phase alloy (J mol^{-1})
F_S	Free energy of the stress free bulk solid phase (J mol^{-1})

F_L	Free energy of the bulk liquid phase (J mol^{-1})
F_{COH}	Free energy of the coherently strained solid phase (J mol^{-1})
$F_{S,LEAD}$	Calculated free energy of the leading solid phase (J mol^{-1})
$F_{L,LEAD}$	Calculated free energy of the leading liquid phase (J mol^{-1})
$F_{S,TRAIL}$	Calculated free energy of the trailing solid phase (J mol^{-1})
$F_{L,TRAIL}$	Calculated free energy of the trailing liquid phase (J mol^{-1})
$F_S^{(Al)}$	Free energy of solid aluminum (J mol^{-1})
$F_S^{(Cu)}$	Free energy of solid copper (J mol^{-1})
$F_L^{(Al)}$	Free energy of liquid aluminum (J mol^{-1})
$F_L^{(Cu)}$	Free energy of liquid copper (J mol^{-1})
$F_{COH,LEAD}$	Calculated coherency strain energy for the leading solid phase (J mol^{-1})
$F_{COH,TRAIL}$	Calculated coherency strain energy for the trailing solid phase (J mol^{-1})
$F_{CURV,LEAD}$	Calculated energy due to curvature for the phase at the leading interface possessing positive curvature (J mol^{-1})
$F_{CURV,TRAIL}$	Calculated energy due to curvature for the phase at the trailing interface possessing positive curvature (J mol^{-1})
ΔF	Driving force for the transfer of material from the coherent layer to the stress free α particle (J mol^{-1})
ΔF_M	Free energy of mixing (J mol^{-1})
ΔF_{TOT}	Total driving force available for the transfer of material from the coherent layer to the stress free solid (J mol^{-1})
ΔF_{DIFF}	Free energy dissipated by solid state diffusion ahead of the migrating interface (J mol^{-1})
ΔF_M	Driving force for LFM (J mol^{-1})
G_Y	Geometrical factor used in the calculation of $Y(\mathbf{n})$
G_0	Shear modulus of the substrate (parent solid) (J m^{-3})
G_S	Shear modulus of the thin layer (J m^{-3})
J	Flux of solute across the liquid film (m^{2}s^{-1})
k	Solute distribution coefficient ($C_{S,TRAIL}$ / $C_{L,TRAIL}$)

k_B	Boltzmann's constant
K	Mean curvature of the liquid film (m^{-1})
K^A	Curvature of the solid A - liquid interface (m^{-1})
K^B	Curvature of the solid B - liquid interface (m^{-1})
K_{LEAD}	Curvature of the leading solid - liquid interface (m^{-1})
K_{TRAIL}	Curvature of the trailing solid - liquid interface (m^{-1})
l m & n	Directional cosines
L	Diffusion layer thickness (m)
L_C	Critical diffusion distance for loss of coherency, obtained using the Matthews analysis (m)
(L)	Liquid phase designation in the aluminum - copper system
LFM	Liquid film migration
n	Plane normal of the coherently strained grain
n^i	Plane normal of grain 'i'
n_A	Plane normal of grain A
n_B	Plane normal of grain B
N	Total number of indents measured on a particular level
N_P	Number of grid corners falling on the phase being estimated.
O[i]	Origin for level 'i'
P	Pressure
P_0	Pressure in the matrix phase; used in the illustration of the Gibbs - Thompson effect
P_l	Pressure in the liquid phase; used in the illustration of the Gibbs - Thompson effect
Q	Activation energy for diffusion ($J\ mol^{-1}$)
r	Extent of the elastic stress field (m)
R	Gas constant ($\equiv 8.314\ J\ mol^{-1}\ K^{-1}$)
S	Dislocation spacing (m)
SEM	Scanning electron microscope

t	Time (s)
t'	Time to collapse of the liquid film (s)
t_0	Initial time (for the purpose of integration) (s)
t^i	Time value used in the i'th iteration of the model algorithm (s)
T	Temperature (K)
T_{EXP}	Experimental temperature for liquid phase sintering experiments (from literature) (K)
T_{EUT}	Eutectic temperature (K)
T_{SINTER}	Equilibration temperature in liquid phase sintering experiments (from literature) (K)
v	Velocity of the liquid film in the positive Z-direction (m s^{-1})
$v(t)$	Velocity of the liquid film in the positive Z-direction after time t (m s^{-1})
$v(Z)$	Velocity of the of the liquid film in the positive Z-direction at position Z (m s^{-1})
v_0	Initial velocity of the liquid film used in the modelling of LFM (m s^{-1})
v^i	Instantaneous velocity of the liquid film used in modelling of LFM: velocity calculated in the i'th iteration of the model algorithm (m s^{-1})
V_a	Atomic volume (m)
V_f	Measured volume fraction
V_m	Molar volume of the parent solid phase (m^3 mol^{-1})
W	Measured width of liquid film (m)
w_{EL}	Elastic strain energy density (J m^{-3})
X	X-coordinate (m)
X_{PIN}	X-coordinate of pinning point (m)
X_B	Mole fraction of solute species B in a binary alloy
X_B^{α}	Mole fraction of solute species B in the α-phase
$X_B^{\alpha 1}$	Mole fraction of solute species B in the α-phase at point α_1
$X_B^{\alpha 2}$	Mole fraction of solute species B in the α-phase at point α_2
$X_B^{\alpha E}$	Mole fraction of solute species B in the α-phase at equilibrium

X_B^{β}	Mole fraction of solute species B in the β-phase
$X_B^{\beta 1}$	Mole fraction of solute species B in the β-phase at point β_1
$X_B^{\beta 2}$	Mole fraction of solute species B in the β-phase at point β_2
$X_B^{\beta E}$	Mole fraction of solute species B in the β-phase at equilibrium
X_B^{ALLOY}	Mole fraction of solute species B in the two-phase alloy
Y	Y-coordinate (m)
$Y(\mathbf{n})$	Orientation dependent elastic constant (J m^{-3})
Y_A	Orientation dependent elastic constant for grain A (J m^{-3})
Y_B	Orientation dependent elastic constant for grain B (J m^{-3})
Y_{ISO}	Isotropic approximation for $Y(\mathbf{n})$ (J m^{-3})
Z	Coordinate in the direction of liquid film migration (positive Z-direction) (m)
Z'	Total distance travelled in the positive Z-direction before collapse of liquid film (m)
$Z(t)$	Z-coordinate at time t (m)
$Z(t_0)$	Z-coordinate at time t_0 (m)
Z^i	Z-coordinate of level 'i' (m)
Z_{LEAD}	Z-coordinate of the leading interface (m)
Z_{TRAIL}	Z-coordinate of the trailing interface (m)
$Z_{LEAD}(t)$	Z-coordinate of the leading interface after time t (m)
$Z_{TRAIL}(t)$	Z-coordinate of the trailing interface after time t (m)
Z_{LEAD}^{i}	Z-coordinate of the leading interface, calculated in the i'th iteration of the model algorithm (m)
Z_{TRAIL}^{i}	Z-coordinate of the trailing interface, calculated in the i'th iteration of the model algorithm (m)
ΔZ	Amount of material removed between polishing stages (m)
ΔZ^i	Amount of material removed between levels 'i' and 'i+1' (m)
ΔZ_j^i	Amount of material removed between levels 'i' and 'i+1' for indent 'j' (m)
ΔZ_{AVG}^{i}	Average amount of material removed between level 'i' and 'i+1' (m)
α	Hypothetical phase of matter

α_1	Point defining the initial composition and the free energy of the alloy
α_2	Point defining the composition and the free energy of the alloy after time, t
α_T	Thermal expansion coefficient (°C^{-1})
α_Y	Factor used in the calculation of $Y(\mathbf{n})$
β	Hypothetical phase of matter
β_1	Point defining the initial composition and the free energy of the alloy
β_2	Point defining the composition and the free energy of the alloy after time, t
β_Y	Factor used in the calculation of $Y(\mathbf{n})$
γ_{iS}	Activity coefficient of species 'i' in the solid phase
γ_{iS}'	Activity coefficient of species 'i' in the strained solid phase
γ_{iL}	Activity coefficient of species 'i' in the liquid phase
γ_S	Activity coefficient of solute in the stress free solid phase (in a binary system)
γ_L	Activity coefficient of the solute in the liquid phase (in a binary system)
δ	Liquid film thickness (m)
$\delta(t)$	Liquid film thickness measured parallel to the Z-axis after time t (m)
$\delta(0)$	Initial liquid film thickness measured parallel to the Z-axis (m)
δ^i	Liquid film thickness measured parallel to the Z-axis calculated in the i'th iteration of the model algorithm (m)
ϵ	Strain in the coherent layer
ϵ^*	Elastic strain which minimizes the sum of E_{grid} and E_ϵ
η	Lattice misfit parameter
η_1	Lattice misfit parameter of solute species 1 in the parent solid phase
η_2	Lattice misfit parameter of solute species 2 in the parent solid phase
θ	Intermediate phase (Al_2Cu) in the aluminum - copper alloy system
θ_Y	Geometrical factor used in the calculation of $Y(\mathbf{n})$
λ	Interatomic spacing (m)
μ	Chemical potential ($J\ mol^{-1}$)
$^\circ\mu_{iS}$	Standard chemical potential of species 'i' in the solid phase ($J\ mol^{-1}$)
$^\circ\mu_{iL}$	Standard chemical potential of species 'i' in the liquid phase ($J\ mol^{-1}$)

μ_A^{α}	Chemical potential of A atoms in the α-phase at composition X_B (J mol^{-1})
$\mu_A^{\alpha 1}$	Chemical potential of A atoms in the α-phase at composition $X_B^{\alpha 1}$ (J mol^{-1})
$\mu_A^{\alpha 2}$	Chemical potential of A atoms in the α-phase at composition $X_B^{\alpha 2}$ (J mol^{-1})
$\mu_A^{\beta 1}$	Chemical potential of A atoms in the β-phase at composition $X_B^{\beta 1}$ (J mol^{-1})
$\mu_A^{\beta 2}$	Chemical potential of A atoms in the β-phase at composition $X_B^{\beta 2}$ (J mol^{-1})
μ_B^{α}	Chemical potential of B atoms in the α-phase at composition X_B (J mol^{-1})
$\mu_B^{\alpha 1}$	Chemical potential of B atoms in the α-phase at composition $X_B^{\alpha 1}$ (J mol^{-1})
$\mu_B^{\alpha 2}$	Chemical potential of B atoms in the α-phase at composition $X_B^{\alpha 2}$ (J mol^{-1})
$\mu_B^{\beta 1}$	Chemical potential of B atoms in the β-phase at composition $X_B^{\beta 1}$ (J mol^{-1})
$\mu_B^{\beta 2}$	Chemical potential of B atoms in the β-phase at composition $X_B^{\beta 2}$ (J mol^{-1})
$\Delta\mu_A^1$	Driving force for the transfer of A atoms from alloy state α_1 to β_1 (J mol^{-1})
$\Delta\mu_B^1$	Driving force for the transfer of B atoms from alloy state β_1 to α_1 (J mol^{-1})
$\Delta\mu_B^2$	Driving force for the transfer of B atoms from alloy state β_2 to α_2 (J mol^{-1})
ν	Poisson's ratio
ρ	Radius of curvature of the solid - liquid interface (m)
ρ_1	Principal radius of curvature of solid - liquid interface (m)
ρ_2	Principal radius of curvature of solid - liquid interface (m)
ρ_{LEAD}	Radius of curvature of the leading solid - liquid interface (m).
ρ_{TRAIL}	Radius of curvature of the trailing solid - liquid interface (m).
σ	Specific solid - liquid interfacial free energy (J m^{-2})
σ_{Vf}	Standard deviation in the volume fraction measurements
σ_{xx}	Biaxial stress
ϕ_Y	Geometrical factor used in the calculation of Y(n)
Φ_S	Temperature dependent interaction parameter for the solid phase
Φ_L	Temperature dependent interaction parameter for the liquid phase
Ω_S	Temperature dependent interaction parameter for the solid phase
Ω_L	Temperature dependent interaction parameter for the liquid phase
Ψ_S	Temperature dependent interaction parameter for the solid phase
Ψ_L	Temperature dependent interaction parameter for the liquid phase

LIST OF FIGURES

LIST OF TABLES

CHAPTER ONE

INTRODUCTION

1.1 INTRODUCTION

This chapter introduces the phenomenon of liquid film migration (LFM). LFM was first recognized as a novel solidification mechanism in 1979 by Yoon and Huppmann [1]. They reported that during the liquid phase sintering of tungsten with liquid nickel, pure tungsten grains, initially placed in contact with pure liquid nickel, first dissolved and then reprecipitated as a solid solution saturated with nickel. The process has the appearance of the intrusion of a liquid film (which initially is separating large tungsten grains) into the dissolving grain, while the expanding grain grows by the deposition of an approximately equilibrium W-Ni solid solution.

A physical understanding of the process of LFM is best obtained by considering the case of two grains separated by a thin liquid film. The surfaces of the two grains are assumed to be in local equilibrium with the liquid phase. Figure 1.1 shows a schematic diagram of a migrating liquid film illustrating the assumed driving force for migration. It can be seen that the adjacent grains are under different stress states (*i.e.*, one side is coherently strained and the other strain free) such that the liquid in local equilibrium with each grain has a different composition. A composition gradient therefore exists across the liquid film leading to diffusion and migration of the liquid film. The question then remains on how to quantify these ideas and develop a kinetic model to describe LFM.

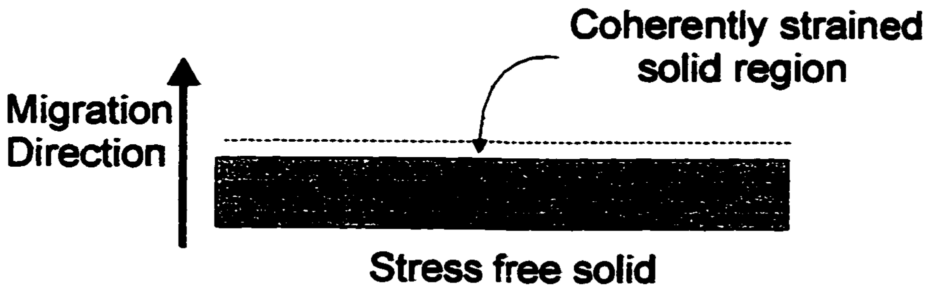

Figure 1.1: **Schematic Diagram of a Migrating Liquid Film Migration (LFM) Event.**

Using the fact that LFM has only been observed to occur in systems exhibiting at least a 10% difference in atomic size, Hillert [2,3], expanding upon the work of Sulonen [4-6], proposed that the lattice diffusion of solute ahead of the migrating liquid film creates a composition variation over a thin layer that is coherent with the parent lattice. The resulting strain energy would then be the proposed driving force for LFM. Yoon *et al.* [7] and Handwerker *et al.* [8] developed this argument further for the case of LFM. They used the thermodynamic analysis of self-stress in a crystalline solid developed by Larché and Cahn [9] to derive equations for the boundary conditions for diffusion of solute across the liquid film. Invoking the condition of local equilibrium, and by use of Fick's law along with the appropriate conservation of mass criteria, they were able to develop an approximate expression for the rate of LFM in binary systems.

However, most experimental tests of the coherency strain theory have been qualitative in nature, and although they are relatively convincing (see Chapter Two), the kinetic model developed by Yoon *et al.* [7] has proven difficult to apply due to the fact that many assumptions about the thermodynamic properties of the alloy must be made. In most cases dilute or ideal solution behaviour has been assumed, both of which are severe over-simplifications (especially for the liquid phase). It should also be noted that experimental measurements of the migration distances are obtained from two-dimensional slices of very three-dimensional structures (i.e., from the plane of polish). In many cases this can lead to erroneous values being assigned to the migration distance, since as will be shown in Chapter Three, the two-dimensional slice may or may not be the cross-section of the LFM event that gives the maximum migration distance when measured from the initial location of the film (i.e., from the grain boundary). Much care is therefore required when using these measurements to test such a model.

Although there is experimental evidence to support the theory that the coherency strain energy ahead of the migrating liquid film is the driving force for LFM (see Chapter Two), a comprehensive analysis of the kinetics of LFM has not yet been performed on a binary system.

1.2 OBJECTIVE

The main objective of this research was to investigate the phenomenon of liquid film migration (LFM) in an aluminum - copper alloy (containing 3.3 percent copper by weight). Specifically, the objective was to further develop the kinetic modelling of LFM, and to quantitatively test the model using experimental data. In order to fulfill this objective, the following steps were taken:

- The current state of research and modelling of LFM was reviewed, and previously developed models were applied to the aluminum - copper system.
- Experiments to induce LFM were performed using aluminum copper alloys.
- A procedure to obtain reasonable estimates of migration distances from the two-dimensional measurements of LFM events was developed. This was

done in two stages:

    - The general three-dimensional morphology of several LFM events was obtained through the use of a serial polishing / sectioning technique and the scanning electron microscope.
    - From the results of the three-dimensional morphology study, and through the analysis of two-dimensional slices of hypothetical 'ideal' LFM events, a method was developed to obtain reasonable estimates of migration distances.

- A model was developed to describe LFM in the aluminum - copper system. The model is based on the hypothesis that the leading and trailing solid - liquid interfaces are each characterized by a constrained local equilibrium, as determined by chemical, coherency, and capillary terms, and that the process is driven by the liquid concentration gradient resulting from the different equilibrium concentrations at the two interfaces. Through the use of current mathematical software, it was possible to calculate the equilibrium concentrations of solute in the solid and liquid phases at the leading and trailing interfaces by direct application of the common tangent method. The calculated concentration difference along with an appropriate conservation of mass criterion at the trailing interface were used to obtain predictions of migration distances as a function of time.
- The developed model underwent calibration and was tested against the experimental measurements of interface position as a function of time.
- An analysis of the sensitivity of the developed model to variations in parameters such as the experimental temperature was performed. The sensitivity of the predictions to uncertainties in the material parameters such as the solid - liquid interfacial energy and elastic modulus (at the experimental

temperature) was also investigated.

Chapter Two provides some background on liquid film migration, including a review of the literature as well as a full description of the kinetic model of Yoon *et al.* [7]. Experimental evidence to support the coherency strain hypothesis is presented, and limitations of theory are also discussed. Chapter Three discusses the design of experiments to study LFM, the choice of alloy system, and the experimental procedure that was followed. Results of the various experiments are presented in Chapter Four, including measurements of migration distances and composite three-dimensional images of LFM events. Modelling of liquid film migration is described in Chapter Five; a velocity expression is developed for the trailing interface in which loss of solute from the liquid to the growing grain is incorporated, where the concentration difference across the liquid film is calculated using the direct common tangent method. The implementation of the model using MAPLE mathematical software is also described. Chapter Six discusses the application of the kinetic model to the aluminum - copper system, including model calibration and sensitivity to certain key parameters. A general discussion of the modelling and experimental results is presented in Chapter Seven. The thesis concludes with conclusions and recommendations for further work in Chapter Eight.

CHAPTER TWO

BACKGROUND ON LIQUID FILM MIGRATION

2.1 INTRODUCTION

This chapter introduces the phenomenon of liquid film migration (LFM). The alloy systems in which LFM has been observed are discussed from a historical perspective. This is followed by a description of the coherency strain hypothesis which has been proposed to be the driving force for LFM. The kinetic model of Yoon *et al.* [7] is then discussed in detail. Initially, an expression for the concentration difference across the liquid film (ΔC) is derived from the basic laws of thermodynamics, and several simplified cases are obtained. An expression for the velocity of the liquid film is then developed using the estimated liquid compositions (which define ΔC) as boundary conditions for the diffusion of solute across the liquid film. A discussion of the initiation of LFM and the subsequent growth after coherency loss follows. Experimental evidence from literature which qualitatively supports the coherency strain hypothesis is then presented. The chapter concludes with a discussion of the limitations of previously developed kinetic models.

2.2 EXPERIMENTAL OBSERVATIONS - HISTORICAL PERSPECTIVE

The observation of LFM during the liquid phase sintering of tungsten with liquid nickel by Yoon and Huppmann [1] in 1979 has generated much interest in the phenomenon. A large amount of experimental data have been gathered since then, most of which were obtained during liquid phase sintering experiments designed to determine the driving force for the process. These experiments will be discussed in detail in a later section. This was not the first recorded instance of LFM however. In 1964, Sulonen [10] noted that in the Cu-Cd system, liquid films that initially separated grains in a previously equilibrated solid - liquid system migrated when the temperature was changed (due to the retrograde solidus). Liquid films formed upon the liquation of carbides in a Ni based superalloy were observed to migrate in the heat affected zone of weldments [11]. LFM was also observed during the hot pressing of TaC with additions of Mn, Fe, Co and Ni [12]. A series of experiments by Kucherenko [13,14] designed to observe the growth of the liquid phase during the melting of Cu-Ni, Sb-Bi, and Sb-Sn solid solutions observed extensive LFM when the samples were rapidly heated from room temperature. In an attempt to explain the phenomenon, it is stated that elastic stresses due to the difference in atomic radii of the atoms in the diffusion zone adjacent to the liquid may play an important role in the transformation.

As mentioned previously, the observation of LFM by Yoon and Huppmann [1] led to a series of experiments on liquid phase sintered specimens, at the Korea Advanced Institute of Science and Technology (K.A.I.S.T.) designed to determine the nature of the driving force for LFM. Most of the experiments were performed using metallic liquid phase sintering systems such as: W-Ni upon adding Fe to the melt [15], Mo-Ni upon changing temperature [16], Mo-Ni with Fe added to the liquid phase [17,18,19], Mo-Ni with W added to the liquid phase [20,21], Mo-Ni with Sn and Co added to the liquid phase [22,23], Mo-Ni with W and with Co added to the liquid phase [24], and Co-Cu with the addition of Sn to the liquid phase [25]. The purpose and implications of these experiments will be discussed in detail in Section 2.5. LFM was also observed in a Mo-Ni alloy prepared by powder metallurgy techniques [26]. Other metallic systems in which LFM has been observed include: the Cu-In system in which liquid films were observed to migrate during the study of melting [27], the Al-Cu system in which LFM was observed upon changing the temperature after previous equilibration in the solid - liquid phase region [28], the Fe-Al system in which LFM was induced by the penetration of Zn along a 43° <001>{001} tilt boundary in Fe-5%Al [29], in B-doped Ni_3Al

intermetallics in which Cu was electroplated to the surface as the solute source [30], and in the heat affected zone of weldments of Ni alloy 718 caused by the constitutional liquation of NbC [31,32], and in weldments of Incoloy 903 caused by the constitutional liquation of MNP phosphides and MC carbides where M was either Al, Ti and/or Nb [33,34]. LFM has also been observed in some ceramic systems, such as: during the aging of partially stabilized ZrO_2 treated with CaO and MgO [35], during the phase equilibration of ZrO_2 - Y_2O_3 alloys [36], in MgO-V_2O_5 alloys treated with NiO and CoO to induce the migration [37], during the infiltration treatment of TiC-Fe cermets [38], in ZrO_2 - Y_2O_3 alloys using mixtures of MgO and Y_2O_3 to induce the migration [39], in TiN-Ni alloys treated with TiC [40], and in CeO_2 stabilized tetragonal ZrO_2 polycrystals [41]. All these experiments will be discussed in more detail in Section 2.5 in the context of coherency strain energy being the driving force for the phenomenon. A summary of alloy systems in which LFM has been observed along with the specimen type, and whether solute is added to (alloying) or removed from (de-alloying) the solid phase during migration is given in Table 2.1. It should be noted that 'bulk' refers to LFM being observed at grain boundaries in bulk specimens, and that the element in brackets is believed to be the diffusing species that induces the migration.

Table 2.1: Alloy systems in which LFM has been observed.

System solvent (solute)	Specimen Type	Composition Change	Reference(s)
Al-(Cu)	Bulk	alloying / de-alloying	[28]
Co-(Cu)	Liquid Phase Sintered	alloying	[25]
Co-Cu-(Sn)	Liquid Phase Sintered	alloying	[25]
Cu-(Cd)	Bulk	de-alloying	[10]
Cu-(In)	Bulk	de-alloying	[27]
Cu-(Ni)	Bulk	de-alloying	[13]
Fe-Al-(Zn)	Bicrystal	alloying	[29]
Incoloy 903	Bulk	alloying	[33][34]

System solvent (solute)	**Specimen Type**	**Composition Change**	**Reference(s)**
Mo-(Ni)	Powder	alloying	[26]
Mo-(Ni)	Liquid Phase Sintered	alloying / de-alloying	[16]
Mo-Ni-(Co-Sn)	Liquid Phase Sintered	alloying / de-alloying	[22][23][24]
Mo-Ni-(Fe)	Liquid Phase Sintered	alloying / de-alloying	[17][18][19]
Mo-Ni-(W)	Liquid Phase Sintered	alloying / de-alloying	[20][24]
Mo-Ni-(W)	Liquid Phase Sintered	alloying	[21]
Ni alloy 718	Bulk	alloying	[31][32]
Ni-base superalloy	Bulk	---	[11]
Ni_3Al-(Cu)	Bulk	alloying	[30]
Sb-(Bi)	Bulk	de-alloying	[13][14]
Sb-(Sn)	Bulk	de-alloying	[13]
TaC-(Mn,Fe,Co,Ni)	Liquid Phase Sintered	de-alloying	[12]
TiN-Ni-(TiC)	Bulk	alloying	[40]
TiC-Fe-(Fe)	Bulk	alloying	[38]
W-(Ni)	Powder	alloying	[1]
W-(Ni-Fe)	Liquid Phase Sintered	alloying	[15]
MgO-V_2O_5-(NiO,CoO)	Liquid Phase Sintered	alloying	[37]
ZrO_2-(CaO-MgO)	Bulk	alloying	[35]
ZrO_2-(CeO_2)	Bulk	de-alloying	[41]
ZrO_2-(Y_2O_3)	Bulk	alloying	[36]
ZrO_2-Y_2O_3-(MgO-Y_2O_3)	Bulk	alloying	[39]

In the alloy systems discussed above it was seen that the liquid films often migrate against their mean radii of curvature, indicating that the migration could not purely be driven by capillarity effects. The phenomenon of LFM is similar to Diffusion Induced Grain Boundary Migration (DIGM) in polycrystalline solids, in which grain boundaries experience a diffusion flux along their length, and migrate into one of the parent grains, depositing a solid solution of altered composition in their wake. In both processes, there is clearly a persistent driving force, which is capable of moving interfaces (often against their curvature), and which leaves a new solid solution in the region swept by the migrating interface (in the case of LFM, the composition of the new solid solution is often the equilibrium solidus composition at the temperature of the experiment).

There are then several questions which need to be answered in order to obtain a full understanding of LFM. For example, why would the interface migrate during the equilibration of the phases? How is the migration initiated? What determines the direction of migration? How does it continue over extended ranges of time and distance? The answers, and discussions of these questions will be addressed during the course of this thesis.

In the 1960's Sulonen [4-6] made the observation that discontinuous precipitation (DP) only seemed to occur in systems exhibiting at least a 10% difference in atomic size. He proposed that during DP, lattice diffusion ahead of moving grain boundaries could create a composition variation over a thin layer that was coherent with the parent lattice, and the resulting strain energy was the driving force. Hillert [2,3] developed this idea into a quantitative form in his search for the driving force(s) for DP, DIGM, and LFM. Yoon *et al.* [7], and Handwerker *et al.* [8] developed this argument further for the case of LFM. Using the thermodynamic analysis of self-stress in a crystalline solid developed by Larché and Cahn [9] they derived equations for the boundary conditions of diffusion of solute across the liquid film. Then, invoking the condition of local equilibrium, and by use of Fick's law along with the appropriate conservation of mass criteria, they were able to develop an approximate expression for the rate of LFM in binary systems. A full description of the diffusional coherency strain theory, and the application to LFM now follows.

2.3 PROPOSED DRIVING FORCE FOR LFM - COHERENCY STRAIN HYPOTHESIS

The effect of a coherency strain field caused by a solute concentration gradient in a solid phase was first studied by Cahn [42] in his treatment of spinodal decomposition. He included a strain energy term into the total Helmholtz free energy expression, which would then affect the criteria for the boundary of the unstable region on the phase diagram (*i.e.* the locus of $\partial^2 F/\partial^2 C=0$). This extra energy arises from the fact that the molar volume of a solid is generally a function of composition. As a result there is an energy increase where adjacent regions of different composition (and thus lattice parameter) are coherently connected. For cubic crystals, under the assumptions of linear elasticity, Cahn [42] shows that the local elastic strain energy per unit volume is given by:

$$w_{EL} = Y(\boldsymbol{n})(C_S'-C_0)^2\eta^2 \tag{2.1}$$

Where:

$Y(\mathbf{n})$	Orientation dependent elastic modulus. (Note: for isotropic material, $Y=E/(1-\nu)$, where E is Young's modulus, and ν is Poisson's ratio). An expression for Y for cubic crystals as a function of orientation is included in Chapter Six. Note: $\mathbf{n}$ is a unit vector representing the normal of the biaxially stressed plane.
C_S'	Concentration of solute in coherent layer (maximum value, *i.e.* concentration in the solid immediately adjacent to the liquid).
C_0	Concentration of solute in the parent crystal.
η	Lattice misfit parameter. Note: if Vegard's law applies to the system under study, then η is constant, and is given by $\eta = d(\ln(a))/dC$, where a is the lattice parameter.

With the above prescription for the local elastic strain energy density, it is now possible to describe the thermodynamics of LFM in terms of coherency strain theory. This was first done by Hillert [3] who considered a liquid film separating two grains, and assumed a thin layer of a different composition to be coherent with a parent grain of composition C_0. He assigned to material in this layer an extra energy due to coherency given by $(V_m)\cdot(w_{EL})$ (w_{EL} given by Equation (2.1)). Figure 2.1(a) shows the molar free energy diagram for a binary system in which a thin stressed α layer, coherent with a large α grain, is in supposed equilibrium with a B-rich liquid phase. The equilibrium compositions are obtained through use of the common tangent construction. Hillert then derived the driving force ΔF for the transfer of material from the coherent layer to the stress free α particle assuming ideal solution behaviour, and obtained (in the small η regime) ΔF equal to the coherency strain energy (*i.e.*, $\Delta F = (V_m)\cdot(w_{EL})$).

2.4 MODELLING OF LFM

2.4.1 Kinetic Model of Yoon *et al.*

The initial formulation of Hillert [3] to describe the thermodynamics of LFM was expanded upon by Yoon *et al.* [7], and Handwerker *et al.* [8], who used it to develop equations for the concentrations of liquids in equilibrium with coherently stressed and curved solids, and liquids in equilibrium with stress-free, planar solids. These were then used to obtain boundary conditions for diffusion of solute across the liquid film. This can be seen schematically in Figure 2.1, in which the free energy curves are shown for coherently strained solid and unstrained solid phases which are in supposed equilibrium with a B-rich liquid phase (Figure 2.1(a)). The accompanying concentration profile that develops in the neighbourhood of the liquid film is also shown (Figure 2.1(b)).

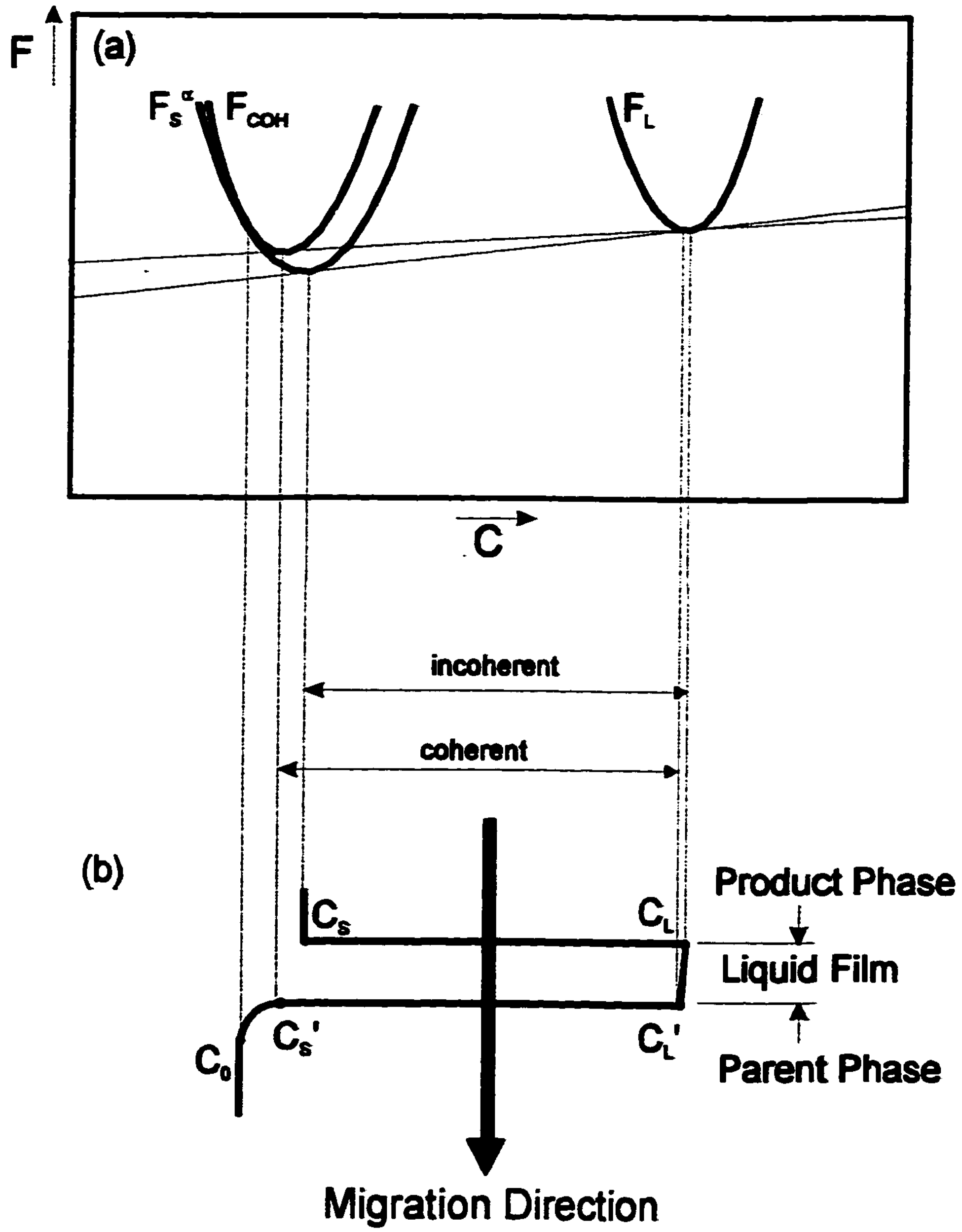

Figure 2.1: **(a) Schematic Molar Free Energy Curves of Stress Free and Coherent Solid Phases in Equilibrium with A Liquid Phase; (b) the Associated Concentration Profile Across A Migrating Liquid Film.**

Equation For the Concentration Difference Across the Liquid Film (ΔC)

For cubic crystals in the small strain approximation, the elastic energy of a thin*, coherent layer enriched in solute with respect to the bulk crystal is given by:

$$w_{EL} = Y(\boldsymbol{n})\epsilon^2 \tag{2.2}$$

Where;

n	Plane normal of stressed surface
ϵ	Strain in the coherent layer

Equation (2.2) is equivalent to Equation (2.1) provided that the change of lattice parameter with composition follows Vegard's law, such that the strain (ϵ) can be approximated by $\eta(C_S'-C_0)$. Equation (2.2) thus gives the increased energy of the coherent layer with respect to the underlying stress free crystal. There will then exist a local equilibrium between the coherently stressed solid and the adjacent liquid phase. Larché and Cahn [9] derived the relevant equilibrium conditions from the thermodynamics of solids. For the case of a dilute, binary solution, with a stressed and curved solid in equilibrium with the liquid, the equilibrium conditions are defined by:

$$\begin{aligned} {}^\circ\mu_{1S} - {}^\circ\mu_{2S} + RTln\left(\frac{\gamma_{1S}'C_S'}{\gamma_{2S}'(1-C_S')}\right) + 2V_m Y(\boldsymbol{n})\eta^2(C_S'-C_0)^2 \\ = {}^\circ\mu_{1L} - {}^\circ\mu_{2L} + RTln\left(\frac{\gamma_{1L}C_L'}{\gamma_{2L}(1-C_L')}\right) \end{aligned} \tag{2.3a}$$

and

---

* Note: the diffusion zone is thin with respect to the principal radii of curvature of the solid surface.

$$
\begin{aligned}
{}^{\circ}\mu_{2S} + RTln\left(\gamma_{2S}'(1-C_S')\right) + V_m\left(Y(n)\eta^2\left(C_0^2-(C_S')^2\right) + \sigma K\right) \\
= {}^{\circ}\mu_{2L} + RTln\left(\gamma_{2L}(1-C_L')\right)
\end{aligned}
\qquad \textbf{(2.3b)}
$$

For an unstressed and planar solid in equilibrium with the liquid, Equations (2.3a) and (2.3b) simplify to:

$$
\begin{aligned}
{}^{\circ}\mu_{1S} - {}^{\circ}\mu_{2S} + RTln\left(\frac{\gamma_{1S}C_S}{\gamma_{2S}(1-C_S)}\right) \\
= {}^{\circ}\mu_{1L} - {}^{\circ}\mu_{2L} + RTln\left(\frac{\gamma_{1L}C_L}{\gamma_{2L}(1-C_L)}\right)
\end{aligned}
\qquad \textbf{(2.4a)}
$$

and

$$
{}^{\circ}\mu_{2S} + RTln\left(\gamma_{2S}(1-C_S)\right) = {}^{\circ}\mu_{2L} + RTln\left(\gamma_{2L}(1-C_L)\right) \qquad \textbf{(2.4b)}
$$

Where:

${}^{\circ}\mu_{iS}$ and ${}^{\circ}\mu_{iL}$	Standard chemical potentials of species i in the solid and liquid respectively.
γ_{iS} and γ_{iL}	Activity coefficients of the i'th component in the solid and liquid respectively.
C_S and C_L	Mole fractions of component 1 (solute) in the solid and liquid.
V_m	Molar volume of the solid.
σ	Specific solid - liquid interfacial energy.
K	Mean curvature, (= $1/\rho_1 + 1/\rho_2$, where ρ_1 and ρ_2 are the principal radii of curvature of the solid - liquid interfaces).

Note: All primed quantities are with respect to the stressed state.

Equations (2.3), for the stressed, curved solid in equilibrium with the liquid phase, and (2.4), for the unstressed planar solid in equilibrium with the liquid phase, imply that the Gibbsian common tangent construction is valid for both cases. If it is now assumed that the changes in solubility due to stress and curvature are small[**] (*i.e.* $C_S' \approx C_S$), and that $C_S \ll C_L$, it is possible to expand Equations (2.3a) and (2.3b) to the second order about C_0. Using Equations (2.4a) and (2.4b), it is possible to solve for C_L and C_L'. This gives the following equation [7,8,43,48]:

$$\Delta C = C_L' - C_L = \frac{\dfrac{f_{EL}\, f_{MS}}{(f_{EL} + f_{MS})}\,(C_S - C_0)^2 + \sigma K V_m}{2(C_L - C_S)\, f_{ML}} \tag{2.5}$$

Where:

$$f_{EL} = V_m Y(n) \eta^2 \tag{2.6}$$

$$f_{MS} = \frac{1}{2}\,\frac{\partial^2 F_S}{\partial C_S^2} = \frac{1}{2}\, RT\, \frac{\left(1 + \dfrac{\partial \ln \gamma_S}{\partial \ln C_S}\right)}{C_S(1 - C_S)} \tag{2.7}$$

$$f_{ML} = \frac{1}{2}\,\frac{\partial^2 F_L}{\partial C_L^2} = \frac{1}{2}\, RT\, \frac{\left(1 + \dfrac{\partial \ln \gamma_L}{\partial \ln C_L}\right)}{C_L(1 - C_L)} \tag{2.8}$$

[**] Note: in the small strain regime this is a valid approximation; referring to Figure 2.1, it can be seen that C_S' is very close to C_S.

Note:

f_{EL}	Coefficient of strain energy
f_{MS}	Coefficient of the free energy of mixing of the solid phase
f_{ML}	Coefficient of the free energy of mixing of the liquid phase
F_S and F_L	Molar free energies of the stress free solid and liquid respectively.
γ_S and γ_L	Activity coefficient of the solute in the stress free solid and liquid respectively.

If it is assumed that all solid phases are dilute, then it is a fair assumption that they are Henrian solids. Equation (2.7) then simplifies to:

$$f_{MS} = \frac{1}{2}\,\frac{RT}{C_S(1-C_S)} \qquad (i.e.;\ \frac{\partial \ln\gamma_S}{\partial \ln C_S} = 0) \qquad \textbf{(2.9)}$$

In the following expressions, Equation (2.9) will be used to estimate the coefficient of the free energy of mixing (f_{MS}), since most systems exhibiting LFM have dilute solid components.

Equation (2.5) therefore yields the concentration gradient of solute across the liquid film in terms of well defined physical parameters. Most of these parameters can be obtained from independent sources (and /or experiment), with the exception of K, the mean curvature of the solid, as well as the solute activity coefficients. Through the elastic energy term, the coupling is provided between the free energy of mixing due to diffusion at the interface, and boundary motion, (*i.e.* part of the available free energy of mixing is converted into the coherency strain energy, which may then drive the migration). Figure 2.2 can be used to illustrate.

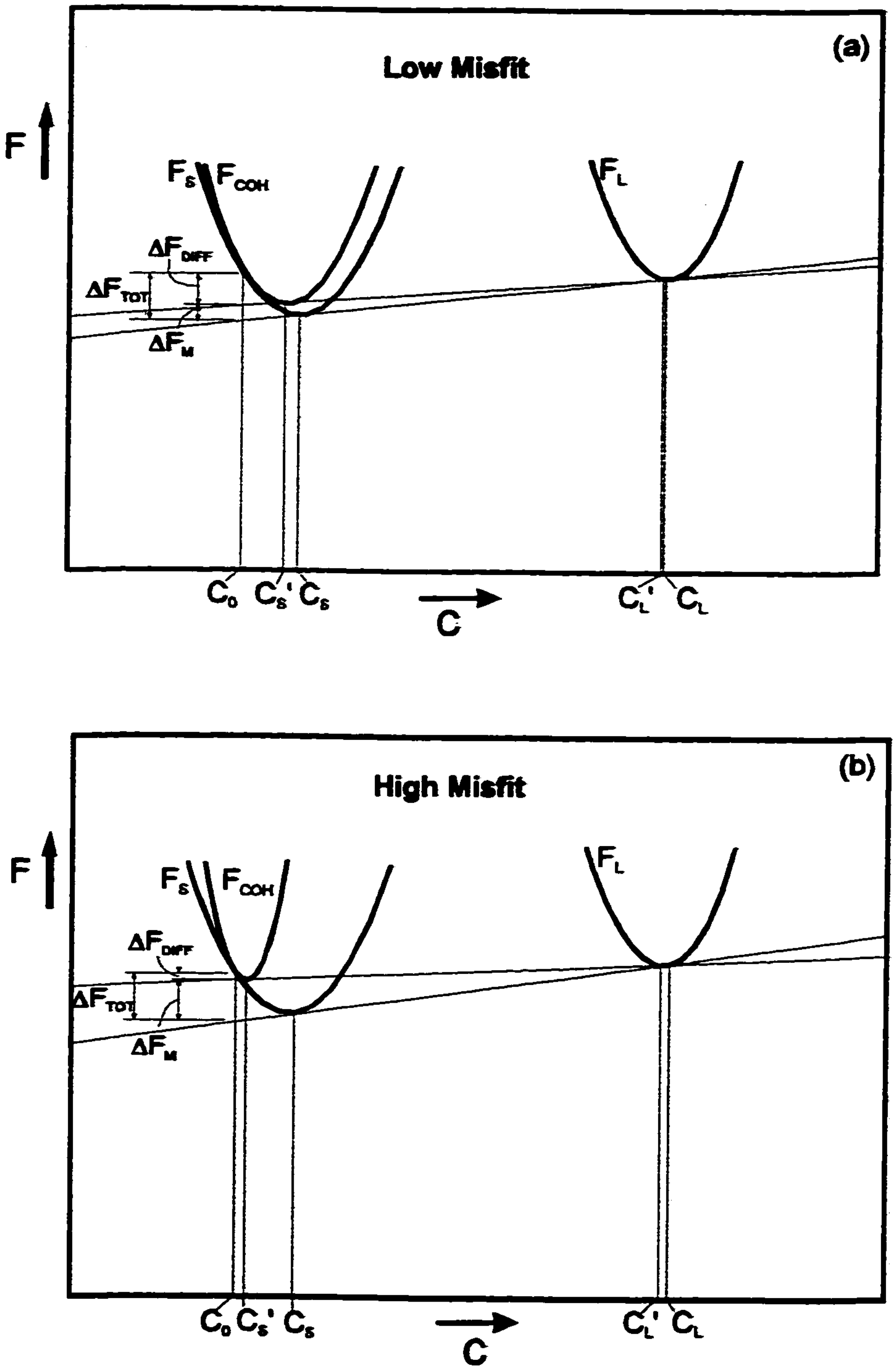

Figure 2.2: **Schematic Molar Free Energy Curves of Stress Free and Coherent Solid Phases in Equilibrium with A Liquid Phase for the Case of: (a) Low Misfit; (b) High Misfit.**

The total free energy change associated with the transformation of the parent solid (composition C_0) into a stress free solid product (composition C_S) is denoted ΔF_{TOT} . According to Yoon [48] the term:

$$\Delta F_M = \frac{f_{EL}\, f_{MS}}{(f_{EL} + f_{MS})}\,(C_S - C_0)^2 + \sigma K V_m \tag{2.10}$$

is the driving force for LFM, and the difference $\Delta F_{DIFF} = \Delta F_{TOT} - \Delta F_M$ is the free energy dissipated by diffusion during the frontal diffusion process. In reference to Equation (2.10) it can be seen that for low misfit (*i.e.*, $f_{EL} << f_{MS}$) indicative of alloy systems that exhibit LFM, ΔF_M simplifies to:

$$\Delta F_M = f_{EL}\,(C_S - C_0)^2 + \sigma K V_m \tag{2.11}$$

In reference to Equation (2.6) this implies that the driving force for migration is equal to the coherency strain energy (= $V_m \cdot w_{EL}$) in the absence of any interfacial curvature. Figure 2.2(a) shows the free energy curves for this case, and it can be seen that only a fraction of the free energy available for migration (ΔF_{TOT}) is used to drive the migration, and a large fraction (ΔF_{DIFF}) is dissipated in the diffusion process to form the coherent layer. Figure 2.2(b) shows the free energy curves for the case of high misfit. In this case the driving force for migration (ΔF_M) is almost equal to the total free energy available for migration (ΔF_{TOT}), with only a small fraction (ΔF_{DIFF}) dissipated during the frontal diffusion process to form the coherent layer. It should be noted that in the preceding discussions, the coherency strain energy given by Equation (2.2), is valid only for cases where the solute enriched zone is perfectly coherent with the underlying bulk crystal. As a result, ΔC ($\equiv C_L' - C_L$) given by Equation (2.5), is an upper bound to the composition difference across the liquid film, and will be reduced by stress relief mechanisms such as plastic flow, and the production / attraction of misfit dislocations. It is therefore possible that ΔC, estimated using Equation (2.5), is valid for the case of low misfit (Figure 2.2(a)), but unlikely to be valid for the case of high misfit (Figure 2.2(b)). This is due to the fact that coherency will only be maintained ahead of the migrating liquid film if the interface is moving at a velocity (v), such that the effective penetration distance (D_S/v) is small enough to maintain coherency, where D_S is the diffusion coefficient of solute in the solid phase. This will be discussed in more detail in Section 2.4.2.

Special Cases of Equation 2.5

(i) Small η Regime

In the condition of low coherency strain energy with respect to the free energy of mixing (see Figure 2.2(a)), which is indicative of most systems exhibiting LFM, $f_{EL} \ll f_{MS}$, and Equation (2.5) becomes:

$$\Delta C = C_L' - C_L = \frac{f_{EL}\,(C_S - C_0)^2 + \sigma K V_m}{2(C_L - C_S)\,f_{ML}} \tag{2.12}$$

(ii) Large η Regime

In the condition of high coherency strain energy with respect to the free energy of mixing (see Figure 2.2(b)), $f_{EL} \gg f_{MS}$, and Equation (2.5) becomes:

$$\Delta C = C_L' - C_L = \frac{f_{MS}\,(C_S - C_0)^2 + \sigma K V_m}{2(C_L - C_S) f_{ML}} \tag{2.13}$$

Equations (2.12) and (2.13) are drawn schematically in Figure 2.2 to indicate the effect of elastic energy upon the solidus and liquidus compositions. Assuming that coherency is maintained it should be noted that for a binary system with a high elastic energy, the assumption that the solute solubility does not change with stress is no longer valid, and

(C_S-C_0) must be replaced by $(C_S'-C_0)$ in Equations (2.5) and (2.13).

(iii) Two Different Solids Separated by the Liquid Film

Consider two grains (A and B) separated by a liquid film. Each solid has different initial compositions, but are of the same phase, *i.e.* (C_0^A, C_0^B); each has different elastic coefficients $(Y(\mathbf{n}^A), Y(\mathbf{n}^B))$, and different curvatures (K^A, K^B). Assuming that the coherency strain energy is low with respect to the free energy of mixing, the concentration difference across the liquid film is calculated using Equation (2.12) for each solid in turn, and the difference taken between the two equations, giving:

$$\Delta C = C_L^{A\,\prime} - C_L^{B\,\prime}$$

$$= \frac{f_{EL}^A(C_S-C_0^A)^2 - f_{EL}^B(C_S-C_0^B)^2 + \sigma(K^A-K^B)V_m}{2(C_L-C_S)f_{ML}} \qquad \textbf{(2.14)}$$

The variation in f_{EL} between grain A and grain B in this approximation is simply due to the different orientations of the two grains, and thus a difference in elastic moduli $(Y(\mathbf{n}^i))$.

(iv) Two Solids of the Same Initial Composition

This case is a special case of Equation (2.14), in which we have $C_0^A=C_0^B=C_0$. This is a common occurrence in systems that have been observed to undergo LFM. Equation (2.14) then simplifies to:

$$\Delta C = C_L^{A\,\prime} - C_L^{B\,\prime} = \frac{(f_{EL}^A-f_{EL}^B)(C_S-C_0)^2 + \sigma(K^A-K^B)V_m}{2(C_L-C_S)\,f_{ML}} \qquad \textbf{(2.15)}$$

(v) Two Solids with the Stress Completely Relaxed in One Grain

This is a special case of the above two equations, in which f_{EL}^B is reduced to zero (*i.e.*, coherency is lost in grain B), Equation (2.15) then simplifies to:

$$\Delta C = C_L^{A\,\prime} - C_L^B = \frac{f_{EL}^A (C_S - C_0)^2 + \sigma(K^A - K^B) V_m}{2(C_L - C_S)\, f_{ML}} \qquad \textbf{(2.16)}$$

Equations (2.12), (2.14), (2.15), and (2.16) describe the concentration difference across a liquid film that separates grains of varying stress states, curvature, and initial compositions for the case of low misfit. In all these equations it is assumed that Vegard's law holds. If Vegard's law is not valid, then in order to apply the above equations, the expression $\eta(C_S-C_0)$ should be replaced by the strain ϵ. Depending upon the experimental situation under consideration, the corresponding equation can be used to define boundary values for diffusion of solute across the liquid film. This is done in the next section in order to obtain an expression for the velocity of the liquid film.

Expression For the Velocity of the Liquid Film

Assuming that diffusion across the liquid film is conductive (*i.e.*, convection is negligible), the flux of solute across the liquid film can be adequately approximated by Fick's First Law, that is:

$$J = -D_L(\nabla C) \qquad \textbf{(2.17)}$$

Where:

D_L	Diffusion coefficient for the solute in the liquid phase
∇C	Gradient in solute concentration across the liquid film.

Now, at the solidification front (*i.e.*, at the trailing interface), the rate at which solute diffuses down the concentration gradient is equal to the rate at which solute is rejected from the solidifying liquid, that is:

$$-D_L \nabla C = v(C_L - C_S) \tag{2.18}$$

Where:

C_L and C_S — Concentrations of solute in the liquid and solid phases respectively at the trailing (solidifying) interface. For a planar, stress-free product phase, these can be assumed to be the equilibrium concentrations (obtained from the phase diagram).

v — Velocity of the solidifying interface.

If it is now assumed that solute diffuses directly across the liquid film (*i.e.*, one-dimensional diffusion path), ∇C can be approximated by $\Delta C/\delta$, where δ is defined as the liquid film thickness measured parallel to the migration direction. Equation (2.18) can therefore be written:

$$v = \frac{D_L \, \Delta C}{(C_L - C_S)\,\delta} \tag{2.19}$$

Equation (2.19) defines the velocity of the liquid film under conditions where there is assumed to be an unlimited supply of solute to the growing phase. The concentration difference across the liquid film (ΔC) is given by Equations (2.12) to (2.16), depending upon the specific experimental conditions. The limitations of this expression are discussed in more detail in Section 2.6.

2.4.2 Initiation of LFM and Coherency Loss

Initiation of LFM.

Consider two initially stress free and homogenous grains, separated by a thin liquid film. If it is assumed that both grains are initially in local equilibrium with the liquid phase, then nothing will happen unless the experimental conditions are changed. For instance, changing the temperature or in the case of a binary system the introducing a third or fourth element, will lead to transient behaviour during which diffusional processes attempt to re-achieve local equilibrium. Solid-state diffusion of solute into (or out of) the two grains will ensue. If there is an atomic mismatch between atoms in the system under study, there will then be an accompanying energy increase in the surface layers of the grains due to coherency strain (see Equation (2.2)). This will affect the liquid compositions in local equilibrium with the two grains. LFM will then initiate in the direction of the more highly stressed solid. Differences in the increase of energy between the two grains are due to:

- Differences in the elastic constants of the two grains ($Y(\mathbf{n}^i)$), since each solid has different atomic planes parallel to the liquid film. Note: for cubic materials, the variation of $Y(\mathbf{n})$ with orientation has been calculated by Hilliard [44], and is discussed in Chapter Six.
- Stress relaxation in one of the grains.
- Different initial composition of the two grains.

The velocity of the liquid film in the early stages of migration is therefore given by Equation (2.19), with the composition difference (ΔC) obtained from either Equation (2.14) or (2.15), depending on the initial conditions. For systems with negligible initial curvature, and with $C_0^A = C_0^B = C_0$, it can be seen that the film will migrate into the grain with the higher modulus ($Y(\mathbf{n})$).

Coherency Loss

Migration will continue as described above until some stress relaxation occurs in one of the grains. The stresses due to coherency may relax due to plastic flow, or through various possible dislocation mechanisms. As can be seen from Equations (2.14), (2.15) and (2.19), this will affect the velocity of the migrating film. However, the stress due to coherency will not be reduced significantly until the diffusion distance in the solid has reached a critical thickness (L_C), where dislocation generation becomes significant [45,46]. It first appeared that the critical diffusion thickness (L_C) varied inversely with the elastic modulus of the grain in question, and coherency would therefore be broken in the grain with the highest value for$Y(\mathbf{n})$; however this is likely not the case [18,22,43]. This is possibly due to the fact that while the elastic energy of a coherent layer is proportional to $Y(\mathbf{n})$, the energy of the misfit dislocations is also approximately proportional to $Y(\mathbf{n})$ [47]. It is therefore possible that L_C is not strongly dependent on $Y(\mathbf{n})$, and as a result it is likely that coherency will be broken locally at the surface on either side of the liquid film, depending on the presence of pre-existing dislocations and dislocation sources, as well as the local probability of dislocation nucleation. This hypothesis is consistent with the fact that liquid films, present on the same grain boundary, have often been observed to migrate in opposite directions, resulting in a characteristic "zig-zag" microstructure. Baik and Yoon [18] have applied the analysis of Matthews [47], who looked at the loss of coherency in thin epitaxial layers due to the production of misfit dislocations, to the case of coherency loss in LFM and DIGM. However, their analysis considered only the nucleation of misfit dislocations, and as a result their predictions must be used with some care. The meaning of the parameter D_S/v with respect to loss of coherency is discussed in more detail below.

In the absence of any film migration, a characteristic diffusion layer thickness is of the order of $\sqrt{D_S\ t}$ where D_S is the lattice diffusivity of solute in the alloy in question, and t is time.

Consider now a liquid film migrating at a constant velocity, v. In the growing grain, the diffusion layer thickness (L) is approximately given by:

$$L = \sqrt{D_S t} + vt \tag{2.20}$$

While in the dissolving grain, L will be given by a steady state thickness (D_S /v), and will be of the form [7]:

$$L = \sqrt{D_S t}\left(\frac{\sqrt{D_S t}}{\sqrt{D_S t} + vt}\right) \tag{2.21}$$

Therefore:

if $\sqrt{D_S t} >> vt$ then $L = \sqrt{D_S t}$

and if $\sqrt{D_S t} << vt$, then $L = D_S /v$.

It should now be possible to describe liquid film migration behaviour, from the early stages of migration when the experimental conditions are changed (as the system attempts to re-equilibrate), up until coherency is lost in one of the grains, and the so-called "steady-state" migration that follows. Consider again the case of two identical grains separated by a liquid film. When the experimental conditions are changed, the system will attempt to reach a new equilibrium, and diffusion of solute will commence into (or out of) the solid phase on either side of the liquid film. A concentration difference between the two grains will then develop across the liquid film, due to differences in elastic moduli, and/or curvature, which may be obtained from Equation (2.15). Migration is assumed to initiate in the direction of the highest energy increase; therefore substituting the concentration difference (Equation (2.15)) into the velocity expression (Equation (2.19)) will give the initial velocity of the liquid film. The film will continue to migrate at this velocity until some coherency loss occurs. If the initial velocity is greater than D_S/L_C, then coherency will be lost after some time in the growing grain (in the wake of the migrating film). However, since many other factors influence the velocity of the film, such as the difference in $Y(\mathbf{n})$ between the growing and dissolving grains, and the solubility of the solute in the liquid, it is quite possible that $v \ll D_S/L_C$. In this case, the velocity does not significantly affect the diffusion layer thicknesses, and coherency will most likely be lost in the grain of higher $Y(\mathbf{n})$. This would result in the film reversing its direction of migration. Predictions of liquid film position in the latter case are difficult to obtain, since the 'initial' stages of migration last only a very short time, and it is most likely that if $v \ll D_S/L_C$, coherency will be lost on both sides of the liquid film and the film will become stationary.

Steady State Growth After Coherency Loss

If the initial velocity is greater than D_S/L_C as described in the previous section, coherency will be lost in one of the grains while the other grain remains coherently stressed. The grain in which coherency is lost is referred to as the 'growing' grain, while the coherently stressed grain is referred to as the 'dissolving' grain. Under these conditions, the concentration difference, and thus velocity, depend only upon the value of $Y(\mathbf{n})$ in the dissolving grain. The concentration difference will therefore be given by Equation (2.16), and the corresponding velocity obtained from Equation (2.19). If the ends of the liquid films are effectively pinned, then migration will progress, and bulges of "new" alloy are formed in the wake of the migrating interface. The relative differences in curvature may then become significant enough so that the term $\sigma(K^A-K^B)$ is dominant in Equation (2.16), and migration may stop or be reversed. The validity of the term $\sigma(K^A-K^B)$, and other limitations of the Yoon *et al.* model [7] will be discussed further in Section 2.6.

2.5 EXPERIMENTAL EVIDENCE FOR COHERENCY STRAIN ENERGY AS THE DRIVING FORCE FOR LFM

In this section, observations of liquid film migration (LFM) are discussed from the viewpoint that coherency strain energy is the driving force for the phenomenon. A series of experiments performed predominantly on metallic liquid phase sintered specimens at K.A.I.S.T. designed to determine whether the coherency strain energy due to solute diffusion ahead of the migrating liquid film is the driving force for LFM are discussed in some detail. Other observations of LFM are then discussed within the context of the coherency strain energy hypothesis.

Since the observation of LFM in 1979 by Yoon and Huppmann [1], a large amount of evidence to support the coherency strain hypothesis has been gathered. Many of the experiments were performed at K.A.I.S.T. using metallic liquid phase sintering systems, particularly molybdenum based alloys [7,16-24], tungsten based alloys [1,15], and Co-Cu alloys [25]. Their experiments have provided evidence that the migration behaviour is consistent with the coherency strain hypothesis. That is, there is a strong indication that part of the chemical free energy is dissipated during lattice diffusion ahead of the migrating interface forming a strained layer, and that the resulting strain energy remains as the driving force for LFM during the 'steady-state' migration period. Many of the experiments were performed using ternary systems, in which the coherency strain can be varied in both sign and magnitude, and perhaps most importantly independent of the free energy of mixing [7]. A brief discussion of coherency strain in ternary alloys follows, before discussing the experiments in detail.

Consider a ternary system with a liquid film separating two grains. If it is assumed that a thin layer of composition (C_{S1},C_{S2}) is coherent with the parent grain of composition (C_{01},C_{02}), then the elastic energy of the coherent layer is given by Equation (2.2), with the coherency strain, ϵ, assumed to be:

$$\epsilon = \eta_1(C_{S1}-C_{01}) + \eta_2(C_{S2}-C_{02}) \qquad (2.22)$$

Where:

η_1 and η_2 Lattice misfit parameters of solute species 1 and 2 in the solid phase.

It should be noted that in this set of experiments it is usually assumed that both solute species are dilute enough that η_1 and η_2 can be obtained from binary data. It can therefore be seen that the strain, ϵ, can be positive, negative, or zero, depending upon the values of η_1, η_2, $(C_{S1}-C_{01})$, and $(C_{S2}-C_{02})$. Ternary alloys can therefore be used as a qualitative test of the coherency strain model. By the appropriate choice of solute species, the coherency strain can therefore be varied systematically; in particular, the migration velocity should reduce to zero, if the estimated coherency strain is zero. It should be noted that experiments of this type only indicate the variation of migration rate with the estimated coherency strain, and no direct coupling of the coherency strain energy to the composition of the liquid in local equilibrium with the stressed grain has yet been attempted. As a result, an analytical expression for the velocity of the film cannot be obtained as yet.

Before discussing specific experiments in the context of the coherency strain energy hypothesis, it should be noted that one of the major assumptions of the coherency strain theory developed in the course of this introduction, is that part of the available chemical free energy is converted to coherency strain energy (from lattice diffusion ahead of the migrating interface). It is this energy that drives the migration, and not the total available chemical free energy. Other driving forces for interface migration have been proposed (see [48] for a review), including the theory that the interfaces migrate due to the free energy reduction resulting from equilibration. Cahn *et al.* [49], and Baluffi and Cahn [50] used the example of the free energy available from isotope mixing, and showed that this driving force could not universally lead to interface migration. That is to say that the driving force could not arise from either the ideal entropy of mixing, or from the deviation from ideality.

Most of the liquid phase sintering experiments performed follow the same kind of procedure, in which a sample was initially liquid phase sintered for a relatively long time in order to equilibrate the liquid and solid phases. The volume fraction of liquid was usually low, such that most of the liquid was dispersed as thin films separating the grains. When the liquid phase composition was altered by either changing the temperature or adding elements which had some solid solubility in the parent grains, extensive LFM was observed in cases where the estimated coherency strain energy was non-zero. These experiments are discussed further below.

In a liquid phase sintered Mo-Ni alloy, Baik and Yoon [16] observed that liquid films migrated when the temperature was either increased or decreased from the initial equilibration temperature. The migration rate varied parabolically with the difference in composition (ΔC), that is the difference in composition between the solidus composition at the equilibration temperature (T_{SINTER}) and the solidus composition at the heat treatment temperature (T_{EXP}).

LFM has also been observed in Mo-Ni alloys where a third and / or fourth element was added to the liquid phase [15,17-24]. In all cases, liquid films were observed to migrate when the estimated coherency strain was non-zero. The coherency strain in these systems was estimated by assuming that the local equilibrium compositions at the solid - liquid interfaces could be described by the final equilibrium conditions (determined by the tie lines between the phases). Since the liquid phase additives, Ni, Fe, and Co form dilute solid solutions with Mo, it can be assumed that the liquid phase composition will remain constant in the early stages of the migration; the solid phase in local equilibrium with the liquid would therefore have a constant composition (in the early stages) if this assumption were valid. This was indeed true of the observations of LFM when liquid phase sintered Mo-Ni was treated with Fe or Co additives [17,18,22,23]. The measured composition difference between that of the parent solid and that formed in the wake of migrating liquid films can therefore be used to estimate the coherency strain (through Equation (2.22)) for varying liquid compositions. The most convincing of these experiments added different combinations of two solute species to the liquid phase to vary both the sign and the magnitude of the coherency strain, ϵ, in accordance with Equation (2.22) [18,20,22,23]. For instance, Rhee, Song, and Yoon [22], and Rhee and Yoon [23] added both Co and Sn in different ratios to the liquid phase in a Mo-Ni alloy. The addition of Sn caused the Ni concentration in the solid grain surfaces to decrease resulting in compressive strains, while the Co addition caused tensile strains in the solid Mo-Ni grain surfaces. It was observed that the rate of LFM varied parabolically with the coherency strain, ϵ, and no migration was observed when $\epsilon = 0$. Another important result of these particular studies is that even when no LFM was observed (*i.e.*, the $\epsilon = 0$ condition), diffusion of Ni (out of the grains) and Co (into the grains) will occur since the solid - liquid system is chemically unstable. This indicates that the prediction of Baluffi and Cahn [50], *i.e.*, that the reduction in chemical free energy is a necessary but insufficient criterion for interface migration is correct. Similar experiments were performed by Baik and Yoon [18] in which the coherency strain, ϵ, was varied by the simultaneous addition of Fe and the reduction of the Ni content in the liquid phase. Again, LFM was not observed when the estimated coherency strain was zero. Kang, Hackney, and Yoon [20] induced LFM by simultaneously adding W to the liquid phase while decreasing the temperature (to decrease the Ni content). Since W has a large solid solubility in Mo, the W content in the wake of the migrating film decreased with distance migrated, making the coherency strain energy more difficult to estimate. However, little or no LFM was observed when $\epsilon \approx 0$. Blendell *et al.* [37] also observed that during the liquid phase sintering of MgO-V_2O_5, with NiO and CoO added to the liquid phase in varying ratios, no LFM occurred when the $\epsilon = 0$ condition was achieved.

Other experimental work has attempted to induce LFM under a variety of conditions. In a different set of experiments Baik and Yoon [19] induced an instability in the solid - liquid interface of Mo-Ni grains with a relatively high volume fraction of liquid, by changing the temperature, or introducing a third element. Upon changing the temperature of the heat treatment, some migration of the liquid films was observed where the grains were separated by a thin liquid film; in addition an instability in the solid - liquid interface developed as shown in Figure 2.3. It can be seen that there are regions of the original grain stressed due to coherency, resulting in a dissolution / reprecipitation process on adjacent regions of the same grain, (the hatched areas of Figure 2.3 represent the reprecipitated region). Similar microstructures developed when iron was added to the liquid matrix, with the undulations having a different amplitude depending upon the estimated magnitude of the coherency strain. Perhaps most importantly, no instability in the solid - liquid interface was observed when the estimated coherency strain was zero, further enforcing the coherency strain theory as the driving force for this process. A similar surface corrugation was also observed in the ZrO_2 - Y_2O_3 system treated with mixtures of MgO and Y_2O_3 in varying ratios [39]. Again, the coherency strain was systematically varied from compression to tension and no surface corrugation was observed when the estimated coherency strain was zero.

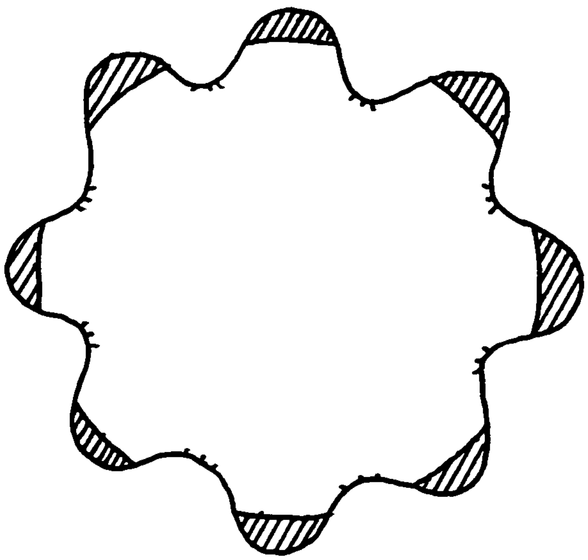

Figure 2.3: **Solid - Liquid Instability That Develops During the Liquid Phase Sintering of Systems with High Liquid Volume Fractions. The Hatched Areas Represent the Reprecipitated Region, While the Troughs Represent Regions Coherent with the Parent Phase.**

In yet another set of experiments, Baik and Yoon [24], attempted to test the prediction of Yoon *et al.* [7], that migration occurs in the direction of the grain with the greatest magnitude of coherency strain energy. This was done by adding tungsten or tin to a Mo-Ni sample that was already undergoing LFM; this would cause these atoms to momentarily diffuse into both the growing and retreating grains. Since the growing grain was initially stress free, the "new" strain is mainly due to diffusion of the third atom, while in the retreating grain the coherency strain is due to both nickel and third element diffusion. The difference in energy between the growing and retreating grains will thus change according to which element was added, and how much was added. Their results show that if a third element is added such that the strain in the retreating and growing grains is equal, then the migration will stop; if the strain in the retreating grain remains higher than in the growing grain the direction of migration remains unchanged but a different velocity was observed. Finally, if the strain in the retreating grain is less than that in the growing grain, the migration reverses direction. The results show that the predictions of Yoon *et al.* [7] are qualitatively correct.

Lee and Yoon [21] used the Mo-Ni system with W added to the liquid phase to determine if LFM occurs in a system where the effective diffusion distance (D_S / v) ahead of the migrating interface is smaller than the interatomic spacing (λ). The concept of coherency strain in such an alloy system is therefore quite ambiguous. That is to say that if LFM occurs in a system with (D_S / v) < λ, it can be assumed that no solute diffusion ahead of the leading solid - liquid interface is possible, and therefore local equilibrium cannot exist. The results of the study show that LFM was observed even where (D_S / v) << λ, and that the driving force was of the same order of magnitude as the coherency strain energy (*i.e.*, the total chemical free energy change associated with the transformation was approximately 5000 times too large). It was concluded that (D_S / v) is not a meaningful measure of the penetration distance of solute during the migration. This is possibly due to the fact that diffusion over very small distances (of the order of λ) may not accurately be described by the usual diffusion equations, and as a result, it is possible that some diffusion does occur ahead of the leading solid - liquid interface forming a coherent zone.

Kim and Yoon [25] in their study of LFM in Co-Cu alloys showed that there exists a high temperature limit and a minimum critical driving force for the phenomenon. They observed that for a relatively large coherency strain energy, corresponding to a high Cu content in the liquid phase, LFM was observed at both low and high temperatures. For a relatively small coherency strain energy, corresponding to a low Cu content in the liquid phase, LFM was observed only at low temperatures. They explained this observation in reference to the solute penetration distance (D_S / v). At high temperatures and with a low value for the coherency strain energy, the parameter (D_S / v) is so large that coherency was not maintained in the frontal diffusion zone, resulting in the loss of the driving force. At lower temperatures, the parameter (D_S / v) was in the range allowable for coherency to be maintained ahead of the leading interface, and LFM occurred. In another study of LFM in Co-Cu alloys, Baik, Kim, and Yoon [51] observed facetted growth during LFM. It was observed that two grains of different orientation that were growing into another grain developed nearly parallel liquid film facets. This indicates that the facetting of migrating liquid films in this case is determined by the orientation of the dissolving grain (and thus $Y(\mathbf{n})$), it will therefore not necessarily reflect the equilibrium shape of the growing grain.

Muschik *et al.* [27], observed that during the melting of copper-8.3%indium alloys, the originally smooth boundary developed sharp bulges. Electron microprobe analysis showed that the indium content in the wake of the moving film was less than in the original alloy, and was in fact the equilibrium solidus composition at the temperature of the experiment. The authors used the analysis of Yoon *et al.* [7] to obtain the In content in the liquid which is in local equilibrium with a coherently stressed solid, and in turn to obtain a velocity expression similar to that of Yoon *et al.* [7]. The results are shown to be consistent with the coherency strain theory. It is interesting to note that in this case indium is diffusing out of the parent crystal creating the coherent zone, rather than the usual case of solute diffusing into the parent crystal and distorting the lattice. As a result, the liquid film gains solute as it migrates, and thus the films widen as migration progresses.

LFM has been observed in the Al-Cu system by Kuo and Fournelle [28]. Migration was induced by changing the temperature after previous equilibration in the solid - liquid phase region. Kuo and Fournelle [28] state that the migration distance decreases monotonically with annealing time, and obeys a power law relationship. Furthermore, they indicate that the coherency strain energy developed in the dissolving grain is insufficient to drive the migration against the curvatures observed. These conclusions require some discussion. The fact that the migration distance and time obey a power law relationship is irrelevant in terms of determining the driving force for the reaction. The shape of their plot of migration distance as a function of time can be explained as follows: since the liquid films are pinned at their ends, it is possible that the coherency strain energy is partially counterbalanced by the increasing energy due to curvature of the liquid lens as the migration progresses. It is also possible that the effective Cu content in the parent phase increases with time, due to the fact that liquid pools, present in the grain interiors, lose solute as they solidify. Both of which will reduce the effective driving force for migration. Their analysis of the coherency strain energy is based upon the measured Cu concentration difference between the parent and product phases, which is of the same order of magnitude as the random error in their microprobe analysis. Since any error in the measured concentrations is effectively magnified due to the parabolic dependence of coherency strain energy on composition (Equation (2.1)), any conclusions based on their calculated coherency strain energy must therefore be made with care.

The observation of LFM in a TiN-Ni alloy induced by C diffusion (from a TiC source) [40] shows that the migration rate increases parabolically with the observed lattice parameter difference between TiN and Ti(NC). This is consistent with the coherency strain model, indicating that diffusion induced LFM occurs in systems possessing relatively strong covalent bonding. Two types of migrating liquid film shapes were observed. The first type had the smoothly curved morphology indicative of most systems exhibiting LFM. The second type showed facets on growing grains while the dissolving grains remained smoothly curved. LFM was also observed in the ZrO_2 system with CeO_2 additions [41]. Evidence was found to indicate that Ce de-alloying occurred in the volume swept by the migrating film. It was suggested that the coherency strain due to the partial reduction of Ce, resulting in the diffusion of Ce^{3+} out of the ZrO_2 lattice and along the grain boundaries to the free surface, was the driving force. Since the liquid films were pinned, the migration was opposed by the increasing energy due to curvature. It was noted that the liquid films stopped migrating when the calculated energies due to coherency and curvature were approximately equal.

Some of the observations of LFM in the heat affected zones of weldments [32-34] have been explained in terms of the coherency strain energy hypothesis. Radhakrishnan and Thompson [32] determined that LFM was induced by the constitutional liquation of NbC at the grain boundaries of Ni alloy 718. Nakkalil *et al.* [33,34] determined that the constitutional liquation of MNP phosphides and MC carbides (where M was either Al, Ti and/or Nb) were the cause of LFM in Incoloy 903. In both cases the system was no longer in chemical equilibrium after the infusion of heat from the weld pool, and diffusion of solute atoms into the matrix at the solid - liquid interface occurred in an attempt for the system to re-equilibrate. The resulting strain energy was assumed to be the driving force. A quantitative analysis was not attempted due to the complex chemistry of the specimens involved.

Other observations of LFM discussed in Section 2.2 have not generally been discussed in terms of the coherency strain hypothesis. However, in cases where the composition profile was measured, the solute content in the wake of the liquid film was approximately constant, and in all cases, liquid films were observed to migrate against their mean radii of curvature.

The experimental observations presented above seem to confirm the hypothesis that the driving force for LFM is the dissipation of the coherency strain energy ahead of the migrating liquid film. That is, during migration, part of the chemical free energy is converted into coherency strain energy through the process of lattice diffusion. This increase in energy in the solid phase will change the equilibrium concentration of solute in the liquid phase, and will define the boundary conditions in concentration across the liquid film, leading to LFM.

2.6 LIMITATIONS

Experimental results of LFM experiments were described in some detail in Section 2.5. It can be concluded that the coherency strain energy ahead of the migrating liquid film is the major driving force for the process. However, quantitative kinetic modelling of LFM based on the coherency strain hypothesis has had limited success. In this section a critical evaluation of the model of Yoon *et al.* [7] will be performed; in addition, general considerations that must be taken into account when applying coherency strain theory to the analysis of LFM will be discussed. This will be done as follows:

- The development and limitations of the expression for the concentration difference across the liquid film (ΔC) given by Equation (2.5), and Equations (2.12) through (2.16) will be discussed.
- The limitations of the 'steady state' velocity expression given by Equation (2.19) will be outlined.
- Other issues which arise during the application of the Yoon *et al.* model [7], including the process of coherency loss and the analysis based upon the critical diffusion distance (L_C), will be considered.

Equations for ΔC

The equilibrium conditions derived from the thermodynamics of solids by Larché and Cahn [9] given by Equations (2.3) and (2.4) were developed by the application of a minimum number of assumptions. The most important assumption is that local equilibrium is maintained at the solid - liquid interfaces. Consider now the case of a dissolving grain and a solidifying grain. For the case of the dissolving grain, atom detachment from solid surfaces into liquids is expected to occur relatively rapidly providing that there exists a driving force for the solid to liquid transition. For the case of the solidifying grain, atom attachment occurs rapidly provided that the surface atomic structure of the growing solid - liquid interface is diffuse, and that the driving force for solidification exists. For the case of LFM, the assumption of local equilibrium at the leading and trailing solid - liquid interfaces is therefore not unreasonable.

The equilibrium described by Equations (2.3a) and (2.3b) derived by Larché and Cahn [9] were expanded to the second order about C_0, and through the use of Equations (2.4a) and (2.4b), Yoon *et al.* [7] developed an equation for the concentration difference across the liquid film (ΔC), given by Equations (2.5) through (2.8). The assumptions that $C_S' \approx C_S$ and $C_S \ll C_L$ made during the expansion are fairly reasonable for most systems that have been observed to exhibit LFM. However, through the expansion to the second order, some assumptions are being made about the shape of the free energy curves of the phases under consideration (*i.e.*, parabolic shape). The resulting equations will likely only be valid for relatively small composition differences (*i.e.*, (C_S - C_0)). The further simplification of this set of equations into a somewhat usable form, requires several more assumptions. For example, the assumption that the solid phase obeys Henry's Law may or may not be a valid assumption depending upon the system under consideration. For systems with very low solid solubility, it is quite possible that they are Henrian solids (*e.g.*, Mo-Ni alloys with additions of Co, Sn, *etc.*), but for systems with some degree of solid solubility (*e.g.*, Al-Cu), this assumption is likely to be in error. For full application of the kinetic model, in the absence of accurate activity coefficient data, it is required that the same assumption be made for the liquid phase, in which case it is a severe over simplification. Most of the assumptions made in obtaining special cases for ΔC (Equations (2.12) through (2.16)) are described in the main text, however a few points should be made. The curvature term given in these equations is corrected from the way it was originally presented, the term '$\sigma K V_m$' replacing Yoon's '$2\sigma K V_m$', where the curvature K is correctly given by $2/\rho$ for a sphere, and $1/\rho$ for a cylinder, where ρ is the radius of curvature. In Equations (2.12) and (2.13), the curvature K refers to the mean curvature of the liquid lens. This incorporates an implicit assumption that the two solid - liquid interfaces involved have approximately the same curvature. This assumption may not be unreasonable for most of the liquid phase sintered specimens, since the liquid films are very long, thin, and are not strongly pinned at their ends. In cases where the liquid films are shorter, and are pinned at their edges, this assumption is no longer valid and each interface must be treated separately. This was attempted in obtaining Equations (2.14) through (2.16) [7]. In these equations the energy due to curvature is denoted as '$\sigma(K^A - K^B)V_m$', where A and B refer to the dissolving and growing grains respectively. In later stages of migration, when the liquid film has a crescent moon shape, this equation has a fairly unambiguous meaning provided that when migration opposes curvature, the overall energy due to curvature is defined to be negative. The equation is consistent with the observation that if curvature is considered from the perspective of the liquid phase, it can be seen that the liquid possesses positive curvature at the leading interface, and negative curvature at the trailing interface. In the early stages of migration however, this expression becomes somewhat ambiguous in its meaning, especially in cases where LFM occurs after liquation of precipitates along the grain boundaries of the matrix phase. In this case, the liquid phase forms lenses at grain boundaries upon liquation; *i.e.*, the liquid phase at the leading interface and at the trailing interface possesses positive curvature, and will remain this way during the very early stages of migration. This possibility was not considered by Yoon *et al.* [7,48] since in the liquid phase sintering experiments performed by Yoon and co-workers [15-25], the liquid films observed were flat initially (*i.e.*, the liquid phase at the trailing interface never possessed positive curvature). As a result, much care is required in application of the model during all stages of the migration in cases where the solid - liquid phases possess significant curvature.

It should finally be noted that in all the above equations for the concentration difference across the liquid film (ΔC) the coherent zones are assumed to be fully coherent with the parent lattice, and therefore predictions for ΔC will be an upper limit.

'Steady State' Velocity Expression

Development of the velocity expression (Equation (2.19)) required several assumptions. The first of which is that diffusion of solute across the liquid film is conductive. This seems reasonable since the solid dissolution at the leading interface and solidification at the trailing interface are by definition isothermal processes. This will generally rule out convection in the liquid due to thermal gradients. It is also assumed that the only source of solute that is required to maintain the coherent frontal diffusion zone is the solute rejected from the solidifying liquid at the trailing interface. That is, no other sources of solute exist. For most LFM experiments, the liquid composition is well defined by the experimental conditions (*i.e.*, temperature). As a result, there will likely not be any long range fluctuations in composition; any composition variations that remain are due to variations in curvature and / or stress states of the solid grains. However, since the associated changes in liquid compositions are very small, it is possible that liquid composition variations do exist, feeding (removing) solute to the frontal diffusion zone. The diffusion paths for these other sources / sinks of solute will most likely be long with respect to the liquid film thickness (δ). Therefore, the assumption does not seem unreasonable. Equation (2.19) also assumes a constant value for δ. As will be discussed in Section 5.2.3, the analysis of Brechet and Purdy [52] indicates that in the case where there is limited solute available to form the growing phase, the liquid film will shrink with time as solute is lost to the growing solid, since LFM is also a mechanism for solidification. The analysis predicts that in the absence of interfacial curvature the film will accelerate with time, and will eventually collapse to form a grain boundary.

Other Considerations

In the previous section, the initiation of LFM and loss of coherency in terms of the critical diffusion distance L_C was discussed. Several facts are evident about the initiation, coherency loss, and 'steady-state' migration of liquid films:

- In the very early stages of migration, relatively symmetrical solute diffusion fields develop in the two grains on either side of the liquid film. The energy due to the coherency strain fields on each side will likely differ due to different biaxial elastic moduli. The liquid film will therefore begin to migrate into the grain with the larger coherency strain energy.

- At some early stage, the growing grain will lose coherency while the dissolving grain does not (or to a much lesser degree). This loss of coherency is attributed to the fact that enough solute has diffused into the growing grain such that the energy due to coherency is greater than that of a grid of misfit dislocations. However, the nucleation of dislocations is known to be difficult [47], and it is likely that dislocations will only nucleate at approximately two to five times the calculated critical diffusion distance (L_C). It is also possible that pre-existing dislocations may be attracted to the coherently strained lattice at any stage during the early stages of migration. Whatever the case, this stage is very difficult to model with any accuracy.

- Once coherency is lost completely in the growing grain, it is assumed that the film will migrate in a steady-state manner. The surface layers of the dissolving grain are assumed to remain fully coherent with the parent lattice during the steady-state migration period. It is possible that dislocations already in the vicinity of the leading solid - liquid interface may partially decrease the elastic energy ahead of the liquid film.

- According to the Yoon *et al.* model [7], migration will then continue in this manner until the energy due to curvature becomes of the same order of magnitude as the coherency strain energy. In this case the liquid film will slow down resulting in an eventual loss of coherency in the dissolving grain, and migration will cease. Although not mentioned in the Yoon model, the liquid films will eventually disappear through isothermal solidification. If the liquid films are not pinned significantly such that the energy due to curvature is negligible then the kinetic model of Yoon *et al.* [7] (constant film thickness, δ) implies that the liquid films will continue to migrate without any loss of liquid (*i.e.*, constant liquid volume fraction) until the experiment is stopped. Since LFM is also a mechanism of solidification, this would seem impossible. The analysis of Brechet and Purdy [52] implies that the film will shrink as it migrates, therefore avoiding this seeming impossibility.

Finally, it should also be noted that any model is only as good as the data available. As will be shown in Chapter Six, variations of experimental and literature values can have profound effects upon model predictions of liquid film morphology.

CHAPTER THREE

EXPERIMENTAL DESIGN

3.1 INTRODUCTION

In Chapter Two considerable evidence was presented to support the theory that coherency strain energy ahead of the migrating interface is the driving force for liquid film migration (LFM). However, a comprehensive analysis of the kinetics of LFM has not yet been performed on a binary system. In order to test the accuracy of models describing LFM certain experimental conditions must be met. The binary system should have some degree of solid solubility, so as to allow for diffusion of the solute species into the parent crystal, an atomic misfit between the parent phase and the solute enriched diffusion zone is required, and the variation of lattice parameter with solute content should follow Vegard's law to allow for simple analysis. The aluminum - copper system was chosen for the experiments. Experiments were performed in two stages. In the first stage, LFM was induced in a diffusion couple type of experiment, with the two halves of the couple containing different copper concentrations. The two halves were separated by a thin foil of copper, which liquates at the experimental temperature. The second stage of the experiments involved the precipitation of the θ-phase (Al_2Cu) at low temperature and the subsequent liquation of these precipitates (to initiate LFM) by rapidly boosting the temperature above the eutectic temperature. These experiments are discussed in detail in following sections.

3.2 THE ALUMINUM - COPPER SYSTEM

The aluminum rich portion of the aluminum copper phase diagram (0 to 33%Cu) is shown in Figure 3.1 after that of Murray [53]. It can be seen that (Al) melts by the eutectic reaction (Al) + $\theta \rightarrow$ L at 548.2°C. The assessed value of the eutectic composition is 17.1 ± 0.05%Cu. A composition of 3.3 weight percent copper (1.46 atomic percent) therefore lies in the two-phase region for temperatures less than approximately 475°C, and in the one-phase (Al) region for temperatures above (within the temperature ranges used in these experiments).

3.3 DIFFUSION COUPLE EXPERIMENTS

The objective of these experiments was to observe and quantify LFM in the Al-Cu system. The initial conditions were chosen in order to approximate 'steady-state' conditions as defined by Yoon *et al.* [7] (see Chapters Two and Five). The experimental procedure for the diffusion couple experiments is described with reference to Figure 3.2. Figures 3.2(a) and 3.2(b) show schematic diagrams of the diffusion couple assembly prior to heat treatment, and at the experimental temperature (560°C) respectively. It can be seen that a new equilibrium is attained at the higher temperature as the now unstable pure copper foil forms an equilibrium aluminum / copper liquid solution through diffusional processes. Figure 3.2(c) shows the associated concentration profile that is assumed to develop once the diffusion couple reaches the experimental temperature. At this temperature, the equilibrium solid and liquid compositions are denoted C_S and C_L respectively. The diffusion couple thus has one side at a composition C_S, and the other side at another composition C_0 (parent copper composition). A thin foil (<20μm thick) of the solute material was placed between the two sides of the couple, along with a thin ring of iron to mark the initial location of the liquid film (iron was chosen since it is virtually insoluble in all phases present). The entire assembly was then pressed together, and placed in the furnace at 560°C. Migration of the liquid film will ensue once a solute enriched zone coherent with the solid at composition C_0 has

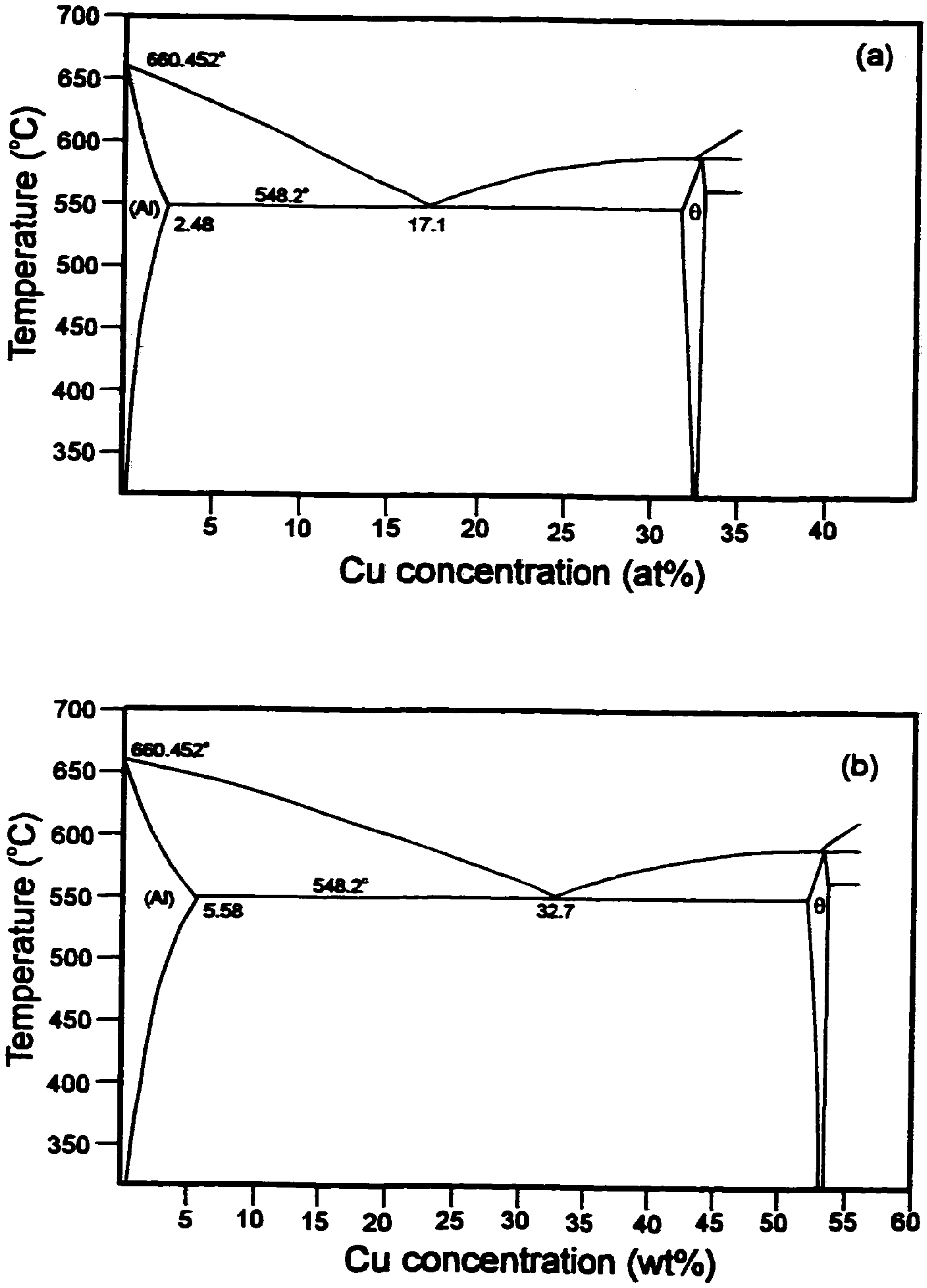

Figure 3.1: Aluminum Rich Portion of the Isobaric Aluminum - Copper Phase Diagram (P = 1 Atm): (a) Atomic Percent, (b) Weight Percent.

developed. Since one side of the diffusion couple was at the equilibrium solidus composition C_S, no diffusion of solute into this half of the couple occurred, and it was therefore assumed to be stress free. The conditions described therefore correspond to the condition of 'steady state migration', with the stress completely relaxed in the growing grain. A detailed account of the procedure now follows.

3.3.1 Material Processing and Heat Treatments

A 1 cm diameter Al - 3.3 wt% Cu and a 1 cm diameter Al - 2.1 wt% Cu alloy rod were cast using directional solidification equipment. The resulting microstructure consisted of relatively large columnar grains (approximately 100 μm wide by 1000 μm long) for the 3.3 wt% Cu alloy, and a single crystal for the 2.1 wt% Cu alloy. It should be noted that a single crystal was not necessary for the experiments, but a sample with a large grain size is necessary so as to minimize grain boundary diffusion effects, and to obtain relatively planar solid - liquid interfaces. Each half of the diffusion couple was obtained by sectioning the appropriate alloy rod, and one side of each was then polished using 5 or 6μm SiC paper prior to assembling the diffusion couple. Pure copper disks and a length of iron wire were rolled to a thickness of approximately 20 μm using standard flat rolling techniques. After cleaning the halves of the couple in a chromic acid cleaning solution to remove the oxide (see Appendix for constituents), the couple was assembled and pressed as shown in Figure 3.2(a) using the assembly shown in Figure 3.3. The sample was placed in the furnace at 560°C for times ranging from one hour to several hours. The samples were then removed from the furnace and quenched to room temperature in a water bath.

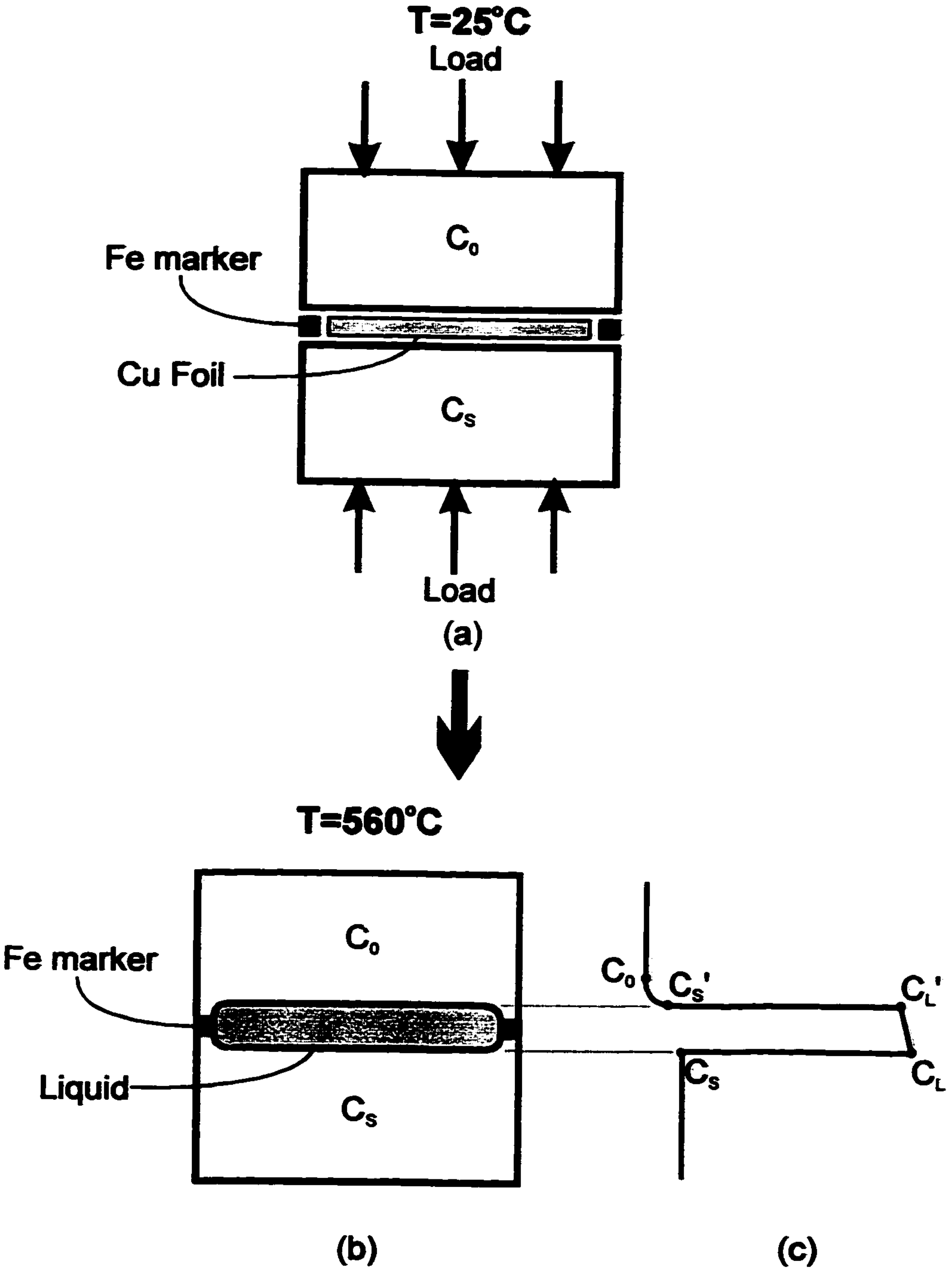

Figure 3.2: **Diffusion Couple Assembly: (a) Prior to Heat Treatment At Room Temperature (T=25°C), (b) At the Experimental Temperature (T=560°C), and (c) Composition Profile That Develops Across the Liquid Film At the Experimental Temperature.**

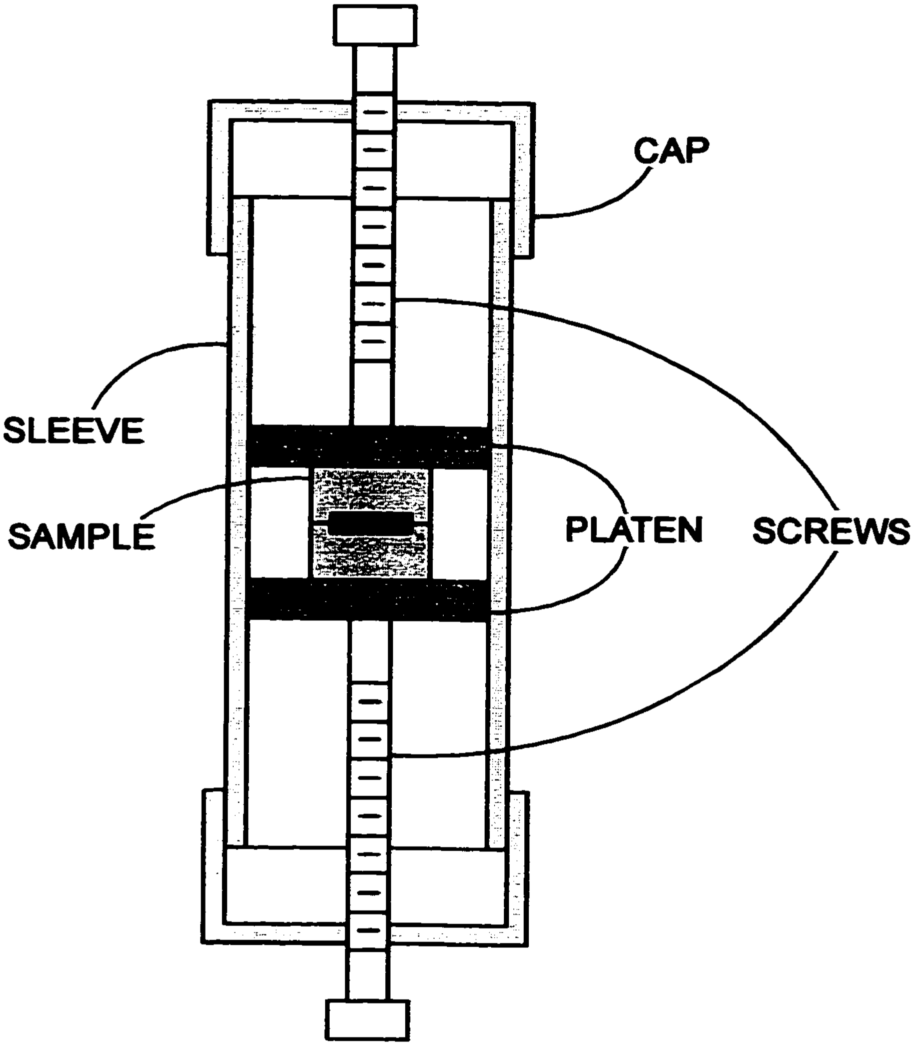

Figure 3.3: Diffusion Couple Apparatus

3.3.2 Sample Preparation for Microscopy

Each sample was sectioned perpendicular to the plane of the liquid film and mounted in bakelite. The samples were ground on 220, 320, 400, and 600 grit SiC papers using water as a lubricant, and polished with a 6μm and 1μm diamond abrasive lubricated with kerosene. Final polishing was performed with a 0.3μm Al_2O_3 abrasive using water as a lubricant. The samples were then cleaned with soap and water and dried using methanol after the final grinding stage and between all polishing stages. The samples were ultrasonically cleaned in methanol for twenty minutes once polishing was complete. The samples were etched using Poulton's reagent (see Appendix for constituents).

3.3.3 Optical Microscopy

Optical microscopy of all samples was performed on a Leitz Metalloplan microscope using 35mm negative film.

3.4 PRECIPITATION TYPE EXPERIMENTS

In this set of experiments, liquid film migration (LFM) was induced in the aluminum copper system as follows: an initial low temperature precipitation of the θ phase (Al_2Cu) was followed by rapid heating in a salt bath furnace to a temperature just above the eutectic temperature in order to liquate the θ precipitates. Precipitates initially present in the grain interiors eventually form transient liquid spheres, while grain boundary precipitates melt and wet the boundary forming thin liquid regions upon liquation. If the two grains separated by the liquid film are favourably oriented, LFM will ensue. A detailed account of the material processing and heat treatments performed follows.

3.4.1 Material Processing and Heat Treatments

A 1 cm diameter Al - 3.3 wt% Cu alloy rod was cast using directional solidification equipment. The microstructure obtained consisted of relatively large columnar grains (approximately 100 μm wide by 1000 μm long). The rod was then homogenized at a temperature of 543 ± 2°C for 8 days in an argon atmosphere (*i.e.*, in the one - phase (Al) region). The composition of the rod was verified using a Jarrell-Ash ICAP 9000 mass spectrometer to be 3.377 ± 0.1178 percent copper by weight.

In order to facilitate rapid heating of the entire sample during the liquation stage of the heat treatment, the sample must be thin. Sections of the alloy rod were rolled using standard flat rolling techniques to a thickness of 0.5mm with an intermediate anneal. This had the additional advantage of refining the grain size. The flat samples were further sectioned, ultrasonically cleaned, and sealed in quartz under an argon atmosphere.

Stage One - Initial Precipitation of the θ Phase

The sealed samples described above underwent one of the following heat treatments:

(a) 28 days at 400°C

(b) 8 days at 480°C, followed by a slow cool (≈ 10 days) to a temperature of 400°C and then held for 28 days.

Heat treatments were performed using a standard tube furnace; the resulting microstructures are shown in Figure 3.4. It can be seen that the microstructure resulting from heat treatment (a) is markedly different to that resulting from heat treatment (b). The microstructure for (a) shows a large number of predominantly non-faceted precipitates that are distributed along the grain boundaries and within some of the grain interiors. The microstructure for (b) shows fewer precipitates, but they are much larger, generally faceted, and located predominantly within the grain interiors. It should be noted that very few of the precipitates were formed on the grain boundaries. A discussion of the microstructures formed and the reasons for performing each heat treatment is presented in Section 4.3.1.

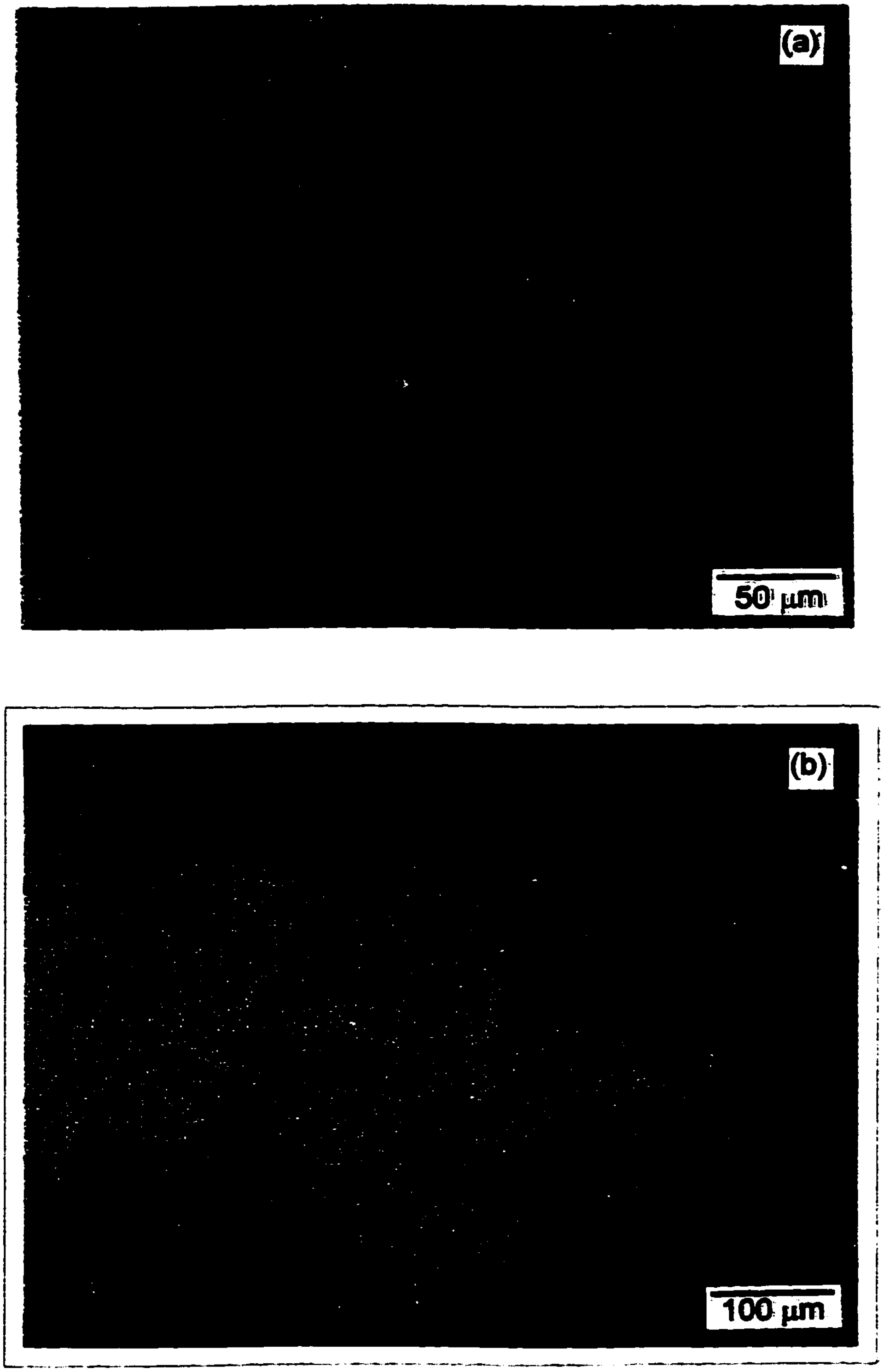

Figure 3.4: Microstructures Obtained From Heat Treatments (a) and (b).

Stage Two - Salt Bath Experiments

The precipitated samples formed by heat treatments (a) or (b) were then cut into 5mm × 5mm squares with a hole drilled in the corner through which a length of Kanthal wire was attached. In order to avoid premature dissolution of the θ precipitates prior to liquation, the sample must be heated rapidly to the experimental temperature of 560 °C. A molten salt bath was determined to be the most effective way to achieve this due to the high rate of heat transfer between the surface of the sample and the molten salt. LFM was therefore induced by immersing each sample in a molten salt (Thermoquench 290) held at a temperature of 560°C for times ranging from 3 to 3600 seconds. Rapid quenching was achieved by the use of an air jet located at the exit of the salt bath. The air jet was determined to be the best method for quenching the samples since it could be applied the instant the sample left the salt bath furnace. It should be noted that the heating and quenching times were measured using a K-type thermocouple (chromel / alumel) attached to the specimens. The results showed that the temperature of the sample was above the eutectic temperature within 1.5 seconds of insertion, and similarly for quenching. After quenching, each sample was then cleaned, sectioned, mounted in bakelite, and polished using the procedure outlined below.

3.4.2 Sample Preparation for Microscopy

Each sample was sectioned and mounted in bakelite. The samples were then ground on 220, 320, 400, and 600 grit SiC papers using water as a lubricant, and polished with a 6μm and 1μm diamond abrasive lubricated with kerosene. Final polishing was performed with a 0.3μm Al_2O_3 abrasive using water as a lubricant. The samples were cleaned with soap and water and dried using methanol after the final grinding stage and between all polishing stages. The samples were ultrasonically cleaned in methanol for twenty minutes once polishing was complete. No etching was required to view the LFM events.

3.4.3 Optical Microscopy

Optical microscopy of all samples was performed on a Leitz Metalloplan microscope using Type 53 positive proof Polaroid film. This served two purposes: to obtain information on the general morphology (and location) of the liquid, and to obtain two - dimensional measurements of the migration distance of both leading and trailing interfaces, as well as the width of the liquid lens for LFM events as functions of time. The analysis of these measurements is discussed in Section 3.4.6

3.4.4 Volume Fraction Measurements

Volume fraction measurements of the second phase for each time were performed. For both heat treatments, this involved measurement of the volume fractions of the liquid phase. The volume fraction measurements were performed using a manual point counting method with a 6 × 6 grid (36 points) attached to the eye-piece of the microscope. The manual method was chosen over the computer controlled image analyser method because during polishing of the samples a halo appears around the copper rich regions of quenched liquid. This halo is a region that has been polished more vigorously than either the quenched liquid or the matrix. This dark band around each region of quenched liquid thus interferes with the computer determining the region to be measured during an area fraction calculation. That is to say that the difference in contrast level between the quenched liquid and the halo was insufficient to allow the computer to perform some kind of image subtraction. This error leads to a systematic over prediction of the area fraction of second phase measured. Area fraction measurements of several samples were initially performed on the computer controlled image analyser prior to realizing that all measurements were over predictions.

The manual method involved randomly moving the sample on the microscope stage while looking away from the eye-piece. Any region of quenched liquid located at one of the intersection points of the grid is counted. The sample was again moved on the microscope stage, and the counting process repeated until one hundred measurements were obtained. This process was performed on each of the salt bath treated samples obtained from both heat treatments ((a) and (b)). The volume fraction was then calculated by averaging the number of points counted of a particular feature by the total number of points (= 3600). Error analysis follows the method of Hilliard and Cahn [54] and is discussed in detail in Section 4.3.2.

3.4.5 Scanning Electron Microscopy

In all previous studies of liquid film migration, only two-dimensional cross-sections of LFM events in the form of micrographs have been obtained. Data obtained from such micrographs must be used very carefully since not all two-dimensional cross-sections of LFM events give true representations of the maximum migration distance. This is illustrated in Figure 3.5. This diagram shows one half of an idealized three-dimensional LFM event, as well as sections taken at several different planes (model predictions illustrated in Figure 6.7 using a time of 15 seconds were used to create this figure). An idealized three-dimensional LFM event is defined as the volume enclosed by two non-concentric spheres coinciding in the $Z = 0$ plane, each with its center of curvature on the Z-axis. The outer sphere represents the leading interface, while the inner sphere represents the trailing interface. Sectioning the three-dimensional figure in a plane that passes through the origin and that is parallel to the Z-axis gives the cross-section at which the positions of the leading and trailing interfaces give the true measure of maximum migration distance. Sectioning the three-dimensional figure in any other plane will give a false measurement of the migration distance. Referring to Figure 3.5(e), the section in the $Z = 1$ plane shows that the LFM event may not appear crescent shaped at all, but doughnut shaped or possibly simply circular in cross-section. This concept was used in determining a method for deriving meaningful data from measurements of leading and trailing interface positions obtained from two-dimensional micrographs and is discussed further in Section 3.4.6. Scanning electron microscopy in conjunction with a micro-indenting and polishing procedure was used to create partial three-dimensional images

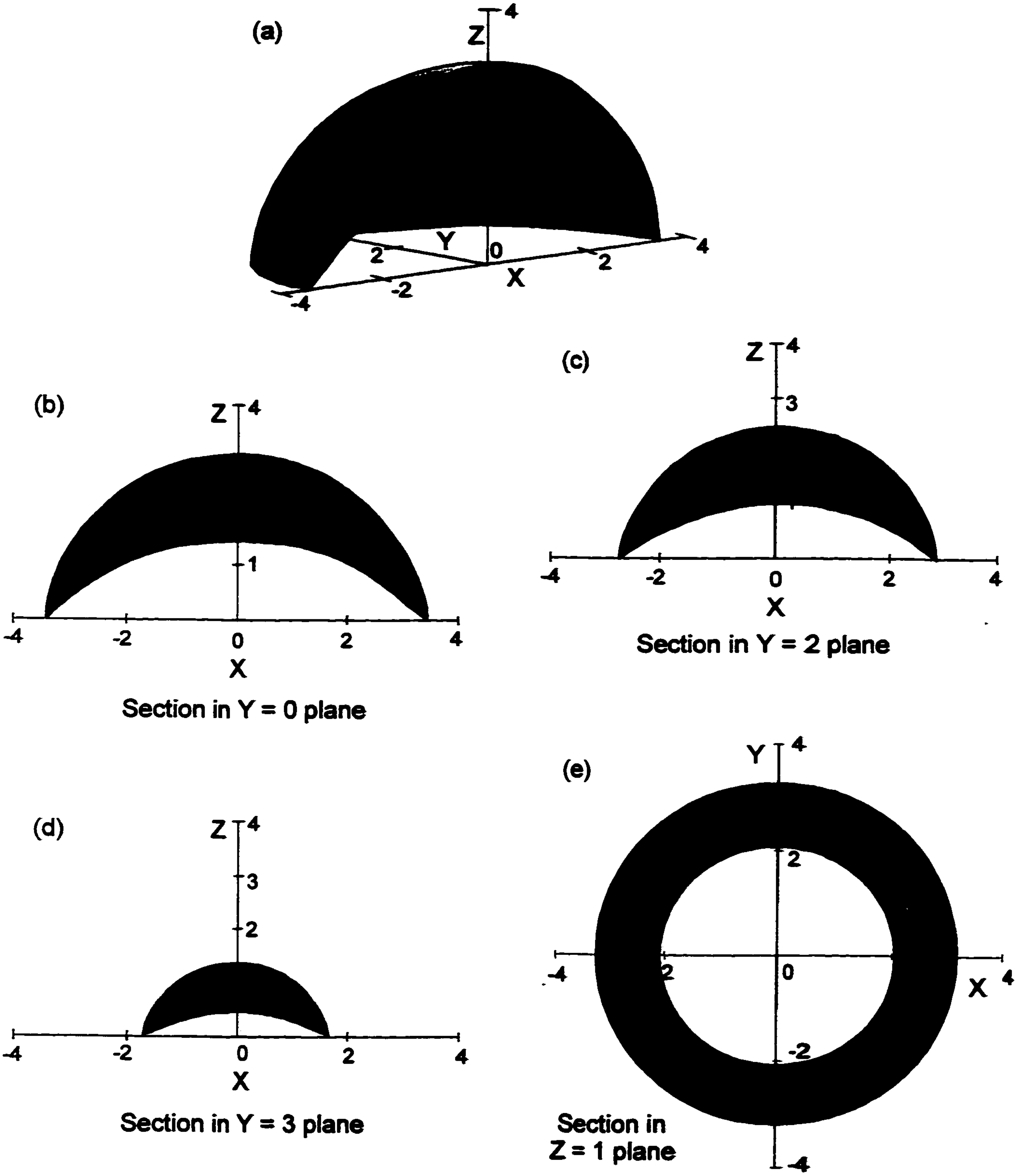

Section in Y = 0 plane

Section in Y = 2 plane

Section in Y = 3 plane

Section in Z = 1 plane

Figure 3.5: **Idealized Three-Dimensional LFM Event (a), Along With: (b) Section at Y=0; (c) Section at Y=2; (d) Section at Y=3; and (e) Section at Z=1.**

of LFM events.

The three-dimensional imaging technique was performed on one of the samples from the salt bath experiments. The 'P400(a)/15s' sample was chosen because the results of the image analysis and microscopic inspection indicated that the highest volume fraction of LFM events were present in the sample (from heat treatment (a)) immersed in the salt-bath for 15 seconds.

The procedure used to obtain the (X, Y, Z) coordinates for each LFM event will be now be described. Before starting a step-by-step procedure, a general overview of the methodology will be discussed. Initially, several interesting events were located. A pyramidal micro-indent (using a standard Vickers micro-hardness tester) was placed adjacent to each event. SEM micrographs of each event and each indent were taken, as well as a plan view that included the event(s) of interest and the nearest indent. The sample was then re-polished, and another set of indents were made adjacent to the events. This procedure was then repeated for the following levels (after polishing); that is, micrographs were taken of each event, each new indent, and each old indent, along with a plan view that encompassed all three features (on each level). Typical before and after photographs of indents are shown in Figure 3.6. The amount of material removed in each polishing stage can be calculated from the measurements of the micro-indents before and after polishing since the angle that forms the pyramid on the indentor tip is known to be 136°. The layers obtained as described above (for each LFM event), were then aligned using the technique described below, and the (X, Y, Z) coordinates of the LFM event were calculated. These events were plotted using a combination of MAPLE VR3 for Windows, and CORELDRAW Version 6.0; the results are shown in Section 4.3.3.

A step-by-step outline of the procedure involved in obtaining the (X, Y, Z) coordinates of the LFM event is described below. First, the general experimental procedure will be outlined, followed by the steps taken to obtain the (X, Y, Z) coordinates.

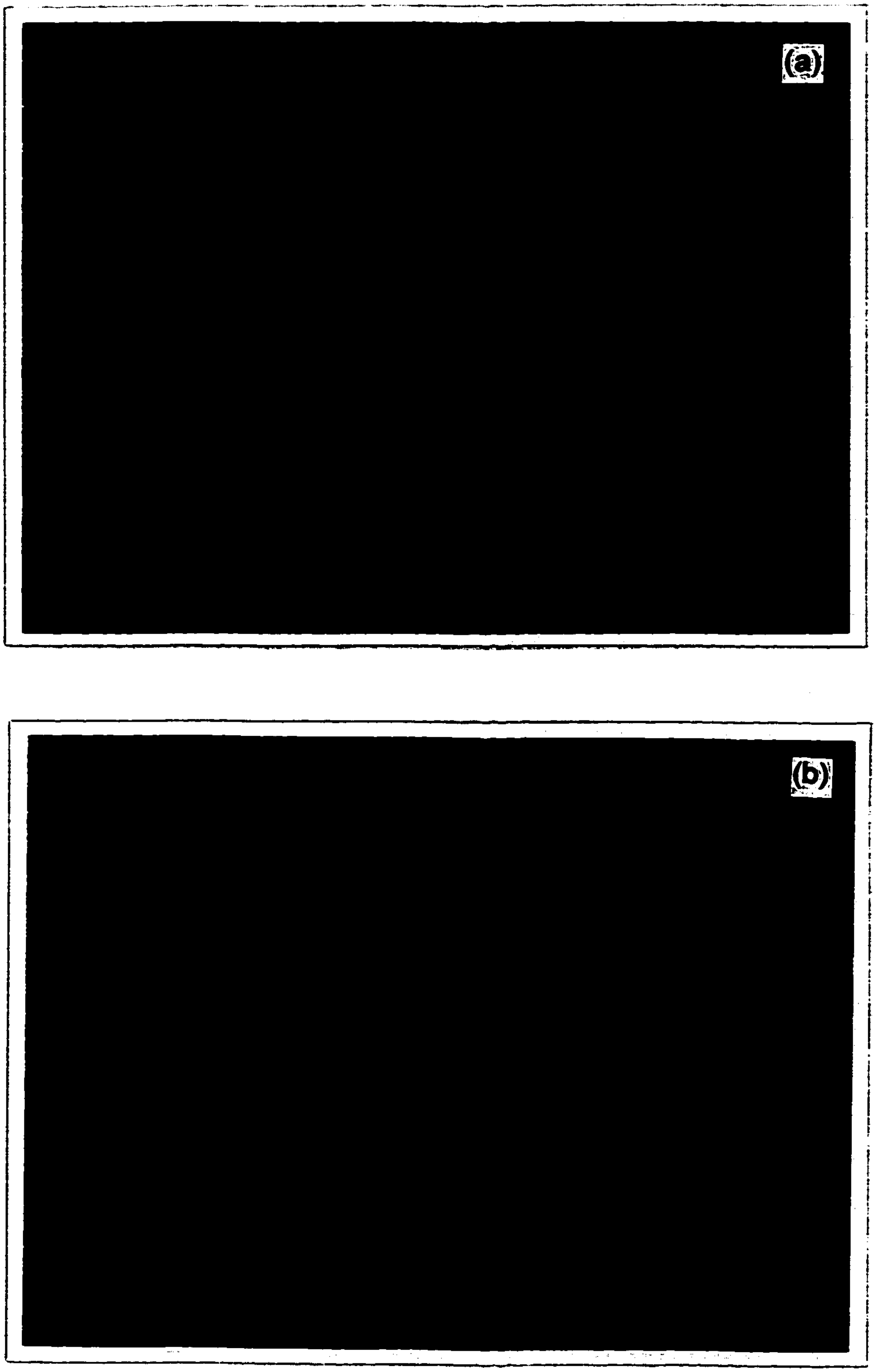

Figure 3.6: **Typical Photographs of Micro-indents: (a) After Indentation; (b) Same Indent After Further Polishing.**

Experimental Procedure

1. The 'P400(a)/15s' sample was sectioned, mounted in bakelite, ground and polished as described in Section 3.4.2.

2. Several interesting LFM events were located. A pyrimidal micro-indent using a Shimadzu microhardness tester - type M was placed adjacent to each event (using a 25g load and 15 second dwell time).

3. The sample was then prepared for viewing in the scanning electron microscope (SEM):
   - (i) An aluminum stub was glued to the bottom of the mounted sample in order to facilitate insertion in the SEM, and to allow for excess charge removal.
   - (ii) A conductive paste of equal amounts white glue and colloidal graphite was prepared. A continuous strip of this mixture was then painted from the top surface of the bakelite to the aluminum stub. This was required to prevent charge build-up on the viewing surface during observation in the SEM.
   - (iii) A thin layer of gold ($\approx$ 10 nm) was evaporated onto the sample surface using a Polaron SEM Coating System.

4. The prepared sample was then placed in the ISI-DS130 Dual Stage Scanning Electron Microscope, and pumped to a vacuum of 3×10^{-7} torr. The microscope was equipped with a LaB_6 filament, and operated at a voltage of 20kV.

5. SEM micrographs using type 53 positive proof Polaroid film were then taken of each event and each indent individually as well as a plan view including the event of interest and the nearest indent(s).

6. The sample was then removed from the microscope and cleaned in soap and water to remove the graphite and glue mixture, taking care not to scratch the surface of the sample.

7. The sample was then re-polished. This involved use of the 6μm, 1μm and 0.3μm polishing stages as described in Section 3.4.2. Much care was taken in this stage, since polishing too vigorously may lead to the complete removal of the micro-indents, and therefore the loss of the ability to determine the amount of material removed.

8. New micro-indents were then placed close to the old indents and the LFM events of interest as described in Step 2.

9. Steps 3 ((ii) and (iii) only) to 9 were then repeated until enough layers were compiled to obtain a reasonable approximation of the three-dimensional morphology.

Procedure to obtain (X, Y, Z) coordinates

Z-coordinates

In the following discussion, it is assumed that each LFM event on a particular layer has one Z value associated with it. The amount of material removed during polishing (ΔZ) can be calculated from measurements of the micro-indents before and after each polishing stage. This is illustrated in Figure 3.7, where D_1 and D_2 are the micro-indent widths before and after polishing respectively. Since the angle that forms the pyramid on the indentor tip is known to be 136°, the amount of material removed between polishing stages (ΔZ) in the vicinity of a particular indent is given by Equation (3.1).

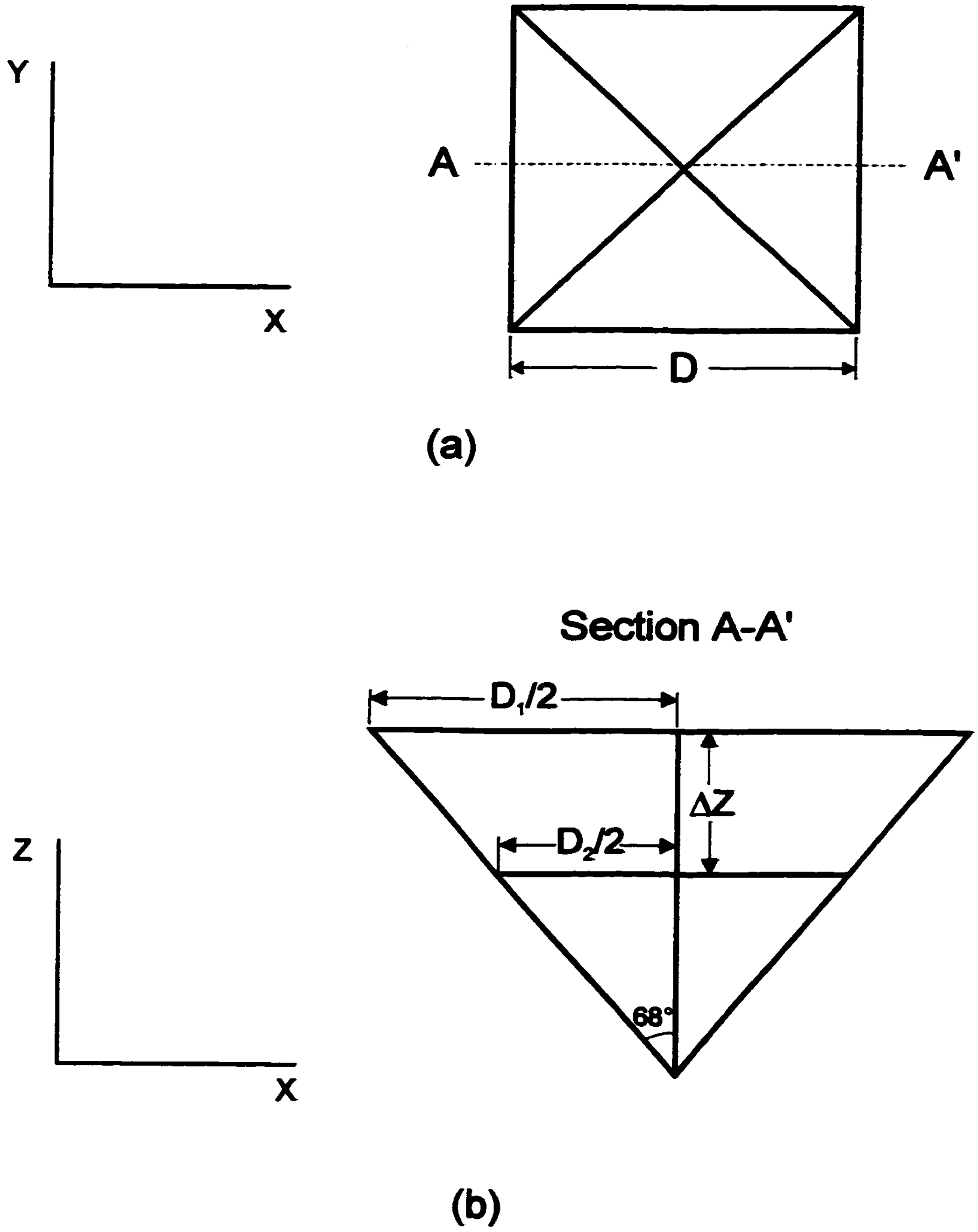

Figure 3.7: Cross-section Of An Indent In The X-Z Plane Before And After Polishing: (a) View Of The Plane Of Polish ((X,Y) plane); (b) Section A-A′ ((X,Z) Plane).

$$\Delta Z = \frac{(D_1 - D_2)}{2\tan 68^\circ} \tag{3.1}$$

Values for D_1 and D_2 for each indent were obtained by measuring the width of the indent at the plane of polish from the micrograph in ten different locations (five per side), and then computing an average value. For the indents measured after polishing, some care was required in obtaining D_2. Since the indents were often damaged during the polishing procedure, the exact outline of the indent was often difficult to determine. Measurements were obtained by tracing the most probable outline of the indent onto a transparency, and D_2 was obtained by the same method as for D_1. The amount of material removed between level [i] and level [i+1] ($= \Delta Z^i$) was then calculated for each indent in turn using Equation (3.1). If there are N indents per level, then the average value for the material removed between level [i] and level [i+1] can be calculated as follows:

$$\Delta Z^i_{AVG} = \frac{1}{N} \sum_{j=1}^{N} \Delta Z^i_j \tag{3.2}$$

The Z-coordinate of layer [i+1] is therefore:

$$Z^{i+1} = Z^i + \Delta Z^i_{AVG} \tag{3.3}$$

It can be seen that the errors involved in determining the exact Z-coordinate become larger as more layers are added to the composite three-dimensional image (i.e., as 'i' becomes larger). These errors will be discussed in more detail in Section 4.2.3.

X and Y coordinates

The (X,Y) coordinates of the LFM events were determined in three stages. The first stage involved measurement of the event directly from the SEM micrograph. These measurements in effect contain information about the two-dimensional morphology of the event on a particular layer, but no information on how to orient the layers with respect to each other. In the second stage, measurements were taken from SEM plan view micrographs of LFM events and surrounding indents on each successive level. In the third stage the measurements from the first and second stages were combined, which along with the Z-coordinates already determined, resulted in a three dimensional representation of the LFM events. A step-by-step outline of the procedure follows.

Stage One - Event Morphology Measurements

This stage of the procedure involved obtaining measurements along the solid - liquid interface for each level of each LFM event that is being constructed.

1. A 100mm × 100mm grid was generated with divisions every millimeter. This was then photocopied onto a transparency.
2. The grid was then placed directly on the close-up SEM micrograph of each event on a particular layer, usually with the left-hand pinning point of the event at (0,0) if possible. Coordinates along the solid - liquid interface were then recorded (approximately forty points).
3. Step 2 was then repeated for all other events on all layers.

Stage Two - Measurement of Event Orientation

LFM events by definition are regions of liquid separating crystals of different orientation. In polycrystalline specimens, LFM events will likely be located along grain boundaries. Since, in most polycrystalline specimens, grain boundaries are randomly oriented with respect to the surface, it can be seen that the measurement of the three-dimensional morphology of any LFM event requires that the apparent shift in the (X,Y) coordinates of the LFM event from one level to the next be recorded accurately. In order to orient the layers of LFM events with respect to each other, they must be measured from the same origin. The centers of the micro-indents can be used as origin for two successive layers because they can be resolved both before and after each polishing stage. Figure 3.8 shows a schematic view of a typical LFM event on two successive levels - indicated as level [i] and level [i+1]. The orientation of any particular LFM event in the X-Y plane on successive layers [i] and [i+1] was determined as follows:

1. The transparent grid used in the Stage One procedure was placed on the plan view micrograph for level [i]. The plan view micrographs show the event(s) of interest, the micro-indent from the previous level ([i-1]), and the freshly made micro-indent (level [i]).

2. Coordinates on the perimeter of the LFM event were measured (at least twenty points) as well as the coordinates of the centers of the micro-indents.

3. Steps one and two were then repeated for level [i+1]. This plan view micrograph shows the same event(s) of interest, the same level [i] micro-indent as in the level [i] micrograph, and the freshly made micro-indent (level [i+1]).

The coordinates of the micro-indent centers were then used as origins. Since the micro-indent denoted O[i] can be seen in the micrographs of levels [i] and [i+1], it can be used as the origin to which the coordinates of the LFM event on levels [i] and [i+1] can be referred. Similarly, O[i-1] can be used to align levels [i-1] and [i] of the LFM event, and O[i+1] to align levels [i+1] and [i+2] of the LFM event.

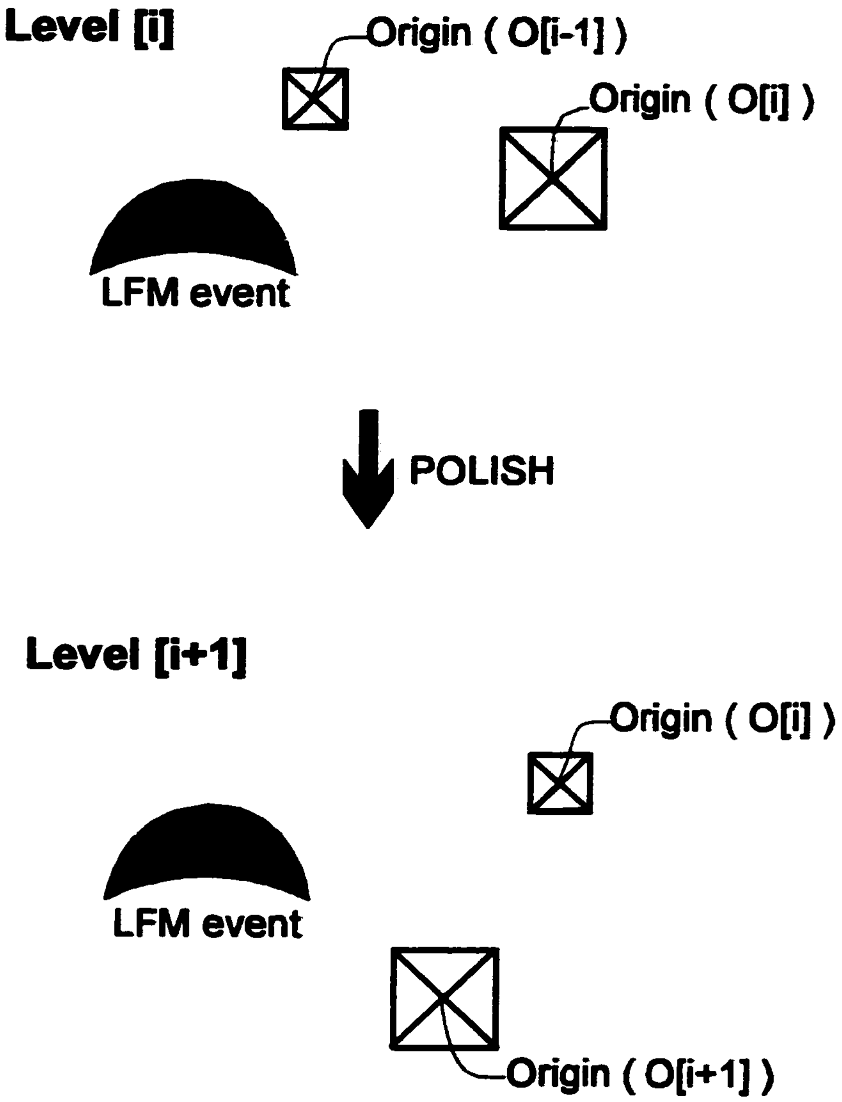

Figure 3.8: **Illustration of Indents and LFM Event (on X-Y plane) For Level [i] and Level [i+1] Showing the Orientation of the Event From One Level to the Next.**

Stage Three - Coordinate Shift

In this stage, the coordinates of the LFM event on levels [i] and [i+1] obtained in the Stage One procedure were then shifted by the amount determined in the Stage Two procedure. This is described below.

1. The coordinates of the event (from the Stage Two procedure) were plotted relative to O[i] for levels [i] and [i+1], and the relative shift noted.
2. The Stage One coordinates from level [i+1] were shifted relative to those of level [i] by the amount determined in Stage Two.

Stages One, Two and Three were then repeated for each level and for all LFM events. The (X,Y) coordinates were then combined with the Z-coordinates to create a three-dimensional representation of each of the LFM events. This is described below.

Three Dimensional Representation of LFM Events

A three-dimensional representation of each of the LFM events was then developed by combining the (X,Y) and Z-coordinates (obtained as described in a previous section). Each level has a particular Z-value associated with it. The first level was assigned a value of Z = 0. The Z-coordinates of subsequent levels were then obtained using Equations (3.1), (3.2), and (3.3). The (X,Y) coordinates for level [i] were assigned the Z-value corresponding to that level.

The (X,Y,Z) coordinates were then plotted using MAPLE mathematical software. The resulting plot was rotated within the MAPLE program until an orientation was obtained that best illustrated the morphology. This plot was then exported to CORELDRAW for further enhancement since it is difficult to observe the morphology from the MAPLE three-dimensional point plot. Plots of the events are shown in Section 4.3.3. The assumptions and errors involved in obtaining the three-dimensional morphology plots will be discussed in Section 4.3.3.

3.4.6 Estimation of Migration Distances

As was described in Section 3.4.3, optical microscopy was performed on all samples in order to obtain two-dimensional measurements of the LFM events. The position of the leading and trailing interfaces (Z_{LEAD} , Z_{TRAIL}), as well as the width of the liquid lens (W) were measured. Not all of these measurements can be used to test model predictions for the reasons discussed in the introduction to Section 3.4.5 with reference to Figure 3.5. That is, not all two-dimensional cross sections of LFM events give true measurements of Z_{LEAD} and Z_{TRAIL}. The question remains how to obtain reasonable estimates of migration distances from the two-dimensional measurements. Examination of Figure 3.5 shows that the true migration distances are obtained when the idealized event is sectioned through the origin parallel to the Z-axis. Figure 3.9 shows apparent values of Z_{LEAD} and Z_{TRAIL}, as well as the ratio of Z_{LEAD} to Z_{TRAIL} for sections taken of such an idealized LFM event described earlier in Section 3.4.5 at several planes parallel to the Z-axis.

It can be seen that sections close to the Z-axis have low Z_{LEAD} to Z_{TRAIL} ratios, with the ratio increasing with distance from the Z-axis. If other possible cross-sections are considered, such as any random plane cut through the three-dimensional idealized event, the ratio of measured Z_{LEAD} to Z_{TRAIL} will be higher than for the cross-section that gives the true measure of Z_{LEAD} and Z_{TRAIL}. The procedure involved in obtaining useful average values for each sample is described as follows.

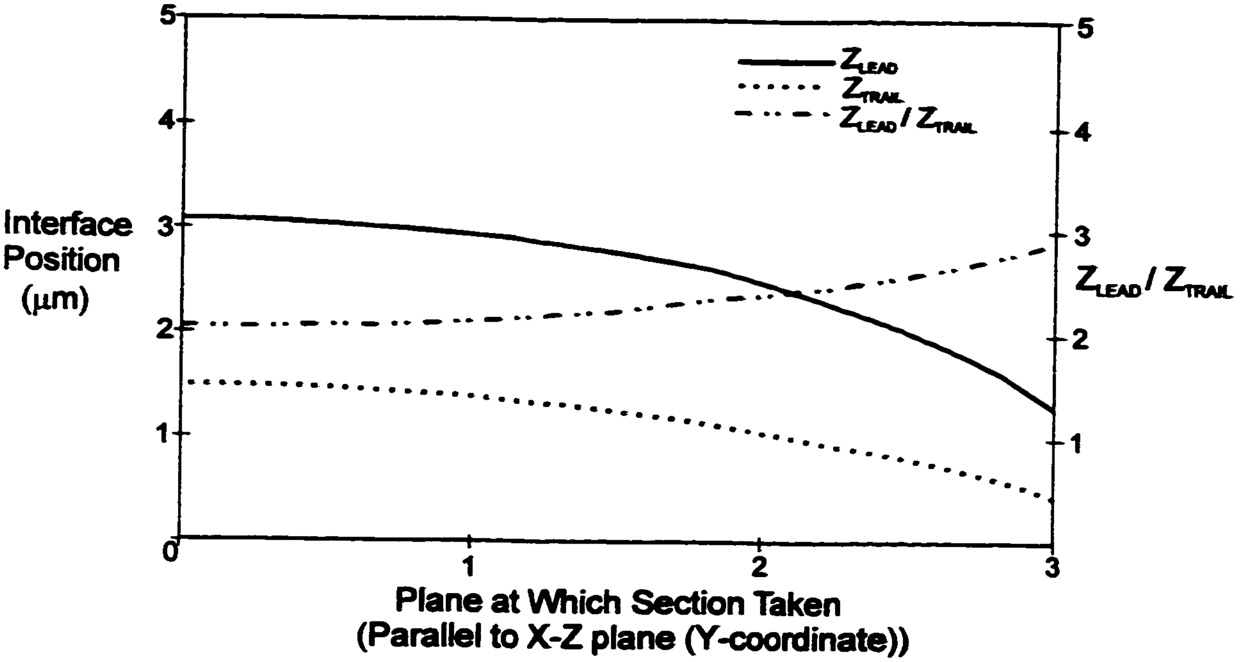

Figure 3.9: **Predictions of the Apparent Position of the Leading and Trailing Interfaces, and the Ratio of Z_{LEAD} to Z_{TRAIL} As A Function of the Plane At Which the Section is Made (t=15s).**

1. Measurements of Z_{LEAD}, Z_{TRAIL}, and W are obtained from optical micrographs of LFM events as shown in Figure 3.10. A 7X magnifier with divisions every 0.1mm was used.

2. All measurements are then entered into a spreadsheet program (Microsoft Excel) and the ratio of Z_{LEAD} to Z_{TRAIL} was calculated and plotted.

3. Those measurements with a ratio very much larger than the average were rejected. The remaining ratios were averaged, and only those measurements with a Z_{LEAD} : Z_{TRAIL} ratio less than or equal to the average Z_{LEAD} : Z_{TRAIL} ratio were used.

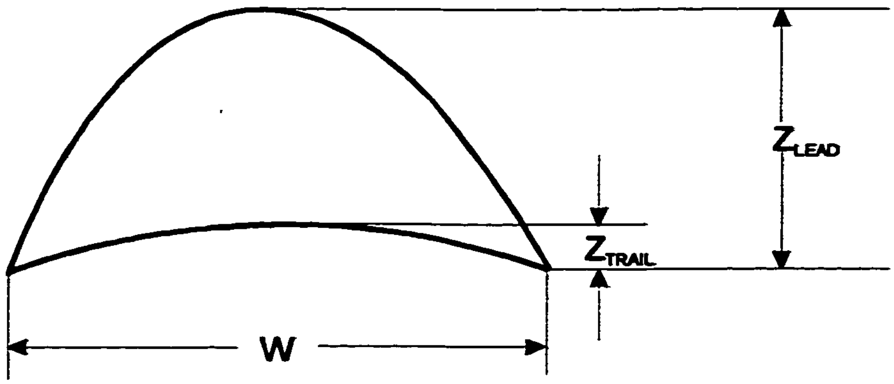

Figure 3.10: Measurements taken from two-dimensional micrographs of LFM events.

4. The remaining data were then averaged to obtain values of Z_{LEAD}, Z_{TRAIL} and W to which the kinetic model developed in Chapter Five could be compared.

The results are discussed in Section 4.3.4.

CHAPTER FOUR

EXPERIMENTAL RESULTS AND DISCUSSION

4.1 INTRODUCTION

This chapter contains the results of the experiments described in Chapter Three, and is organized in much the same manner. The results of the diffusion couple experiments are outlined in Section 4.2; since these experiments are predominantly qualitative, the results are mostly in the form of photo-micrographs. Section 4.3 outlines the results of the precipitation type experiments. Optical micrographs are presented of microstructures that develop during partial liquation of alloys obtained from both heat treatments as described in Chapter Three (*i.e.*, for times ranging from 3 seconds to 30 minutes). The volume fraction of the liquid phase as a function of time is then presented, including a discussion of the errors involved following the analysis of Hilliard and Cahn [54]. The results of the scanning electron microscopy performed on the 15 second sample (*i.e.*, the 'P400(a)/15s' sample using material from heat treatment (a)) are then presented. Micrographs of several interesting LFM events are shown along with composite three-dimensional representations of some particular LFM events, constructed using the method described in Section 3.4.5. The chapter concludes with a presentation of the migration distances obtained from two-dimensional measurements (from optical microscopy).

4.2 DIFFUSION COUPLE EXPERIMENTS

Preliminary attempts to induce LFM in aluminum - copper alloys were performed using a diffusion couple type of experiment. The objective of these experiments was to observe and quantify LFM in aluminum rich Al-Cu alloys. The compositions of each half of the couple were chosen so as to approximate 'steady-state' migration conditions as defined by Yoon *et al.* [7] (see Section 3.3 for the experimental details). As these experiments are predominantly qualitative, the results are mostly in the form of photo-micrographs. The results of selected experiments, along with descriptions of the morphologies observed are presented. The measured migration distances are then illustrated and the difficulties involved in this experimental approach are discussed.

Morphologies Obtained From Diffusion Couple Experiments

This section outlines the results obtained from selected diffusion couple experiments. A general outline of the experiments performed is followed by a presentation of the morphologies obtained. The section concludes with a presentation of the measured migration distances, and a discussion of the experimental difficulties experienced in attempting to induce LFM using the diffusion couple approach.

General Outline

All diffusion couple experiments performed were assembled using the procedure described in Chapter Three (*i.e.*, as shown in Figures 3.2 and 3.3). Several couples were constructed, however, only those listed inTable 4.1 were considered to be relevant.

Table 4.1: Diffusion Couple Experiments.

Experiment	Diffusion Couple*	Time (h)	Figure
1	Al - 1.12%Cu / Al - 1.46%Cu	0.5	4.1
2	Al - 1.12%Cu / Al - 1.46%Cu	7.5	4.2
3	Al - 1.12%Cu / Al - 1.46%Cu	13.5	4.3
4	Al / Al - 1.46%Cu	0.5	4.4

Note: * Copper concentrations quoted in atomic%

As was mentioned in Chapter Three, the experimental temperature was chosen such that one side of the diffusion couple contained the equilibrium amount of solute (*i.e.*, composition C_S). In all cases (Experiments 1 through 4) this was the Al - 1.46%Cu half of the diffusion couple. An experimental temperature of 582°C was determined from the phase diagram assessed by Murray [53] by matching the solid composition of the alloy ($C_S = 0.0146$) with the solidus curve for the (Al) + (L) equilibrium. This was measured experimentally within ± 2°C of the target temperature. The time values quoted are the total time the sample (housed in the holder shown in Figure 3.3) was in the furnace at the experimental temperature. The microstructures that resulted from the heat treatments outlined in Table 4.1 are shown in Figures 4.1 to 4.4. It should be noted that the magnitude of the coherency strain ($= \eta(C_S - C_0)$, see Chapter Two) in these experiments was chosen to be approximately of the same order of magnitude as the strains experienced during the liquid phase sintering experiments of Yoon and co-workers [15-25] (of the order of 10^{-3} to 10^{-4}). A compressive strain of approximately 4×10^{-4} was calculated for Experiments 1 to 3 at the experimental temperature of 582°C.

Morphologies Obtained

This section qualitatively describes the microstructures that were obtained from the experiments listed in Table 4.1, and are shown in Figures 4.1 through 4.4. The measured migration distances are presented in the following section, and their interpretation in Chapter Seven. Figure 4.1 shows the morphology obtained when the Al - 1.12%Cu / Al - 1.46%Cu diffusion couple was held at a temperature of 582 ± 2°C for 0.5 hours (*i.e.*, Experiment 1). The columnar structure of the Al - 1.46%Cu side of the diffusion couple can be seen, as well as the single crystal on the Al - 1.12%Cu side. A line has been drawn from the line of no wetting* to indicate the direction and the extent to which migration has occurred. It can be seen that significant migration has occurred into the side of the diffusion couple not originally at the equilibrium solid composition (*i.e.*, the Al - 1.12%Cu side), which is as expected. It should be noted that the liquid phase has leaked out at some time during the heat treatment; the dark band running from left to right of the micrograph marks the location of the liquid film at the time liquid loss occurred. Further examination of the micrograph shows that the liquid film was approximately uniform in thickness with the exception of some large pools of liquid (*i.e.*, at the very center of the micrograph and at the boundary between the Al - 1.12%Cu / Liquid / Al - 1.46%Cu zone and the line of no wetting). In these regions, less migration has occurred due to the longer diffusion paths for solute across the liquid film. It also appears that the copper concentration diffusion profile is visible in advance of the liquid film. That is to say that areas with a copper concentration above some limiting value, etch more darkly than areas with low copper concentrations (etched in Poulton's reagent - see Appendix for constituents).

Figure 4.2 illustrates the microstructure obtained when the same couple described above was held at the experimental temperature for 7.5 hours (*i.e.*, Experiment 2). Figure 4.2(a) shows

---

* This is the region outside the copper foil where no liquid was created. In this region an Al - 1.12%Cu / Al - 1.46%Cu joint was formed.

an overall view of the couple, where it can be seen that significant migration has occurred into the Al - 1.12%Cu side of the couple as in the previous experiment. In regions where large pools of liquid existed (*i.e.*, in the centre of the figure) it can be seen that little or no migration has occurred into the dissolving crystal; however, some grain boundary grooving is visible on the equilibrium Al - 1.46%Cu half of the couple formed as the system attempted to attain equilibrium. As in the previous experiment, the liquid phase appears to have leaked out prior to fully completing the solidification process through LFM; it is likely that this occurred early during the heat treatment (*i.e.*, in the first half hour) as in Experiment 1. Figure 4.2(b) shows a close up of the solid/ liquid interface that develops during the heat treatment. At the bottom of the micrograph is the equilibrium 3.38 wt.%Cu alloy (1.12 at%Cu), showing characteristic grain boundary grooving. Looking closely at the central boundary grooves, it can be seen that segments of the grain boundaries have migrated (both into the same grain), with their final locations indicated by arrows. This is most likely a result of diffusion induced grain

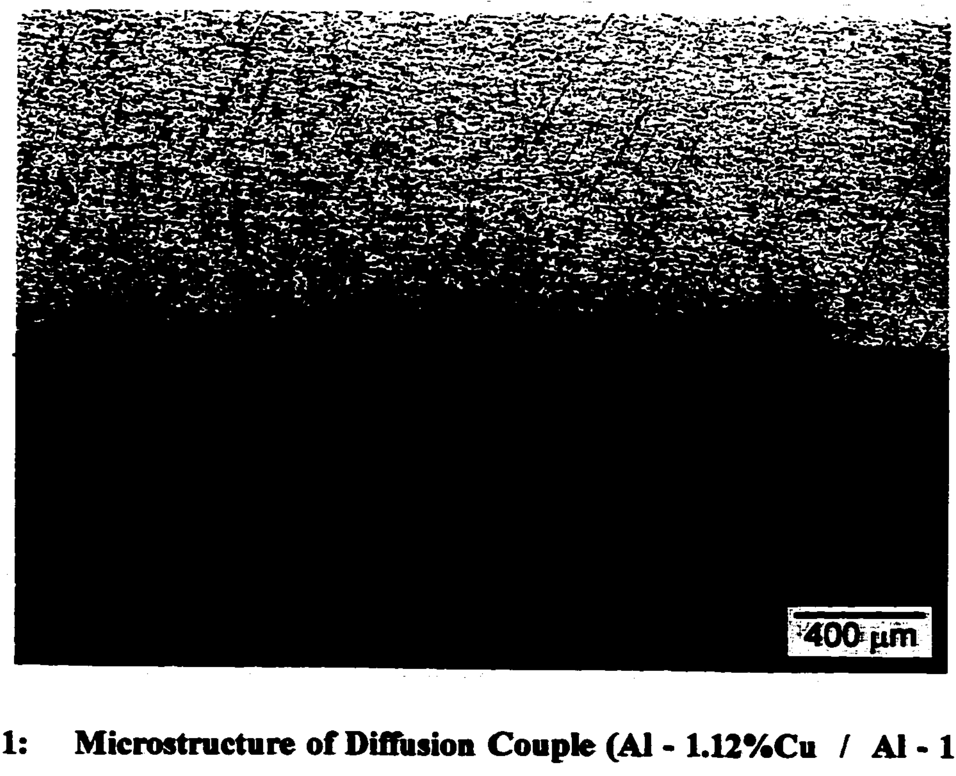

Figure 4.1: **Microstructure of Diffusion Couple (Al - 1.12%Cu / Al - 1.46%Cu) After 0.5 Hours At A Temperature of 582 ± 2°C.**

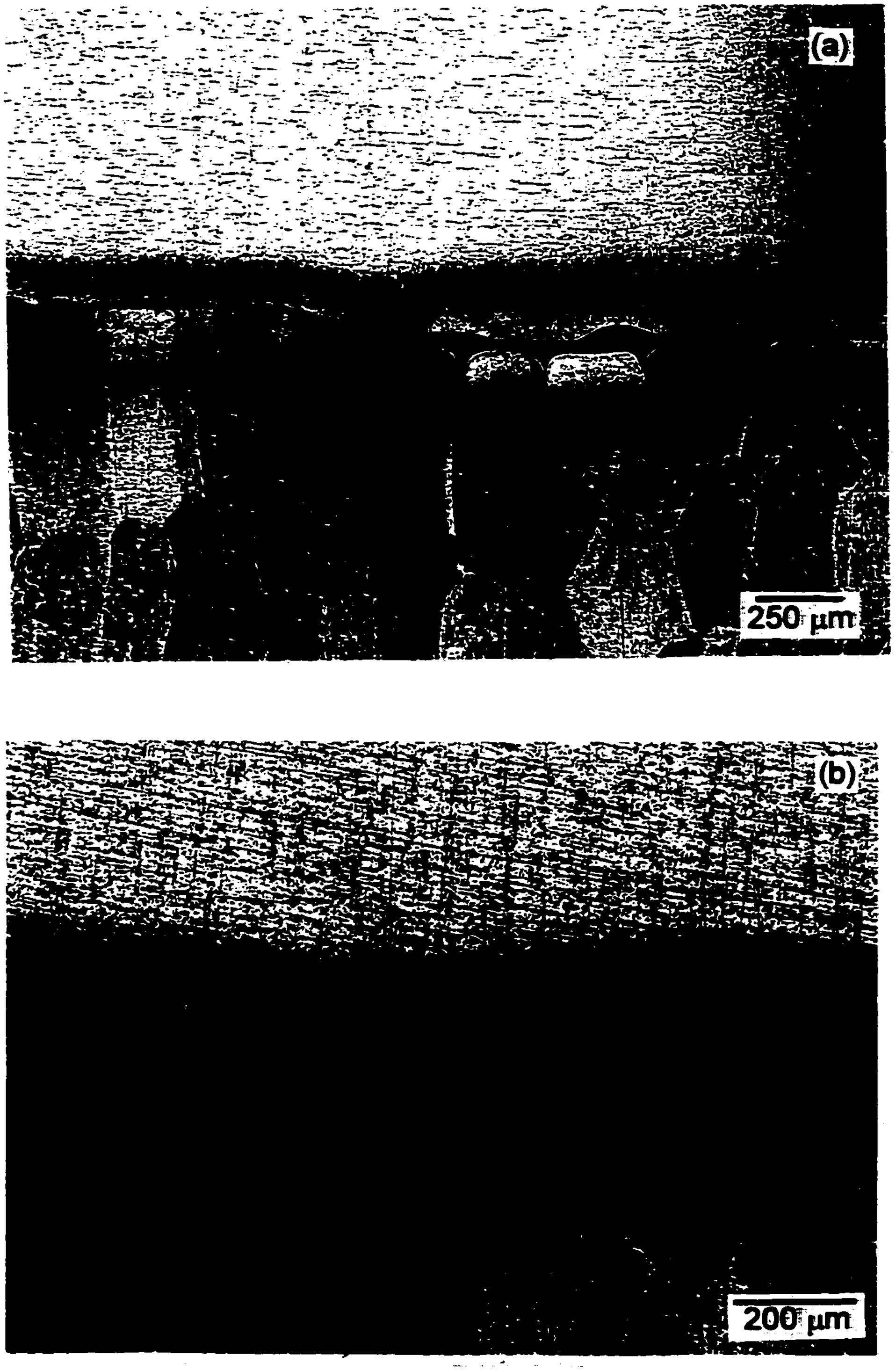

Figure 4.2: Microstructure of Diffusion Couple (Al - 1.12%Cu / Al - 1.46%Cu) After 7.5 Hours At A Temperature of 582 ± 2°C: (a) Overall View; (b) Magnified View Showing Equilibrium Grain Boundary Grooving and Diffusion Induced Grain Boundary Migration (DIGM).

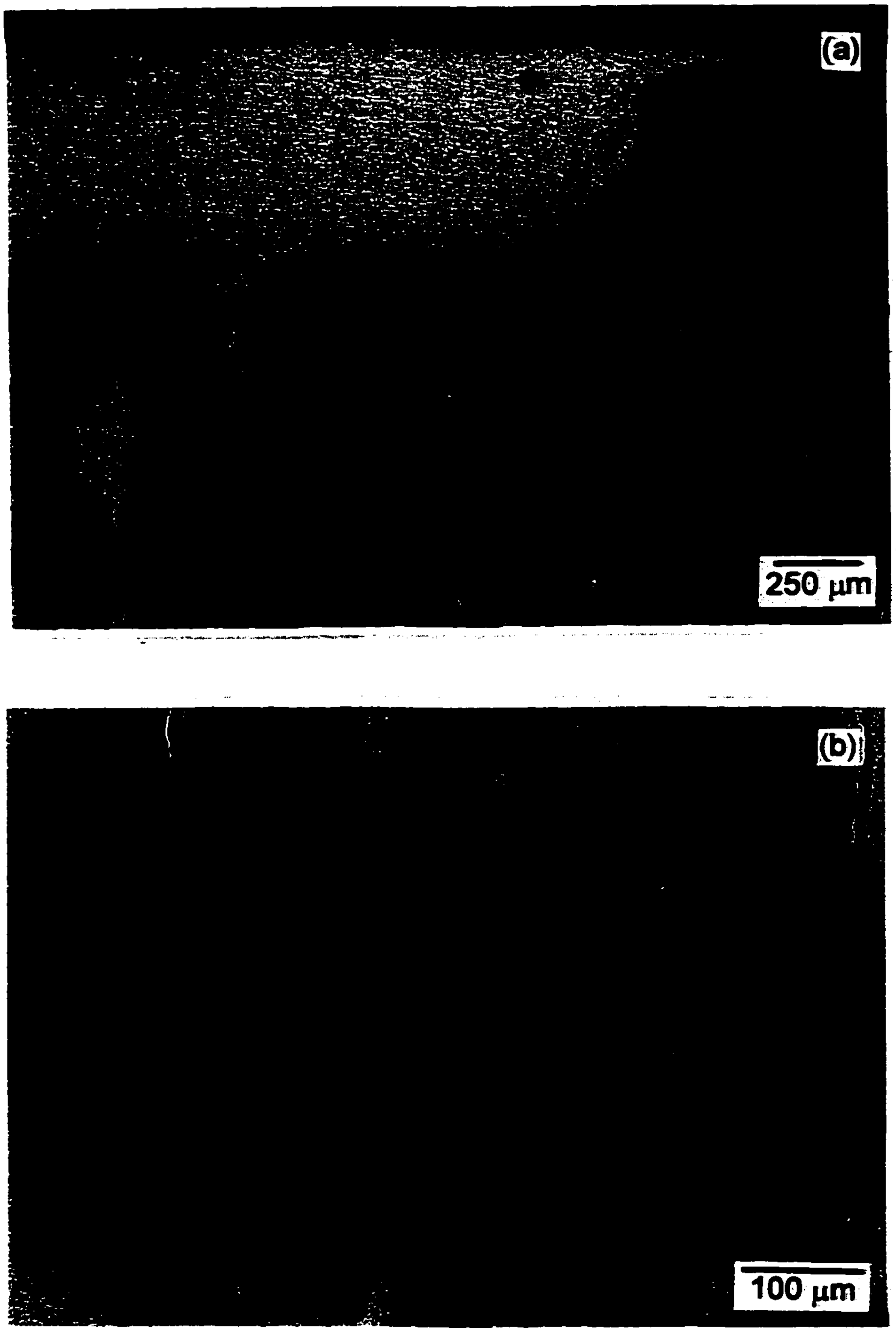

Figure 4.3: Microstructure of Diffusion Couple (Al - 1.12%Cu / Al - 1.46%Cu) After 13.5 Hours At A Temperature of 582 ± 2°C: (a) Overall View of Migrated Region, (b) Magnified View Showing 'Zig-Zag' DIGM.

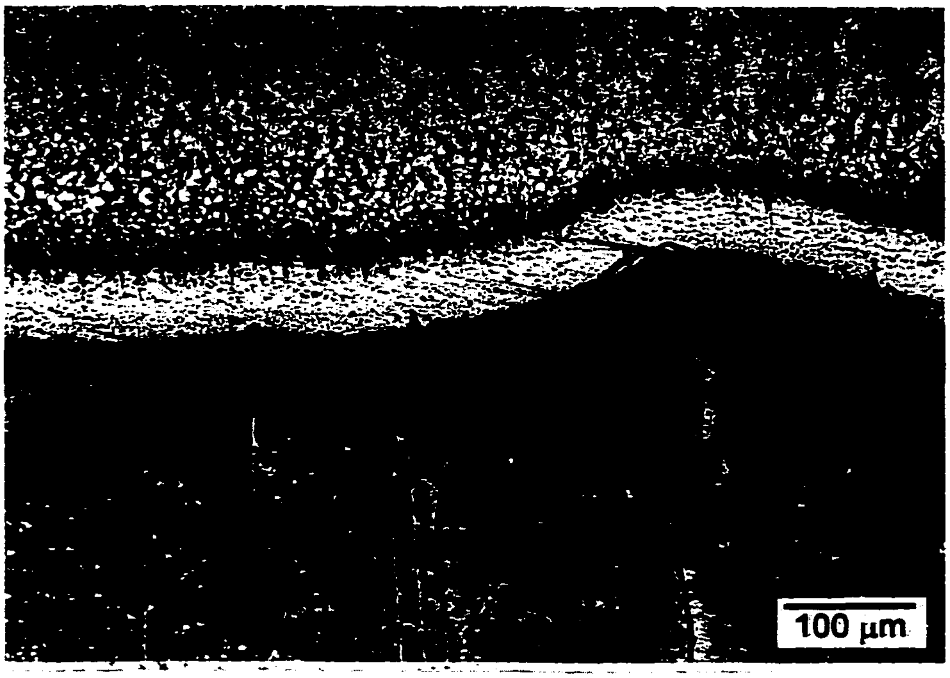

Figure 4.4: **Microstructure of Diffusion Couple (Al / Al - 1.46%Cu) After 0.5 Hours At A Temperature of 582 ± 2°C.**

boundary migration (DIGM), where the driving force for migration is believed to be essentially the same as that for LFM; in this case the liquid phase acts as a solute source, with copper atoms diffusing along the grain boundaries and into the grains they separate. A concentration difference then develops across each boundary, leading to migration. It also appears that at positions where the liquid film was thinnest (in general, the center points of the columnar grains) the interface has moved further into the non-equilibrium Al - 1.12%Cu phase than in the groove regions. This is a direct result of diffusion of solute across the liquid film being the rate determining process in these experiments. The diffusion profile of copper into the non-equilibrium phase is also visible as in the previous micrograph.

Figure 4.3 illustrates the results obtained from the same couple run for 13.5 hours (*i.e.*, Experiment 3). Figure 4.3(a) shows that some migration has occurred in the direction of the non-equilibrium Al - 1.12%Cu phase as in the previous experiments. The microstructure is similar to those shown in Figures 4.1 and 4.2, except that migration does not appear to have been uniform across the sample in this case, and the etching of the copper diffusion profile ahead of the migrating interface is irregular. Figure 4.3(b) shows a region of the equilibrium solid close to the solid/liquid interface. It can be seen that two seperate grain boundary segments have migrated in opposite directions along a single boundary; this phenomenon occurs in many systems that exhibit LFM, and is termed 'zig-zag' DIGM (see Yoon [48] for review).

A micrograph of the Al / Al - 1.46%Cu diffusion couple held at 582 °C for 0.5 hours is shown in Figure 4.4. The diffusion of copper into the non-equilibrium aluminum (Al) half of the couple is evident from the etched region adjacent to the solid - liquid interface as in the previous experiments. In the region where the liquid film was thinnest, a significant amount of LFM has occurred.

Measurements of Migration Distances

Figures 4.1, 4.2(a), 4.3(a) show the overall migration behaviour for Experiments 1, 2 and 3 respectively. . In each case significant migration has occurred in the direction of the non-equilibrium solid (Al - 1.12%Cu) as expected. The migration distances obtained from these experiments are summarized in Table 4.2.

It was expected that the measured migration distances would increase with time at the experimental temperature. With reference to Table 4.1 it can be seen that although the migration distance for Experiment 2 is substantially larger than that for Experiment 1 as expected, the migration distance obtained from Experiment 3 does not follow this trend. Possible reasons for these discrepancies are outlined in Chapter Seven.

Table 4.2: Migration Distances Obtained From Diffusion Couple Experiments.

Experiment	Measured Migration Distance (μm)*	Measured Liquid Film Thickness (μm)**
1	60 ± 12	21 ± 8
2	130 ± 10	19 ± 6
3	84 ± 22	15 ± 12

Note: *Measured from the line of no wetting to the location of the liquid film after quenching (measurements in at least twenty locations were used to obtain this average).
**Measured after experiment was completed.

Experimental Difficulties

There are several experimental aspects of the diffusion couple approach that can possibly lead to ambiguity in the results obtained. These are summarized below:

- The liquid phase leaked out during all experiments listed in Table 4.1. The time at which this occurred is unknown.
- The actual stress state in the diffusion couple is difficult to estimate with any certainty (*i.e.*, residual stresses are present due to the loading procedure).
- The slow heating rate and the fact that the cooling rate is non - linear make quantitative analysis difficult.
- The liquid films obtained in these experiments (see Table 4.2) are much thicker than those from liquid phase sintering (LPS) experiments performed by Yoon and co-workers [15-25] (generally < 5 μm).

The implications these experimental difficulties have upon the interpretation of the migration distance measurements are discussed in Chapter Seven.

4.3 PRECIPITATION TYPE EXPERIMENTS

The second method used to induce LFM in aluminum rich Al-Cu alloys was performed using a precipitation type of experiment, as outlined in Section 3.4. The objective of these experiments was the same as that in the diffusion couple experiments: *i.e.*, to observe and quantify LFM in aluminum rich Al-Cu alloys. The experimental difficulties associated with the diffusion couple experiments discussed in the previous section make the acquisition of data amenable for quantitative analysis very difficult. A set of experiments were therefore required to obtain data suitable for modelling and analysis.

The use of θ precipitates as a source of liquid has several advantages over the use of the copper foil in the diffusion couple experiments. These include:

- Thinner liquid films: as the precipitates liquate upon raising the temperature to a value slightly above the eutectic, the liquid films that form along the grain boundaries of the sample have thicknesses (δ) of the order of 2 to 5 μm. When compared to the thicknesses of the liquid films that form during the diffusion couple experiments (see Table 4.1), it can be seen that the films created in the precipitation experiments provide a shorter path for the diffusion of solute.

- The liquid phase is contained within the sample in the precipitation experiments, therefore alleviating the problem of liquid loss due to leakage experienced during the diffusion couple experiments.

- Any stressed regions within the sample (*i.e.*, parent phase) can be assumed to be due to coherency effects only. That is, any long range strain fields that existed prior to equilibration at 400°C were relieved during the heat treatment.

- Better temperature control: heating the sample to the experimental temperature can be performed quickly and accurately using a salt bath furnace.

- The parent phase can be considered homogeneous with composition C_0. The composition was determined from the θ solubility at the equilibration temperature of 400 °C.

The morphologies obtained from these experiments are presented in Section 4.3.1. These include several micrographs of interesting morphologies from early samples (*i.e.*, thicker samples with a thickness of approximately 5 mm), and micrographs of thinner samples from which measurements for the positions of the leading and trailing solid - liquid interfaces, and the distance between pinning points for several time values could be obtained. Volume fractions of liquid as a function of time are presented in Section 4.3.2 for both heat treatments. SEM micrographs of selected LFM events obtained from the liquation of the sample treated for 15 seconds (heat treatment (a)) are presented in Section 4.3.3; composite three-dimensional reconstructions of several events created using the procedure described in Section 3.4.6 are also included. The section concludes with a presentation of the migration distances obtained from two-dimensional optical micrographs (Section 4.3.4).

4.3.1 Optical Microscopy

This section presents the morphologies obtained from the liquation of the two-phase (Al) + θ structure obtained from heat treatments (a) and (b) (described in Section 3.4.1). The initial microstructures obtained from both initial heat treatments are described. This is followed by a presentation of the microstructures obtained from partially liquated samples, formed using material from both heat treatments as the starting material.

Starting Microstructures

The microstructures obtained from the initial low temperature precipitations are shown in Figure 3.4. In both cases, care was taken to insure that the initial conditions were relatively close to equilibrium at the lower (equilibration) temperature of 400°C; that is, that the α Al-Cu solid solution ((Al) phase) was very nearly of a uniform composition equal to the equilibrium solubility of the θ phase. Figure 3.4(a) shows the microstructure obtained from heat treatment (a). It can be seen that the precipitates are predominantly non-faceted; those present along the grain boundaries lie in strings, and are larger than those that lie within the grain interiors. The microstructure obtained from heat treatment (b) is shown in Figure 3.4(b). It can be seen that the structure is much coarser than that obtained in heat treatment (a) with the majority of the θ phase present as large faceted Widmanstätten plates (*i.e.*, within the grain interiors). The starting microstructure for the early precipitation experiments is

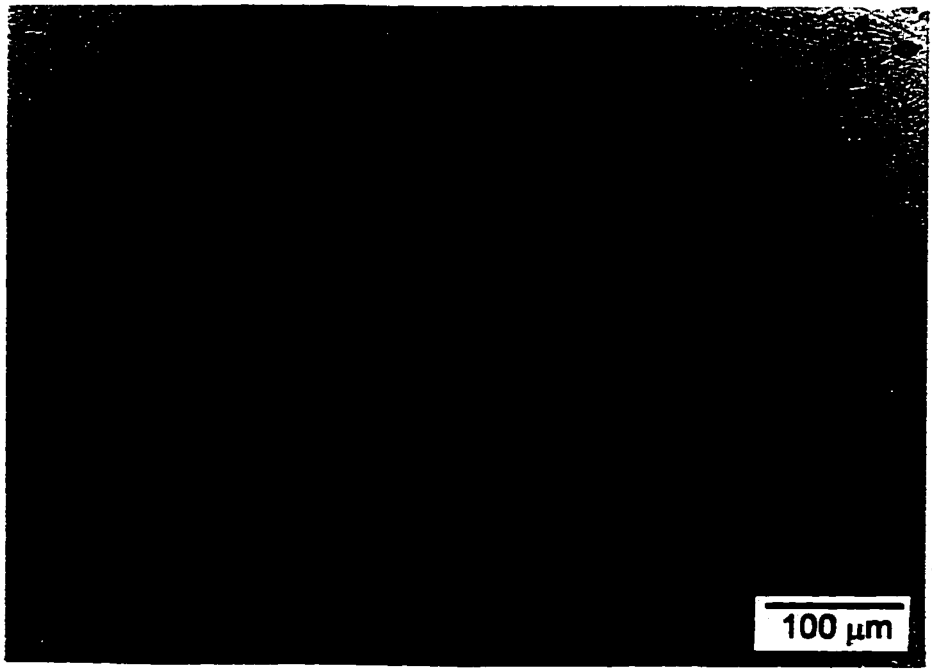

Figure 4.5: **Microstructure of the Alloy Used For Early Precipitation Type Experiments.**

shown in Figure 4.5. This sample was subjected to the same heating schedule as was heat treatment (a). It can be seen however that the precipitates are larger, with very few located within the grain interiors. Possible reasons for the differences between the starting microstructures are discussed in Chapter Seven.

Microstructures Developed During Partial Liquation of Samples Formed During Heat Treatment (a).

This section contains micrographs of the morphologies that develop during the partial liquation of samples formed during heat treatment (a). Micrographs of a few interesting regions obtained from the early precipitation experiments are presented in Figures 4.6, 4.7, 4.8, and 4.9. In all cases the sample was held at an experimental temperature of 558 °C for a time of 15 seconds. Significant LFM can be observed in all micrographs. It can be seen that in most cases, liquid lenses present along any particular grain boundary of the sample migrate in one direction only; however along the grain boundary on the left hand side of Figure 4.6, LFM can be observed to occur into both of the grains that the liquid film separates. The LFM events present along the right hand segment of the grain boundary visible in Figure 4.8 apparently possess greater curvatures and have migrated further than most other events. LFM events possessing very narrow liquid films can be seen in Figure 4.9; these events have migrated a distance that is approximately twice that of most others, but do not possess the curvature of those in Figure 4.8. An interpretation of these observations is included in Chapter Seven.

Micrographs from the second set of precipitation experiments are shown in Figures 4.10 to 4.14, corresponding to time values of 3, 15, 30, 60, and 120 seconds. It should be noted that the samples were not etched since this damaged the LFM events such that the positions of the leading and trailing solid - liquid interfaces were unclear. The grain boundaries are therefore only visible through the observation of the liquid morphology. That is to say that along the grain boundaries, the liquid phase is present in the form of strings of relatively large liquid

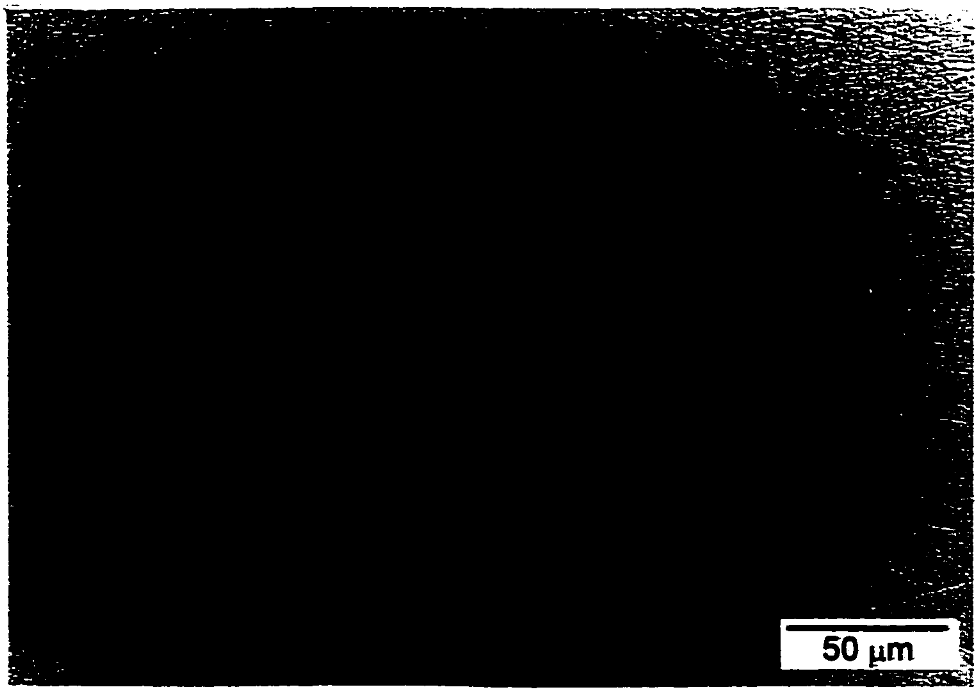

Figure 4.6: Microstructure of Sample Held for 15 Seconds At 558°C (Heat Treatment (a) - Early Experiments).

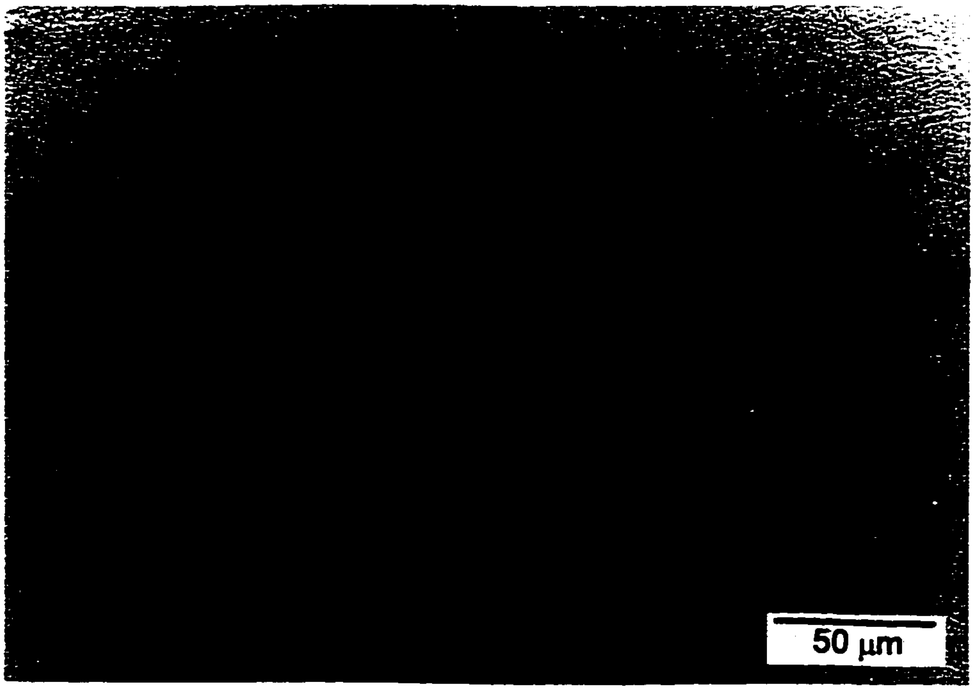

Figure 4.7: Microstructure of Sample Held for 15 Seconds At 558°C (Heat Treatment (a) - Early Experiments).

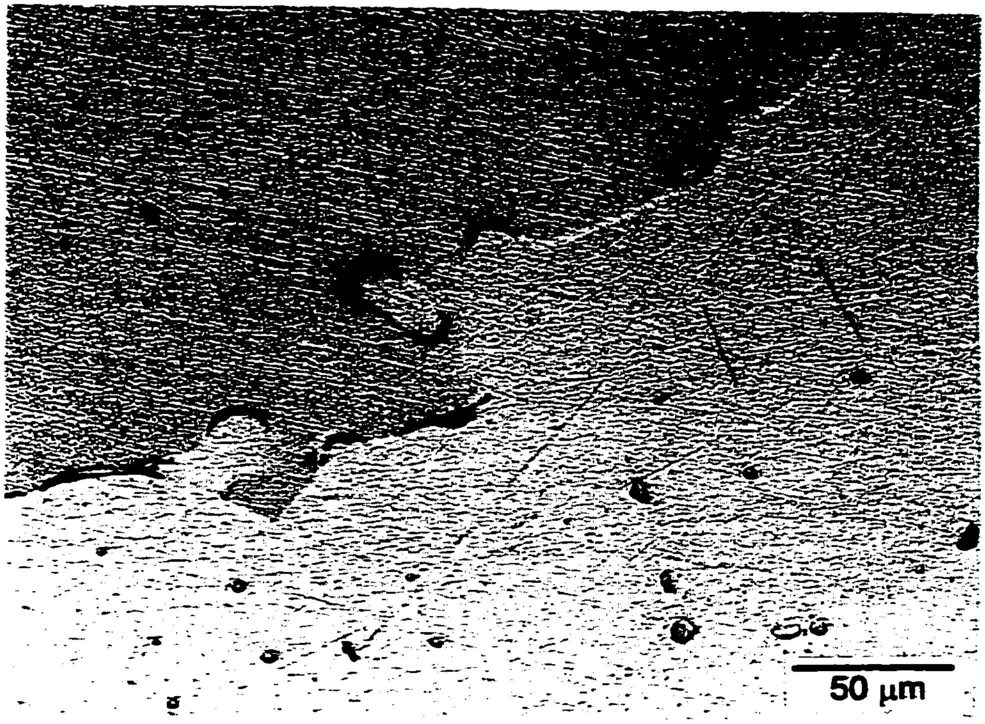

Figure 4.8: Microstructure of Sample Held for 15 Seconds At 558°C (Heat Treatment (a) - Early Experiments).

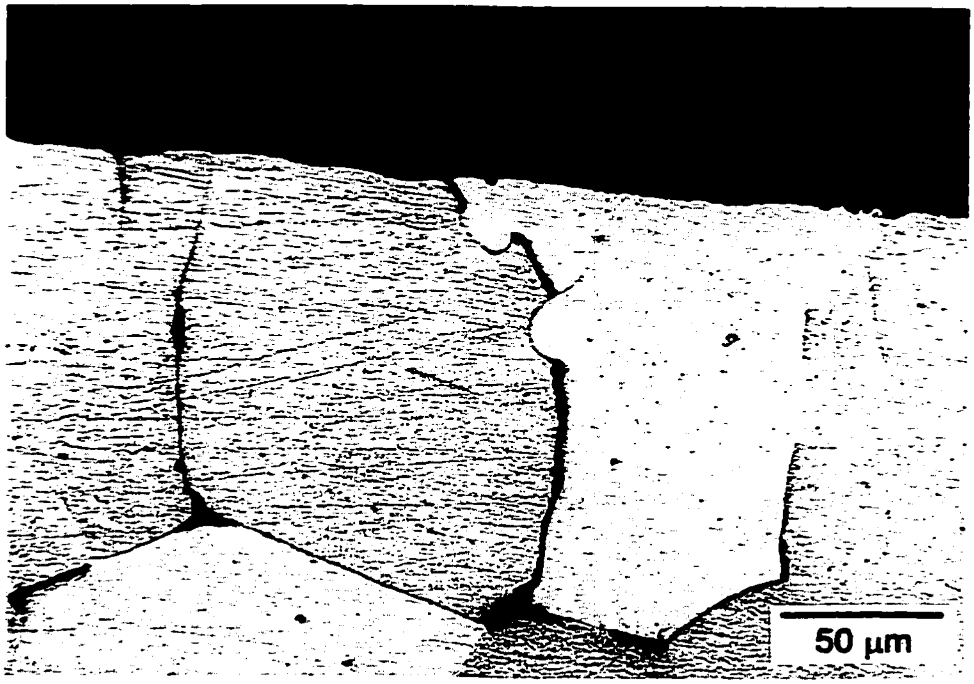

Figure 4.9: Microstructure of Sample Held for 15 Seconds At 558°C (Heat Treatment (a) - Early Experiments).

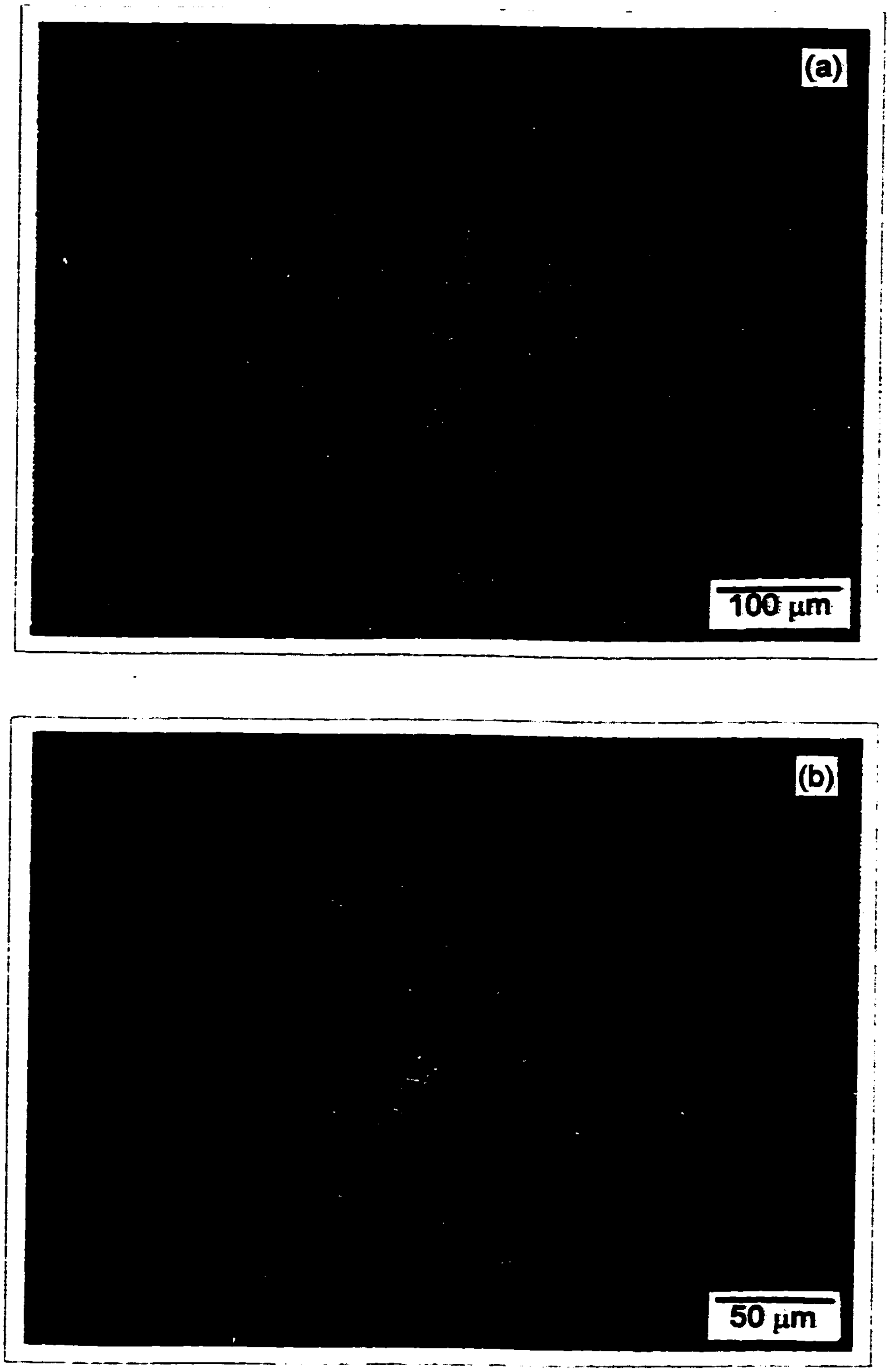

Figure 4.10: **Microstructure of Sample Held for 3 Seconds At 560°C (Heat Treatment (a)). (a) Overall Morphology; (b) Higher Magnification.**

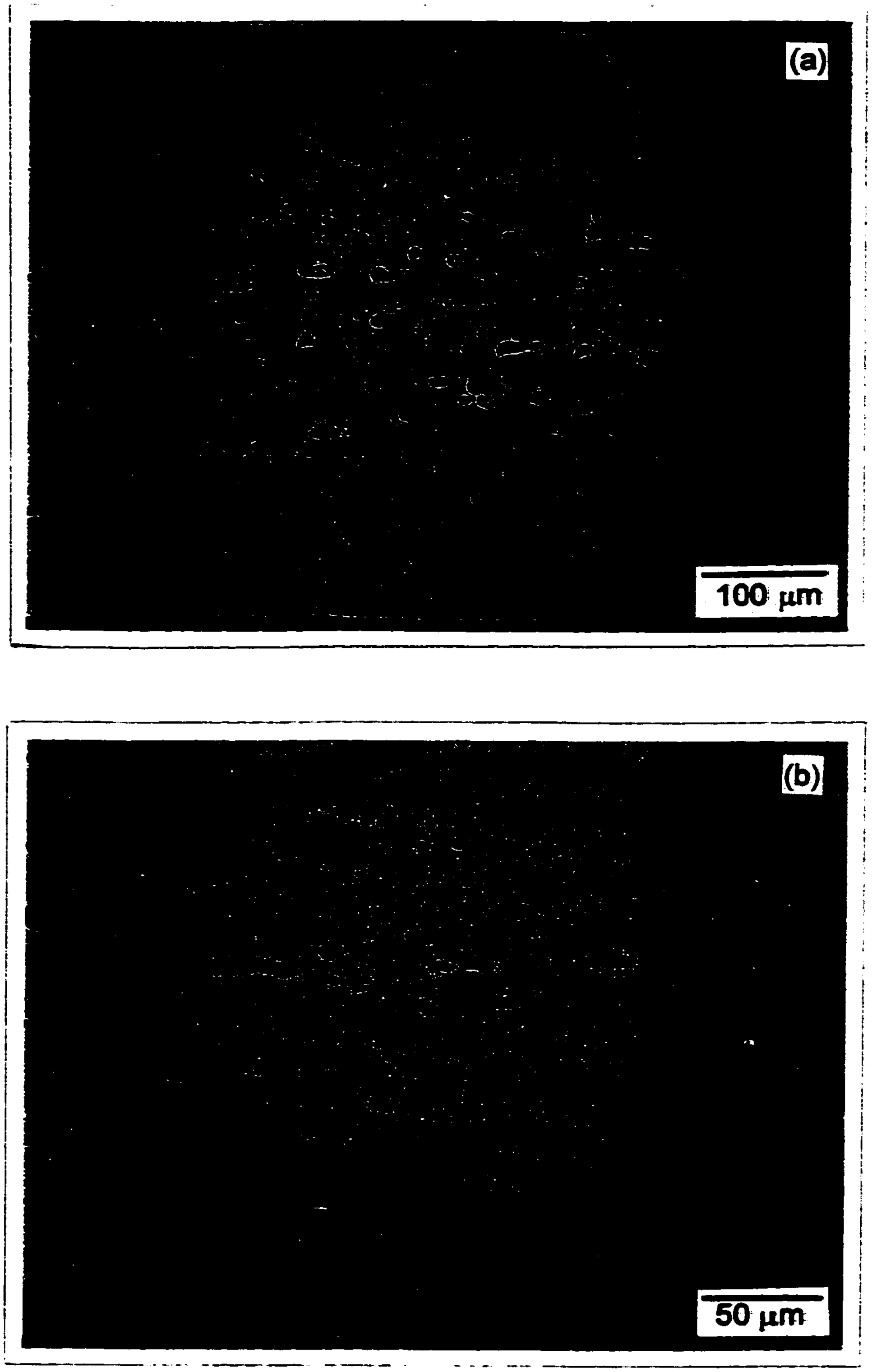

Figure 4.11: Microstructure of Sample Held for 15 Seconds At 560°C (Heat Treatment (a)). (a) Overall Morphology; (b) Higher Magnification.

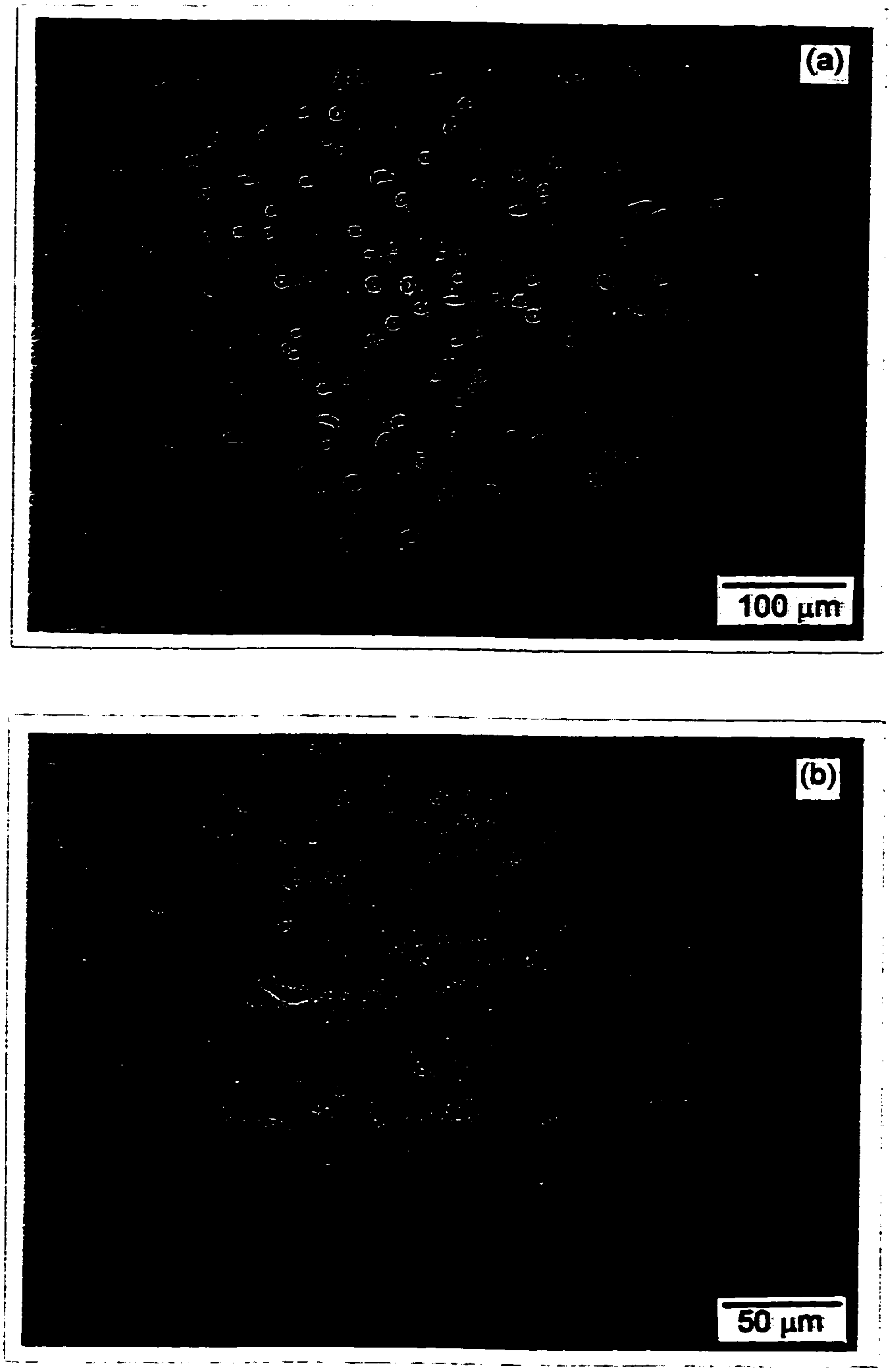

Figure 4.12: **Microstructure of Sample Held for 30 Seconds At 560°C (Heat Treatment (a)). (a) Overall Morphology; (b) Higher Magnification.**

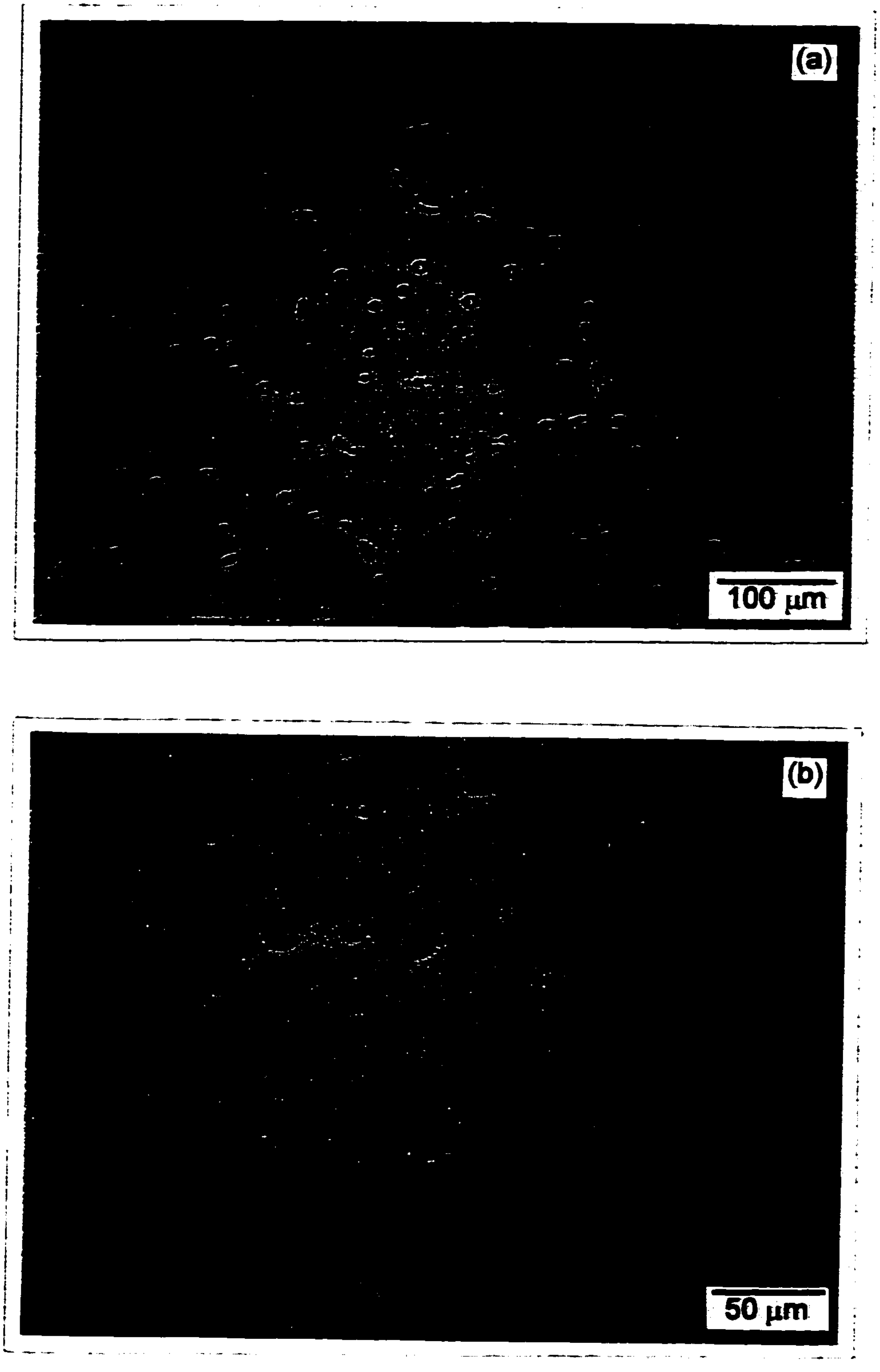

Figure 4.13: Microstructure of Sample Held for 60 Seconds At 560°C (Heat Treatment (a)). (a) Overall Morphology; (b) Higher Magnification.

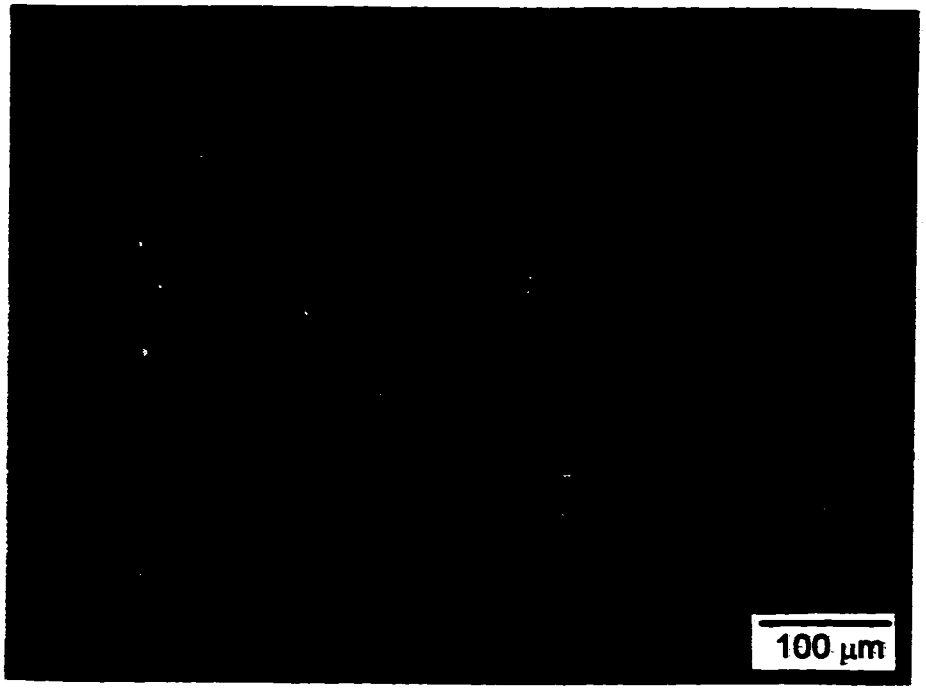

Figure 4.14: Microstructure of Sample Held for 120 Seconds At 560°C (Heat Treatment (a)).

pools, while within the grains the liquid is present as small spheres. It can be seen that as early as 3 seconds after insertion into the salt bath held at the experimental temperature of 560°C the θ phase has fully liquefied; in fact a few actual LFM events are visible. That is to say that significant migration has occurred only 1.5 seconds after reaching the temperature at which the first liquid appears (*i.e.*, the eutectic temperature (see Chapter Three)). The process obviously occurs very rapidly in the initial stages. LFM events can be seen in all samples; in many cases strings of events lie along the same grain boundary, either migrating into the same grain (Figure 4.13(b)) or into both grains (Figures 4.11(b) and 4.12(b)). It can be seen from the sequence of micrographs that the amount of liquid present decreases with time as is expected (see also Section 4.3.2). Further examination of these microstructures indicates that after a period of rapid migration the liquid films often stabilized as crescent-shaped pools of liquid. That is, the positions of the leading and trailing solid - liquid interfaces do not noticeably change with time after reaching a certain limiting curvature; *i.e.*, whatever the size of the LFM event, the general shape (curvature) of the solid - liquid interfaces is similar. This is discussed further in Chapter Seven.

Microstructures Developed During Partial Liquation of Samples Formed During Heat Treatment (b).

This section contains micrographs of the morphologies that develop during the partial liquation of samples formed during heat treatment (b). From these micrographs (Figures 4.15 to 4.19) and the initial microstructure (Figure 3.4(b)), it can be seen that this treatment resulted in a much coarser microstructure (compared to heat treatment (a)) with a grain size of the order of the thickness of the sample, *i.e.*, 500 μm. The initial microstructure is therefore dominated by large Widmanstätten plates of the θ phase. On liquation, these plates gave rise to disc-shaped liquid pools, which evidently did not migrate; instead, their rims were observed to cylinderize, as a (presumed) first stage of spheroidization. As was the case for heat treatment (a), the amount of the liquid phase present gradually decreases with time at the experimental temperature of 560°C. After a time of 300 seconds (Figure 4.17), it can be seen that the liquid present within the grains has almost fully spheroidized. The liquid located along the grain boundaries of the sample generally narrows with time and does not exhibit LFM to the same degree as for heat treatment (a); however, evidence that some LFM has occurred can be seen at the bottom of Figure 4.18. An interpretation of these observations is included in Chapter Seven.

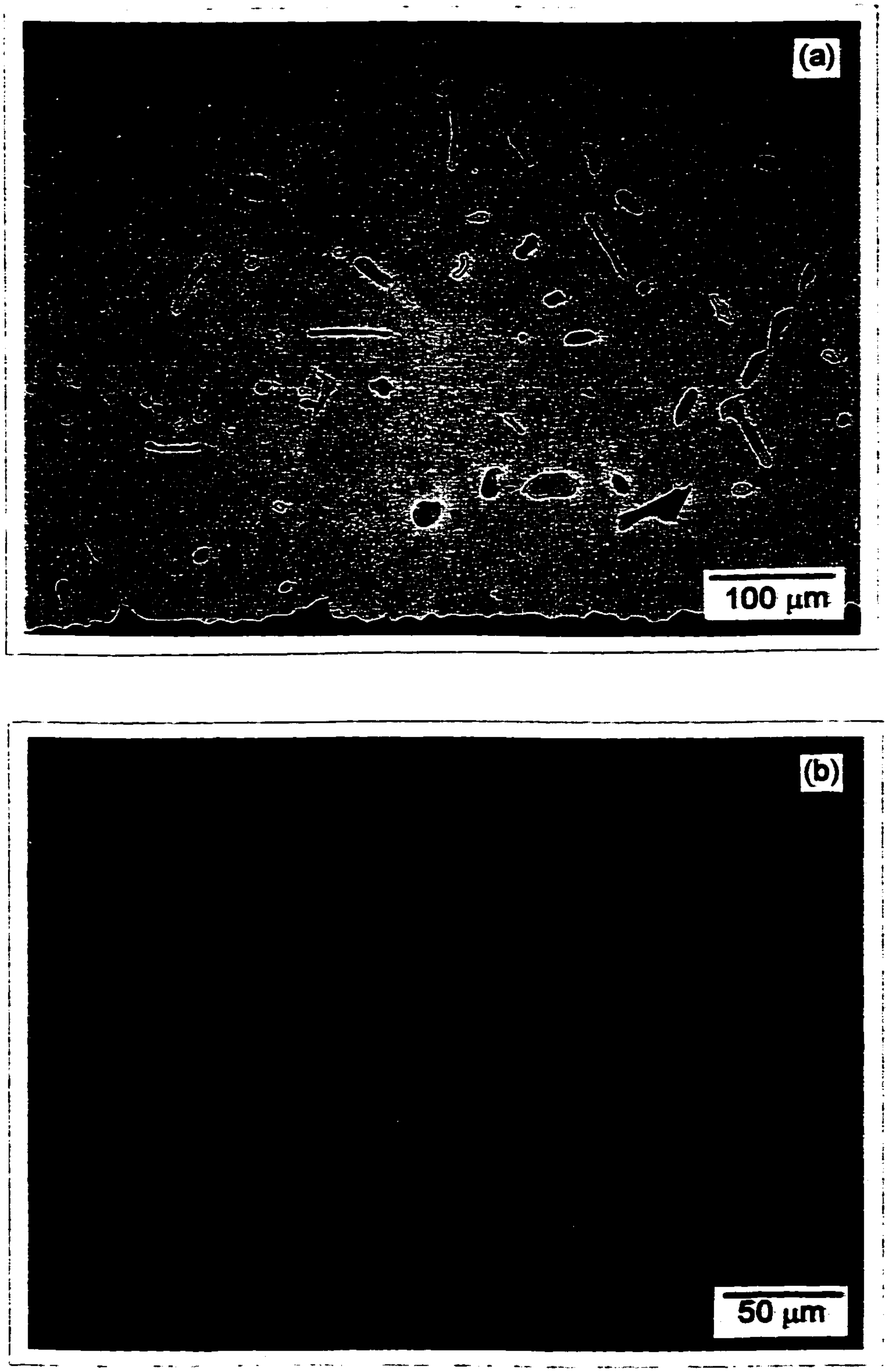

Figure 4.15: **Microstructure of Sample Held for 15 Seconds At 560°C (Heat Treatment (b)). (a) Overall Morphology; (b) Higher Magnification.**

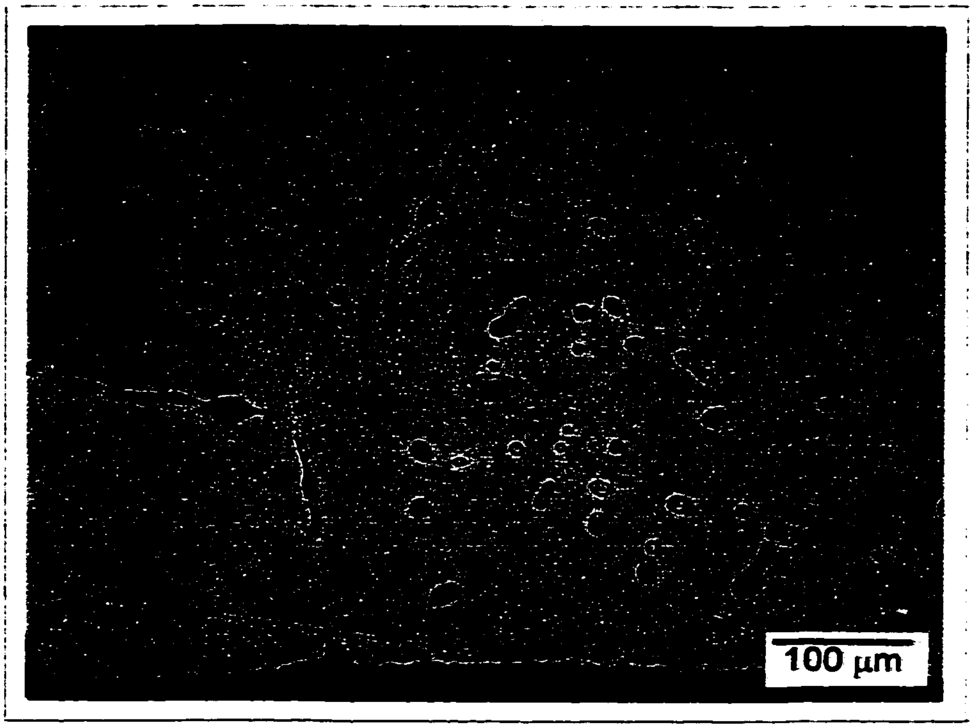

Figure 4.16: Microstructure of Sample Held for 60 Seconds At 560°C (Heat Treatment (b)).

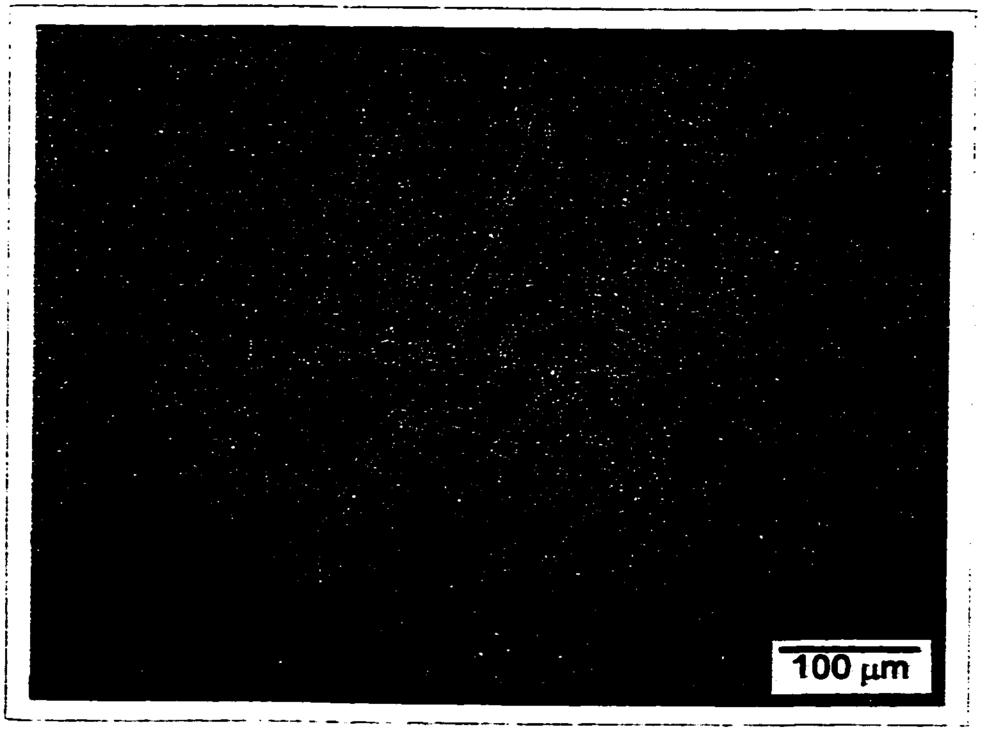

Figure 4.17: Microstructure of Sample Held for 300 Seconds (5 Minutes) At 560°C (Heat Treatment (b)).

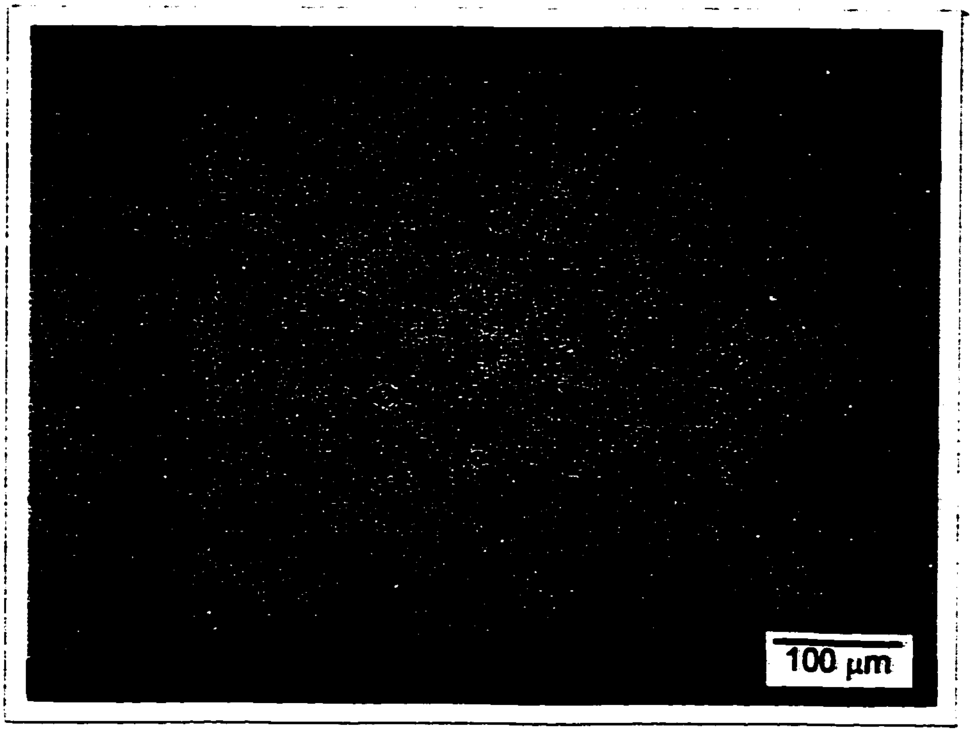

Figure 4.18: **Microstructure of Sample Held for 900 Seconds (15 Minutes) At 560°C (Heat Treatment (b)).**

Figure 4.19: **Microstructure of Sample Held for 1800 Seconds (30 Minutes) At 560°C (Heat Treatment (b)).**

4.3.2 Volume Fraction Measurements

Quantitative measurements of the volume fraction of quenched liquid as a function of time are given in Figures 4.20 and 4.21. Figure 4.20 shows the measurements obtained for time values ranging from 0 to 3600 seconds for both heat treatments((a) and (b)); the plots indicate that the liquid phase is consumed with time. This is to be expected since at the experimental temperature of 560°C the bulk composition of the alloy (= 1.46 ± 0.05 atomic% (*i.e.,* 3.38 ± 0.18 weight%)) lies in the one phase (Al) region, *i.e.*, any liquid present is thermodynamically metastable. It can be seen that the liquid phase is removed more rapidly from samples obtained using material from heat treatment (a) than using the material from heat treatment (b). It should be noted however, that the overall shape of the plots is approximately the same. Since much of the information obtained from the short time samples is obscured in the figures described above, a second set of plots were created from the measurements for time values ranging from 0 to 120 seconds (Figure 4.21). It can be seen that in both heat treatments there is an initial increase in the volume fractions, peaking in the range of 7 to 10 seconds. Since the volume fraction measured at 0 seconds is that of the θ phase in both cases, a peak would be expected due to the volume expansion during the θ to liquid transition. The reasons for the similarities and differences described above are discussed in more detail in Chapter Seven.

The errors in the measurements were obtained using the method described by Hilliard and Cahn [54]. The purpose of their analysis was to determine the best method for obtaining volume fraction measurements of a randomly located second phase (in three-dimensions). It was determined that a systematic point counting method where a grid is superimposed on a sequence of randomly selected areas from the plane of polish was the best method (as was employed: see Section 3.4.4). That is, this method gives an unbiased estimate of the volume fraction of the second phase. An estimate of the standard deviation in the measured volume fraction values is obtained using the following expression [54]:

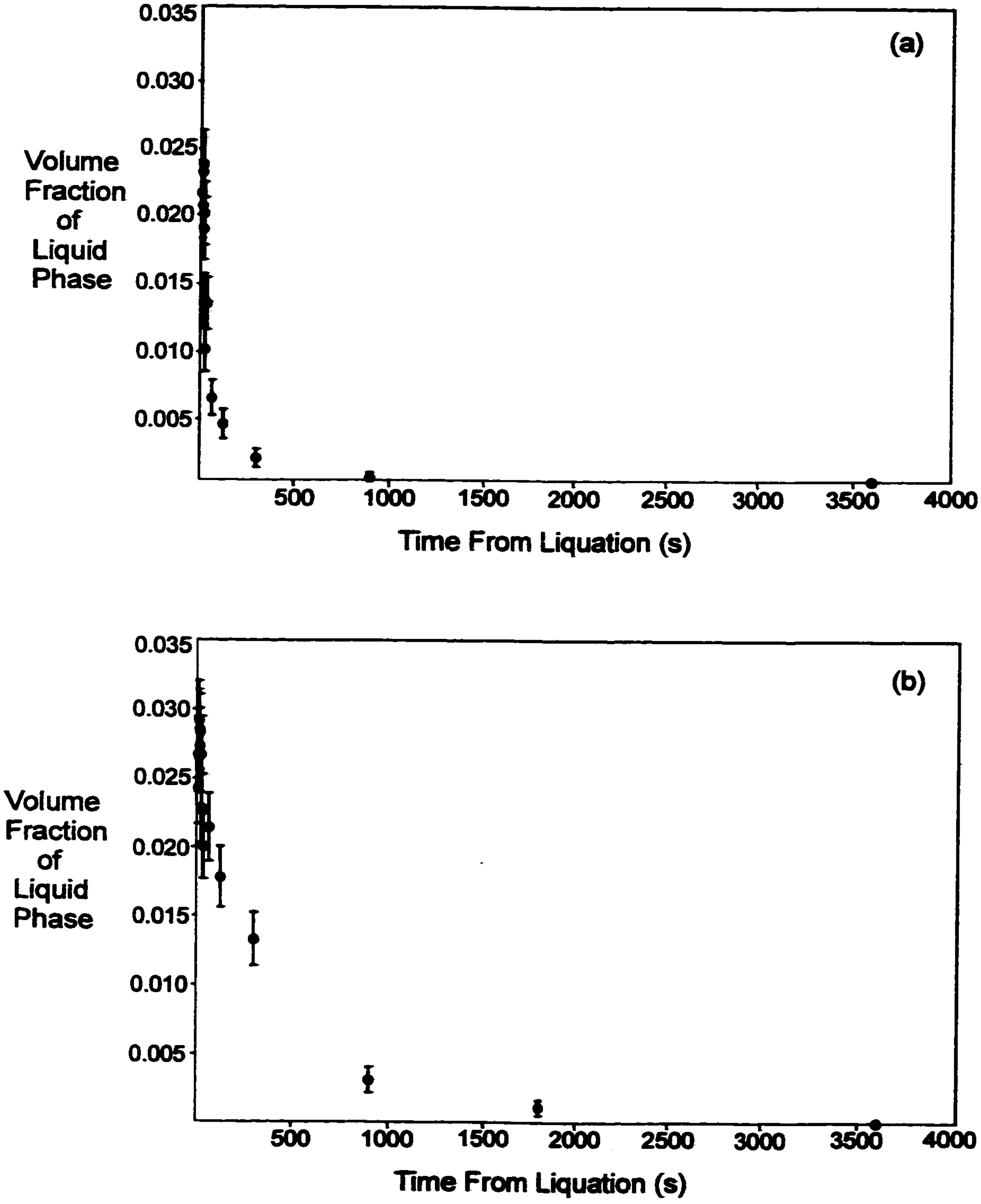

Figure 4.20: **Volume Fraction Measurements As a Function of Time (0 - 3600s.) For: (a) Heat Treatment (a); (b) Heat Treatment (b).**

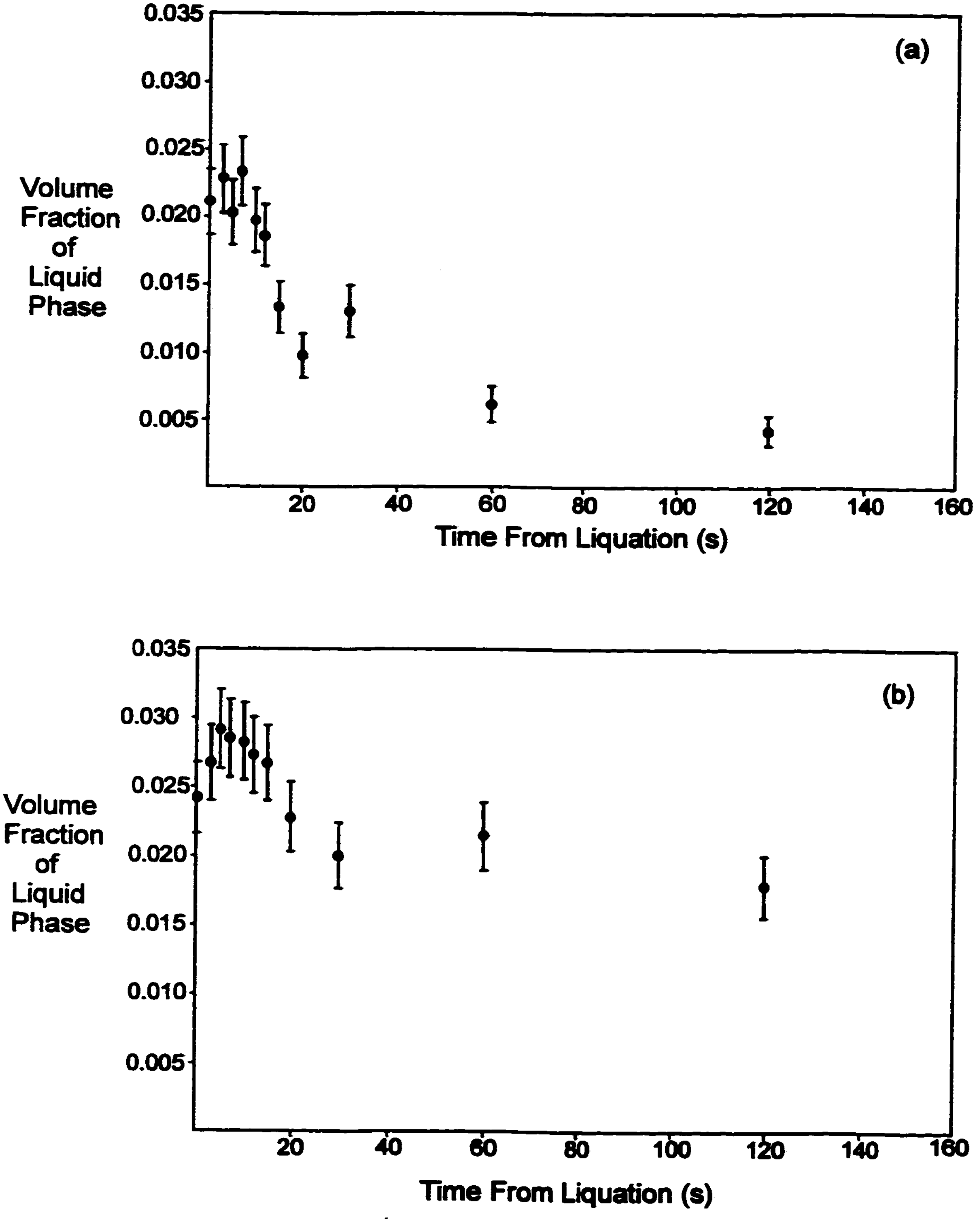

Figure 4.21: **Volume Fraction Measurements As a Function of Time (0 -120s.) For: (a) Heat Treatment (a); (b) Heat Treatment (b).**

$$\sigma_{V_f} = \frac{V_f}{\sqrt{N_P}} \tag{4.1}$$

Where:

σ_{Vf} Standard deviation in the volume fraction measurements

V_f Measured volume fraction

N_P Number of grid corners[**] falling on the phase being estimated.

The error bars for the volume fraction plots were obtained through the use of Equation (4.1); the measurements quoted are assumed to have an error of ± σ_{Vf}.

4.3.3 Scanning Electron Microscopy

This section outlines the results of the scanning electron microscopy performed on the sample held at the experimental temperature of 560 °C for 15 seconds after undergoing initial heat treatment (a) (*i.e.*, the 'P400(a)/15s' sample). Sample micrographs for each LFM event chosen for three-dimensional reconstruction are presented, as well as a few micrographs to illustrate some of the possible two-dimensional sections of LFM events that can be obtained. Composite three-dimensional representations of some particular LFM events, constructed using the method described in Section 3.4.5 are then presented. This is followed by a brief discussion of the morphologies obtained and the accuracy of the reconstructions.

Micrographs

Figures 4.22 to 4.33 show SEM micrographs of selected LFM events obtained after 15

[**] For the 6 × 6 grid used in the procedure described in Section 3.4.4, there are a total of 36 grid corners for each randomly selected area.

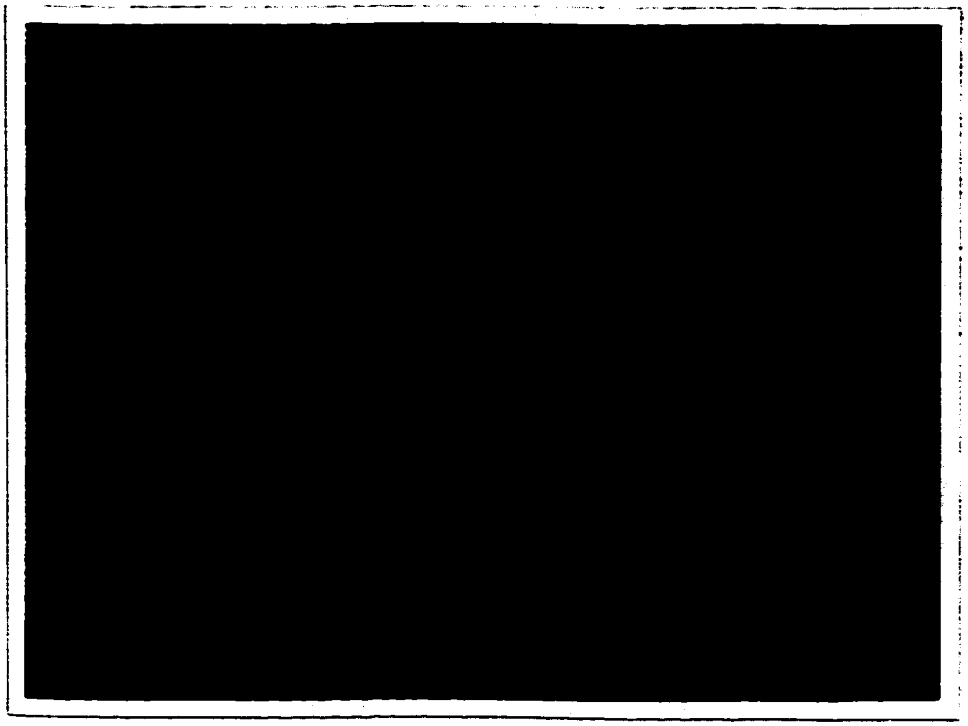

Figure 4.22: SEM Micrograph of Sample Held for 15 Seconds At 560°C (Heat Treatment (a)); Level Three of Figure 4.34.

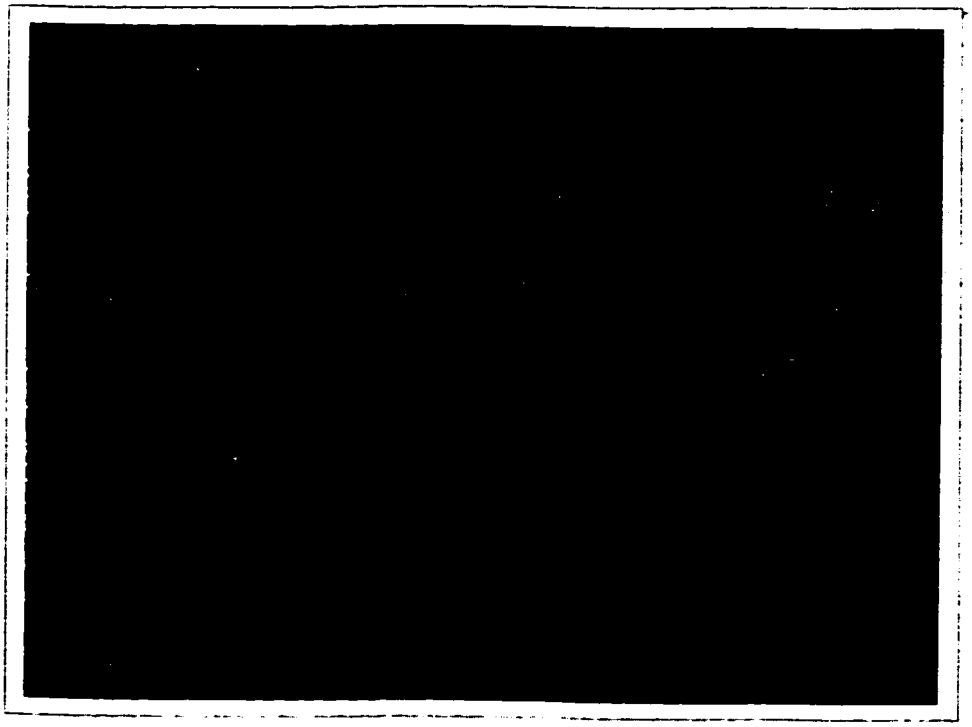

Figure 4.23: SEM Micrograph of Sample Held for 15 Seconds At 560°C (Heat Treatment (a)); Level Two of Figure 4.35.

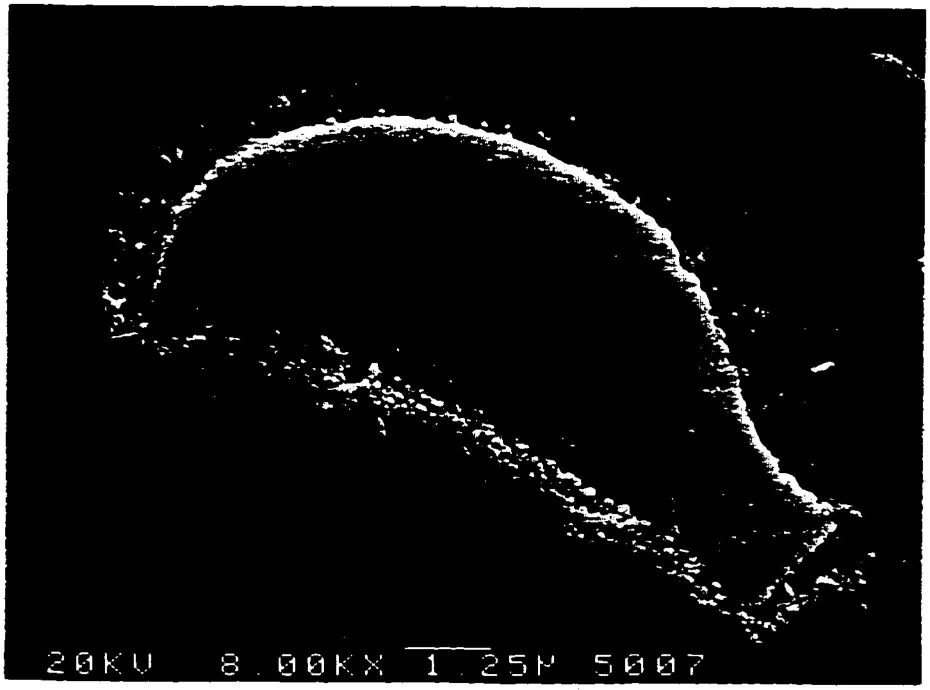

Figure 4.24: SEM Micrograph of Sample Held for 15 Seconds At 560°C (Heat Treatment (a)); Level Six of Figure 4.36.

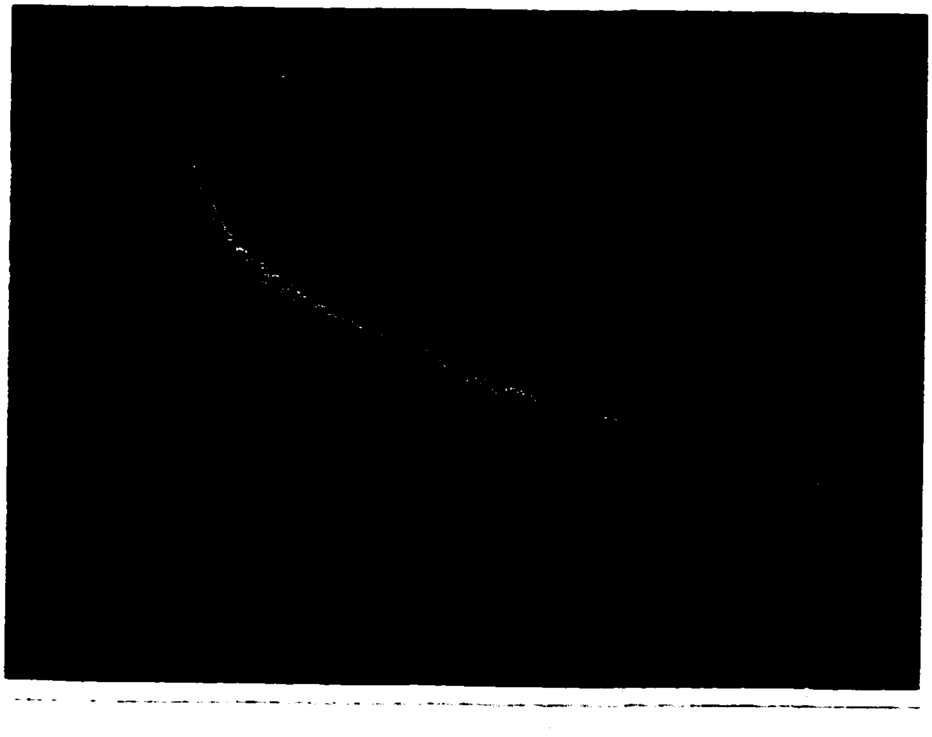

Figure 4.25: SEM Micrograph of Sample Held for 15 Seconds At 560°C (Heat Treatment (a)); Level Two of Figure 4.37.

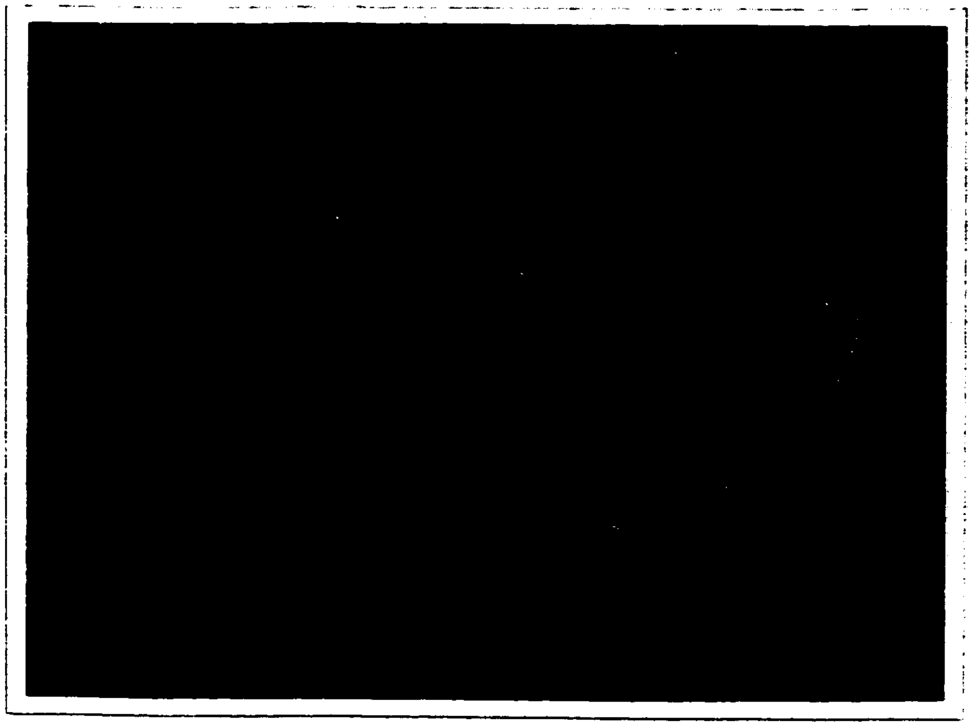

Figure 4.26: SEM Micrograph of Sample Held for 15 Seconds At 560°C (Heat Treatment (a)); Level Two of Figure 4.38.

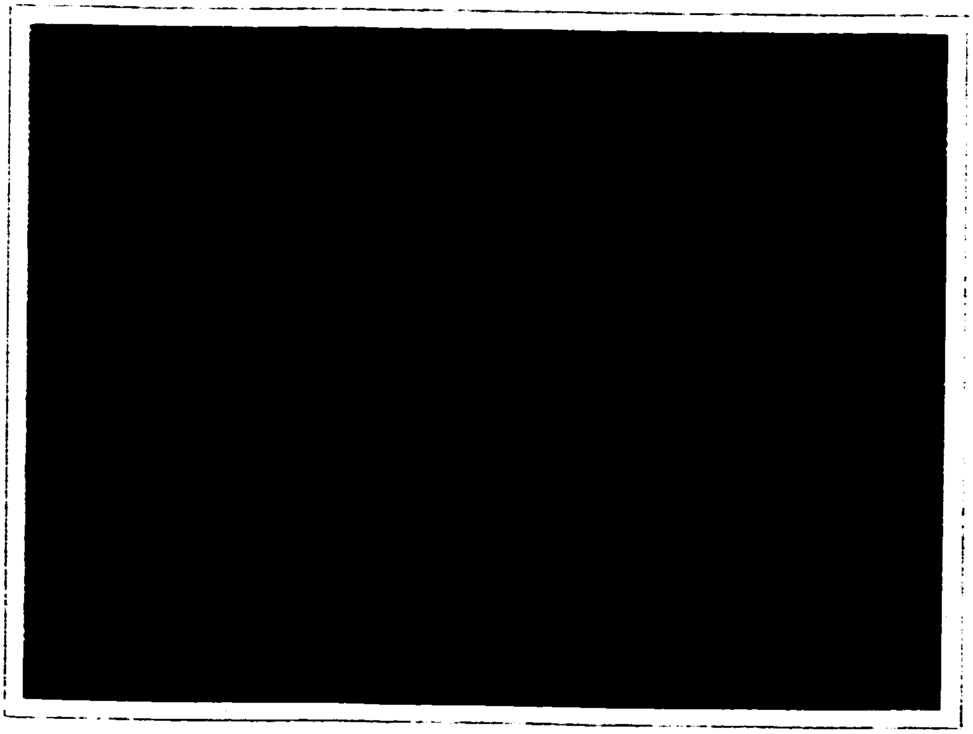

Figure 4.27: SEM Micrograph of Sample Held for 15 Seconds At 560°C (Heat Treatment (a)); Level Five of Figure 4.39.

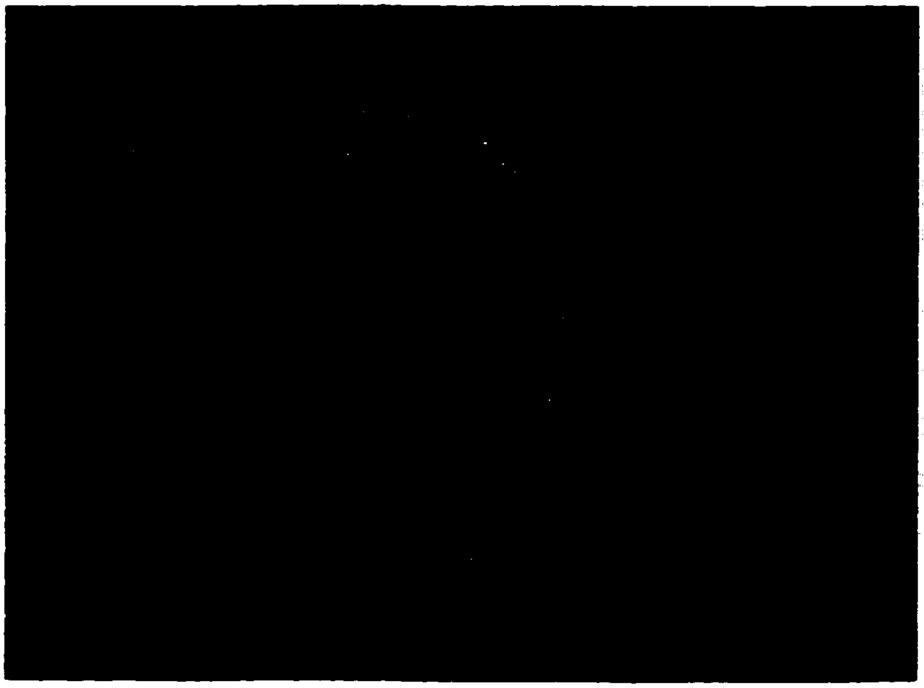

Figure 4.28: SEM Micrograph of Sample Held for 15 Seconds At 560°C (Heat Treatment (a)); Level One of Figure 4.40.

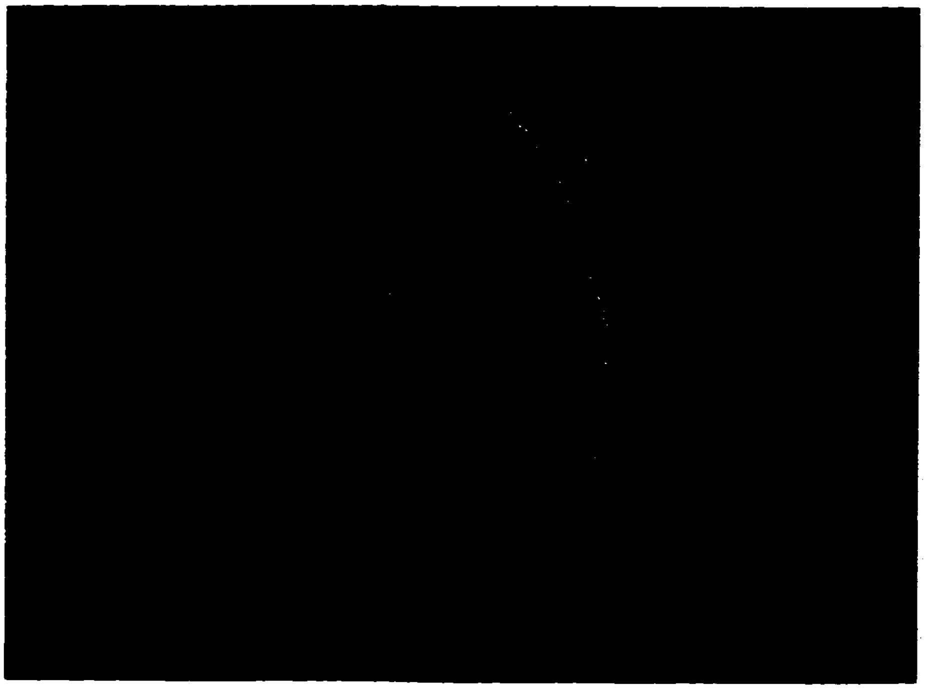

Figure 4.29: SEM Micrograph of Sample Held for 15 Seconds At 560°C (Heat Treatment (a)); Level One of Figure 4.41.

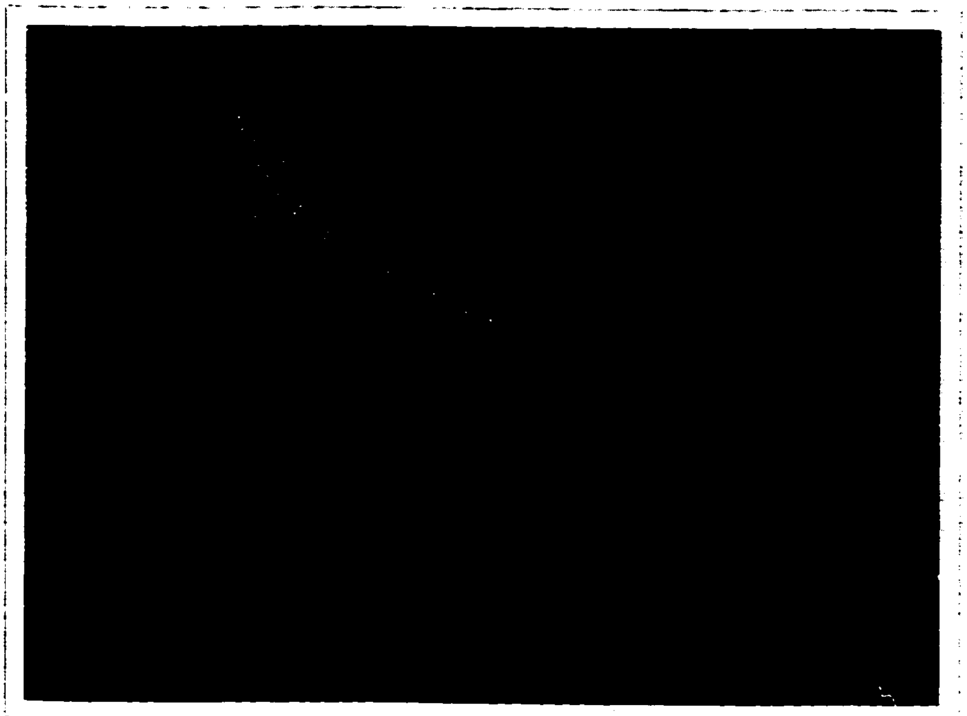

Figure 4.30: SEM Micrograph of Sample Held for 15 Seconds At 560°C (Heat Treatment (a)); Level Three of Figure 4.42.

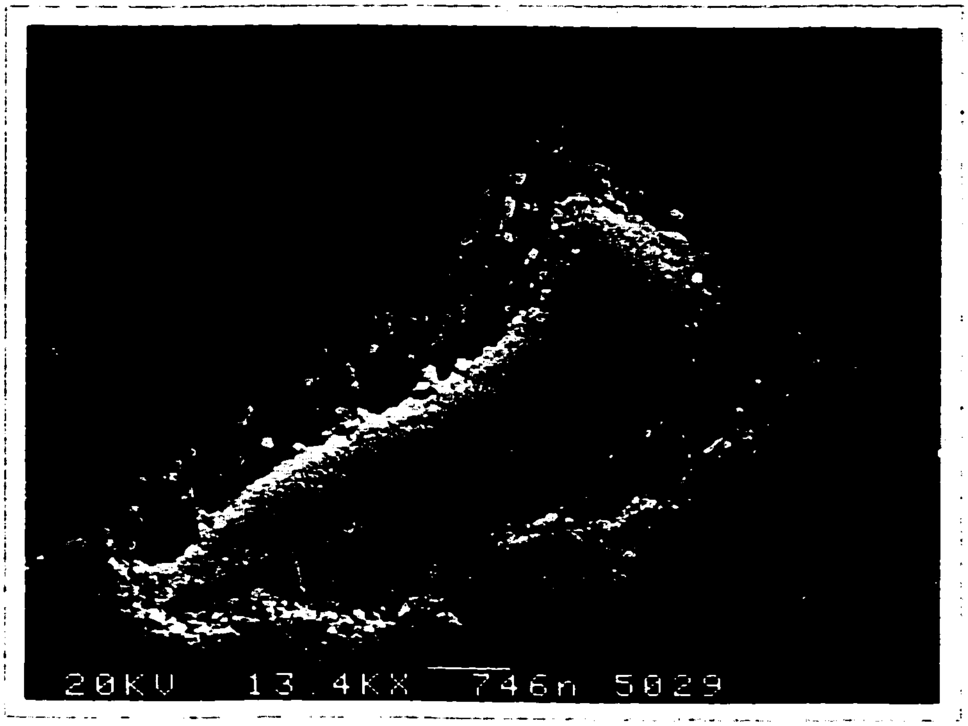

Figure 4.31: SEM Micrograph of Sample Held for 15 Seconds At 560°C (Heat Treatment (a)); Level Six of Figure 4.43.

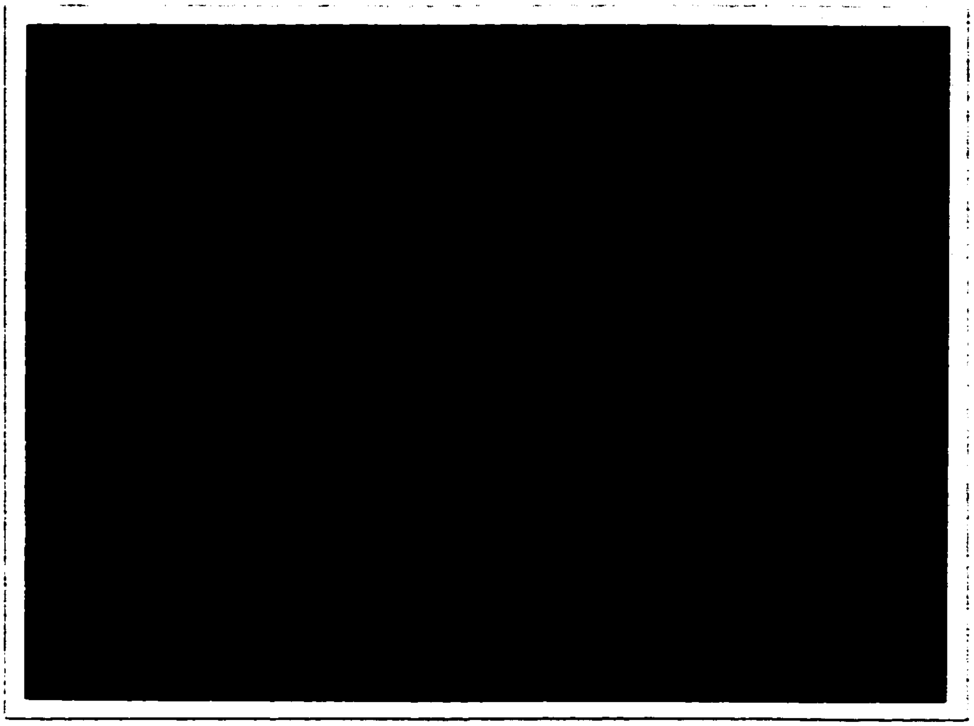

Figure 4.32: SEM Micrograph of Sample Held for 15 Seconds At 560°C (Heat Treatment (a)); Interesting Cross -Section.

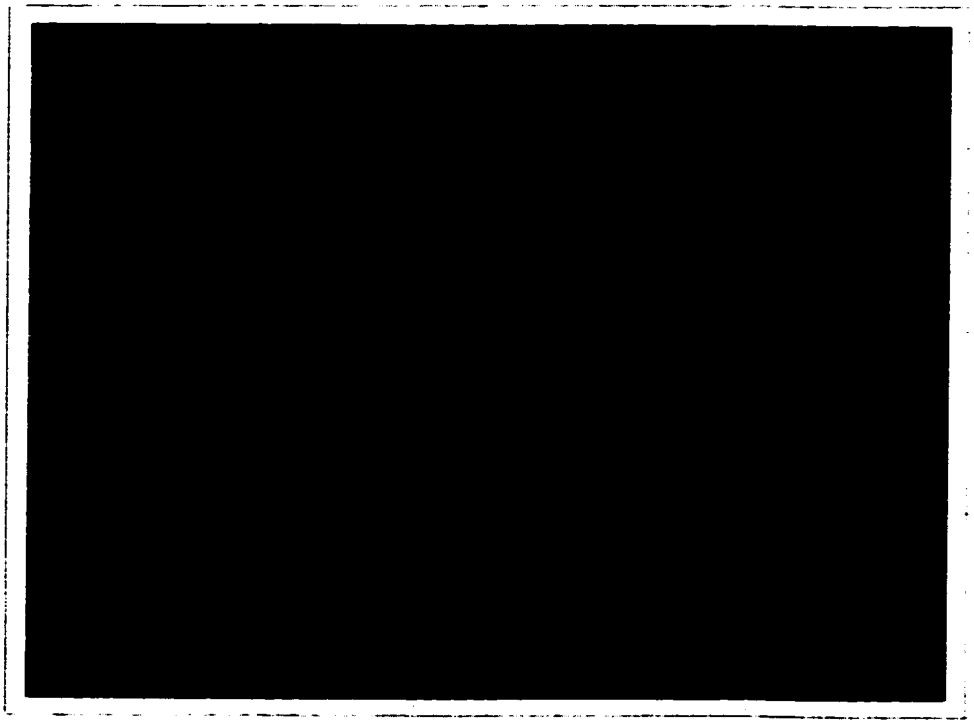

Figure 4.33: SEM Micrograph of Sample Held for 15 Seconds At 560°C (Heat Treatment (a)); Plan View Micrograph.

seconds at the experimental temperature (*i.e.*, the 'P400(a)/15s' sample). Most of the micrographs correspond to a particular level of the LFM events used to create the three-dimensional reconstructions, however Figure 4.32 shows a section of an LFM event in a plane approximately perpendicular to the overall migration direction. This event has a similar cross-section as the section made of the idealized LFM event in the Z = 1 plane as was introduced in Chapter Three (Figure 3.5(e)). Figure 4.33 is an example of the plan view micrographs referred to in Section 3.4.5, which are used to orient each level of an LFM event with the next. This figure shows the region surrounding the fifth layer of the LFM event shown in Figure 4.27; the LFM event, the freshly made micro-indent, and the micro-indent from the previous layer can be seen. The three-dimensional representation of this particular LFM event is shown in Figure 4.39. The polishing artifact described in Section 3.4.4, *i.e.*, the 'halo' that is observed in the matrix adjacent to the solid - liquid interface, is clearly shown in these micrographs.

Three-Dimensional Reconstructions

Three-dimensional composite images of suitable LFM events were created using a series of micrographs similar to those presented in the previous section, according to the method described in Section 3.4.5. The micrographs yielded the X-Y coordinates of each event on every level. The Z-coordinates associated with each level were obtained from measurements of the micro-indents before and after polishing; the average amount of material removed during each polishing stage and the associated Z-coordinates are presented in Table 4.3. The derived three-dimensional information for events is presented in Figures 4.34 to 4.43. It is clear that in most cases, the lenses have one radius of curvature considerably greater than the other (*i.e.*, $\rho_{TRAIL} > \rho_{LEAD}$), and the liquid lenses are more closely approximated by cylinders rather than spheres. In all cases however, the lenses are seen to bow against their curvature. Consider events such as those illustrated in Figures 4.34, 4.35, 4.38, and 4.41. It can be seen that on each level of the event (2-D slice), the events appear thicker than average. If any of these events were to be observed from an angle such that all levels were in line with each other, the projection of the event on a plane perpendicular to the line of sight will indicate the true thickness of the liquid film (as defined in Section 3.4.5).

Table 4.3: Material Removed During Polishing and the Associated Z-Coordinates.

Level	Average Material Removed (μm)	Standard Deviation (μm)	% Standard Deviation	Z-Coordinate (μm)
1	—	—	—	0.00
2	1.15	0.15	13	1.15
3	1.94	0.25	13	3.09
4	1.80	0.22	12	4.89
5	1.86	0.18	10	6.75
6	1.74	0.23	13	8.49
7	1.94	0.15	8	10.43
Average:	1.74	0.20	12	

This is a direct illustration of the sectioning problem described in Sections 3.4.5 and 3.4.6. Figures 4.36, 4.42, and 4.43 indicate that many of the liquid films that undergo LFM are connected with other liquid regions within the sample. For instance, Figure 4.43 indicates that although the liquid film has an almost perfect crescent shape indicative of LFM in the earlier levels, it can be seen that the final level may not even be recognized as an LFM event, and certainly would not be used to obtain measurements of LFM distances (according to the criteria described in Section 3.4.6).

Accuracy of Three-Dimensional Reconstructions

The information provided by the plots shown in Figures 4.34 to 4.43 are intended as a semi-quantitative illustration of the general morphology trends of migrating liquid films in a polycrystalline aluminum - copper alloy. The errors involved in obtaining these plots are

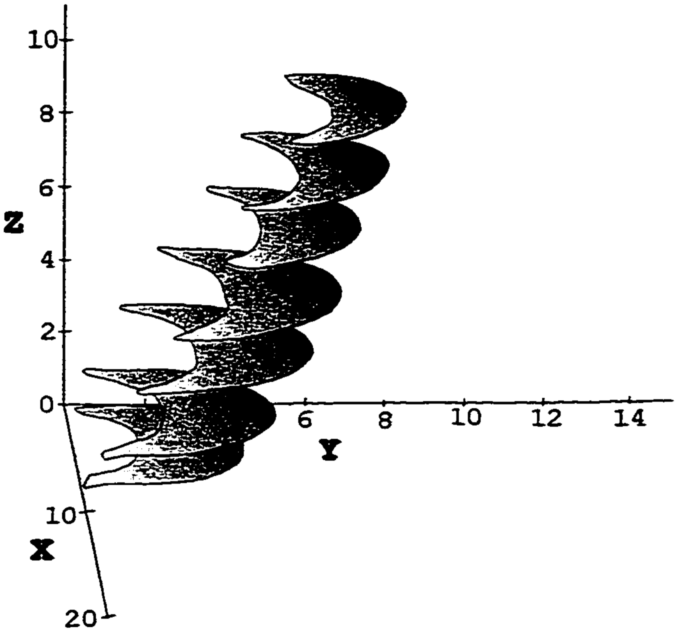

Figure 4.34: **Three-Dimensional Reconstruction of an LFM Event; Sample Held for 15 Seconds At 560°C (Heat Treatment (a)) (see Figure 4.22).**

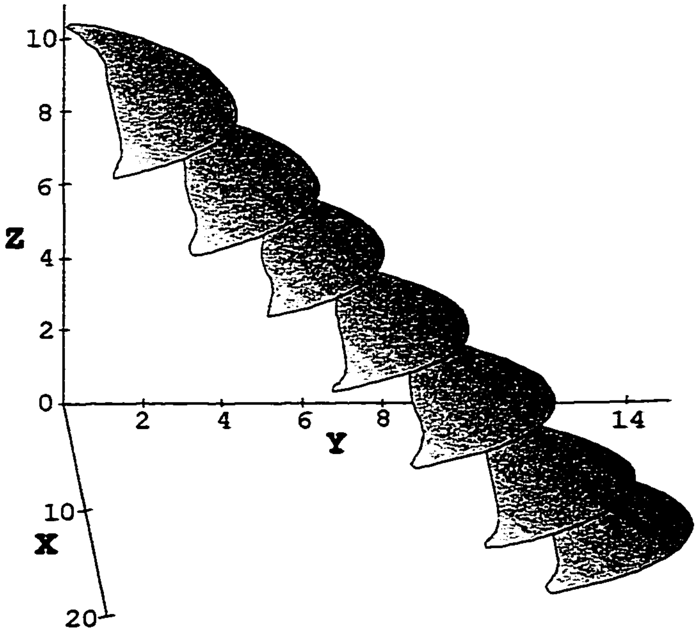

Figure 4.35: **Three-Dimensional Reconstruction of an LFM Event; Sample Held for 15 Seconds At 560°C (Heat Treatment (a)) (see Figure 4.23).**

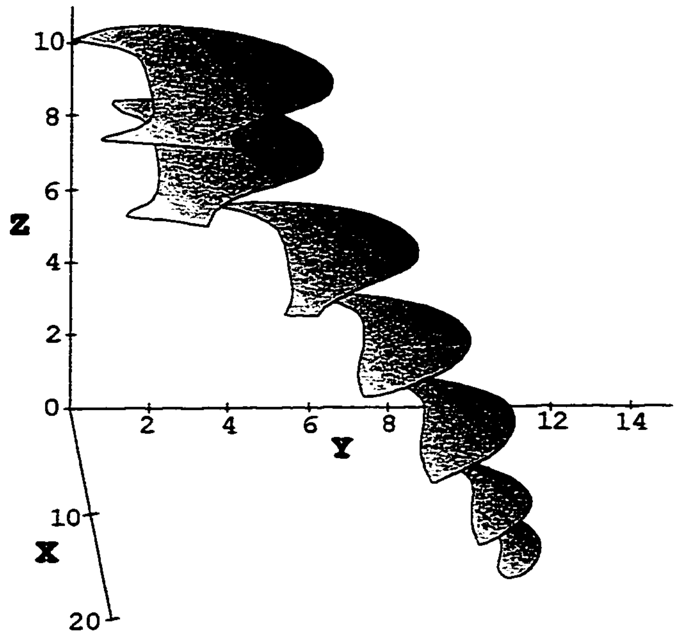

Figure 4.36: **Three-Dimensional Reconstruction of an LFM Event; Sample Held for 15 Seconds At 560°C (Heat Treatment (a)) (see Figure 4.24).**

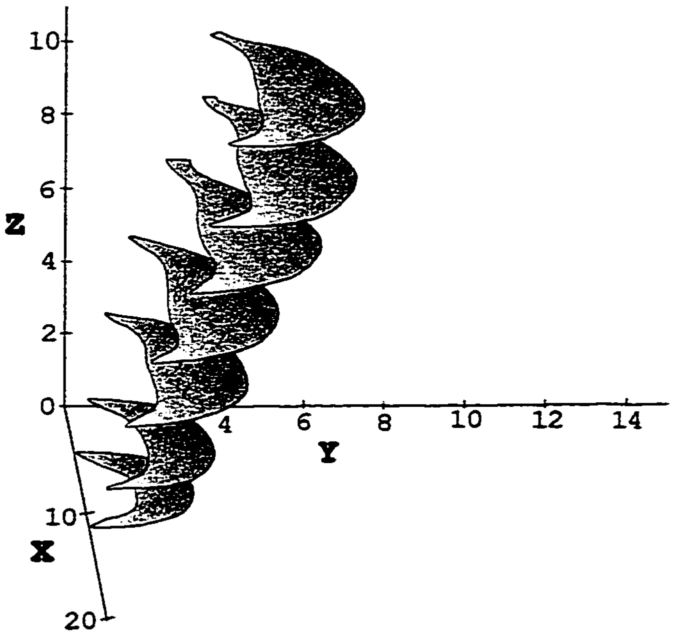

Figure 4.37: **Three-Dimensional Reconstruction of an LFM Event; Sample Held for 15 Seconds At 560°C (Heat Treatment (a)) (see Figure 4.25).**

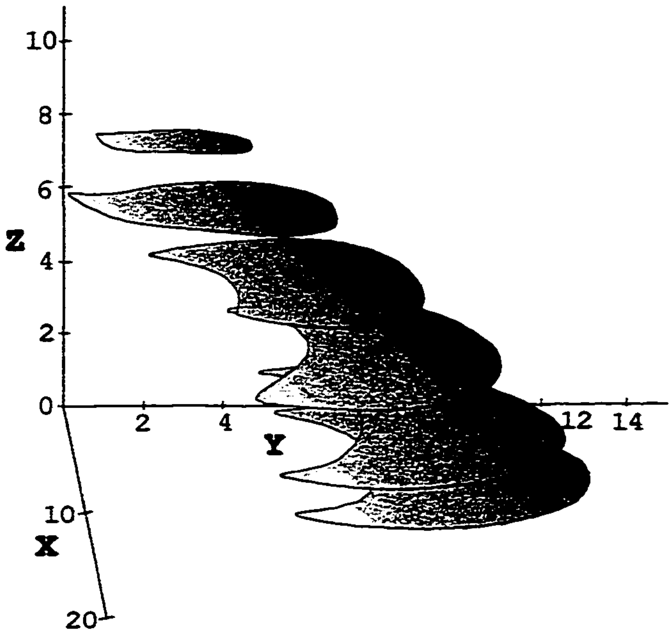

Figure 4.38: Three-Dimensional Reconstruction of an LFM Event; Sample Held for 15 Seconds At 560°C (Heat Treatment (a)) (see Figure 4.26).

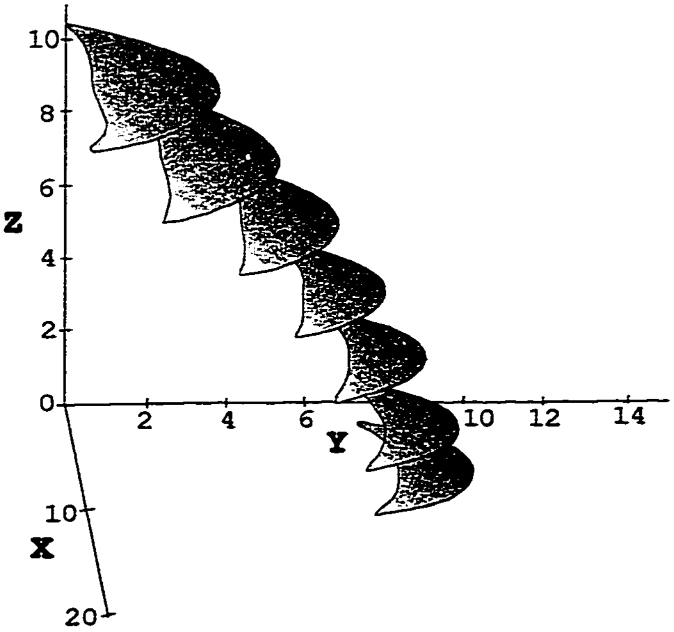

Figure 4.39: Three-Dimensional Reconstruction of an LFM Event; Sample Held for 15 Seconds At 560°C (Heat Treatment (a)) (see Figure 4.27).

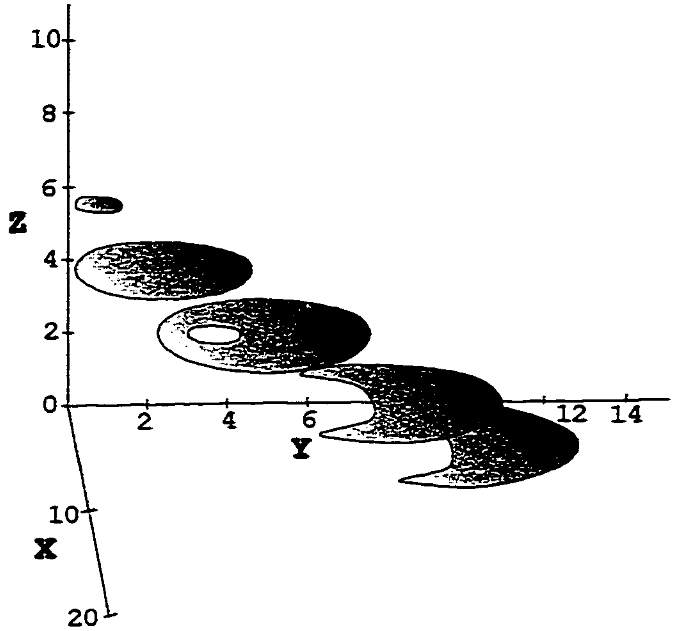

Figure 4.40: Three-Dimensional Reconstruction of an LFM Event; Sample Held for 15 Seconds At 560°C (Heat Treatment (a)) (see Figure 4.28).

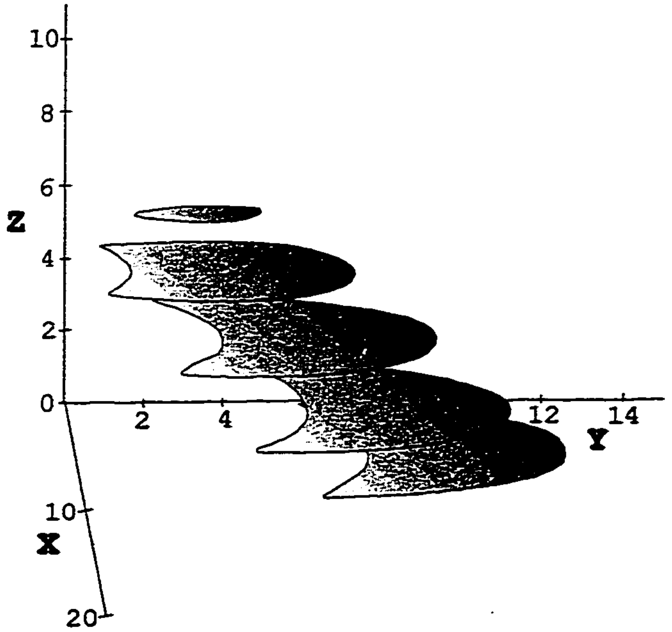

Figure 4.41: Three-Dimensional Reconstruction of an LFM Event; Sample Held for 15 Seconds At 560°C (Heat Treatment (a)) (see Figure 4.29).

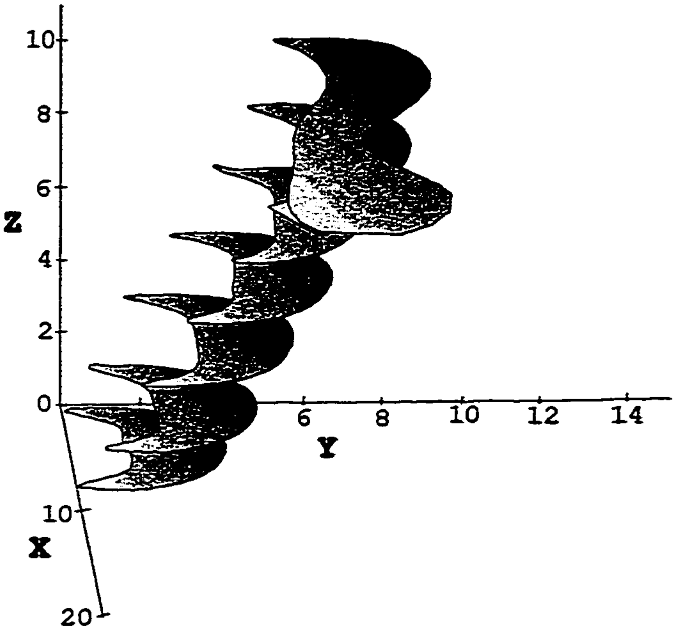

Figure 4.42: Three-Dimensional Reconstruction of an LFM Event; Sample Held for 15 Seconds At 560°C (Heat Treatment (a)) (see Figure 4.30).

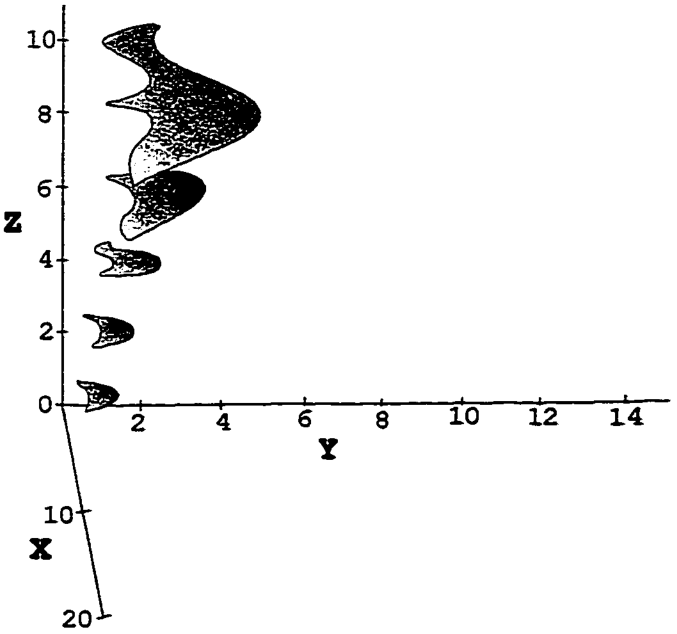

Figure 4.43: Three-Dimensional Reconstruction of an LFM Event; Sample Held for 15 Seconds At 560°C (Heat Treatment (a)) (see Figure 4.31).

discussed in this section. Each stage of the measurement process has an associated error. Consider the measurement of the Z-coordinate of the LFM events. The average amount of material removed during each polishing stage can be obtained using Equation (3.2); the error involved can be estimated from the scatter in the measurements obtained from each individual micro-indent (Equation (3.1)). As indicated in Table 4.1, an average standard deviation of 12% was obtained for the amount of material removed in all polishing stages. It can be seen that these errors will compound as more layers are added to the image; *i.e.*, the position (Z-coordinate) of the seventh layer cannot be determined to the same accuracy as for the first or second layers. However, the errors involved in obtaining the relative positions of any particular event on consecutive layers (X-Y coordinates) do not compound in this manner. Since the micro-indents do not move during polishing, the relative positions of each LFM event can be measured with respect to the centers of the micro-indents (see Chapter Three). The errors in the X-Y coordinates are due to measurement error, and will differ for each layer of each event depending on the scale of the micrographs used for measurement. These errors are negligible compared to the error in the Z-coordinate. The reconstructions nonetheless provide a reasonable three-dimensional illustration of the morphologies of several LFM events.

4.3.4 Migration Distances

Measurements of migration distances (for heat treatment (a)) were obtained from optical micrographs using the method described in Section 3.4.6. Acceptable measurements[***] for the positions of the leading and trailing interfaces (Z_{LEAD} and Z_{TRAIL}) were then averaged for each time value. The experimentally measured positions of Z_{LEAD} and Z_{TRAIL} are shown in Figure 4.44. It can be seen that after a period of rapid migration, the liquid films appear to reach a stable shape with $Z_{LEAD} \approx 3.3$ μm and $Z_{TRAIL} \approx 1.2$ μm. The average distance between pinning points (W) was calculated using all LFM events; a value of W = 6.9 ± 1.3

[***] Acceptable according to the criteria listed in Section 3.4.6.

(μm) was obtained.

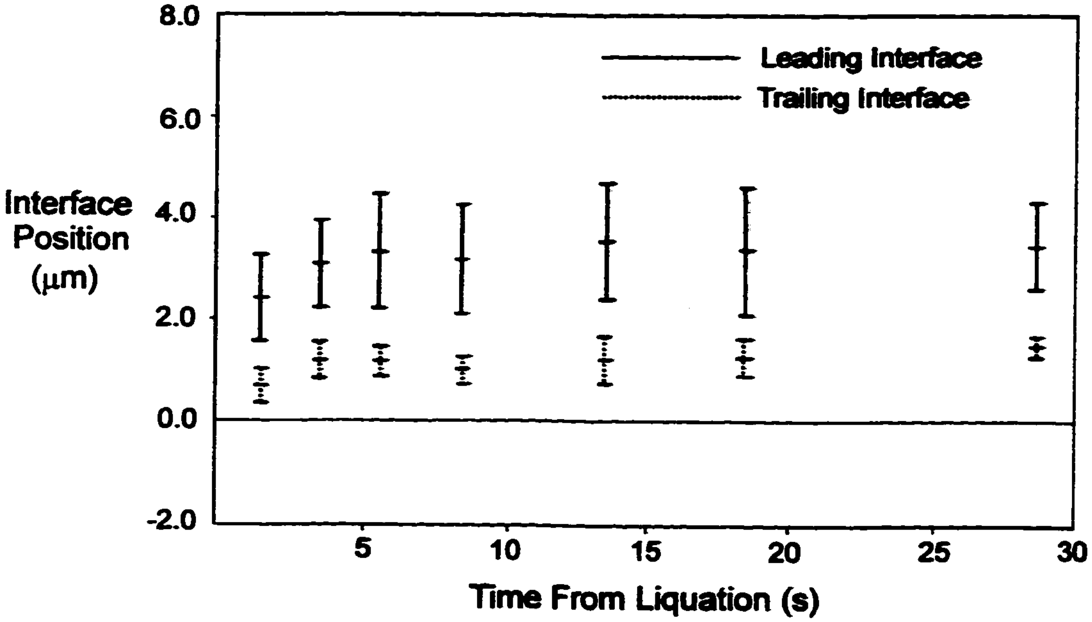

Figure 4.44: **Experimentally Measured Migration Distances (0 - 30 Seconds).**

CHAPTER FIVE

MODELLING OF LIQUID FILM MIGRATION

5.1 INTRODUCTION

In Chapter Two it was shown that the coherency strain energy caused by the diffusion of solute in advance of the leading solid - liquid interface is likely the driving force for Liquid Film Migration (LFM). That is to say that most of the experimental observations described in Chapter Two fit into the framework prescribed by the coherency strain hypothesis. The work of Yoon and others has been invaluable to the understanding of the phenomenon. However, much of the evidence presented is qualitative in nature, and attempts at quantifying the migration kinetics have had limited success. For example, consider the analysis of Yoon *et al.* [7] described in Section 2.4.1. The velocity expression that was developed (Equation (2.19)) assumed that there was an unlimited supply of solute to the growing phase. Since LFM is a mechanism of solidification, this assumption is likely to be invalid for most alloy systems as solute is used to form the growing equilibrium solid phase. It should be noted that Equation (2.19) was developed to describe LFM during the liquid phase sintering experiments performed by Yoon and co-workers, and is therefore essentially correct over the time frame of their experiments (*i.e.*, for a low solute distribution coefficient, *k*). Also, the equations developed for the concentration difference across the liquid film (ΔC) are in practice very difficult to apply to real systems. This is due to the fact that thermodynamic properties such as the activity coefficient of the solute in both liquid and solid phases must be estimated, experimentally determined, or assumed to follow simple thermodynamic laws such as Henry's law. In the aluminum - copper system, these assumptions (especially for the liquid phase) are severe over-simplifications.

As was mentioned in the preceding paragraph, the model for LFM developed by Yoon *et al.* [7] is difficult to apply to most alloy systems due to the large number of assumptions required in the calculation of ΔC. Also in the Yoon model, no account is made of the fact that in cases where there is limited amount of solute available to form the growing solid phase, the liquid film will shrink as it migrates, resulting in an acceleration of the liquid film. Current mathematical computer software packages, such as MAPLE or MATHEMATICA, make it possible to obtain ΔC without having to assume values for many thermodynamic properties of the system. Calculation of the concentration difference across the liquid film therefore involves the use of well developed expressions for the free energies of the liquid and solid phases, to which are added the energies of curvature and / or coherency strain as appropriate. As was discussed in Chapter Two, the work of Larché and Cahn [9] implied that the Gibbsian common tangent construction is valid for solid - liquid equilibria in cases where stressed and curved solids are in contact with the liquid phase, as well as for the well known case where planar, stress-free solids are in contact with the liquid phase. The analytical equivalent to the common tangent construction (see Section 5.3.2) is therefore used to solve for the solid and liquid compositions. In this manner, the concentration difference across the liquid film is constantly adjusted to reflect the changing conditions (*e.g.*, curvature). This is referred to as the direct common tangent method of calculating ΔC.

This chapter describes the development of a kinetic model for LFM, and is organized in the following manner. Section 5.2 outlines the development of an appropriate velocity expression for LFM. Since the velocity of the liquid film is determined by the rate at which solute is rejected from the growing solid phase (*i.e.*, trailing interface), any expression for the velocity of the liquid film must then account for this transfer of solute. Two methods were applied; the rate at which solute is rejected from the trailing solid - liquid interface is assumed to be a function of either:

1. The initial velocity of the trailing interface.
2. The instantaneous velocity of the trailing interface.

Both velocity expressions developed in Section 5.2 require the calculation of the concentration difference across the liquid film (ΔC). This is calculated using the direct common tangent approach as described in Section 5.3.

Details of the current modelling approach are outlined in Section 5.4. The calculation of energy due to curvature of the solid - liquid interfaces is outlined in Section 5.4.1. The assumptions made concerning the initial morphology of the liquid film, and the initial solute profile are discussed in Section 5.4.2. Free energy expressions for the solid and liquid phases at both solid - liquid interfaces (leading and trailing) during the various stages of migration are developed in Section 5.4.3. Section 5.4 concludes with a brief outline of the model algorithm as well as a description of how the process was modelled using MAPLE mathematical software. The kinetic model of Yoon *et al.* [7] (described in Chapter Two) is used for comparison with model predictions. This is described in Chapter Six.

5.2 DEVELOPMENT OF VELOCITY EXPRESSION

The following section describes the kinetics of LFM. Variable definitions and the coordinate system used are described in Section 5.2.1. A general velocity expression is then developed in Section 5.2.2, which is common to all modelling approaches. Specific velocity expressions are then developed for the case where the rate of solute transfer is determined by the initial velocity in Section 5.2.3, and for the case where solute transfer is determined by the instantaneous velocity in Section 5.2.4.

5.2.1 Definitions and Coordinate System

A section in the X-Z plane of an idealized event as introduced in Chapter Three is shown in Figure 5.1. The liquid film is assumed to be symmetrical about the Z-axis (*i.e.*, film has rotational symmetry in the X-Y plane), with the direction of migration being in the positive Z-direction. The predictions for the position of the leading (Z_{LEAD}) and trailing (Z_{TRAIL}) interfaces therefore apply along the Z-axis (*i.e.*, X=Y=0). The liquid film thickness δ(t) is defined below.

$$\delta(t) = Z_{LEAD}(t) - Z_{TRAIL}(t) \tag{5.1}$$

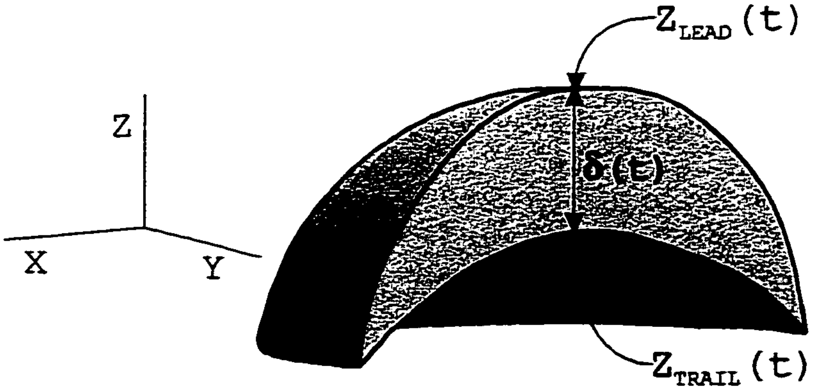

Figure 5.1 **One Half of An Idealized LFM Event. Both Z_{TRAIL}(t) and Z_{LEAD}(t) Are Measured From the Grain Boundary (Pinning Points, *i.e.*, Z = 0).**

5.2.2 General Velocity Expression

An expression for the velocity, *v*, of the liquid film in a direction parallel to the Z-axis is now developed based on that of Yoon *et al.* [7] (see also Equation (2.19)). Assuming that diffusion across the liquid film is conductive (*i.e.*, convection is negligible), the flux of solute across the liquid film can be adequately approximated by Fick's First Law, that is

$$J = -D_L(\nabla C) \qquad \textbf{(5.2)}$$

Where:

D_L	Diffusion coefficient for the solute in the liquid phase
∇C	Gradient in solute concentration across the liquid film. Note The direction of ∇C is parallel to the Z-axis.

Now, at the solidification front (trailing interface), the rate at which solute diffuses down the concentration gradient is equal to the rate at which solute is rejected from the solidifying liquid, that is

$$-D_L\left(\frac{\partial C}{\partial Z}\right) = v\ (C_{L,TRAIL} - C_{S,TRAIL}) \qquad \textbf{(5.3)}$$

Where:

$C_{L,TRAIL}$ and $C_{S,TRAIL}$	Concentrations of solute in the liquid and solid phases respectively in local equilibrium at the trailing (solidifying) interface.

Rearranging the above equation gives:

$$v = \frac{-D_L\left(\frac{\partial C}{\partial Z}\right)}{(C_{L,TRAIL} - C_{S,TRAIL})} \qquad \textbf{(5.4)}$$

If δ(t) is now defined as the liquid film thickness along the Z-axis of the liquid film as a function of time (t), then ∂C/∂Z can be approximated by ΔC(t)/δ(t), where ΔC(t) is the concentration difference across the liquid film after time t. The following equation is then obtained:

$$v(t) = \frac{D_L(\Delta C(t))}{(C_{L,TRAIL} - C_{S,TRAIL})\delta(t)} \tag{5.5}$$

It should be noted at this point that Equation (5.5) is valid for all following versions of the model. The differences between subsequent models is simply due to different ways to estimate δ(t) (based on the initial or instantaneous velocity), and ΔC(t) (Yoon *et al* [7] or through direct common tangent calculations). It should also be noted that $C_{L,TRAIL}$ and $C_{S,TRAIL}$ are assumed constant for the case where ΔC(t) is calculated using the analysis of Yoon *et al.* [7] (*e.g.*, assumed to be equal to the equilibrium solid and liquid compositions at the experimental temperature, obtained from the phase diagram), and are assumed to be functions of time for the case where ΔC(t) is obtained through direct common tangent calculations.

5.2.3 Velocity Expression Based Upon the Initial Velocity of the Liquid Film

Consider the migration of a segment of the liquid film in the positive Z-direction. If lateral solute transport is not allowed, that is to say that all solute transport within the liquid phase is from the trailing interface to the leading interface, in a direction parallel to the Z-axis, then since the process of LFM is also a mechanism of solidification there will only be limited solute available to form the equilibrium solid phase. According to the analysis of Brechet and Purdy [52], the liquid film will shrink as it migrates losing solute to the growing solid, and will eventually collapse to form a grain boundary after it has travelled a distance Z' given by:

$$Z' = \frac{\delta(0)}{k} \tag{5.6}$$

Where:

$\delta(0)$	Initial film thickness parallel to the Z-axis
k	Solute distribution coefficient (= $C_{S,TRAIL}/C_{L,TRAIL}$)

The velocity of the lens element at a position Z, is given by the following equation [52]:

$$v(Z) = \frac{v_0}{\left(1 - \frac{Z}{Z'}\right)} \tag{5.7}$$

Note, the v_0 parameter in this case is the initial velocity of the liquid film, given by:

$$v_0 = \frac{D_L\ (\Delta C)_0}{(C_{L,TRAIL} - C_{S,TRAIL})\delta(0)} \tag{5.8}$$

Equation (5.8) is also equivalent to the so-called "steady state velocity" expression of Yoon *et al.*[7] (see Section 2.4.1 - Equation (2.19)). Here $(\Delta C)_0$ is the concentration difference across the liquid film at the start of the migration process.

Noting that the velocity v is equal to the change in Z-coordinate with time (dZ/dt), Equation (5.7) can be rewritten:

$$\left(1 - \frac{Z}{Z'}\right) dZ = \left(v_0\right) dt \tag{5.9}$$

Integration of Equation (5.9) gives the time to collapse, t′:

$$t' = \frac{Z'}{2v_0} \tag{5.10}$$

Substitution of Equation (5.6) into Equation (5.10), gives the following equation:

$$t' = \frac{\delta(0)}{2\ k\ v_0} \tag{5.11}$$

It seems reasonable to write the following expression for the liquid film thickness as a function of time:

$$\delta(t) = \delta(0)\left(1 - \frac{t}{t'}\right) \tag{5.12}$$

Substitution of Equation (5.11) into Equation (5.12) and rearranging gives the following:

$$\delta(t) = \delta(0) - 2\ k\ v_0\ t \tag{5.13}$$

The velocity of the liquid film as a function of time as determined by the initial velocity is therefore obtained by substitution of Equation (5.13) into Equation (5.5) for the velocity v(t). This yields:

$$v(t) = \frac{D_L(\Delta C(t))}{(C_{L,TRAIL} - C_{S,TRAIL})\ (\delta(0) - 2\ k\ v_0\ t)} \tag{5.14}$$

Equation (5.14) is therefore the predicted velocity of the liquid film as a function of time. It can be seen that the velocity will not be constant and the liquid film will accelerate with time in contrast with the predictions of Yoon and his co-workers. The rate of acceleration of the liquid film will therefore depend on the initial velocity of the film (Equation (5.8)), and on the solute distribution coefficient, *k*. It should be noted that in many of the liquid-phase sintered specimens used by Yoon and co-workers, the systems have very low values for the solute distribution coefficient, *k* (*e.g.*, W-Ni, Mo-Ni), and the liquid films are attached to large reservoirs of liquid (and therefore solute) at the film ends. As a result, the liquid films do not shrink noticeably over the time frame of their experiments, leading to the false assumption that their experiments were occurring under "steady-state" conditions.

Since the velocity of the liquid film described by Equation (5.14) is determined by the initial velocity (v_0), it is possible to integrate Equation (5.14) to obtain a specific equation for the position of the trailing interface as a function of time. For a constant temperature T, we can define the following parameter:

$$A(t) = \frac{D_L(\Delta C(t))}{(C_{L,TRAIL} - C_{S,TRAIL})} \tag{5.15}$$

Equation (5.14) then becomes:

$$v(t) = \frac{dZ}{dt} = \frac{A(t)}{(\delta(0) - 2\,k\,v_0\,t)} \tag{5.16}$$

Rearranging Equation (5.16) yields:

$$\int_{t_0}^{t} dZ = A(t)\int_{t_0}^{t} \frac{dt}{(\delta(0) - 2\,k\,v_0\,t)} \tag{5.17}$$

It should be noted at this point that although the concentration difference across the liquid film changes with time (due to changing curvature), it is assumed that the interval between time t_0 and t is small enough that the curvature and thus the concentration difference across the liquid film is constant. Therefore the parameter A(t) can be assumed to be constant over the period of integration. Solving the integral (Equation (5.17)), the following result is obtained:

$$Z(t) - Z(t_0) = \frac{A(t)}{2\,k\,v_0} \ln\left|\frac{\delta(0) - 2\,k\,v_0\,t_0}{\delta(0) - 2\,k\,v_0\,t}\right| \tag{5.18}$$

Equation (5.18) therefore describes the change of position of the liquid film as a function of time. It can be seen that the equation lends itself to computer implementation, that is, the position at time t is equal to the position at time t_0 plus an amount determined by the physical parameters of the system under study (*e.g.*, ΔC, k, and $\delta(0)$). $Z(t)$ is essentially the position of the trailing interface after time t. Setting $Z(t) = Z_{TRAIL}(t)$, and $Z(t_0) = Z_{TRAIL}(t_0)$ in Equation (5.18) gives the following equation:

$$Z_{TRAIL}(t) = Z_{TRAIL}(t_0) + \frac{A(t)}{2\,k\,v_0} \ln\left|\frac{\delta(0) - 2\,k\,v_0\,t_0}{\delta(0) - 2\,k\,v_0\,t}\right| \tag{5.19}$$

and the position of the leading interface is given by:

$$Z_{LEAD}(t) = Z_{TRAIL}(t) + \delta(t) \tag{5.20}$$

Where $Z_{TRAIL}(t)$ is obtained from Equation (5.19), and $\delta(t)$ is obtained from Equation (5.13). Model results obtained in this case show good predictions for one interface only. This is due to the fact that the predicted liquid film thickness decreases too rapidly over time, as a result of using the initial velocity (v_0) in determining the rate at which solute is rejected from the growing solid. The initial velocity described by Equation (5.8) is always larger than the average velocity of the liquid film. As a result the predicted loss of solute to the growing phase from the liquid occurs at a rate too high to fit the experimental data, and the liquid film thickness defined by Equation (5.13) is always under-predicted.

5.2.4 Velocity Expression Based Upon the Instantaneous Velocity of the Liquid Film

Results of model predictions using Equations (5.19) and (5.20) indicate the need for constant parameter adjustment. That is to say that the values of parameters such as the 'initial' film thickness ($\delta(0)$), and the velocity parameter (v_0) require constant readjustment in each iteration of the algorithm to predict the liquid film morphology of an ideal LFM event as a function of time (see Sections 5.2.1 and 5.4). The equations developed in the previous section are still valid, and it is only necessary to re-write Equations (5.13) and (5.14) in order to facilitate programming. Consider the i'th iteration of the algorithm, the initial film thickness ($\delta(0)$) corresponds to the film thickness from the previous iteration, δ^{i-1}, and similarly, the velocity parameter (v_0) is written as v^{i-1}. Equation (5.13) therefore becomes:

$$\delta^i = \delta^{i-1} - 2\,k\,v^{i-1}\,(t^i - t^{i-1}) \tag{5.21}$$

and Equation (5.14) for the velocity can be re-written as follows:

$$v^i = \frac{D_L\,(\Delta C^i)}{(C^i_{L,TRAIL} - C^i_{S,TRAIL})\,\delta^i} \tag{5.22}$$

The positions of the leading and trailing interfaces are therefore determined by first calculating the instantaneous velocity using Equation (5.22), with Equation (5.21) for the film thickness. The position of the trailing interface for the i'th iteration is then obtained using the following equation:

$$Z^i_{TRAIL} = Z^{i-1}_{TRAIL} + v^{i-1}(t^i - t^{i-1}) \tag{5.23}$$

The position of the leading interface is therefore:

$$Z^i_{LEAD} = Z^i_{TRAIL} + \delta^i \tag{5.24}$$

Where, $Z_{TRAIL}{}^{i}$ is calculated using Equation (5.23) and δ^{i} is calculated using Equation (5.21).

In order to apply the model it is necessary to calculate the concentration difference across the liquid film (ΔC). This is accomplished using the free energy expressions of all phases involved and solving for the compositions at the leading and trailing interfaces using the analytical equivalent of the common tangent construction. ΔC is then calculated directly at each time increment. This method for the calculation of ΔC and the calculation of liquid film morphology as a function of time are described further in the following sections.

5.3 CALCULATION OF ΔC

This section describes the method used to calculate the concentration difference across the liquid film (ΔC). Assuming that local equilibrium exists at the leading and trailing solid - liquid interfaces, estimation of ΔC involves the use of well developed free energy expressions for the liquid and solid phases along with the analytical equivalent to the common tangent construction. The concentrations of solute in the solid and liquid phases can therefore be calculated directly. It should be noted that the energies per mole due to coherency and curvature can be added directly to the molar free energies of the solid and / or liquid phases as appropriate. Differences in stress states between the two solids, and / or differences in curvature between the two interfaces will result in different local equilibria at the leading and trailing interfaces. The concentration difference across the liquid film (ΔC) is then obtained by difference.

Common Tangent Construction

In this section, the differential equation used to calculate the solid and liquid compositions in local equilibrium at a solid - liquid interface will be developed. This is done graphically by use of the common tangent construction, and is described below (after Hillert [55]).

It is possible to represent extensive thermodynamic properties of alloys such as molar volume and molar Gibbs free energy graphically as functions of composition (*i.e.*, mole fraction X_B, where B is the solute species in a binary alloy). The molar diagram defined in this manner has a simple but important property, which is illustrated with reference to Figure 5.2. If points α and β represent the free energies of the α and β phases respectively (*i.e.*, points (X_B^α, F^α), and (X_B^β, F^β)), it can be shown [55], that any point representing a two-phase alloy (α +β) lies on the straight line drawn between the two points (*i.e.*, for mole fraction X_B^{ALLOY}, the free energy per mole is F^{ALLOY}).

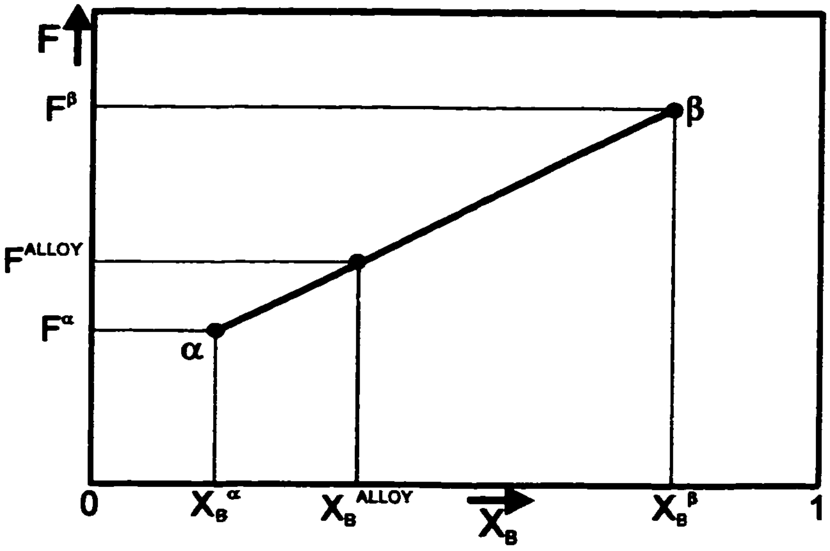

Figure 5.2: **Molar Free Energy Diagram Where Points α and β Represent the Free Energies of Hypothetical α and β Phases. The Free Energy of A Two Phase Alloy (F^{ALLOY}) is Shown for the Composition X_B^{ALLOY}.**

The chemical potential (μ) is now defined with reference to Figure 5.3. Figure 5.3 shows the molar free energy of a hypothetical α-phase as a function of composition. If a tangent is drawn to the curve at some composition X_B, the intercept the tangent makes at $X_B = 0$ (*i.e.*, pure A), defines the chemical potential of A atoms in the α-phase at X_B (*i.e.*, μ_A^α), and the intercept at $X_B = 1$ (*i.e.*, pure B), defines the chemical potential of B atoms in the α-phase at X_B (*i.e.*, μ_B^α).

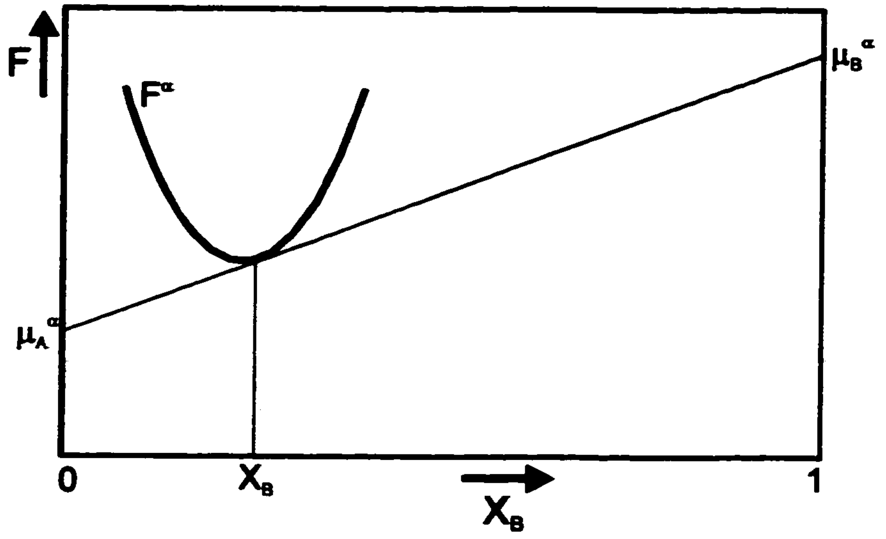

Figure 5.3: **Schematic Molar Free Energy Curve of A Hypothetical α-Phase As A Function of Composition. The Tangent Drawn At Composition X_B Defines the Chemical Potentials of Species A and B in the α-Phase (μ_A^α and μ_B^α).**

Consider now two phases (α and β) whose molar free energies vary with composition as shown in Figure 5.4. Assume α_1 and β_1 to be the initial state of the alloy. The tangent drawn to the F^α curve at composition $X_B^{\alpha 1}$ yields chemical potentials $\mu_A^{\alpha 1}$ and $\mu_B^{\alpha 1}$, while the tangent drawn to the F^β curve at composition $X_B^{\beta 1}$ yields chemical potentials $\mu_A^{\beta 1}$ and $\mu_B^{\beta 1}$. Consider the chemical potentials of B atoms in the two phases. The potential of B atoms in the α-phase ($\mu_B^{\alpha 1}$), is lower than that of the β-phase ($\mu_B^{\beta 1}$), meaning that there exists a driving force ($\Delta\mu_B^1 = \mu_B^{\beta 1} - \mu_B^{\alpha 1}$) for the transfer of B-atoms from β_1 to α_1. Similarly, there exists a driving force ($\Delta\mu_A^1 = \mu_A^{\alpha 1} - \mu_A^{\beta 1}$) for the transfer of A-atoms from α_1 to β_1. It is therefore energetically favourable for the compositions of the α and β phases to approach each other, and the driving force gradually decreases (*i.e.*, $\Delta\mu_B^1 > \Delta\mu_B^2$, where $\Delta\mu_B^2$ is the driving force for the transfer of B-atoms from β_2 to α_2). It is important to note, that both driving forces vanish when the two tangents coincide (*i.e.*, the common tangent), and the system is therefore in equilibrium. The graphical approach described above therefore yields the well

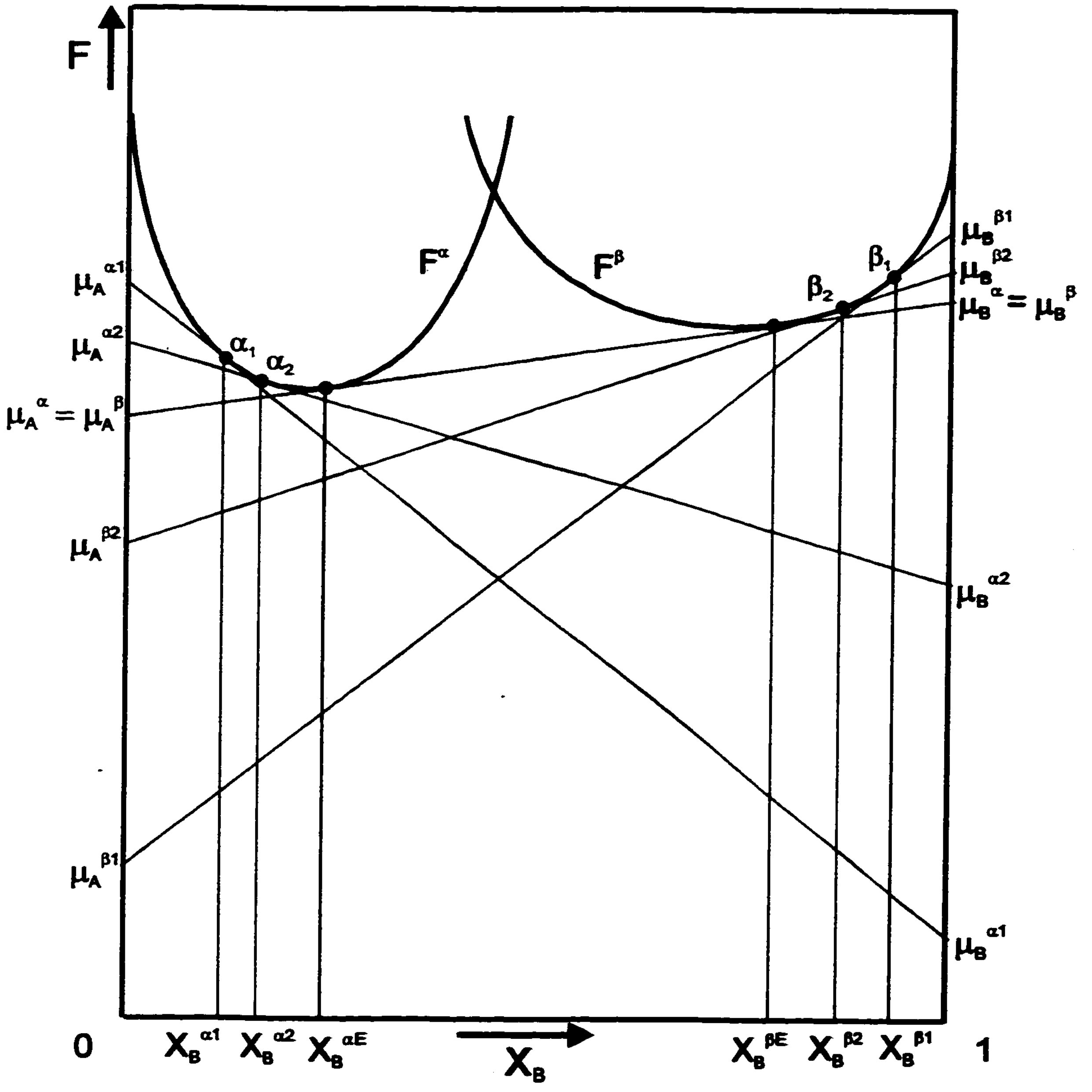

Figure 5.4: **Schematic Molar Free Energy Diagram of Hypothetical Phases (α and β) As Functions of Composition Illustrating the Origin of the Driving Force for Equilibration.**

known criteria for equilibrium that the chemical potentials of each species are equal in all phases. For a binary system:

$$\begin{aligned} \mu_A^{\alpha} &= \mu_A^{\beta} \\ \mu_B^{\alpha} &= \mu_B^{\beta} \end{aligned} \qquad (5.25)$$

Figure 5.5 shows the molar Gibbs free energy of a hypothetical solid phase (S) and a hypothetical liquid phase (L) as functions of composition.

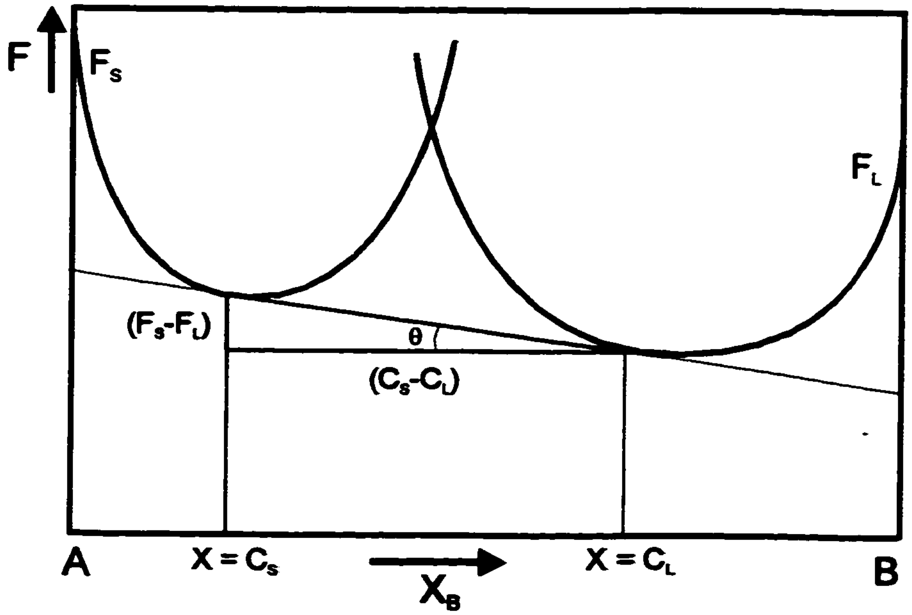

Figure 5.5: **Schematic Molar Free Energy Diagram of Hypothetical Solid and Liquid Phases As A Function of Composition Demonstrating the Common Tangent Construction.**

The common tangent is shown in Figure 5.5 along with the equilibrium compositions of both solid and liquid phases. Simple geometry is then used to obtain the following equation:

$$F_S - F_L = \left(C_S - C_L\right) \tan\theta \qquad (5.26)$$

Noting that:

$$\tan\theta = \frac{dF_S}{dC_S} = \frac{dF_L}{dC_L} \quad (5.27)$$

Gives the following:

$$F_S - F_L = \frac{dF_S}{dC_S}(C_S - C_L) \quad (5.28)$$

Subject to the condition of equal slopes:

$$\frac{dF_S}{dC_S} = \frac{dF_L}{dC_L} \quad (5.29)$$

The composition of the solid and liquid phases in local equilibrium are therefore calculated by solving the differential Equation (5.28) subject to the condition of equal slopes (5.29).

In order to apply the concepts discussed above to the calculation of the equilibrium compositions at the leading and trailing interfaces, expressions for the full optimized free energies of the liquid and solid phases are required, to which are added the energies due to curvature and coherency strain as appropriate. The free energy expressions used for the aluminum - copper system are described in Chapter Six.

5.4 Model Development

In this section, specific considerations required during the modelling of LFM are outlined. In particular, the conversion of the appropriate velocity expression into a working computer model to predict the liquid film morphology as a function of time is described. Section 5.4.1 outlines the calculation of the radius of curvature and the subsequent energy due to curvature through application of the Gibbs - Thomson effect. Section 5.4.2 describes the assumptions made about the initial conditions of the liquid lens (morphology and solute profile). A detailed account of the considerations required during modelling of the various stages of migration for the current model (*i.e.*, direct calculation of ΔC using the common tangent approach along with the velocity expression based upon the instantaneous velocity) is given in Section 5.4.3. A brief outline of the MAPLE algorithm is described in the final section.

5.4.1 Calculation of Energy Due to Curvature

In this section, the method used to calculate the energy due to curvature is outlined. The Gibbs-Thomson effect is described and its application to LFM discussed. This is followed by a description of the mathematical approach used to calculate the radii of curvature of the leading and trailing interfaces.

Gibbs-Thomson Effect

Consider a sphere of liquid of radius ρ embedded in a solid matrix. Assume that the pressure in the matrix is P_0, and the pressure in the liquid is P_l. If the solid - liquid interfacial energy is σ, then the Gibbs-Thomson effect indicates that:

$$P_l = P_0 + \frac{2\sigma}{\rho} \tag{5.30}$$

When extending this argument to LFM it was assumed that the leading and trailing interfaces were sections of spheres as described in Chapter Three. The Gibbs-Thomson effect indicates that the energies due to curvature for the leading and trailing interfaces can be obtained as follows:

$$F_{CURV,LEAD} = 2\ \sigma\ V_m \left(\frac{1}{\rho_{LEAD}} \right) \tag{5.31}$$

$$F_{CURV,TRAIL} = 2\ \sigma\ V_m \left(\frac{1}{\rho_{TRAIL}} \right) \tag{5.32}$$

Where:

σ	Specific solid - liquid interfacial energy (J m^{-2})
V_m	Molar volume (m^3 mol^{-1})
ρ_{LEAD}	Radius of curvature of the leading solid - liquid interface (m)
ρ_{TRAIL}	Radius of curvature of the trailing solid - liquid interface (m)

The energy calculated using Equations (5.31) and (5.32) assumes positive curvature. This energy was therefore added to the phase that possessed positive curvature at that instant in time. It can be seen that in order to calculate the energy due to curvature (Equations (5.31) and (5.32)), the radii of curvature must be estimated for both the leading and trailing interfaces. This is done in the following section.

Calculation of the Radius of Curvature

In the previous section, equations were developed for the molar free energy due to curvature for the leading and trailing interfaces. It was assumed that the solid - liquid interfaces possessed spherical curvature, and as a result it is necessary to calculate the radii of curvature of both leading and trailing interfaces. In order to calculate the radius of curvature of the liquid lens, three points on the circumference of the sphere must be known, and these three points can then be used to calculate the centre of the sphere. From this, the radius of curvature can be obtained; that is to say that the radius is equal to the distance between the central point and one of the points on the circumference of the sphere. Equations for the magnitude of the radius of curvature were obtained in the following manner. Figure 5.6 shows a two-dimensional representation of a sphere in the (X,Z) plane.

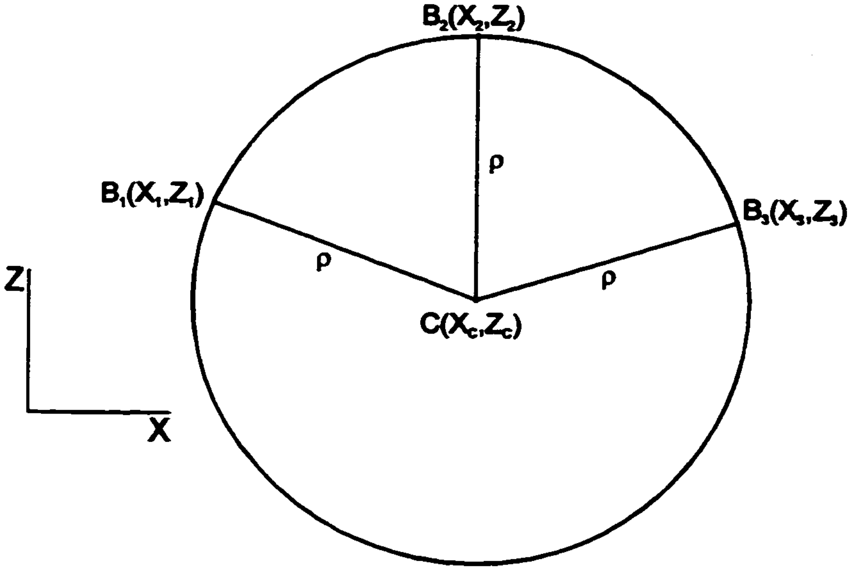

Figure 5.6 **Two-Dimensional Representation of A Sphere in the (X,Z) Plane Used in the Calculation of the Radius of Curvature.**

The three points on the circumference of the sphere were designated $B_1(X_1,Z_1)$, $B_2(X_2,Z_2)$, and $B_3(X_3,Z_3)$, and the centre of the sphere was designated $C(X_C,Z_C)$. The radius of curvature is then equal to the distance between points B_1 and C, between B_2 and C, as well as between B_3 and C. The well known distance formula was then used to obtain two equations in the two variables X_C and Z_C. Algebraic manipulation leads to the following equations for X_C and Z_C.

$$X_C = \frac{\left(M_1 - \frac{L_1}{L_2} M_2\right)}{\left(K_1 - \frac{L_1}{L_2} K_2\right)} \tag{5.33}$$

And:

$$Z_C = \frac{\left(M_1 - \frac{K_1}{K_2} M_2\right)}{\left(L_1 - \frac{K_1}{K_2} L_2\right)} \tag{5.34}$$

Where:

$$\begin{aligned} K_1 &= X_2 - X_1 \\ K_2 &= X_3 - X_1 \\ L_1 &= Z_2 - Z_1 \\ L_2 &= Z_3 - Z_1 \\ M_1 &= \frac{1}{2}\left((X_2^2 - X_1^2) + (Z_2^2 - Z_1^2)\right) \\ M_2 &= \frac{1}{2}\left((X_3^2 - X_1^2) + (Z_3^2 - Z_1^2)\right) \end{aligned} \tag{5.35}$$

The radius of curvature (ρ) was then obtained by calculating the distance between point C(X_C,Z_C) calculated using Equations (5.33) to (5.35), and any of the three points on the circumference of the sphere. For B_1 this gives:

$$\rho = \sqrt{(X_C - X_1)^2 + (Z_C - Z_1)^2} \tag{5.36}$$

For the case of a model LFM event (see Sections 3.4.5 and 5.2.1), some simplifications can be made. For instance, since the LFM event was defined to be symmetrical about the Z-axis, the central point (Z_{LEAD} or Z_{TRAIL}) has an X-value equal to zero (*i.e.*, $X_2 = 0$). This also implies that the X-coordinate of the center of curvature will also be equal to zero (*i.e.*, $X_C = 0$). The end points of the liquid film were also assumed to be pinned at $Z = 0$, which gives $Z_1 = 0$, and $Z_3 = 0$. With these simplifications, Equations (5.33) and (5.34) become:

$$X_C = 0 \tag{5.37}$$

and

$$Z_C = \frac{M_1}{L_1} = \frac{\left(Z_{LEAD}^2 - X_1^2\right)}{2Z_{LEAD}} \tag{5.38}$$

The calculated values for X_C and Z_C (Equations (5.37) and (5.38)) were then substituted into Equation (5.36) to obtain the radius of curvature of the leading interface. The radius of curvature of the trailing interface was also calculated in a similar manner using Equations (5.37) and (5.38), replacing Z_{LEAD} with Z_{TRAIL}. The radius of curvature of the trailing interface was then calculated using Equation (5.36).

5.4.2 Initial Conditions For Modelling

For application of any kinetic model, the starting conditions for the process must be explicitly defined. For the case of modelling LFM, this includes assumptions made concerning the initial geometry of the liquid film, the initial solute distribution, and the direction in which the migration process is initiated. This is described in detail as follows.

Consider a well equilibrated two-phase alloy, in which the precipitated second phase is primarily distributed along the grain boundaries of the sample. The matrix composition is defined to be C_0. If the sample is rapidly heated to a temperature slightly above the minimum liquid forming temperature, it can be assumed that the precipitates will dissolve forming thin regions of liquid which separate two favourably oriented grains of the parent material (composition (C_0)). In the following discussion, it is assumed that at the beginning of modelling, all precipitates have dissolved forming regions of liquid. The liquid pool geometry at the start of the migration process is described as follows.

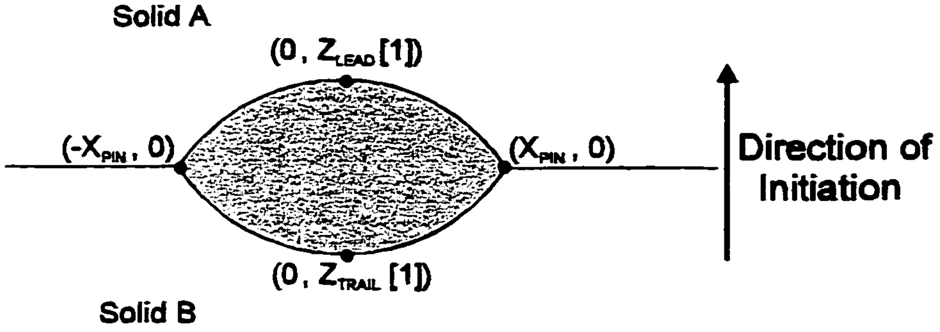

Figure 5.7: **Assumed Geometry of the Liquid Film At the Start of the Migration Process.**

With reference to Figure 5.7, the assumptions about the initial geometry of the liquid film can be listed as follows:

- The two solid - liquid interfaces were assumed to possess spherical curvature.
- It was assumed that at as a starting point for modelling and subsequent calibration, the two grains separated by the thin liquid film are aligned such that the orientation dependent elastic modulus (Y(**n**)) has a maximum value in one of the grains (defined to be grain A), and a minimum value in the other grain (defined to be grain B). As will be discussed in detail in Chapter Six, grains with a <111> type surface normal possess the maximum value of Y(**n**), while grains with a <100> type surface normal possess the minimum value for aluminum rich aluminum - copper alloys.

- It was assumed that the liquid film is geometrically symmetrical about the Z=0 plane, and pinned at points $(-X_{PIN}, 0)$ and $(X_{PIN}, 0)$.

With the initial geometry of the liquid film defined as described above, it is now necessary to describe other assumptions that were made in order to model the initiation stage of the migration process (at time, t = 0):

- It was assumed that all precipitates had dissolved; those along the grain boundaries forming thin regions of liquid, and those within the grain interiors forming approximately spherical regions of liquid.
- It was assumed that the liquid film had not yet migrated, but a limited degree of solute diffusion had occurred, such that fully coherent regions exist in the solid at both interfaces. The coherency strain energy for each region is calculated by application of Equation (2.1) multiplied by the molar volume of the solid phase (*i.e.*, $w_{EL}*V_m$)
- It was assumed that migration initiates into the grain with the higher free energy. This will be in the direction of grain A assuming that the liquid film is symmetrical in all respects as described previously, except for the different moduli of the two grains.

5.4.3 Current Model For LFM

This section describes the approach taken in the development of a model for LFM. In particular, emphasis is placed upon the assumptions made during each stage of modelling. The overall modelling approach is outlined with reference to Figure 5.8, where each stage of migration is described in terms of the local equilibria that exist at both leading and trailing interfaces. Modelling of LFM was split into three main regimes: (a) initial stages of migration (initiation), (b) early stages of migration, where coherency has been lost in one of the grains, but the trailing solid still possesses negative curvature (*i.e.*, for $Z_{TRAIL} < 0$), and (c) final stages

(a) Initial Stages:

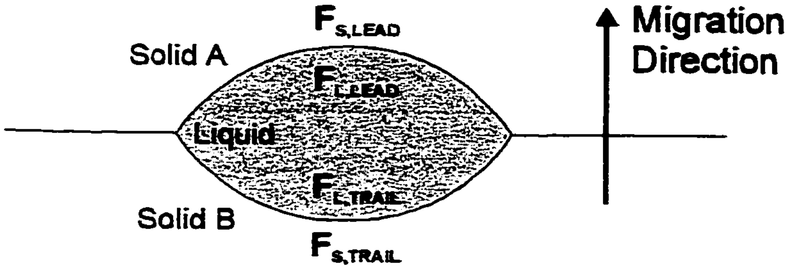

$$F_{S,LEAD} = F_S + F_{COH,\,LEAD}$$
$$F_{L,LEAD} = F_L + F_{CURV,\,LEAD}$$
$$F_{L,TRAIL} = F_L + F_{CURV,\,TRAIL}$$
$$F_{S,TRAIL} = F_S + F_{COH,\,TRAIL}$$

(b) Early Stages:

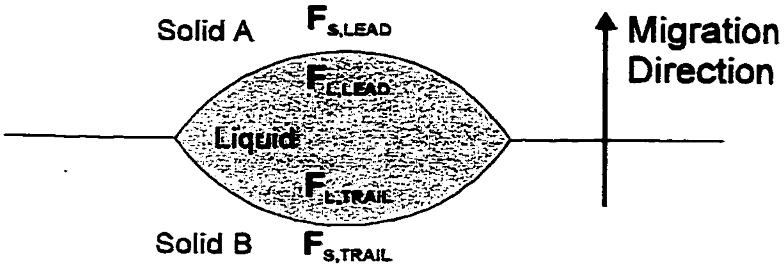

$$F_{S,LEAD} = F_S + F_{COH,\,LEAD}$$
$$F_{L,LEAD} = F_L + F_{CURV,\,LEAD}$$
$$F_{L,TRAIL} = F_L + F_{CURV,\,TRAIL}$$
$$F_{S,TRAIL} = F_S$$

(c) Later Stages:

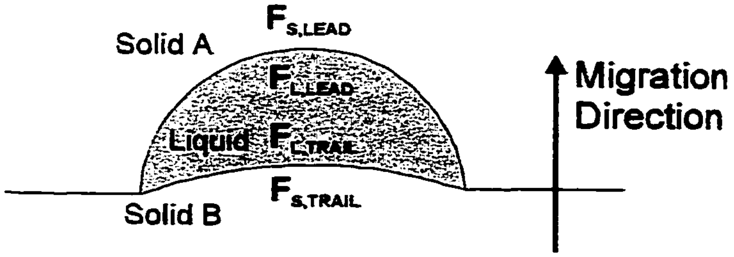

$$F_{S,LEAD} = F_S + F_{COH,\,LEAD}$$
$$F_{L,LEAD} = F_L + F_{CURV,\,LEAD}$$
$$F_{L,TRAIL} = F_L$$
$$F_{S,TRAIL} = F_S + F_{CURV,\,TRAIL}$$

Figure 5.8: Modelling Approach Used for the Migration of Liquid Lenses.

of migration, where the trailing solid now possesses positive curvature (*i.e.*, for $Z_{TRAIL} > 0$). These stages are discussed further below.

Initiation Stage of LFM

Using the initial liquid film conditions outlined in Section 5.4.1, it is now possible to describe the initiation stage of LFM in some detail. That is to say that it is now possible to write expressions for the free energies of all phases involved, from which the concentration difference across the liquid film (ΔC) can be obtained. At the very start of migration (Figure 5.8(a)) it was assumed that fully coherent regions exist in the solid at both interfaces. It was also assumed that the liquid lens is symmetrical in all respects, except that solid A and solid B are oriented such that different atomic planes lie parallel to the liquid lens. The elastic moduli ($Y(\mathbf{n})$) will therefore differ for the two solids (*i.e.*, $Y_A \neq Y_B$). The appropriate coherency strain energy was then added to the free energy of the solid phases. Migration was assumed to initiate into the grain with the larger modulus, which was defined to be grain A. The respective energies due to curvature (see Section 5.4.1) were added to the free energies of the leading and trailing liquids in this case. The resulting free energy expressions for the leading and trailing solid and liquid phases for this stage of migration are therefore:

$$\begin{aligned} F_{S,\,LEAD} &= F_S + V_m Y(\mathbf{n}_A)\eta^2(C_S - C_0)^2 \\ F_{L,\,LEAD} &= F_L + V_m \sigma K_{LEAD} \\ F_{L,\,TRAIL} &= F_L + V_m \sigma K_{TRAIL} \\ F_{S,\,TRAIL} &= F_S + V_m Y(\mathbf{n}_B)\eta^2(C_S - C_0)^2 \end{aligned} \qquad (5.39)$$

Where:

$F_{S,LEAD}$	Calculated free energy of the leading solid phase (J mol^{-1})
$F_{L,LEAD}$	Calculated free energy of the leading liquid phase (J mol^{-1})
$F_{S,TRAIL}$	Calculated free energy of the trailing solid phase (J mol^{-1})
$F_{L,TRAIL}$	Calculated free energy of the trailing liquid phase (J mol^{-1})

F_S	Free energy of the bulk solid phase (J mol^{-1})
F_L	Free energy of the bulk liquid phase (J mol^{-1})
V_m	Molar volume (m^3 mol^{-1})
Y(**n**)	Orientation-dependent biaxial elastic modulus, where **n** is the grain normal. A and B refer to the solid grains separated by the liquid film (J m^{-3})
η	Solute misfit parameter
C_S	Equilibrium solute concentration in the solid phase
C_0	Solute concentration in the parent solid phase
σ	Specific solid - liquid interfacial energy (J m^{-2})
K_{LEAD}	Curvature of the leading solid - liquid interface (m^{-1}) ($=2/\rho_{LEAD}$)
K_{TRAIL}	Curvature of the trailing solid - liquid interface (m^{-1}) ($=2/\rho_{TRAIL}$)
ρ	Radius of curvature (m).

It should be noted that the free energy expressions must be continually updated as the positions of the leading and trailing interfaces change with time (*i.e.*, as the curvature of the interfaces change). The free energy expressions for the solid and liquid phases (F_S and F_L) for the aluminum - copper system are described in Chapter Six.

The initiation stage continues until loss of coherency occurs in the growing grain. This was assumed to occur once the solute penetration distance achieves a critical value such that it becomes energetically favourable to accommodate the atomic misfit with a grid of misfit dislocations, rather than the lattice remaining fully coherent. The solute penetration distance (L) in the growing grain is assumed to be given by Equation (2.20). That is:

$$L = \sqrt{D_S\, t} + vt \tag{5.40}$$

The initiation stage of migration therefore extends from time, t = 0, until the time at which:

$$L \geq 5{*}L_C$$

where, L_C is the critical diffusion distance for loss of coherency. A full description of the calculation of L_C for the aluminum - copper system is described in Section 6.2.8. The modelling of subsequent LFM is described in the following section.

Early Stages of Migration

In the preceding section, the concentration difference across the liquid film (ΔC) was determined by differences in the atomic moduli (*i.e.*, coherency strain energy) of the two grains separated by the liquid film. This stage continues until coherency can no longer be maintained in the trailing solid phase. When modelling the loss of coherency in the growing grain, it should be noted that it was assumed that coherency was lost instantaneously, *i.e.*, one instant, the trailing solid is fully coherent, and the next, fully incoherent, with the entire misfit accommodated by a grid of misfit dislocations. The question remains on how to include the energy of a wall of misfit dislocations into the free energy expression for the trailing solid. Several attempts were made to calculate the energy, all of which made little difference to the overall migration behaviour. The trailing interface was affected by the dislocation wall for at most 0.2 seconds, and inclusion of the relevant energy expression made the computer program less stable. For these reasons it was decided not to include any expression for the energy of the dislocation wall, once it had formed.

Once coherency has been lost in the growing grain, it was assumed that the composition of the deposited material is the equilibrium composition at the experimental temperature, and therefore completely strain free. As a result, once beyond the strain field of the dislocation wall, the free energy of the trailing solid becomes that of the bulk solid phase of equilibrium composition. The leading solid was assumed to remain fully coherent, and the energy due curvature was added to the free energies of the leading and trailing liquids as in the previous stage of migration. The early stage of migration is illustrated in Figure 5.8(b). The free energy expressions for the leading and trailing solids and liquids for this stage are therefore:

$$\begin{aligned} F_{S,\,LEAD} &= F_S + V_m Y(n_A)\eta^2(C_S - C_0)^2 \\ F_{L,\,LEAD} &= F_L + V_m \sigma K_{LEAD} \\ F_{L,\,TRAIL} &= F_L + V_m \sigma K_{TRAIL} \\ F_{S,\,TRAIL} &= F_S \end{aligned} \qquad (5.41)$$

This stage of migration therefore extends from the time at which:

$$L \geq 5^*L_C$$

until the time where the trailing liquid no longer possesses positive curvature (*i.e.*, for values of $Z_{TRAIL} > 0$).

Later Stages of Migration

The early stage was assumed to continue as described above until the trailing solid possessed positive curvature (*i.e.*, for values of $Z_{TRAIL} > 0$). In the later stages of migration (Figure 5.8(c)), it can be seen that the energy due to curvature for the trailing interface was now added to the free energy of the trailing solid. The leading solid was assumed to remain fully coherent, and the energy due to curvature for the leading interface was added to the free energy of the leading liquid. The free energy expressions for the leading and trailing solids and liquids for this stage are therefore:

$$\begin{aligned} F_{S,\,LEAD} &= F_S + V_m Y(n_A)\eta^2(C_S - C_0)^2 \\ F_{L,\,LEAD} &= F_L + V_m \sigma K_{LEAD} \\ F_{L,\,TRAIL} &= F_L \\ F_{S,\,TRAIL} &= F_S + V_m \sigma K_{TRAIL} \end{aligned} \qquad (5.42)$$

This stage of migration therefore extends from the time when Z_{TRAIL} becomes positive until the end of the simulation time (30 seconds) or until the liquid film collapses, whichever occurs first.

A detailed discussion of the application of this model to the aluminum - copper system is presented in Chapter Six. A discussion of the current modelling approach is presented in Chapter Seven.

5.4.4 Modelling in MAPLE - an Outline

MAPLE^{TM} mathematical software was chosen for application of the model. The reasons for this choice lie in the fact that MAPLE makes direct application of the common tangent method as described in Section 5.3.2 possible. That is, it is possible to solve the differential equation which describes the local equilibrium (Equation (5.28)), subject to the condition of equal slopes (Equation (5.29)) for each time interval (*i.e.*, common tangent). MAPLE is also amenable to standard programming commands that might be found in programming languages such as Basic, Fortran, or Pascal. This section outlines the algorithm developed for application of the model developed in the previous section.

The algorithm consists of three major sections: (i) Input of energy expressions, parameter values and array initialization, (ii) Calculation of the positions of the trailing and leading interfaces as a function of time, and (iii) Plotting and tabulation of model predictions. These are described below.

Input of Energy Expressions, Parameter Values and Array Initialization

The molar free energy expressions for the solid phase (Al) and the liquid phase (L) obtained from Murray [53] (see Section 6.2.1) are evaluated at the experimental temperature; the strain free, planar equilibrium is then calculated through Equations (5.28) and (5.29). The coherency strain energy is evaluated for both the leading and trailing solid phases (*i.e.*, V_m × Equation (2.1)). The resulting expression for the coherency strain energy is therefore a function of the solid composition, C_S (*i.e.*, once the appropriate parameter values have been defined). This energy will be added to the free energy of the leading and / or trailing solid phases later in the algorithm, as described in Section 5.4.3. Several parameter values are then initialized, including: the initial positions of the leading and trailing interfaces, the pinning points of the liquid film, the solid - liquid interfacial free energy (σ), and the diffusion coefficients of solute in both solid and liquid phases (D_S and D_L). Several arrays are initialized, including the time (t) array. The time array was set up such that during the early stages of migration, the predictions for the positions of the trailing and leading interfaces (Z_{LEAD} and Z_{TRAIL}) are calculated every 0.01 seconds. During the later stages of migration, predictions are calculated less frequently.

Calculation of the Positions of the Trailing and Leading Interfaces ($Z_{LEAD}(t)$ and $Z_{TRAIL}(t)$)

A 'DO' loop was employed to evaluate the positions of the leading and trailing interfaces as a function of time. During each loop, values were updated to reflect the changing condition of the liquid film; for instance, the energy due to curvature of the leading and trailing interfaces is re-calculated using the positions of the leading and trailing interfaces from the previous loop as input (Equations (5.31), (5.32), (5.36), (5.37), and (5.38)). Then, according to the criteria described in Section 5.4.3 , the free energies of the leading and trailing solid and liquid phases are calculated, adding the energies due to curvature and / or coherency strain as appropriate (*i.e.*, through Equations (5.39), (5.41), or (5.42)). The compositions of the solid and liquid phases in local equilibrium at both leading and trailing interfaces are calculated using Equations (5.28) and (5.29), thus defining the concentration difference across the liquid film (ΔC) at that instant in time. Using the velocity expression based upon the instantaneous velocity of the liquid film (Equation (5.22) with (5.21) for the liquid film thickness (δ)), the positions of the leading and trailing interfaces are updated (Equations (5.23) and (5.24)). The values calculated during this loop are then used as input for the following iteration.

Plotting and Tabulation of Model Predictions

Upon completion of the 'DO' loop described above, several arrays containing parameter values are converted to plots of that parameter as a function of time, or tabulated into a form appropriate for export to a spreadsheet program such as EXCEL. Experimentally measured positions of the leading and trailing interfaces for several times are plotted along with the model predictions, allowing for easy comparison. Arrays containing ΔC and the calculated D_S/v parameter as functions of time are also plotted, and exported.

Application of the model to the aluminum - copper system and the sensitivity of model predictions to variations in particular material parameters is described in some detail in Chapter Six. A comparison of model predictions using the current model to experimentally measured values, as well as to predictions using the Yoon model [7,48], is described in Chapter Seven. A printout of the MAPLE program is included in the Appendix.

CHAPTER SIX

MODEL APPLICATION TO THE ALUMINUM - COPPER SYSTEM

6.1 INTRODUCTION

This chapter discusses the application of the kinetic model developed in Chapter Five to the aluminum - copper system. Model calibration involved performing a literature search to obtain the appropriate material characteristics, as well as determining how to adjust these values to higher temperatures. Several simulations were then performed over a range of possible parameter values. Calibration was complete once predictions were obtained that best matched the experimentally determined positions of the leading and trailing interfaces. Section 6.2 discusses the material parameters used in the modelling of LFM in the aluminum - copper system, with emphasis on the variation in these parameters, as well as the methodology used in converting these values to higher temperatures. An analysis of the sensitivity of the model predictions to variations in particular material parameters is presented in Section 6.3. In the final section, a brief comparison of model predictions to the Yoon *et al.* [7,48] model (described in Chapter Two) is included.

6.2 MATERIAL CHARACTERISTICS

The material characteristics specific to the aluminum - copper system that are required for the application of the kinetic model are discussed in the following section. Values from literature are presented along with a description of the corrections made to those values not measured at elevated temperatures. Experimentally determined parameters such as temperature and the initial positions of the leading and trailing solid - liquid interfaces are discussed in the final section. Table 6.2 provides a summary of the material parameters.

6.2.1 Free Energy Expressions for the Aluminum - Copper System

Free energy expressions for the bulk solid and liquid free energies (F_S and F_L) for the relevant phases of the aluminum - copper system are required for application of the kinetic model developed in Chapter Five. Two sets of free energy expressions were considered for the free energies of the solid (Al) phase and the liquid (L) phase for temperatures greater than the eutectic temperature (≈548 °C). These are those of Hultgren [56] and Murray [53].

The Hultgren representation of the Gibbs free energies for the liquid and solid phases (F_L and F_S) are given by:

$$\begin{aligned} F_L &= 10711\left(1-\frac{T}{933}\right)(1-C) + RT\,(C\ \ln(C) + (1-C)\ \ln(1-C) \\ &\quad + C(1-C)(-34364 - 38000C - 7023C(1-C)) \end{aligned} \tag{6.1}$$

and

$$\begin{aligned} F_S &= 13263\left(1-\frac{T}{1356}\right)(C) + RT\,(C\ \ln(C) + (1-C)\ \ln(1-C) \\ &\quad + C(1-C)(-24500 - 57000C - 7000C(1-C)) \end{aligned} \tag{6.2}$$

Where:

C	Atom fraction of copper
T	Temperature

In the case of the Murray approximation, the polynomial representation of the Gibbs free energies is given by:

$$
\begin{aligned}
F_i = {} & F_i^{(Al)}\,(1-C) + F_i^{(Cu)}\,C + RT\,\big(C\,lnC + (1-C)\,\ln(1-C)\big) \\
& + C(1-C)\big(\Phi_i + \Omega_i\,(1-2C) + \Psi_i\,(6C^2 - 6C + 1)\big)
\end{aligned}
\qquad (6.3)
$$

Where:

i	Phase (solid or liquid)
C	Atom fraction of copper
F_i	Gibbs free energies of the pure metals (Al or Cu)
Φ_i, Ω_i, Ψ_i	Temperature dependent interaction parameters

Values of F_i, Φ_i, Ω_i, and Ψ_i for the relevant portion of the phase diagram (*i.e.*, the solid - liquid equilibrium (Al) +(L)) for the Murray approximation are given in Table 6.1 (temperature in K).

Table 6.1: Thermodynamic parameters used to represent the Gibbs free energies of the solid and liquid phases (after Murray [53]). Used in conjunction with Equation (6.3).

Phase	Parameter	Gibbs Free Energy (J mol^{-1})
Solid	$F_S^{(Al)}$	$-6531.4 + 122.710T + 21.1429T(1-\ln T) - 0.0075545T^2/2 - 0.47781x10^5/2T -0.59x10^{-5}T^3/6$
	$F_S^{(Cu)}$	$-6792.3 + 132.407T + 22.9847T(1-\ln T) - 0.005676T^2/2$
	Φ_S	$-28353 - 13.5780T$
	Ω_S	$22364 + 12.0517T$
	Ψ_S	0
Liquid	$F_L^{(Al)}$	$-804.7 + 174.134T + 31.7566T(1-\ln T)$
	$F_L^{(Cu)}$	$-1607.0 + 184.689T + 32.6350T(1-\ln T)$
	Φ_L	$-33255 - 16.5543T$
	Ω_L	$13308 + 6.6030T$
	Ψ_L	$2260 - 3.2823T$

The two sets of free energy expressions were compared by calculating the equilibrium solid and liquid compositions by use of the common tangent construction described in the previous chapter (Equation (5.28) with Equation (5.29)). This was done for several temperatures above the eutectic temperature. In this way the solidus and liquidus curves can be created. Figure 6.1 shows the predicted solidus and liquidus curves, along with the experimentally determined points obtained from data compiled by Murray [53]. It can be seen that the solidus and liquidus curves predicted using the free energy expressions of Murray fit the experimental data much better than from those of Hultgren. The free energy expressions developed by Murray are therefore used for the calculation of the concentration difference across the liquid film (*i.e.*, $\Delta C = C_{L,TRAIL} - C_{L,LEAD}$).

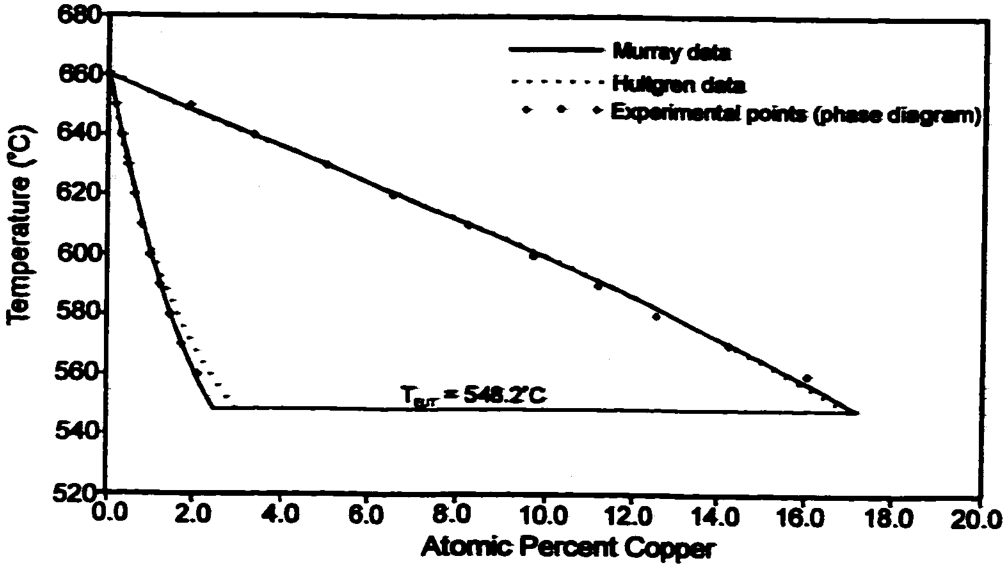

Figure 6.1: **Predicted and experimentally determined solidus and liquidus curves for the aluminum rich end of the Al-Cu phase diagram. Data from Murray [53], and Hultgren [56].**

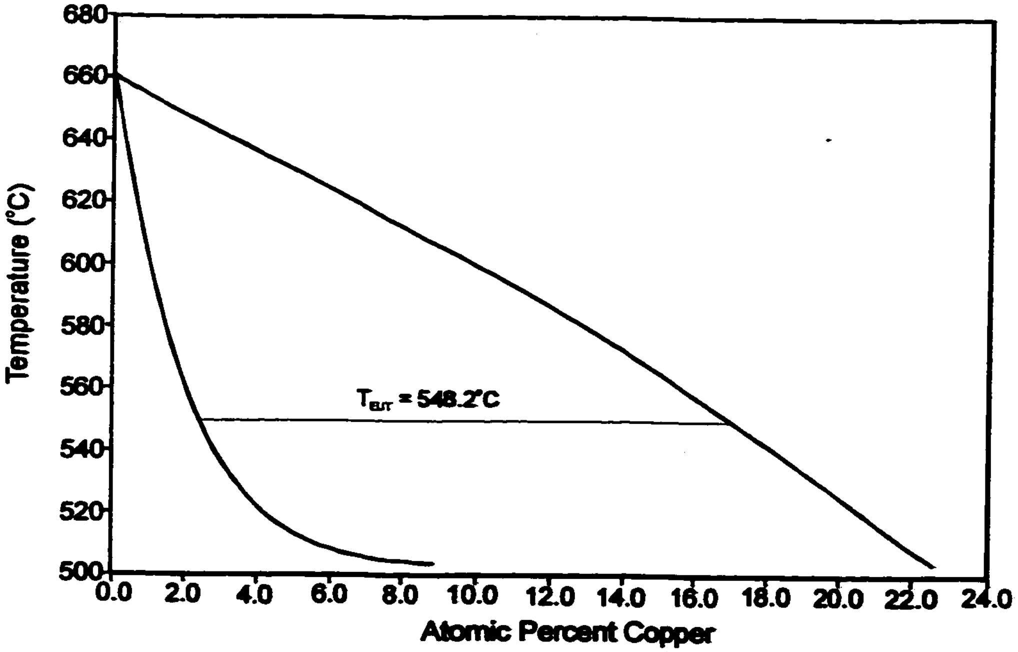

Figure 6.2: **Predicted solidus and liquidus curves for the aluminum rich end of the Al-Cu phase diagram including the meta-stable extension to temperatures below the eutectic temperature. Data from Murray [53].**

The calculations described above were also performed (using the data of Murray [53]) at temperatures below the eutectic temperature forming meta-stable solidus and liquidus curves, as shown in Figure 6.2.

6.2.2 Compositions Required For Model Application (C_L, C_S, C_0)

A number of equilibrium compositions are required in order to apply the kinetic model to the aluminum - copper system. These are the equilibrium solid and liquid compositions at the experimental temperature (C_S and C_L), and the composition of the parent solid phase (C_0).

Liquid and Solid Compositions (C_L and C_S)

Two sets of equilibrium solid and liquid compositions are used during modelling. Where the concentration difference (ΔC) is calculated using the analysis of Yoon *et al.* [7], (see Section 6.4), C_L and C_S are obtained directly from the aluminum - copper phase diagram compiled by Murray [53]. The (Al) + (L) equilibrium at a temperature of 560°C is used to obtain the equilibrium compositions. The values are:

$$C_S = 0.0210 \pm 0.0005$$

$$C_L = 0.155 \pm 0.003$$

Values for C_L and C_S need not be assumed using the kinetic model developed in Chapter Five, since they are calculated directly using the common tangent method (Equations (5.28) and (5.29)) at both solid - liquid interfaces. The calculated solid and liquid compositions at the leading and trailing interfaces are designated $C_{S,LEAD}$, $C_{L,LEAD}$, $C_{S,TRAIL}$, and $C_{L,TRAIL}$.

Composition of Parent Solid (C_0)

The composition of the parent solid phase is obtained directly from the aluminum - copper phase diagram compiled by Murray [53]. Using the (Al) + (θ) equilibrium at a temperature of 400°C gives:

$$C_0 = 0.0063 \pm 0.0007$$

This value is used in all versions of the kinetic model.

The errors in the values for C_L, C_S, and C_0 were obtained directly from the phase diagram; that is to say they were estimated from the experimental scatter in the data collected by Murray [53].

6.2.3 Molar Volume (V_m)

The molar volume (V_m) is used to convert the calculated energy per unit volume due to coherency and / or curvature to a molar quantity such that it may be added directly to the molar free energies of the bulk solid and liquid phases. These energies are used in the calculation of the concentration difference across the liquid film (see Chapter Five).

The molar volume of the solid phase is calculated both at room temperature (25°C) and at the experimental temperature (560°C). V_m is obtained in the following manner.

The volume of the unit cell of the aluminum lattice is required at both temperatures. A lattice parameter of 4.0497 (Å) for pure aluminum at 25°C was obtained from Cullity [57]. In order to calculate the volume of the unit cell at higher temperatures, this value must be corrected to account for thermal expansion. Assuming that the expansion of the aluminum lattice varies linearly with temperature (*i.e.*, for temperatures in the range: $25°C \leq T \leq 560°C$) with a thermal expansion coefficient of $\alpha_T = 23.5 \times 10^{-6}$ ($°C^{1}$) [58], the value of the lattice parameter at higher temperatures (T) is calculated using the following formula:

$$a_T = a_{25} + a_{25}\big(\, \alpha_T(T - 25) \,\big) \tag{6.4}$$

Where:

a_{25} Lattice parameter at room temperature, 25°C (Å)

a_T Lattice parameter at the elevated temperature, T (Å)

This yields a value for the lattice parameter of 4.1006 (Å) at 560°C. The unit cell therefore has a volume of 6.6451×10^{-29} m^3 at 25°C, and a volume of 6.8952×10^{-29} m^3 at 560°C. Since aluminum has a face centered cubic structure, there are 4 atoms per unit cell, and knowing that there are 6.023×10^{23} atoms per mole (Avagadro's number), it is possible to calculate the molar volume. This yields:

$$V_m\,(25°C) = 1.00 \times 10^{-5}\,(m^3\,mol^{-1})$$

$$V_m\,(560°C) = 1.04 \times 10^{-5}\,(m^3\,mol^{-1})$$

The calculation described above assumes that the thermal expansion coefficient is valid up to the experimental temperature of 560°C, as indicated in Equation (6.4). Since the thermal expansion coefficient (α_T) is stated to be valid only up to a temperature of 100°C, and because of the small differences in the calculated molar volume after heating from room temperature to the experimental temperature, the value of the molar volume calculated at room temperature was assigned to the molar volume throughout modelling. That is:

$$V_m = 1.00\,(\pm 0.04) \times 10^{-5}\,(m^3\,mol^{-1})$$

6.2.4 Elastic Modulus (Y(n))

During the calculation of the coherency strain energy (Equation 2.1), the orientation dependent biaxial elastic modulus, Y(**n**), at the experimental temperature is required. This is calculated as follows.

During modelling of LFM, maximum and minimum values of Y(**n**) at the experimental temperature of 560°C are required. For cubic crystals, the variation of elastic modulus with crystallographic orientation was developed by Hilliard [44], and is included below:

$$Y = \tfrac{1}{2}(c_{11} + 2c_{12})\left(3 - \frac{(c_{11} + 2c_{12})}{(c_{12} + c_{44})} \cdot G_Y\right) \tag{6.5}$$

Where:

c_{11}, c_{12}, c_{44}	Stiffness coefficients
G_Y	Geometric factor, given by:

$$G_Y = \frac{3(\alpha_Y - 1)^2\theta_Y + 2\beta_Y(\alpha_Y - 1)\phi_Y + \beta_Y^2}{(\alpha_Y - 1)^2(\alpha_Y + 2)\theta_Y + \beta_Y(\alpha_Y^2 - 1)\phi_Y + \beta_Y^2(\alpha_Y + \beta_Y)} \tag{6.6}$$

Where:

$\theta_Y = l^2\, m^2\, n^2$

$\phi_Y = l^2\, m^2 + m^2\, n^2 + l^2\, n^2$

l, m, n are the directional cosines.

$$\alpha_Y = \frac{(c_{11} - c_{44})}{(c_{12} + c_{44})}$$

$$\beta_Y = \frac{c_{44}}{(c_{12} + c_{44})}$$

For aluminum, using the data of Gault *et al.* [59] ($c_{11} = 108$; $c_{12} = 62.0$; $c_{44} = 28.3$ (GPa); all values measured at 25°C), it can be shown that Y has a maximum value in the <111> direction and a minimum in the <100> direction. In order to calculate Y(<111>) and Y(<100>), the directional cosines *l, m,* and *n* are required. These are:

For <111> directions: $l = m = n = \dfrac{1}{\sqrt{3}}$

For <100> directions: $l = 1$ and $m = n = 0$

Substituting these values along with the stiffness values of Gault *et al.* [59] into Equations (6.5) and (6.6) yield the following values:

$$Y(<111>)^{25^\circ C} = 114 \text{ (GPa)}$$

$$Y(<100>)^{25^\circ C} = 98.8 \text{ (GPa)}$$

These values must be corrected for temperature since an estimate of the coherency strain energy at 560 °C is required for modelling.

The temperature dependence of the moduli ($Y(\mathbf{n})$) is determined as follows. Young's modulus (E) data for dilute aluminum - copper alloys as a function of temperature were obtained [60-62]. A linear regression was then performed on the data, where the Young's modulus was assumed to be a cubic function of temperature. A value of E = 40.2 (GPa) at 560 °C was obtained from the regression function. For an isotropic solid phase: $Y_{ISO} = E/(1-\nu)$. If a value of $\nu = 0.33$ for aluminum at 500 °C is used [63], then $Y_{ISO} = 60.0$ (GPa). Applying the temperature dependence function obtained from the regression of the Young's modulus (E) data to the $Y(\mathbf{n})$ values calculated at 25 °C, yields*:

$$Y(<111>)^{560^\circ C} = 81.9 \text{ (GPa)}$$

$$Y(<100>)^{560^\circ C} = 66.7 \text{ (GPa)}$$

The values of $Y(<111>)^{560^\circ C}$ and $Y(<100>)^{560^\circ C}$ above are therefore used as starting values for kinetic modelling (*i.e.*, $Y(<111>)^{560^\circ C} = Y_A$ and $Y(<100>)^{560^\circ C} = Y_B$). It should be noted that since the <111> and <100> are the directions of maximum and minimum moduli in f.c.c. materials, any calculation of the concentration difference across the liquid film (ΔC) based the use of these moduli, will result in a maximum value for ΔC (independent of the effects of other parameters). In reality, it is likely that any particular LFM event will have the liquid film separated by grains with different orientations other than <111> and <100>. This will result

---

* This seems reasonable since for isotropic materials $Y = E/(1-\nu)$, and Poisson's ratio (ν) is relatively insensitive to temperature.

in a lower value for ΔC. A discussion of the sensitivity of model results to variations in the modulus of the leading solid (Y_A) is discussed in Section 6.3.

6.2.5 Misfit Parameter (η)

The misfit parameter (η) is a measure of the degree to which the atomic lattice of a substance expands or contracts with the addition of a solute species. This parameter is used in the calculation of the coherency strain energy.

η is calculated using the following equation [7]:

$$\eta = \frac{d(\ln(a))}{dC} = \frac{1}{a(C_0)}\left(\frac{da}{dC}\right) \qquad (6.7)$$

Where:

a	Lattice parameter of the parent solid phase
C	Concentration of copper in the solid phase
C_0	Concentration of copper in the parent solid phase

Maximum and minimum slopes were obtained from the plot of lattice parameter as a function of copper concentration using X-ray data compiled by Murray [53]. Using Equation (6.7), η was calculated to have a value of -0.121 ± 0.006. Sensitivity of model predictions to variations in η is discussed in Section 6.3.

6.2.6 Solid - Liquid Interfacial Energy (σ)

The solid - liquid interfacial energy (σ) is used in the calculation of energy due to curvature. Gündüz and Hunt [64] reported a value of 0.1634 ± 0.0212 ($J\ m^{-2}$) for the equilibrium between the solid (Al) phase and the liquid (L) phase. This is the value used during kinetic modelling. Sensitivity of the model predictions to variations in σ is presented in Section 6.3.

6.2.7 Diffusion Coefficients (D_S and D_L)

Coefficients for the diffusion of copper in both liquid and solid states (D_S and D_L) are required in various stages of modelling.

D_L

The diffusion coefficient of copper in liquid aluminum (D_L) is used in the calculation of the velocity of the liquid film (Equation (5.14) or (5.22)), and was obtained from literature. Roy and Chhabra [65] present values of D_L measured at several different temperatures ranging from 700°C to 1027°C. A linear regression was applied to the data, with D_L assumed to be a linear function of temperature. Similarly, a second regression was performed with D_L assumed to be a parabolic function of temperature. Using these calculated regression functions, two different values for the diffusion coefficient at a temperature of 560°C (D_L = 3180 and 2810 ($\mu m^2\ s^{-1}$)) were obtained.

A common method of presenting empirical diffusion data is in the form of an Arrhenius type equation:

$$D = D_0 \exp\left(\frac{-Q}{RT}\right) \qquad \textbf{(6.8)}$$

Where:

D Diffusion coefficient at temperature T.

D_0 Empirical constant.

Q Activation energy.

Owadano *et al.* [66] presented the results of their diffusion study in the form of Equation (6.8) with $Q = 38900$ ($J\ mol^{-1}$) and $D_0 = 8.1 \times 10^5$ ($\mu m^2\ s^{-1}$). A value of 2950 ($\mu m^2\ s^{-1}$) was calculated for a temperature of 560°C. A fourth value for the diffusion coefficient of 3500

($\mu m^2\, s^{-1}$) at the eutectic temperature was obtained independently by Watson and Hunt [67]. The diffusion coefficient of copper in an aluminum rich liquid phase (D_L) used during application of the kinetic model is obtained by taking the average of the four values quoted above. This yields:

$$D_L = 3070 \pm 280\ (\mu m^2\, s^{-1})$$

D_S

The diffusion coefficient of solute in the solid phase is required only during the initial stage of migration. It is used to estimate the distance the solute species has penetrated into the growing grain. D_S was obtained from an empirical relation similar to Equation (6.8) using the data of Butrymovicz [68] and Peterson and Rothman [69] for values of D_0 and Q ($D_0 = 6.47 \times 10^7$ ($\mu m^2/s$) and Q = 135020 ± 1130 (J)). The calculated value of the diffusion coefficient (D_S) ranged from 0.1875 and 0.2600 ($\mu m^2/s$) corresponding to Q values of 136150 and 133890 (J) respectively. A value of D_S = 0.2206 ($\mu m^2/s$) was used during modelling, corresponding to an activation energy of Q = 135020 (J).

6.2.8 Critical Diffusion Distance for Loss of Coherency (L_C)

The critical diffusion distance for coherency loss (L_C) is required during the kinetic modelling of very early stages of migration, and for comparison with the solute penetration distance in advance of the leading interface (D_S/v) (see Chapter Seven). In the kinetic model developed in Chapter Five, coherency is assumed to be lost in the growing grain once the solute penetration distance, L (Equation (5.40), see Section 5.4.2), achieves a critical value, L_C. The analysis of Matthews [47] is used to obtain an estimate of L_C assuming that during the early stages of migration, deposition of material at the trailing solid - liquid interface occurs epitaxially in a manner similar to the deposition of thin films on massive substrates. The calculation is outlined below.

Several assumptions were made during development of the appropriate relations required to obtain an estimate of the critical solute penetration thickness (L_C), these include [47]:

- The film and substrate have cubic structures.
- Deviations from Hooke's law are neglected.
- The variation of surface energy with elastic strain is ignored.
- The misfit dislocations introduced are edge type, with the Burger's vector (b) lying in the interface and arranged in a square grid.

The critical thickness (L_C) is obtained by minimizing the sum of the misfit dislocation energies and the elastic energy due to coherency strain. That is to say that, for $L < L_C$, where L is defined by Equation (5.40), the thin layer will be strained such that it matches the substrate exactly (*i.e.*, fully coherent). For $L > L_C$, it becomes energetically favourable for some of the misfit to be accommodated by dislocation lines. This calculation is described in detail as follows.

For an isotropic solid, the energy associated with the elastic strain (ϵ) is [47]:

$$E_\epsilon = \frac{2G_0\,(1 + \nu)}{(1 - \nu)}\, L\, \epsilon^2 \tag{6.9}$$

Where:

G_0	Shear modulus of the substrate (parent solid).
ν	Poisson's ratio.
L	Thickness of diffusion layer (see Equation (5.40)).

The energy per unit length (E_d) of a single edge dislocation lying in the interface between two crystals with shear moduli (G_0 and G_S) is given by [47]:

$$E_d = \frac{G_0 G_S}{G_0 + G_S}\,\frac{b^2}{2\pi(1 - \nu)}\left[\ln\left(\frac{r}{b}\right) + 1\right] \tag{6.10}$$

Where:

b	Magnitude of the Burger's vector.
r	Extent of the elastic stress field.

If it is assumed that G_S & G_0 are the shear moduli of the thin layer and substrate respectively, and that they are approximately equal[**], then the energy per unit area of a square grid of two non-interacting, perpendicular edge dislocation arrays, each with spacing, $S = b/(f - \epsilon)$, is given by:

$$E_{grid} = \frac{G_0\, b}{2\pi(1 - \nu)}\,(f - \epsilon)\left[\ln\left(\frac{r}{b}\right) + 1\right] \tag{6.11}$$

Where:

f is the misfit between the substrate and the thin film, given by:

$$f = \frac{a_S - a_0}{a_0} \tag{6.12}$$

and a_S and a_0 are the stress free lattice parameters of the thin layer and the substrate (*i.e.*, parent phase) respectively.

In order to minimize the total energy (*i.e.*, Equation (6.9) added to Equation (6.11)) with respect to the strain (ϵ), an estimate for the cut-off distance of the stress field of the dislocation grid (r) in Equation (6.11) must be made. If it is assumed that at the beginning of the coherency loss process, the dislocations are spaced far apart (*i.e.*, partial coherency loss), then as illustrated in Figure 6.3, the strain field of the dislocation grid is determined by the film thickness (L). That is, $r \approx L$.

[**] This seems reasonable since there is a very small difference between the concentrations involved in the LFM experiments (*i.e.*, between C_S and C_0).

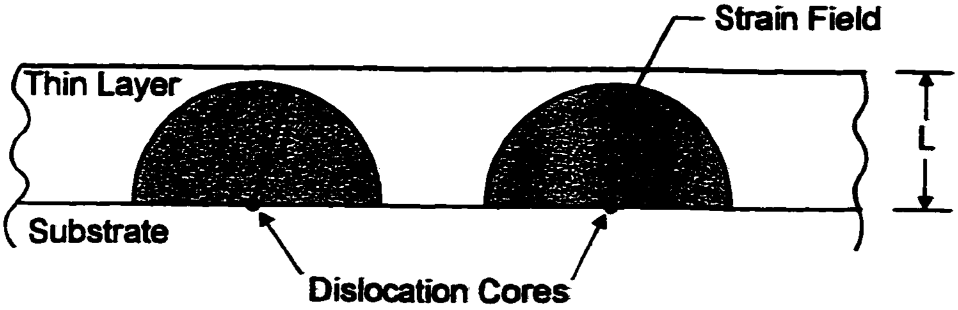

Figure 6.3: Illustration of the Cut-off Distance for the Misfit Dislocation Grid.

The elastic strain (ϵ^*) which minimizes the sum of the dislocation wall energy and the misfit strain energy (Equation (6.9) added to Equation (6.11)) is therefore:

$$\epsilon^* = \frac{b}{8\pi\,(1+\nu)\,L}\left[\ln\left(\frac{L}{b}\right)+1\right] \tag{6.13}$$

The critical thickness (L_C) is obtained by setting $\epsilon^* = f$. That is to say that if $\epsilon^* \geq f$, the thin layer will be strained, but remains coherent. For $\epsilon^* < f$, a portion of the misfit ($f - \epsilon^*$) will be accommodated by dislocation lines. The critical thickness is therefore:

$$L_C = \frac{b}{8\pi\,(1+\nu)\,f}\left[\ln\left(\frac{L_C}{b}\right)+1\right] \tag{6.14}$$

In order to calculate L_C using Equation (6.14), values for f, b and ν for the aluminum - copper system are required. The misfit parameter (f) must be evaluated at the experimental temperature of 560°C. The lattice parameter of the thin layer and the substrate at the experimental temperature (a_S^T and a_0^T) were calculated using the following relations:

$$a_S^T = a_{(C_S)}^{25} + a_{(C_S)}^{25} \cdot \alpha_T (T - 25)$$
$$a_0^T = a_{(C_0)}^{25} + a_{(C_0)}^{25} \cdot \alpha_T (T - 25) \tag{6.15}$$

Where:

$a_{(Cs)}^{25}$ Lattice parameter of the stress free thin layer.

$a_{(Co)}^{25}$ Lattice parameter of the stress free substrate.

α_T Thermal expansion coefficient.

Using the same X-ray data collected by Murray [53] that is used to calculate the misfit parameter (η), values for the lattice parameter at C_0 and C_S were obtained:

$$a_{(Cs)}^{25} = 0.40395 \text{ (nm)}$$
$$a_{(Co)}^{25} = 0.40463 \text{ (nm)}$$

These parameters are then corrected for temperature using Equation (6.15), with $\alpha_T = 23.5 \times 10^{-6}$ (°C^{-1}) [58] and T = 560°C. The resulting values were then substituted into Equation (6.12) giving:

$$f = 0.0016841$$

The Burger's vector (**b**) of the dislocations that form the wall was assumed to be of the type:

$$\boldsymbol{b} = \frac{a}{2} <110>$$

The magnitude of which is:

$$b = \frac{a}{\sqrt{2}}$$

Using the lattice parameter of aluminum corrected for temperature gives the following value for the magnitude of the Burger's vector:

$$b = |\vec{b}| = 2.900\times10^{-4}\ (\mu m)$$

A value of 0.33 is used for Poisson's ratio (ν) [63], and along with f and b calculated above, L_C is calculated to be:

$$L_C = 0.029\ (\mu m)$$

In reality, it is unlikely that the nucleation of dislocations will occur spontaneously once the criteria described above is achieved. That is to say there exists an activation barrier for nucleation. Coherency will be completely lost once the thickness of the epitaxial layer reaches 2 to 5 times the critical thickness, either by nucleation of new dislocations or by the attraction of previously formed dislocations to the strained region [47]. During application of the model, the $5{*}L_C$ criterion is used to determine when and where coherency loss occurs in the growing grain. The validity of this approach is discussed fully in Chapter Seven.

6.2.9 Other Parameters Determined by Experimental Conditions

Several parameters required for application of the kinetic model are obtained from the experimental conditions and results. Starting positions of the leading and trailing interfaces ($Z_{LEAD}(0)$ and $Z_{TRAIL}(0)$) and the width (W) of the liquid film are required, as well as the experimental temperature (T).

Starting Positions of the Leading and Trailing Interfaces ($Z_{LEAD}(0)$ and $Z_{TRAIL}(0)$) and the Location of the Pinning Points (X_{PIN})

Measurements of the positions of the leading and trailing solid - liquid interfaces as well as the width of the particular LFM events were obtained from experimental measurements using the method outlined in Section 3.4.6. The results of these measurements are included in Section 4.3.4. The average liquid film thicknesses for each time ($\delta(t) = Z_{LEAD}(t) - Z_{TRAIL}(t)$) were calculated and plotted as a function of time. Extrapolation of this plot back to zero time results in a value of $\delta(0) = 2.3$ (μm) for the average liquid film thickness at the start of the migration process. Since the liquid film is assumed to be symmetrical at the start of the migration, the values for Z_{LEAD} and Z_{TRAIL} are therefore:

$$Z_{LEAD}(0) = 1.15 \ (\mu m)$$

$$Z_{TRAIL}(0) = -1.15 \ (\mu m)$$

The end points of the liquid film (pinning points) are required for model application, since their position directly influences the calculation of the energy due to curvature. From the measurements outlined in Section 3.4.6, and the results in Section 4.3.4, an average width of $W = 6.9 \pm 1.3$ (μm) was calculated. The pinning points are therefore: (-3.45,0) and (3.45,0).

Experimental Temperature (T)

The experimental temperature was measured using the method outlined in Section 3.4.1. It was estimated to be 560 ± 2°C. This is the temperature used in the calculation of the bulk free energies of the solid and liquid phases.

6.2.10 Summary

Table 6.2 provides a summary of the parameters used for application of the kinetic model.

Table 6.2: Summary of parameters used for model application.

Parameter	Description	Value	Units
C_L	Copper concentration in the liquid phase	0.155 (± 0.003)*	-
C_S	Copper concentration in the solid phase	0.0210 (± 0.0005)*	-
C_0	Copper concentration in the parent solid phase	0.0063 (± 0.0007)	-
V_m	Molar volume of the solid phase	1.00×10^{-5} $(\pm 0.04 \times 10^{-5})$	$m^3\ mol^{-1}$
$Y_{<111>}$	Modulus of grain with <111> surface normal	8.19×10^{10}	$J\ m^{-3}$ (Pa)
$Y_{<100>}$	Modulus of grain with <100> surface normal	6.67×10^{10}	$J\ m^{-3}$ (Pa)
η	Misfit parameter	-0.121 (± 0.006)	-
σ	Solid - liquid interfacial energy	0.1634 (± 0.0212)	$J\ m^{-2}$
D_S	Diffusion coefficient of copper in solid aluminum	0.2206 (± 0.036)	$\mu m^2\ s^{-1}$
D_L	Diffusion coefficient of copper in liquid aluminum	3070 (± 280)	$\mu m^2\ s^{-1}$
L_C	Critical diffusion depth for loss of coherency (due to Matthews [47])	0.029	µm
T	Experimental temperature	560 (± 2)	°C
$Z_{LEAD}(0)$	Starting position of the leading interface	1.15	µm
$Z_{TRAIL}(0)$	Starting position of the trailing interface	-1.15	µm
X_{PIN}	X-coordinate of pinning points → $(X_{PIN}, 0)$ and $(-X_{PIN}, 0)$	3.45 (± 0.65)	µm

*Note: These values are used only when using the method of Yoon *et al.* [7] to calculate the concentration difference across the liquid film (ΔC). (See Section 6.2.2). All concentration values are atomic fractions of copper.

6.3 SENSITIVITY TO MATERIAL PARAMETERS

As described in the previous section, application of the kinetic model developed in Chapter Five requires use of material characteristics specific to the aluminum - copper system. This section describes the sensitivity of model predictions to variations in several of these parameters. Section 6.3.1 discusses the free energy functionals of the solid and liquid phases due to Murray [53] (see Section 6.2.1), emphasizing the degree to which the equilibrium compositions of the solid and liquid phases change upon small changes to the free energy curves (*i.e.*, due to curvature and / or coherency strain energies). The model predictions that best fit the experimental data are presented in Section 6.3.2, as well as a discussion of the model sensitivity to five different parameters. These are: the temperature (T), the biaxial elastic constant of the leading solid phase (Y_A), the specific solid - liquid interfacial energy (σ), the composition of the parent solid phase (C_0), and the misfit parameter (η).

6.3.1 Free Energy Curves for the Solid and Liquid Phases

As was mentioned in Section 6.2.1, the free energy expressions for the solid (Al) and liquid (L) phases developed by Murray are used in the calculation of the concentration difference across the liquid film (ΔC). This section describes the influence the shape of these curves have on the equilibrium compositions of the solid and liquid phases (*i.e.*, C_S and C_L). In particular, how small additions to the free energies of the solid and / or liquid phases (due to coherency strain or curvature energies) lead to significant changes in the equilibrium compositions. Figure 6.4 shows a molar free energy diagram for the solid and liquid phases as a function of copper concentration for the range: $0.0 \leq C_{Cu} \leq 0.5$, at a temperature of 560 °C. The common tangent is illustrated, showing the calculated planar, strain free equilibrium compositions ($C_{SEQ} = 0.0204172$, $C_{LEQ} = 0.156909$). It should be noted that the compositions are quoted to six significant digits since the concentration difference across the liquid film (ΔC) that drives LFM is of the order of 10^{-5}. It can be seen that the actual free energy curves are not typical of those illustrated in Chapter Five, with the relative difference

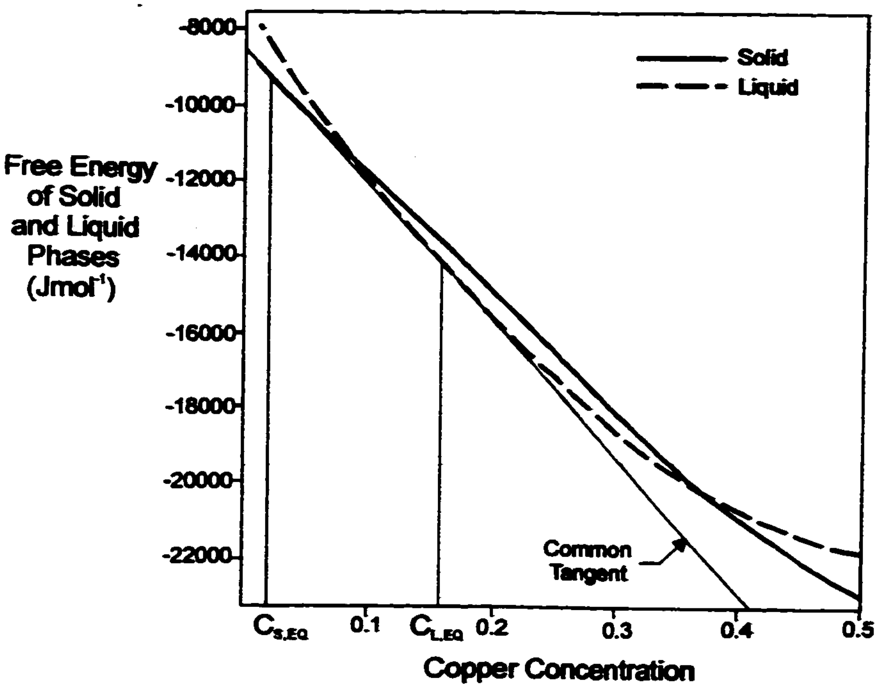

Figure 6.4: **Bulk Free Energies of the Solid (Al) Phase and the Liquid (L) Phase. The Equilibrium Compositions Are Obtained Using the Common Tangent Method Described in Chapter Five.**

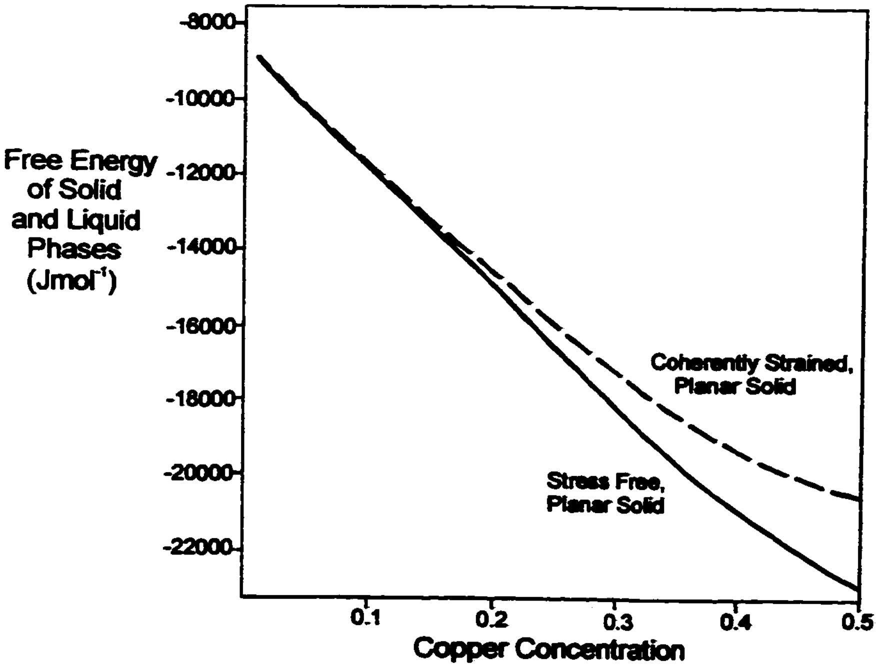

Figure 6.5: **Free Energies of the Bulk Solid Phase and Coherently Strained Solid.**

between the two curves being much smaller than shown in most schematic free energy diagrams. As a result, the equilibrium compositions obtained using the common tangent method are extremely sensitive to small changes in the free energies of either the solid or liquid phases. The free energy of a coherently strained solid phase is illustrated in Figure 6.5, along with the free energy of the bulk solid phase. The coherency strain energy curve illustrated is calculated using Equation (2.1) ($\times V_m$), to which is added the bulk free energy of the solid phase. The values used to calculate the coherency strain energy were: $Y_A = 72.5$ (GPa), $\eta = -0.118$, $C_0 = 0.0065$, and $V_m = 1.0 \times 10^{-5}$ (m^3 mol^{-1}). Using the common tangent method, the new local equilibrium compositions were calculated. These are: $C_S' = 0.0193219$ and $C_L' = 0.156724$. It can be seen that the equilibrium compositions have changed noticeably from the bulk equilibrium values. Plots of the solid and liquid free energy curves including the energy due to curvature are not included since they are indistinguishable from the bulk free energy curves. In order to demonstrate quite how sensitive the equilibrium compositions are to changes in the free energy of the appropriate phase, consider the percentage change in the equilibrium compositions when compared to the percentage change in the free energy of the solid or liquid phase (all with respect to the bulk, planar state). This is illustrated in Table 6.3.

Table 6.3: Sensitivity of Solute Compositions (C_S and C_L) to Changes in the Free Energies of the Solid and Liquid Phases.

Phase (Interface)	**% Change in Free Energy**	**% Change in C_S**	**% Change in C_L**
Coherent solid (lead)	0.0206	5.36 (260×)	0.118 (5.7×)
Curved solid (trail)	0.0065	0.0939 (14.5×)	0.0411 (6.3×)
Curved liquid (lead)	0.0071	0.156 (22.0×)	0.0683 (9.6×)

Note: The parenthesized quantity in the two right-hand columns is the multiple of the percentage change in the free energy.

The local equilibria considered to create Table 6.3 were the bulk solid / bulk liquid equilibrium, the coherent solid / bulk liquid equilibrium, the curved solid / bulk liquid equilibrium, and the bulk solid / curved liquid equilibrium. All free energies used to obtain the above table were calculated using the equilibrium bulk planar compositions (C_S or C_L) at a temperature of 560 °C. When calculating the energy due to curvature, spherical geometry is assumed; the radii of curvature for the leading and trailing interfaces were obtained from the experimentally determined positions at 15 seconds (see Chapter Four). These are: $\rho_{LEAD} = 3.45$ (μm), and $\rho_{TRAIL} = 5.75$ (μm). A value of $\sigma = 0.18$ ($J\ m^{-2}$) was used for the solid - liquid interfacial energy. Examination of Table 6.3 indicates that the equilibrium compositions are indeed extremely sensitive to small changes in the free energy of the solid or liquid phases (due to the addition of coherency strain energy or energy due to curvature). This is a direct result of the extremely shallow free energy curves indicated in Figure 6.4. The composition of the solid phase was affected most significantly. A 5.36% difference in solid composition between the coherent solid / bulk liquid equilibrium and the bulk solid / bulk liquid equilibrium is particularly notable, and has major ramifications for the applicability of the Yoon *et al.* [7] model (*i.e.*, in the development of Equation (2.5) for ΔC). This is discussed further in Chapter Seven. A final point, it should be noted that in the kinetic model, the equilibrium used to obtain the solid and liquid compositions at the leading interface is the coherent solid / curved liquid equilibrium. The resulting change in compositions will be less than those indicated in Table 6.3 (for the leading interface) since the coherency strain in the leading solid phase yields smaller values for C_S and C_L, while the curvature of the leading liquid phase gives larger values. This is as expected, since the increasing curvature of the leading interface during LFM opposes the coherency strain energy driving force. The next section describes the sensitivity of model predictions to variations in several material parameters.

6.3.2 Model Sensitivity

As described in the previous section, small changes to the free energies of either the solid or liquid phase result in significant changes to the equilibrium compositions. This section

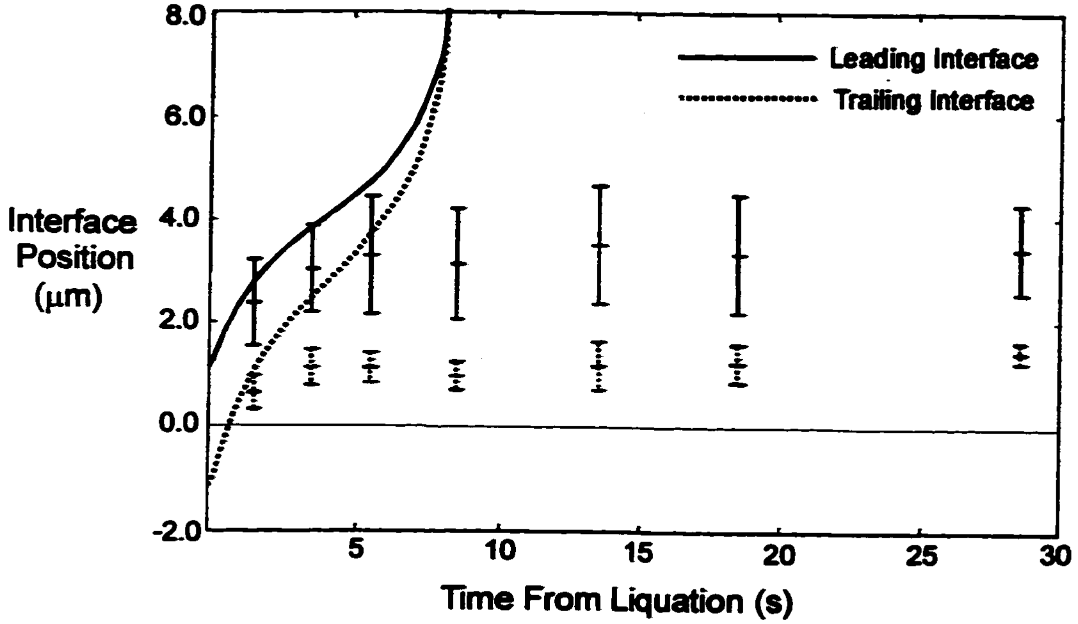

Figure 6.6: Model Predictions for the Positions of the Leading and Trailing Interfaces Using Values Listed in Table 6.2.

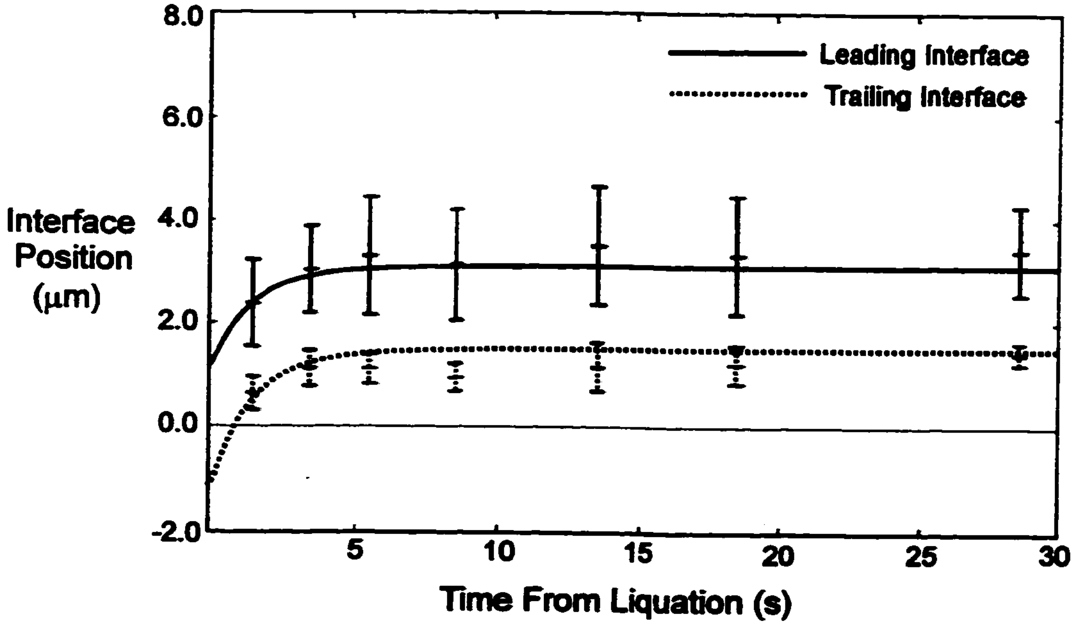

Figure 6.7: Calibrated Model Predictions for the Positions of the Leading and Trailing Interfaces. Values Are Listed in Table 6.4.

describes how these changes affect model predictions. In order to illustrate the effect a particular parameter has on the migration behaviour, a standard set of values are required, to which other model predictions are compared. Figure 6.6 shows the model predictions obtained using the average values for the material parameters and experimental conditions listed in Table 6.2. It can be seen that the positions of the leading and trailing interfaces are over predicted. In order to obtain the best fit to the experimental measurements (see Chapter Four), some of the parameter values must be varied (within the errors listed in Table 6.2). Five parameters were adjusted, these being: the temperature (T), the biaxial elastic constant of the leading solid phase (Y_A), the specific solid - liquid interfacial energy (σ), the composition of the parent solid phase (C_0), and the misfit parameter (η). Figure 6.7 illustrates the model predictions that best match the experimentally measured positions of the leading and trailing interfaces. The parameter values used to obtain these predictions are as listed in Table 6.2, with the exception of the adjustable parameters, listed below (Table 6.4).

Table 6.4: Parameter Values Adjusted to Obtain Best Predictions (Figure 6.7).

Adjustable Parameter	Value
Elastic Modulus (Y_A)	72.5 (Gpa)
Misfit Parameter (η)	-0.118
Specific Solid - Liquid Interfacial Energy (σ)	0.18 (J m^{-2})
Copper Composition of Parent Phase (C_0)	0.0065
Experimental Temperature (T)	560 (°C)

The predictions obtained using the values listed in Table 6.4 are then used as the standard to which all other predictions are compared. Figures 6.8 through 6.12 illustrate the sensitivity of model predictions to variations in Y_A, σ, T, η, and C_0 respectively. The predictions were obtained by systematically varying each parameter while keeping the other parameters constant. All plots include the predictions using the standard parameter values as well as those using the average value for each parameter.

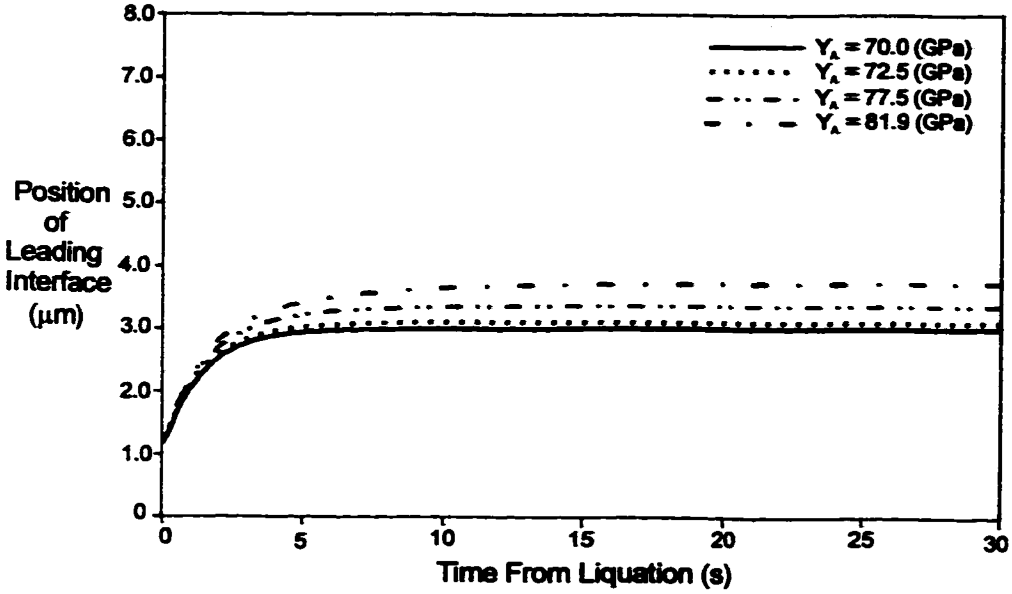

Figure 6.8: **Sensitivity of Model Predictions to Variations in the Biaxial Elastic Modulus (Y_A).**

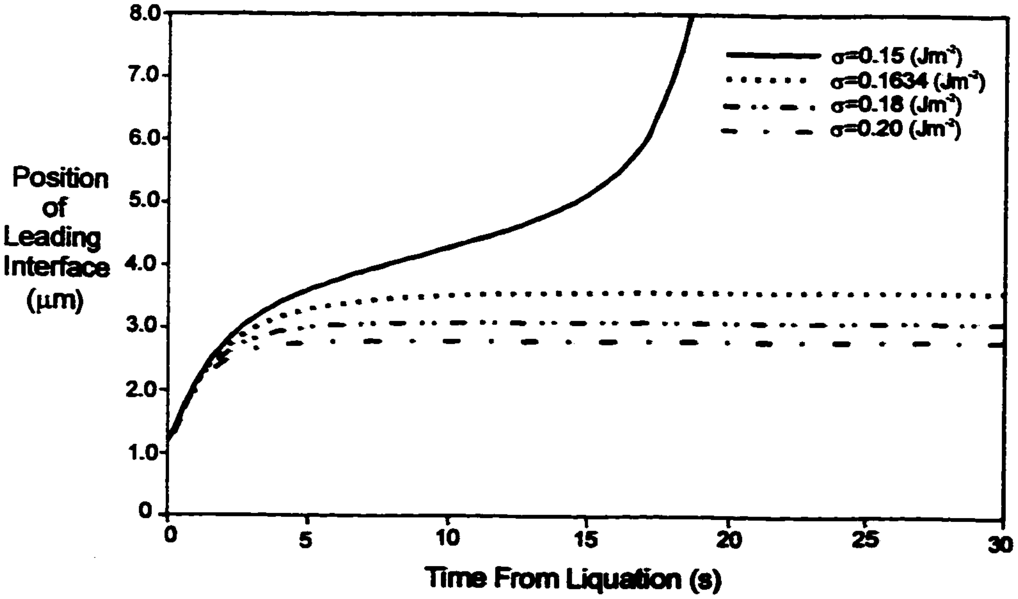

Figure 6.9: **Sensitivity of Model Predictions to Variations in the Specific Interfacial Free Energy (σ).**

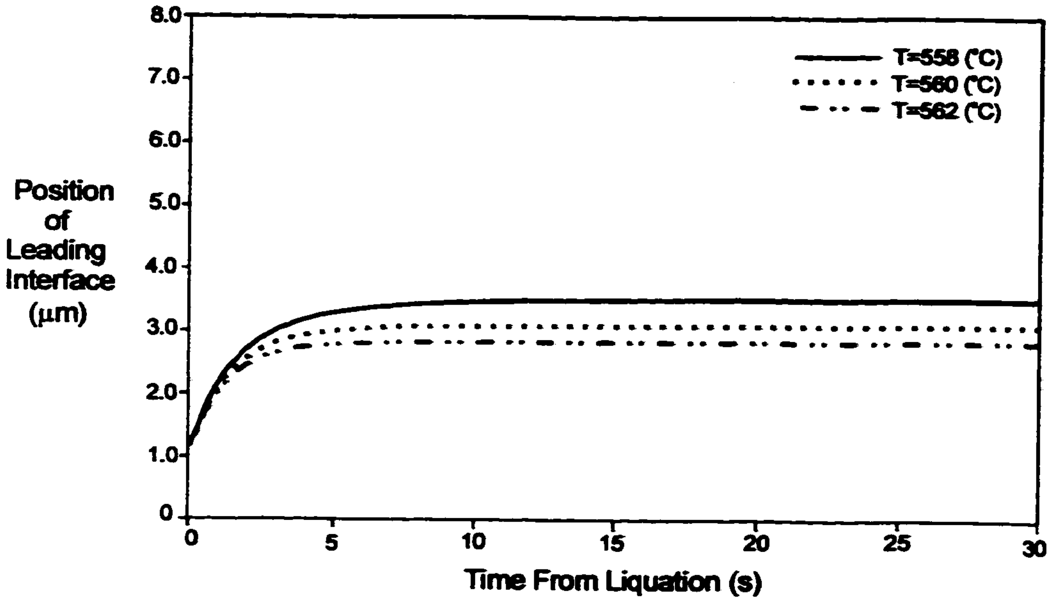

Figure 6.10: **Sensitivity of Model Predictions to Variations in the Experimental Temperature (T).**

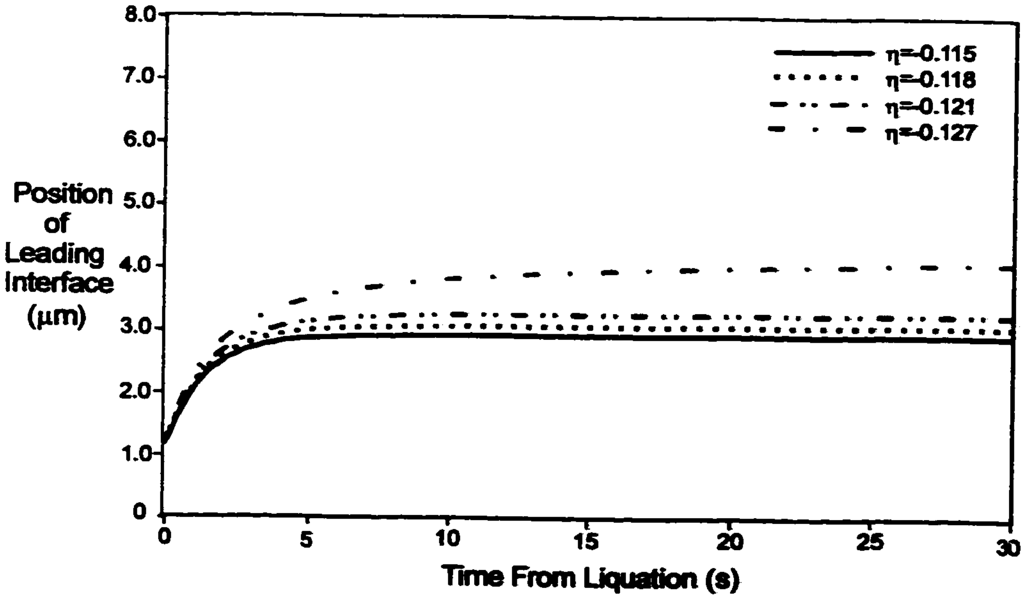

Figure 6.11 **Sensitivity of Model Predictions to Variations in the Misfit Parameter (η).**

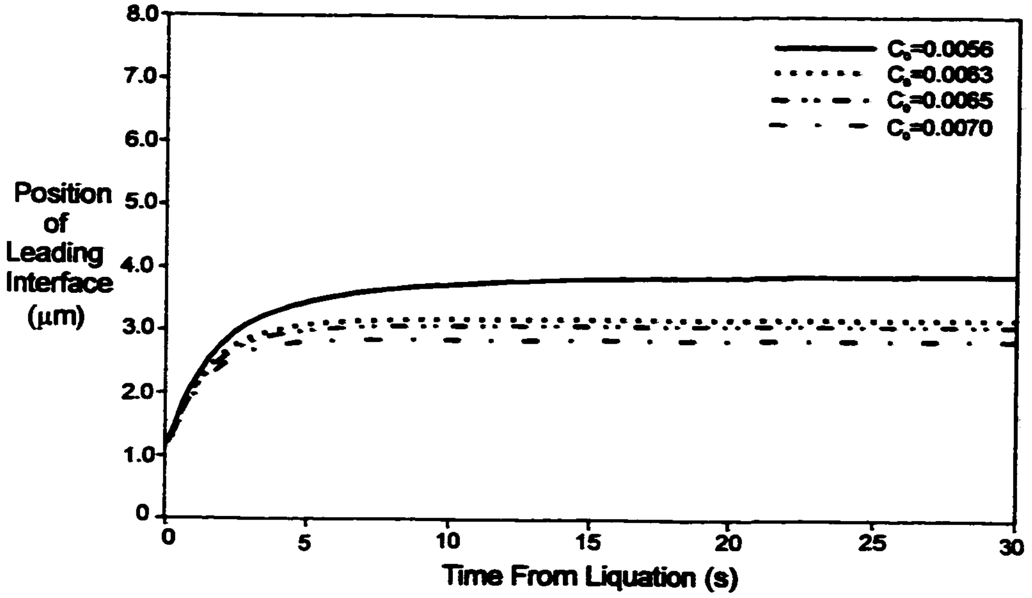

Figure 6.12: Sensitivity of Model Predictions to Variations in the Composition of the Parent Solid Phase (C_0).

Figure 6.8 illustrates the change in model predictions due to variations in the biaxial elastic modulus (Y_A) of the leading solid phase. As expected, as the modulus increases, there is a corresponding increase in the predictions for the position of the leading interface. This is due to the change in equilibrium compositions resulting from the addition of coherency strain energy (through Equation (2.1)) to the free energy of the leading solid phase, as described in the previous section.

The change in model predictions due to variations in the interfacial free energy (σ) are shown in Figure 6.9. As was described in Section 6.3.1, the energy due to curvature at the leading interface causes a change in the equilibrium compositions in an opposite sense to those obtained when the energy due to coherency is added to the free energy of the leading solid phase. The predictions shown in Figure 6.9 are a direct result of this fact. Those obtained using a low value (*i.e.*, $\sigma = 0.15$ (J m^{-2})) indicate that the energy due to curvature in this case is insufficient to overcome the coherency strain energy driving force; that is, the liquid film will accelerate under these conditions, eventually collapsing to form a grain boundary as the film gets thinner. Figure 6.9 also indicates that (for t > 5 seconds) the concentration difference across the liquid film (ΔC) becomes effectively zero for high values for σ (*i.e.*, $\sigma = 0.18$ or 0.20 ($J\ m^{-2}$)); that is, the liquid film becomes immobile as indicated. This is a result of the interplay of the energies due to curvature for the leading liquid and the coherency strain energy for the leading solid, along with the local equilibrium effects at the trailing interface. It can therefore be concluded that the migration behaviour is strongly dependent upon the assigned value of the interfacial free energy (σ).

The experimental temperature (T) is an important parameter to consider when studying the sensitivity of model predictions. This is due to the fact that it was only possible to measure the temperature within ±2 °C of the stated value (Table 6.2). Figure 6.10 illustrates how the predictions for the position of the leading interface are affected by this possible variation. At a time of 15 seconds, a 24% difference is observed between the predicted position at 558 °C and at 562 °C. It can be seen that close measurement of the temperature during experiments to induce LFM in the aluminum - copper system is essential in obtaining the best possible predictions.

Figures 6.11 and 6.12 illustrate the sensitivity of model predictions to variations in the misfit parameter (η) and the composition of the parent solid phase (C_0). Variations in these parameters result in an increase or decrease in the coherency strain energy, given by Equation (2.1). The coherency strain energy has a parabolic dependence upon the value of η, and upon the difference between the equilibrium solid composition and C_0. As expected, larger predicted values were obtained when the calculated coherency strain energies possessed higher values.

It can therefore be concluded that model predictions are extremely sensitive to values assigned to material parameters or to experimentally measured quantities such as the experimental temperature. Predictions seem to be most sensitive to the value assigned to the solid - liquid interfacial energy. Model results and their interpretation are discussed further in Chapter Seven, with emphasis on the general applicability of the model described in Chapter Five to the aluminum - copper system.

6.4 Comparison to Yoon *et al.* Model.

This section describes the predictions obtained using the kinetic model of Yoon *et al.* [7] (described in detail in Chapter Two). The concentration difference across the liquid film (ΔC) was estimated using Equation (2.16) and the velocity using Equation (2.19). The modelling procedure in this case was made as similar as possible to that described in Chapter Five to allow for comparison. That is, the general algorithm remains approximately the same; the only differences being in the calculation of ΔC, and in the calculation of the leading and trailing interface positions through Equation (2.19).

A few notes should be made concerning the calculation of ΔC. As mentioned in Section 2.6, the energy due to curvature (*i.e.*, $\sigma(K_A - K_B)V_m$) has an ambiguous meaning in the early stages of migration (*i.e.*, for $Z_{TRAIL} < 0$). This was accounted for by considering the two interfaces as one, with an average curvature of $(K_A + K_B)/2$; this is a common method of estimating the energy due to curvature in many LFM studies [48]. The energy due to curvature was considered negative with respect to the coherency strain energy (*i.e.*, subtracted from it), and was updated in each iteration of the algorithm. The term 'f_{mL}' was calculated directly through the use of the free energy expression for the liquid phase (Equation (6.3)) using Equation (2.8). That is to say that the second derivative (*i.e.*, $\partial^2 F_L / \partial C_L^2$) was calculated at the experimental temperature of 560°C and evaluated at the equilibrium liquid composition ($C_L = 0.155$). The value obtained was: $f_{mL} = 35633$ (J mol^{-1}). It should be noted that the velocity expression used (Equation (2.19)) makes no account for the loss of solute to the growing phase during solidification.

Model results indicate that the predictions are relatively insensitive to changes in the adjustable parameters introduced in Section 6.3.2. In all cases, the migration distances for the leading and trailing solid - liquid interfaces are over predicted. Figure 6.13 shows the predictions that were obtained using parameter values listed in Table 6.2 that yielded the minimum possible ΔC (within their errors). These were: Y_A=70.0 (GPa), η=-0.115, C_0=0.0070, σ=0.1846 (J m^{-2}), and T=562°C (an increase in the temperature results in an increase in the 'f_{mL}' parameter). Spherical curvature was also assumed to obtain these predictions.

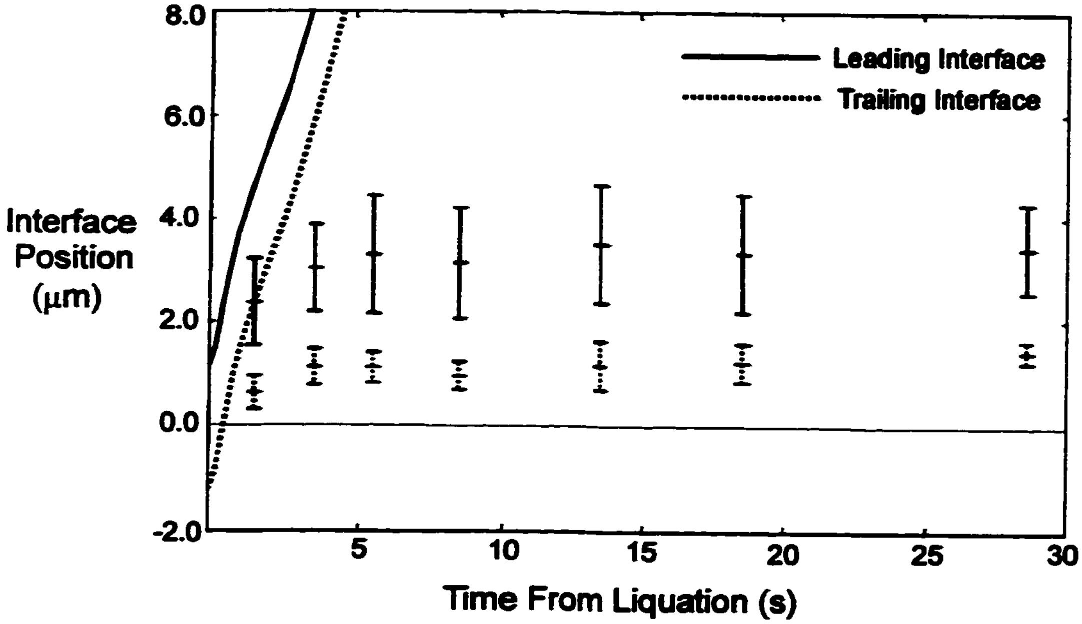

Figure 6.13: **Model Predictions Using the Kinetic Model of Yoon *et al.* [7].**

CHAPTER SEVEN

DISCUSSION

7.1 INTRODUCTION

This chapter provides a general discussion of the work presented in this thesis. A discussion of the experimental results, in particular, an explanation for the morphologies obtained is presented in Section 7.2. The microstructures obtained from the diffusion couple experiments are discussed briefly, as well as those obtained during partial liquation of the samples formed from heat treatments (a) and (b). The results from the volume fraction analysis and the SEM work are also discussed. Section 7.3 contains a discussion of the predictions obtained from the kinetic model described in Chapters Five and Six. Emphasis is placed upon the applicability of the model developed to the aluminum - copper system, in particular, the validity of the coherency strain hypothesis as the driving force for LFM in this system.

7.2 DISCUSSION OF EXPERIMENTAL RESULTS

Results of experiments presented in Chapter Four are examined in this section; the morphologies obtained in all experiments are discussed, including an analysis of the migration distances obtained from both the diffusion couple and precipitation methods of inducing LFM. The marked differences in the microstructures that develop during precipitation heat treatments (a) and (b) are considered, as well as the changes that occur in the microstructures with time at the experimental temperature, with reference to measurements of the volume fraction of liquid. The section ends with a discussion of possible liquid morphologies that may be inferred from the three-dimensional reconstructions obtained.

Diffusion Couple Experiments

The results of the diffusion couple experiments described in Sections 3.3 and 4.2 are discussed in this section. The measured migration distances that were obtained are given in Table 4.2 with reference to Table 4.1; it can be seen that the measured migration distance for the couple held at the experimental temperature for 7.5 hours is higher than that for both the 0.5 and the 13.5 hour samples (*i.e.*, 130 μm compared to 60 μm and 84 μm respectively). It would be expected that the migration distance should increase in a relatively linear fashion (assuming the interfaces possess negligible curvature and that the leading solid phase remains coherent). It is evident that several problems exist with the diffusion couple method for quantifying LFM in the aluminum - copper. These include:

- Loss of the liquid phase occurred at some point during all experiments. It is likely that this occurred within the first 0.5 hour in all cases (*i.e.*, the time of the first experiment). However, since the exact time at which this occurred is unknown it is practically impossible to obtain reasonable predictions for the position of the trailing interface with time since migration would cease immediately once this occurred. The thicknesses of the liquid films indicated in Table 4.2 are the apparent thicknesses measured from micrographs of the corresponding experiments. The expected thickness of the liquid layer that forms from a copper foil of a certain thickness can be calculated using a mass balance; the measured thicknesses (Table 4.2) are thinner than expected. It is likely that during liquation, the pressure applied to assemble the diffusion couple (see Figure 3.3) was relaxed as liquid was forced out the edges.

- The actual stress state in the diffusion couple is difficult to estimate with any certainty. During assembly of the couple (Figures 3.2 and 3.3), pressure was applied perpendicular to the plane of the copper foil / liquid film; if either too much pressure was applied, or if the faces of the components of the couple were not parallel prior to assembly, then dislocations may be created as the sample is plastically deformed near the sample surfaces. The presence of these dislocations may cause coherency loss earlier than would otherwise be expected.

- The slow heating rate and the non - linear cooling rate make quantitative analysis difficult. As described in Section 3.3.1, the entire assembly shown in Figure 3.3 was placed in a tube furnace set to the experimental temperature; as a result, in the time taken for the sample to reach the eutectic temperature, significant diffusion of copper into the two halves of the couple would have occurred prior to liquation of the copper foil. Upon quenching, the sample was removed from the furnace, and the entire assembly submerged in a water bath; the actual sample was then effectively air-cooled in a water cooled iron shell.
- The assumption that convection can be neglected may not be valid for the thickness of liquid films obtained in these experiments (see Table 4.2).

Although these experiments were unsuitable for quantitative analysis, it should be noted that LFM did occur in each case, consistently into the grain not initially in equilibrium with the liquid phase; this is consistent with the coherency strain hypothesis. The averaged migration distance observed in Experiment 3 (t = 13.5 hours) was significantly smaller than that observed in Experiment 2 (t = 7.5 hours); this is contrary to what would be expected. One possible explanation for this observation is that loss of liquid occurred earlier for Experiment 3 than for Experiment 2. It is also possible that coherency was lost very early in the case of Experiment 3 due to the presence of dislocations close to the diffusion zone.

Precipitation Experiments

Initial Microstructures

A number of differences were observed in the microstructures of the samples which underwent the different heat treatments (as described in Chapters Three and Four). Before describing the differences between heat treatments (a) and (b), it is useful to discuss the differences observed between the early samples that also underwent heat treatment (a) (Figure 4.5) and those used to obtain quantitative measurements (Figure 3.4(a)). The finer microstructure obtained in the later experiments (grain size of the order of 100 µm compared to 160 µm) is likely a result of the larger strains imposed during the cold rolling of the alloy rod prior to the precipitation heat treatment (*i.e.*, a 95% reduction as opposed to a 50% reduction); that is to say that the highly deformed structure provided a large number of sites for nucleation of the θ phase. Once these nuclei achieve critical size they continue to grow until equilibrium is achieved. A lower number of nucleation sites would therefore be present in the earlier samples, resulting in the coarser structure. It should be noted that although the distribution of precipitates obtained in the earlier samples seems ideal for inducing LFM (*i.e.*, located predominantly along the grain boundaries), the samples were too thick to be sure that the temperature was constant throughout.

As was discussed in Sections 3.4.4 and 4.3.2, volume fraction measurements of the second phase as a function of time were performed. The presence of liquid within the grain interiors (heat treatment (a)) complicates the analysis of the disappearance of grain boundary liquid which predominantly occurs by LFM. As a result heat treatment (b) was performed. By starting the precipitation at 480 °C it was expected that relatively few nuclei would form, and only at preferred sites such as on the grain boundary. Slow cooling to 400 °C would then cause further growth only at the surface of precipitates already present. The presence of the large faceted (Widmanstätten) precipitates in the microstructure observed (Figure 3.4(b)) indicates that as expected, relatively few nuclei were formed at the higher temperature. However, the nuclei were formed within the grain interiors, not at the grain boundaries as expected. This will therefore adversely affect the chance of initiating LFM in samples formed by heat treatment (b). Although the strains imposed during the cold rolling of the alloy rod prior to heat treatment (b) were the same as those imposed prior to heat treatment (a) (*i.e.*, a 95% reduction), the resulting grain size was much larger. This can be attributed to the long period of time the sample was held at the higher temperature of 480 °C (approximately one week); significant grain growth must have occurred before any significant precipitation. One possibility is that the temperature was such that the bulk composition of the alloy lies in the one-phase (Al) region of the phase diagram; precipitation would then occur as the sample was slowly cooled to 400°C.

Salt Bath Experiments - Morphologies

The microstructures obtained during liquation of the θ precipitates present in the alloy following heat treatments (a) and (b) are discussed in this section. In the case of heat treatment (a) (Figures 4.6 to 4.14) the grain-boundary lenses were observed first to rapidly bow out (as indicated in Figure 4.44), and then often to stabilize as crescent-shaped pools of liquid; on average the shape stabilized after only 7 seconds at the experimental temperature. In later stages, these crescents gradually solidified at a rate determined by the rate at which solute was carried away by solid-state diffusion. In this regard, their behaviour resembled that of the intragranular pools; these small approximately spherical pools of liquid were observed to form within the grain interiors from the liquation of the intragranular θ phase. The spherical shape stems from the isotropic nature of the solid - liquid interfacial energy (σ).

In most of the micrographs, it can be seen that liquid lenses present along any particular grain boundary of the sample generally migrate in one direction only. This can be attributed to the differences between the elastic moduli of grains separated by the liquid films; *i.e.*, the grain into which migration occurs will likely possess the higher value of the biaxial elastic modulus (Y(**n**)). In other cases, for instance along grain boundaries shown in Figures 4.6, 4.11(b), and 4.12(b), LFM can be observed to occur into both of the grains that the liquid film separates. In these cases it is likely that coherency was lost in one of the grains prior to the initiation of migration as a result of the presence of pre-existing dislocations close to the solid - liquid interface which may accommodate the misfit. It can therefore be seen that loss of coherency plays an important role in determining the direction in which migration occurs; *i.e.*, it is possible for migration to occur into the grain with the lower Y(**n**) provided that this grain remains coherent and the other does not.

The LFM events present along the right hand segment of the grain boundary visible in Figure 4.8 apparently possess greater curvatures and have migrated further than most other events; this is due to the sectioning problem described in Section 3.4.5. The grain boundary in this case lies at a significant angle to the surface of the sample, the two - dimensional view of these events is therefore far from the defined 'true' cross section. LFM events possessing very narrow liquid films can be seen in Figure 4.9; these events have migrated a distance that is approximately twice that of most others (8.5 μm as opposed to an average of 4.5 μm for early heat treatment (a) samples), but do not possess the curvature of those in Figure 4.8. The interpretation of these observations in terms of model predictions are discussed later in this chapter. The average migration distances obtained from the 15 second sample which underwent the early version of heat treatment (a) are larger than those obtained from the 15 second sample from the later heat treatment (a) (*i.e.*, $Z_{LEAD} = 4.5$ μm and $Z_{TRAIL} = 2.1$ μm as opposed to $Z_{LEAD} = 3.6$ μm and $Z_{TRAIL} = 1.3$ μm). These differences are due predominantly to the initial size of the precipitates present prior to liquation, and the temperature of the salt bath (558°C as opposed to 560°C), which as was shown in Section 6.3.2 (Figure 6.10) can lead to significant differences in migration behaviour. The general shape of the LFM events appears to be much the same in both treatments; the migration distances and the distance between pinning points from the early heat treatment are larger, but the curvature of the interfaces are similar. A net curvature ($K_{LEAD} - K_{TRAIL}$) of 0.11 μm^{-1} was calculated for the 15 second sample from the earlier heat treatment (a) as opposed to 0.20 μm^{-1} for the 15 second sample that underwent the later heat treatment (a). These observations and calculations (same order of magnitude) are consistent with the prediction that LFM is arrested once the liquid film achieves a critical curvature.

From the measurements of the volume fraction of the liquid phase for the case of heat treatment (a) (Figure 4.21(a)) it can be seen that the volume fraction reaches a peak in the range of 7 to 10 seconds. Since a few LFM events can be seen at a time of 3 seconds (1.5 seconds after liquation) (Figure 4.10), it appears that LFM has already initiated prior to full liquation of the θ phase; the coherent zone that drives the migration must therefore develop as the θ precipitates liquate. A more complete discussion of the volume fraction measurements is contained in the following section.

As indicated in Figure 3.4(b) the initial microstructure for heat treatment (b) is dominated by large Widmanstätten plates of the θ phase. On liquation, these plates gave rise to disc-shaped liquid pools, which evidently did not migrate; instead, their rims were observed to cylinderize, as a (presumed) first stage of spheroidization, suggesting that (as expected) the solid-liquid interfacial energy is much more isotropic than that of the Widmanstätten precipitate interface. The absence of any indication of LFM in these cases might be ascribed to the rather symmetric diffusion profile (and the consequent symmetric elastic field) which is to be expected during the diffusional solidification of a planar intragranular liquid film in a defect-free crystal. Viewed in this light, the migration of grain boundary lenses, as observed after liquation of samples initially subjected to heat treatment (a), can be considered a consequence of the lack of symmetry of the typical grain boundary precipitate environment. This is in turn consistent with the idea that crystalline anisotropy is responsible for the initiation of the migration process; more specifically that the anisotropy of $Y(\boldsymbol{n})$ determines the direction of initial migration.

In most cases any precipitates located along one of the few grain boundaries of the samples from heat treatment (b) formed very thick regions of liquid; as a result, solute transport across the liquid film was most likely too slow for coherency to be maintained ahead of the migrating interface, and no migration occurred. In rare cases where the liquid films formed were thin enough* that coherency would be maintained (at least in the early stages), LFM did occur. Figures 4.17, 4.18, and 4.19 each show at least one LFM event.

It is obvious from these experiments that the initial microstructures that develop during the precipitation heat treatments have a strong effect upon the subsequent liquation behaviour.

---

* From the results of heat treatment (a), this appears to be less than 5 μm.

However, once the initial microstructure has been formed, the liquation experiments are reproducible. Ideally, a thin sample ($\approx$ 0.5 mm thick) with the θ phase distributed as small precipitates located predominantly at the grain boundaries should be used to induce LFM.

Salt Bath Experiments - Volume Fraction Measurements

The volume fraction measurements for the relative amount of the liquid phase with time for heat treatments (a) and (b) are shown in Figures 4.20 and 4.21. The general shape of the volume fraction plots for both heat treatments is approximately the same; *i.e.*, after an initial increase in the volume fraction, ascribed to the increase in volume upon liquation of the θ precipitates, the volume fraction decreases with time as the liquid phase solidifies. This is as expected since the equilibrium state for the alloy at 560°C is a one-phase solid (Al). These plots indicate as expected that the liquid phase undergoes an isothermal diffusional solidification. After cessation of LFM (heat treatment (a)), the liquid phase will solidify at a rate determined by the removal of solute from the liquid phase through solid-state diffusion. There are many similarities between this process and joints made using the transient liquid phase bonding (TLP) technique: in both cases there is a dissolution of a region rich in solute, followed by the isothermal solidification of the liquid region. A study of TLP in a model system (simple eutectic) was performed by Tuah-Poku *et al.* [70]. Using the silver - copper system, they assembled Ag / Cu / Ag joints, which were held at a temperature slightly above the eutectic temperature until the samples fully solidified. The dissolution and subsequent solidification behaviour is therefore very similar in principle to the liquation and solidification that occurred in the LFM experiments presented in this thesis. The results of their study indicate that the width of the liquid region decreases with time in a similar manner to the liquid volume fraction in the samples obtained from heat treatments (a) and (b). In principle, it should therefore be possible to apply their analysis to the isothermal solidification stage of liquid removal in the LFM experiments. However, due to the complicated geometries involved, this was not attempted.

The differences between the solidification behaviour of the liquated samples resulting from heat treatments (a) and (b) (Figures 4.20 and 4.21) can be attributed to the differences in the initial microstructures. In the case of heat treatment (a), it can be seen that the sample was fully solidified approximately 1000 seconds after insertion into the salt bath as opposed to approximately 2700 seconds for heat treatment (b). The larger regions of liquid present in the case of heat treatment (b) require longer to solidify since the removal of solute through solid-state diffusion is the rate limiting process in this stage. The smaller regions of liquid present in the case of heat treatment (a) therefore solidify more rapidly. This is assisted by the fact that the solid solubility increases with increasing curvature of the solid - liquid interface (through the Gibbs - Thompson effect); this results in a larger concentration gradient in the solid phase for the removal of solute.

Salt Bath Experiments - SEM

Micrographs of several events (Figures 4.22 to 4.32) and the associated three-dimensional reconstructions of selected LFM events are presented in Chapter Four (see Figures 4.34 to 4.43). It can be deduced from the reconstructions that regions of liquid that form upon liquation of the θ precipitates spread out along the grain boundaries; these regions are generally thin when viewed perpendicular to the grain boundary, and roughly elliptical in the plane of the grain boundary. If these liquid regions are oriented such that LFM is favourable, the LFM events which form will be more closely approximated by cylinders than spheres. It is also evident from these reconstructions that although the liquid film may have an almost perfect crescent shape indicative of LFM on a particular level, the apparent (two-dimensional) liquid morphology may be quite different on a subsequent level (see Figures 4.36, 4.42, and 4.43). However, it is clear that in all cases the lenses are seen to bow against their curvature, and that in most cases, the events have one radius of curvature considerably greater than the other (*i.e.*, $\rho_{TRAIL} > \rho_{LEAD}$).

As described in Section 4.3.3, the information provided by the three-dimensional reconstructions are therefore semi-quantitative illustrations of the general morphology trends of migrating liquid films in a polycrystalline aluminum - copper alloy.

7.3 DISCUSSION OF MODELLING

Good model predictions were obtained for the positions of the leading and trailing interfaces as a function of time. The predictions shown Figures 6.6 and 6.7 indicate that the material parameters can be adjusted so that the predictions closely match the experimental measurements; this indicates that the energies assumed to drive the migration process appear to be of the correct order of magnitude. Given the assumptions made concerning the spherical geometry of the liquid lenses, the simulations are intended to be a semi-quantitative guide to aid in the interpretation of experimental observations. However, it is clear from the simulations (see Figures 6.6 to 6.12) that the details of the migration process, once it is established, are sensitive to the values assigned to the experimentally controllable quantities, such as the temperatures of initial equilibration and of liquation, and to the intrinsic system parameters, such as the elastic properties of the (Al) phase at temperature and the solid-liquid interfacial free energy.

The model predictions shown in Chapter Six (Figures 6.6 to 6.12) were obtained assuming spherical curvature of the leading and trailing interfaces. However, from the three-dimensional reconstructions of the liquid lenses (Figures 4.34 to 4.43), it can be seen that the morphology of the events is generally more closely approximated by cylindrical rather than spherical geometry. Simulations based upon the assumption of cylindrical curvature indicate that the energy due to curvature is insufficient to stop the migration process, assuming that the leading solid phase remains fully coherent. Using measurements obtained directly from the SEM micrographs of several events (t = 15 seconds), the average energy due to curvature opposing migration ($= \sigma V_m (K_{LEAD} - K_{TRAIL})$) was calculated to be approximately 0.2 (J mol^{-1}), where $\sigma = 0.1634$ (J m^{-2}) [64], $V_m = 1 \times 10^{-5}$ (m^{3} mol^{-1}), and K_{LEAD} and K_{TRAIL} are the measured curvatures of the leading and trailing interfaces respectively ($=1/\rho_{LEAD}$ and $1/\rho_{TRAIL}$ for cylindrical geometry). Using Equation (2.1) ($\times V_m$), the coherency strain energy was calculated to be approximately 2.5 (J mol^{-1}), *i.e.*, the coherency strain energy is an order of magnitude larger than the energy due to curvature. From these calculations, it is evident that the solid phase in advance of the migrating liquid film does not remain fully coherent during the migration process. Referring to Figures 6.6 to 6.12, it can be seen that all predictions pass through the first data point (*i.e.*, 1.5 seconds after liquation); this is also generally the case for simulations based upon the assumption of cylindrical curvature. It therefore seems likely that the leading solid phase remains coherent during the very early stages of migration (at least for the first 1.5 seconds). Once the overall curvature of the interfaces becomes significant (*i.e.*, for $Z_{TRAIL} > 0$), coherency is lost and the liquid films become immobile. The following section discusses the coherency loss process in more detail.

Coherency Loss in the Leading Solid

This section evaluates the applicability of the Matthews analysis [47] (described in Section 6.2.8) to the loss of coherency in the leading solid during LFM. This analysis was developed for the growth of epitaxial thin films on massive substrates, in order to obtain an estimate of the critical film thickness for coherency loss ($\equiv L_C$). The critical thickness (L_C) is obtained by minimizing the sum of the misfit dislocation energies and the elastic energy due to coherency strain. That is to say that, for $L < L_C$, where L is the film thickness, the thin layer will be elastically strained such that it matches the substrate exactly (*i.e.*, fully coherent). For $L > L_C$, it is energetically favourable for the misfit to be accommodated by a grid of misfit dislocations (with the correct Burger's vectors, spacing and orientation) rather than remain coherent.

It can be seen that there are many differences between the case analysed by Matthews [47] and the case of a solute diffusion field ahead of a migrating solid - liquid interface:

- In the epitaxial growth case it is assumed that the change in solute concentration is accommodated by a concentration step located at the substrate - thin film interface; the resulting strain energy is then a linear function of the film thickness. In LFM the change in concentration in advance of the migrating liquid film will be distributed over a concentration gradient; the strain energy in this case will therefore be highest close to the solid - liquid interface rather than at the substrate - thin film interface.

- In the case of epitaxial growth, any dislocations that are created will be located (initially) at the substrate - thin layer interface (as indicated in Figure 6.3), while in LFM dislocations will likely form close to the solid - liquid interface.
- The position of the substrate - film interface is assumed to be fixed in the epitaxial growth case, whereas the position of the 'substrate - film' interface (according to the Matthews definition) during LFM varies with time, and is a function of the liquid film velocity, v. This is discussed in more detail below.

The solute diffusion field (C_S) ahead of the leading solid - liquid interface moving at a steady velocity, v, with a concentration ($C_{S,LEAD}$) maintained at the interface, is identical to that for the liquid zone at the solidification front in a multicomponent system. The solution is [71,72]:

$$C_S(z) = (C_{S,LEAD} - C_0) \exp\left(-\frac{z}{(D_S/v)} \right) + C_0 \tag{7.1}$$

Where:

D_S Lattice Diffusivity (see Section 6.2.7)

C_0 Solute concentration of the parent phase

This expression is plotted for a few appropriate values of D_S/v in Figure 7.1. The effective solute penetration distance in the dissolving grain is therefore given by the decay constant D_S/v (as was introduced in Section 2.4.2).

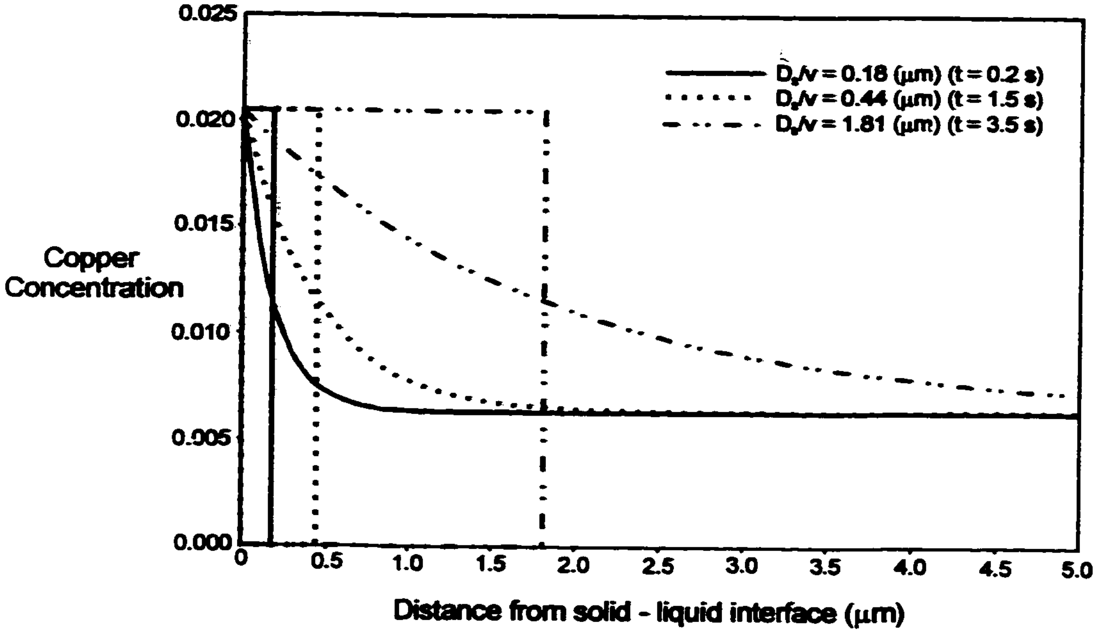

Figure 7.1: Concentration Profiles For Different D_S/v Values (Obtained Using Equation (7.1)).

Previous attempts to model the loss of coherency ahead of migrating liquid films have simply compared the effective solute penetration distance (D_S/v) to the critical thickness (L_C) calculated using the analysis of Matthews [47] described above; if $D_S/v < L_C$ coherency is assumed to be maintained, and if $D_S/v > L_C$ it is energetically favourable for the misfit to be accommodate by dislocations. Implicit in the application of Matthews' analysis to the LFM process is the assumption that all solute present in the leading solid with a composition above that of the parent phase is contained within a concentration step of magnitude ($C_{S,LEAD} - C_0$), extending a distance D_S/v into the leading solid phase. Figure 7.1 also illustrates the equivalent concentration steps for the D_S/v values used to generate the concentration profiles shown (through Equation (7.1)). For a given D_S/v value, it can be seen that the total amount of solute in the gradient region is equal to that present in the concentration step (*i.e.*, the area under each curve is equal).

Application of the Matthews analysis to LFM in the aluminum - copper system, requires values of D_S/v be known as a function of time. Since the predicted instantaneous velocity was calculated during application of the kinetic model developed in Chapter Five, it was possible to obtain plots of D_S/v as a function of time for several sets of parameter values. Using the calibrated parameter values listed in Table 6.4 (predicted migration distances shown in Figure 6.7), the D_S/v plot indicates that, as expected, D_S/v increases rapidly with time with a value of 0.18 μm, 0.2 seconds after liquation. Comparison of these values with L_C (= 0.029 μm) or to 5*L_C (=0.15 μm)[**] indicate that according to this criterion, coherency should be lost within the first 0.2 seconds. If this were true, no LFM due to coherency strain effects would be observed; however, as shown in this thesis extensive LFM occurred in most samples. It can therefore be postulated that this criterion is insufficient in describing coherency loss in the aluminum - copper system, indicating that in this case (moving interface, high misfit system) coherency loss is far from a simple process.

In order to determine criteria for the loss of coherency when the solute distribution is assumed to be given by Equation (7.1), the total energy due to coherency in the gradient region at any instant in time must be compared to the energy of a grid of misfit dislocations. With the solute concentration profile in the diffusion zone given by Equation (7.1), the equations for the coherent elastic strain ($\epsilon(z)$), and coherency strain energy density ($E_\epsilon(z)$) are given by:

$$\epsilon(z) = \eta(C_S(z) - C_0) = \eta(C_{S,LEAD} - C_0)\exp\left(-\frac{z}{(D_S/v)}\right) \qquad \textbf{(7.2)}$$

$$E_\epsilon(z) = Y(\mathbf{n})(\epsilon(z))^2 = Y(\mathbf{n})\eta^2(C_{S,LEAD} - C_0)^2\exp\left(-\frac{2z}{(D_S/v)}\right) \qquad \textbf{(7.3)}$$

[**] The multiple of 5 is to account for the kinetics of forming new dislocations at the 'substrate - thin layer' interface (slow).

Where:

$Y(\mathbf{n})$ Biaxial Elastic modulus (see Section 6.2.4)

η Solute misfit parameter (see Section 6.2.5)

The coherency strain energy density given by Equation (7.3) as a function of the distance from the leading solid - liquid interface is illustrated in Figure 7.2, obtained using the calibrated parameter values listed in Table 6.4. Predicted D_S/v values of 0.18 μm, 0.44 μm, and 1.81 μm were used to generate these plots corresponding to times of 0.2 seconds, 1.5 seconds, and 3.5 seconds from liquation, respectively. It can be seen that most of the strain energy is concentrated in a narrow region near the solid - liquid interface (especially for shorter times).

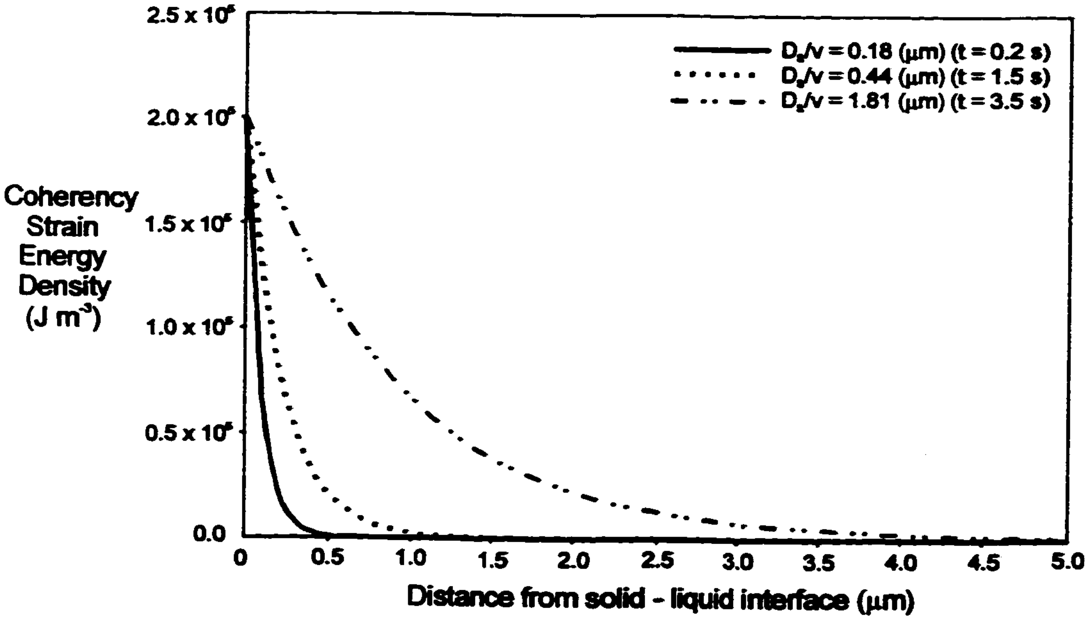

Figure 7.2: Coherency Strain Energy Density As A Function of Distance From the Solid-Liquid Interface (Obtained Using Parameters Listed in Table 6.4).

The total energy in the gradient region was obtained by integrating the energy density function (Equation (7.3)) between $z = 0$ (solid - liquid interface) and $z = \infty$. This was performed for each D_S/v value, and the results plotted as a function of D_S/v in Figure 7.3. The total energy due to the equivalent concentration step is also shown; this was calculated by integrating the strain energy in this region ($=Y(n)\eta^2 (C_{S,LEAD} - C_0)^2$) between $z = 0$ and $z = D_S/v$. The energy of a grid of misfit dislocations shown in the figure was calculated using Equation (6.11); application of this equation assumed that the misfit was completely accommodated by dislocations with the cut-off for the dislocation strain field (r) assumed to be half the dislocation spacing. A value of 0.012 Jm^{-2} was obtained.

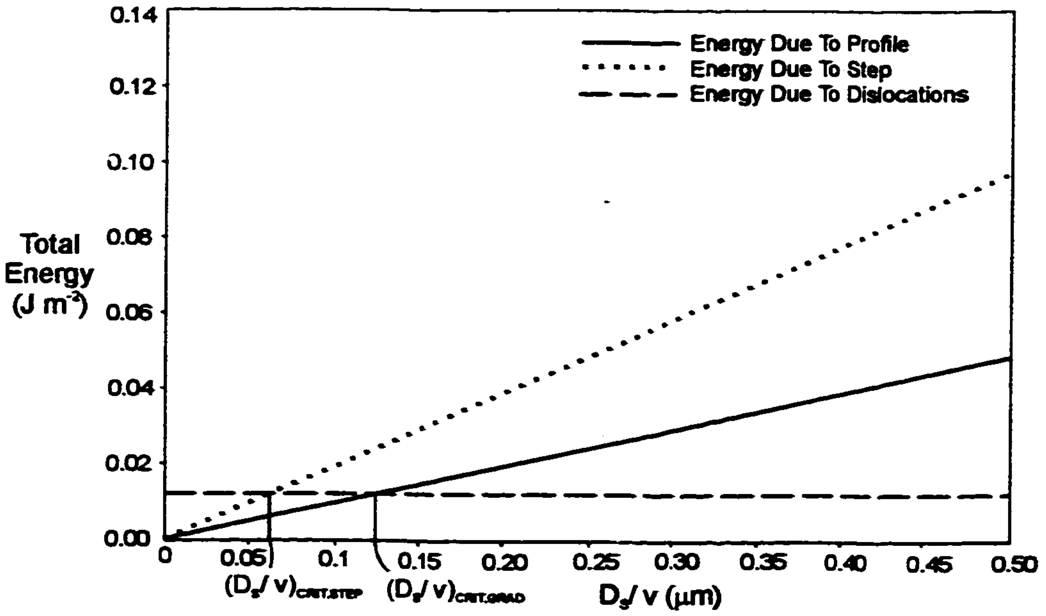

Figure 7.3: **Total Profile and Step Energies As A Function of D_S/v (Obtained Using Parameters Listed in Table 6.4). The Energy of A Grid of Misfit Dislocations is Also Shown.**

It can be seen from Figure 7.3 that the total energy of the solute enriched regions in both the gradient and step approximations increases linearly with D_S/v; this is due to the spreading out of the diffusion profile as the velocity of the liquid film decreases (see also Figure 7.1). The total strain energy due to the concentration gradient is one-half that due to the 'equivalent' step region; the same result is evident from simulation results obtained using parameter values listed in Table 6.2 (predictions shown in Figure 6.6). Loss of coherency is energetically favourable when the total energy due to coherency in the solute enriched region is greater than the energy of the grid of misfit dislocations. For the case of the gradient approximation, this can be seen to occur at a critical D_S/v value of $(D_S/v)_{CRIT} = 0.12$ µm. For the step approximation, a critical D_S/v value of $(D_S/v)_{CRIT,STEP} = 0.06$ µm is obtained. This result indicates that any prediction of coherency loss based on the assumption of a step change in concentration will lead to an underprediction of the critical D_S/v value by a factor of two. It should be noted that the exact values for the critical D_S/v values will change slightly with changes to the model parameters used to generate the D_S/v data; however, the result that $(D_S/v)_{CRIT} = 2*(D_S/v)_{CRIT,STEP}$ holds true in all cases. Noting this result, a modified version of the method used by Matthews [47] described in Section 6.2.8 can be applied. In this case the energy associated with the elastic strain (ϵ) can be assumed to be one-half that given by Equation (6.9). Minimizing the sum of the misfit dislocation energies and the total elastic energy due to coherency strain with respect to ϵ, and solving for the critical thickness (L_C), yields a value of 0.066 µm; a value which is approximately twice that obtained using a direct application of Matthews' analysis. This is the distance at which the formation of dislocations becomes energetically favourable; the calculation implies that the misfit is not fully relaxed (*i.e.*, an equilibrium elastic strain remains). Comparing the modified value of L_C to the critical D_S/v (*i.e.*, $(D_S/v)_{CRIT} = 0.12$ µm, calculated assuming full coherency loss), it can be seen that there is a range of diffusion distances over which it is energetically favourable for loss of coherency to occur. This implies that LFM may occur when the leading solid retains only partial coherency; that is, there still exists an elastic driving force for as long as the misfit is not fully relaxed.

From the preceding discussion it can be concluded that approximating the diffusion gradient by a concentration step of width D_S/v will lead to premature prediction of coherency loss. Predictions for the critical D_S/v value can be obtained using the method described earlier in this section. That is:

1. The total coherency strain energy in the gradient region is determined through integration of Equation (7.3) for several appropriate D_S/v values (obtained from model simulations for a given set of parameter values).
2. The total energy as a function of D_S/v is plotted, as well as the energy of a grid of dislocations with the correct Burger's vector, spacing and orientation to accommodate the misfit.
3. The critical D_S/v value for coherency loss is determined graphically at the point where the two curves are equal. It should be noted that this is purely an energetic criterion, the kinetics of dislocation nucleation should also be known in order to predict coherency loss with any precision.

For the conditions used to generate Figure 7.3, a critical D_S/v of 0.12 μm was obtained (this is an order of magnitude larger than obtained using the Matthews analysis). This indicates that it is energetically favourable for misfit dislocations to be present for all times using the parameter values listed in Table 6.4 (Figure 6.7), *i.e.*, for a time of 0.2 seconds, a D_S/v value of 0.18 μm was predicted, and for a time of 1.5 seconds, a D_S/v value of 0.44 μm was obtained. However, unlike the L_C criterion, these values are of the same order of magnitude as the critical D_S/v.

It is evident from this study that at all times investigated during the migration process, it is energetically favourable for the misfit to be accommodated by dislocations rather than remain coherent. However, as the results of this thesis make clear, significant migration does occur in this system, indicating that the leading solid phase must maintain some degree of coherency in the very early stages of migration. This implies that there must be a kinetic limitation to the formation of a grid of misfit dislocations. If dislocations do form, they will do so in the region of the highest strain energy; as can be seen from Figure 7.2, most of the strain energy is accumulated in the region close to the solid - liquid interface. It is hypothesized that in the early stages of migration the velocity of the leading interface is such that dislocations do not have time to equilibrate with the highly stressed region before the region is swept by the leading solid - liquid interface. As the velocity decreases (due to the increasing curvature of the solid - liquid interfaces), the diffusion profile will spread out as indicated in Figure 7.1, resulting in an increase in the total energy contained in the gradient region. As a result, both the driving force and the time available for the formation of dislocations will increase, and loss of coherency will likely occur. From the experimental and modelling results (Figure 6.7), it appears that loss of coherency occurs approximately 1.5 seconds after liquation.

In reality, dislocations which form will be distributed over the concentration gradient, rather than in a grid. Since coherency loss in a moving frame of reference (*e.g.*, LFM) depends on the velocity of the migrating interface, the climb rate of any dislocations that form along this gradient is of interest. A reasonable expression for the climb rate of an edge dislocation in the presence of a stress, σ_{xx}, is given by [73]:

$$v = \frac{D_S \, V_a \, \sigma_{xx}}{b \, k_B \, T} \tag{7.4}$$

Where:

V_a Atomic volume (m)

k_B Boltzmann's constant

Since the biaxial stress (σ_{xx}) varies with distance from the solid - liquid interface (given by $Y(n) \cdot \eta \cdot (C_S(z) - C_0)$), the climb rate of any dislocation that forms also varies with distance from the interface. Figure 7.4 illustrates the climb rate of an edge dislocation as a function of the distance from the solid - liquid interface for a few D_S/v values. It can be seen that the climb rate decreases very rapidly with distance initially, reaching zero velocity at some specified distance from the solid - liquid interface. This implies that for a given D_S/v value, any dislocation nucleated close to the solid - liquid interface will climb away until it reaches a position where the climb rate is zero. Any dislocations formed in the highly stressed region will therefore eventually move to the position of zero climb rate. As the velocity of the liquid film decreases (increase in D_S/v), the position of zero climb rate moves further from the solid - liquid interface. The results of this analysis indicate that the assumption that misfit dislocations are present in a grid is a reasonable approximation.

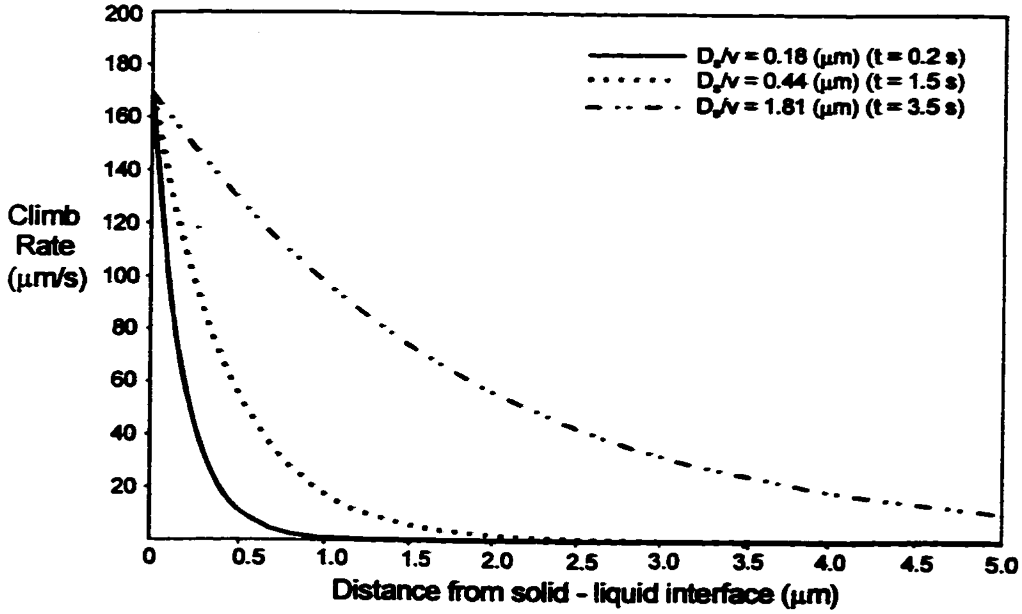

Figure 7.4: Climb Rate of An Edge Dislocation As A Function of Distance From Solid - Liquid Interface (Obtained Using Equation 7.4).

Since the diffusion of solute across the liquid film is taken to be the rate-determining process, it would be expected that very thin liquid films will migrate at high velocities. If the film is thin enough, the velocity may be such that D_S/v is always less than the critical D_S/v for the nucleation of misfit dislocations. As a result, coherency may never be completely lost in the dissolving grain, thus maintaining the driving force for migration. Thicker liquid films would be expected to migrate at a velocity high enough that during the initial stages coherency is maintained. However, as the curvature of the interfaces increases, the film will be slowed down sufficiently that D_S/v becomes greater than the critical D_S/v for the nucleation of misfit dislocations, and at least a partial loss of coherency will likely occur in the dissolving grain. If the concentration profile in advance of the migrating interface were approximated by a concentration step ($C_{S,LEAD}$ - C_0), and the misfit accommodated by a planar grid of misfit dislocations, the calculated energy due to the dislocation wall (using Matthews [47]) at the position of the interface would be approximately 0.2 (J mol^{-1}). This value is approximately equal to the energy due to curvature, but whereas the energy due to curvature acts so as to oppose migration, the energy due to the dislocation wall should act in the migration direction. This is consistent with the experimental observations that the liquid films become immobile (no reversal of migration) once loss of coherency occurs.

Figure 4.9 shows a micrograph of a sample exposed to a temperature of 558°C for 15 seconds. Two LFM events can be seen, both of which have migrated a distance approximately twice the average distance travelled by other events. It is also evident that the liquid films are very thin. These observations can be explained in terms of the critical solute penetration distance (D_S/v) described above. Apparently, these films were thin enough to have migrated at a sufficiently high velocity to maintain coherency in the leading solid (*i.e.*, $D_S/v < (D_S/v)_{CRIT}$). That is to say, the energy of the coherent region must have been sufficient (in this case) to overcome the increasing energy due to curvature to a point where the liquid film collapsed to form a grain boundary. Most other events were thicker than those shown in Figure 4.9. As a result, coherency was likely lost in advance of the leading interface once the energy due to curvature was sufficient to slow the migration down such that D_S/v

$>(D_S/v)_{CRIT}$.

In spite of the small thermodynamic driving forces involved, the process takes place at relatively high speeds. This is ascribed to the very high rate of diffusion in the liquid state, which is taken to be the rate-determining process. Even in the absence of a large concentration difference across the film (converted into a concentration gradient by dividing by the film thickness), the rate of liquid state diffusion is sufficient to drive a typical micron-thick liquid lens at velocities of the order of microns per second, which is very large in comparison with expected rates of block phase translation in solid-solid systems.

The model developed in this thesis was compared to the Yoon *et al.* [7] model for LFM as described in Section 6.4. Results obtained using the Yoon model indicate that positions of the leading and trailing solid - liquid interfaces are always overpredicted (predictions do not pass through the first data point); predictions are also relatively insensitive to changes in parameter values such as the interfacial free energy and the elastic modulus of the leading solid. The calculated energy due to curvature (using the spherical curvature approximation) was insufficient to stop LFM. As was discussed in detail in Section 2.6, the development of the equations for the concentration difference across the liquid film, and its subsequent velocity, required that many assumptions be invoked. Several of these assumptions are not applicable to the aluminum-copper system. For instance, the assumption that the change in solid solubility resulting from the presence of the coherency strain field is small is invalid for the Al-Cu system; a 5.36% difference in solid composition was calculated in Section 6.3.1. As described in Section 6.4, the calculation of the energy due to curvature is ambiguous in the early stages of LFM when the liquid films are formed from the liquation of grain boundary precipitates. The velocity expression used by Yoon makes no account for the loss of solute from the liquid phase to the growing solid phase; this expression is therefore only valid in cases where the solute distribution coefficient (k) is very small.

The model presented in this thesis requires fewer assumptions than the Yoon model in the calculation of the concentration difference across the liquid film; the incorporation of the energy due to curvature can be accomplished without ambiguity in all stages of migration. The model also provides a reasonable interpretation of the experimental measurements of migration distances in the aluminum - copper system consistent with the coherency strain hypothesis. This modelling approach can be applied to the study of LFM in other alloy systems provided that accurate representations of the free energies of the solid and liquid phases are available.

A final point: In assessing the literature on LFM, it is often tempting to think of a liquid film as a single interface, and to pursue the analogy with the motion of grain boundaries which respond to a lateral chemical gradient by migrating, as in DIGM. As the current work makes clear, the liquid film is best described as a pair of interphase interfaces. These interfaces are distinct, although coupled during migration by thermodynamic and kinetic factors. The pair is capable of moving in the absence of a lateral concentration gradient. The analogy, although pleasing, is flawed, or at best, incomplete.

CHAPTER EIGHT

CONCLUSIONS AND RECOMMENDATIONS

8.1 SUMMARY AND CONCLUSIONS

The results of this investigation are:

- The initial microstructures that develop during the precipitation heat treatments are sensitive to previous mechanical and heat treatments. These microstructures have a strong effect upon the morphologies that result from subsequent liquation. The liquation experiments are reproducible in each case once the initial structure has formed.

- Intergranular liquid lenses formed on liquation of previously equilibrated grain boundary θ precipitates are observed first to rapidly bow out against their curvature, and are then slowed by capillary forces as the curvature of the solid - liquid interfaces increases, finally stabilizing as crescent-shaped pools of liquid. For an average LFM event the shape stabilizes after 7 seconds at the experimental temperature. In later stages, these crescents gradually solidify at a rate determined by the rate at which solute is carried away by solid-state diffusion.

- Intragranular liquid films, formed on melting of previously equilibrated Widmanstätten θ plates in an Al-Cu alloy, do not migrate, but tend to cylinderize at their edges. These regions of liquid eventually solidify at a rate determined by solid-state diffusion. The lack of any evidence for migration of these films is seen as a consequence of the symmetry of the diffusion fields (and by implication the coherency strain fields) in the adjoining solid crystal.

- In all precipitation type experiments it was observed that after an initial increase in the volume fraction, ascribed to the increase in volume upon liquation of the θ precipitates, the volume fraction decreases with time as the liquid phase undergoes an isothermal diffusional solidification. The fact that this maximum value occurred after the first LFM event was observed (for heat treatment (a); *i.e.*,1.5 seconds from liquation), indicates that LFM must initiate prior to full liquation of the θ phase.

- It can be deduced from the three-dimensional reconstructions of LFM events that in many cases liquid regions that form upon the liquation of grain boundary θ precipitates spread out along the boundaries; these regions are thin when viewed perpendicular to the grain boundary, and roughly elliptical in the plane of the grain boundary. If these liquid regions are oriented such that LFM is favourable, the morphology of the LFM events that are formed will be more closely approximated by cylindrical rather than spherical curvature, although the actual morphology lies somewhere between the two approximations.

- Although the diffusion couple experiments were found to be unsuitable for quantitative analysis, it should be noted that LFM did occur in each case, consistently into the grain not initially in equilibrium with the liquid phase; this is consistent with the coherency strain hypothesis.

- Good predictions for the positions of the leading and trailing interfaces as a function of time can be obtained using the model presented in this thesis, indicating that the assumed overall driving force (*i.e.*, coherency strain energy - energy due to curvature) is of the correct order of magnitude.

- Predictions were found to be sensitive to the values assigned to the experimentally controllable quantities (such as the temperatures of initial equilibration and of liquation) and to the intrinsic system parameters (elastic properties of the α phase at temperature and the solid-liquid interfacial free energy).

- Simulations based upon the assumption of cylindrical curvature indicate that the energy due to curvature is insufficient to stop the migration process, assuming that the leading solid phase remains fully coherent. It can be postulated that the solid phase in advance of the migrating liquid film does not remain fully coherent throughout the migration process.

- Studies of coherency loss ahead of the migrating liquid film indicate that direct application of Matthews' [47] analysis to LFM (used to determine the critical thickness for loss of coherency, L_C) is not appropriate. That is, any prediction of coherency loss based on the assumption of a step change in concentration will lead to an under prediction of the critical D_S/v value. For the case of a moving interface with the concentration difference more closely approximated by a gradient rather than a step, the Matthews' analysis underestimates the critical distance for loss of coherency by a factor of two (a direct result of the fact that the total energy due to the step approximation is twice that of the gradient approximation). A modified L_C calculation indicates that there is a range of diffusion distances over which it is energetically favourable for partial loss of coherency to occur. This implies that LFM may occur when the leading solid retains only partial coherency; that is, there still exists an elastic driving force for as long as the misfit is not fully relaxed.

- The results of this thesis indicate that migration of liquid films in the Al-Cu system is driven by coherency strain energy in the early stages of migration (first 1.5 seconds). As migration continues, the increasing energy due to curvature decreases the overall driving force for LFM. Once the D_S/v value ahead of the migrating film reaches the critical $(D_S/v)_{CRIT}$ value, it becomes energetically favourable for the misfit to be accommodated by dislocations. It is hypothesized that in the early stages of migration the velocity of the leading interface is such that dislocations do not have time to equilibrate with the highly stressed region before the region is swept by the leading solid - liquid interface. This kinetic barrier to the formation of dislocations implies that coherency may not be fully lost until the velocity of the liquid film is slowed sufficiently to allow complete loss of coherency (*i.e.*, as the solute diffusion field spreads out). The partial loss of coherency decreases the overall driving force, leading to a further reduction of the film velocity. Liquid films become immobile once complete loss of coherency occurs (no reversal of migration).

8.2 RECOMMENDATIONS FOR FURTHER WORK

There are several interesting applications of the kinetic model developed in this thesis. The use of the direct common tangent method in particular has applications to any case where the compositions of phases in local equilibrium have a direct influence on the kinetics of a process. A few possible applications are described below:

- The model could be applied to other alloy systems where LFM has been observed resulting from the liquation of grain boundary precipitates. Knowledge of the free energy expressions of the appropriate solid and liquid phases would be required.
- The direct common tangent method could be applied to the analysis of the transient liquid phase bonding (TLP) process. The solid and liquid compositions that define the boundary conditions for solute diffusion could be calculated directly for each instant in time. This would be especially useful in cases where an atomic misfit exists between solute and solvent.
- The calculation of equilibrium compositions using the direct common tangent method along with the appropriate mathematical software could possibly be applied to solidification research, provided that the free energy expressions of the appropriate solid and liquid phases are known. For instance, one could incorporate a heat balance into the problem in order to predict dendrite morphologies.

Other recommendations for further work:

- Determination of the three-dimensional morphology of liquid regions in other alloy systems that exhibit LFM.
- Further analysis of semi - coherent systems, specifically how to determine semi - coherent equilibria.

REFERENCES

1. D.N. Yoon and W.J. Huppmann, *Acta Metall.*, **27**, 973, (1979).
2. M. Hillert, *Met. Trans. A.*, **3**, 2729, (1972).
3. M. Hillert, *Scripta Metall.*, **17**, 237, (1983).
4. M.S. Sulonen, *Ann. Acad. Sci. Fenn.*, AVI, No.4 (1957).
5. M.S. Sulonen, *Acta Metall.*, **8**, 669, (1960).
6. M.S. Sulonen, *Acta Metall.*, **12**, 748, (1964).
7. D.N. Yoon, J.W. Cahn, C.A. Handwerker, J.E. Blendell, and Y.J. Baik, in "Interface Migration and Control of Microstructure", (ed. C.S. Pande, A.H. King, and J. Walter), p.19, ASM, (1986).
8. C.A. Handwerker, J.W. Cahn, D.N. Yoon, and J.E. Blendell in "Diffusion in Solids: Recent Developements", (ed. M.A. Dayananda and G.E. Murch), p.275, Metall. Soc. of AIME, Warrendale, Pa. (1985).
9. F.C. Larché and J.W. Cahn, *Acta Metall.*, **33**, 331, (1985).
10. M.S. Sulonen, *Z. Metallkd.*, **55**, 543, (1964).
11. W.A. Owczarski, D.S. Duvall, and C.P. Sullivan, *Weld. J.*, **45**, 145, (1966).
12. M. Klerk and E. Roeder, in "The Electron Microprobe", (ed. T.D. McKinly), p.642, Wiley, New York, (1966).
13. Ye S. Kucherenko, *Russ. Metall.*, **6**, 67, (1973).
14. Ye S. Kucherenko, *Phys. Met. Metallogr. (USSR)*, **39**, 815, (1975).
15. Y.D. Song, S.T. Ahn, and D.N. Yoon, *Acta Metall.*, **33**, 1907, (1985).
16. Y.J. Baik and D.N. Yoon, *Acta Metall.*, **33**, 1911, (1985).
17. Y.J. Baik and D.N. Yoon, *Acta Metall.*, **34**, 2039, (1986).

18. Y.J. Baik and D.N. Yoon, *Acta Metall.*, **35**, 2265, (1987).

19. W.H. Rhee and D.N. Yoon, *Acta Metall.*, **35**, 1447, (1987).

20. H.K. Kang, S. Hackney, and D.N. Yoon, *Acta Metall.*, **36**, 695, (1988).

21. K.R. Lee and D.N. Yoon, *Acta Metall. Mater.*, **40**, 107, (1992).

22. W.H. Rhee, Y.D. Song, and D.N. Yoon, *Acta Metall.*, **35**, 57, (1987).

23. W.H. Rhee and D.N. Yoon, *Acta Metall.*, **37**, 221, (1989).

24. Y.J. Baik and D.N. Yoon, *Met. Trans. A*, **18**, 151, (1987).

25. J.K. Kim and D.Y. Yoon, *Acta Metall. Mater.*, **42**, 913, (1994).

26. W.A. Kaysser and S. Pejovnik, *Z. Metallkd.*, **71**, 649, (1980).

27. T. Muschik, W.A. Kaysser, and T. Hehenkamp, *Acta Metall.*, **37**, 603, (1989).

28. M. Kuo and R.A. Fournelle, *Acta Metall. Mater.*, **39**, 2835, (1991).

29. E.I. Rabkin, B.B. Straumal, L.S. Shvindlerman, R.A. Fournelle, and W. Gust, *Scr. Metall. Mater.*, **26**, 901, (1992).

30. C.Y. Ma, W.Gust, and R.A. Fournelle, *Scr. Metall. Mater.*, **27**, 1235, (1992).

31. B. Radhakrishnan and R.G. Thompson, *Metall. Trans. A.*, **24**, 2773, (1993).

32. B. Radhakrishnan and R.G. Thompson, *Scripta Metall.*, **24**, 537, (1990).

33. R. Nakkalil, N.L. Richards, and M.C. Chaturvedi, *Scr. Metall. Mater.*, **26**, 1599, (1992).

34. R. Nakkalil, N.L. Richards, and M.C. Chaturvedi, *Acta Metall. Mater.*, **41**, 3381, (1993).

35. E.P. Butler and A.H. Heuer, *J. Am. Ceram. Soc.*, **68**, 197, (1985).

36. R. Chaim, A.H. Heuer, and D.G. Brandon, *J. Am. Ceram. Soc.*, **69**, 243, (1986).

37. J.E. Blendell, C.A. Handwerker, C.A. Shen, and N.D. Dang, in "Ceramic

Microstructures '86 - Role of Interfaces", (ed. J.A. Pask and A.G. Evans), p.541, Plenum Press, N.Y./London, (1987).

38. K.W. Chae, D.L. Chun, D.Y. Kim, Y.J. Baik, and K.Y. Eun, *J. Am. Ceram. Soc.*, **73**, 1979, (1990).

39. J.W. Jeong, D.N. Yoon, and D.Y. Kim, *Acta Metall. Mater.*, **39**, 1275, (1991).

40. Y.J. Baik and K.Y. Eun, *J. Am. Ceram. Soc.*, **74**, 1397, (1991).

41. H.K. Schmid, *J. Am. Ceram. Soc.*, **74**, 387, (1991).

42. J.W. Cahn, *Acta Metall.*, **9**, 795, (1961).

43. D.N. Yoon, *Ann. Rev. Mater. Sci.*, **19**, 43, (1989).

44. J.E. Hilliard, in "Phase Transformations", (ed. H.I. Aaronson), ASM, Metals Park, OH, p.497, (1970).

45. J.H. van der Merwe, *J. Appl. Phys.*, **34**, 117, 123, (1963).

46. W.A. Jesser and D. Kuhlmann-Wilsdorf, *Phys. Stat. Sol.*, **19**, 95, (1965).

47. J.W. Matthews, Misfit Dislocations in "Dislocations in Solids - Vol.2", (ed. F.R.N. Nabarro), North Holland, Amsterdam, (1979).

48. D.Y. Yoon, *Int. Mater. Rev.*, **40**, 149, (1995).

49. J.W. Cahn, J.D. Pan, and R.W. Baluffi, *Scripta Metall.*, **13**, 503, (1979).

50. R.W. Baluffi and J.W. Cahn, *Acta Metall.*, **29**, 493, (1981).

51. Y.J. Baik, J.K. Kim, and D.Y. Yoon, *Acta Metall. Mater.*, **41**, 2385, (1993).

52. Y. Brechet and G.R. Purdy, *Scripta Metall.*, **22**, 1629, (1988).

53. J.L. Murray, *Int. Metals Reviews*, **30**, 211, (1985).

54. J.E. Hilliard and J.W. Cahn, *Trans. Metall. Soc. A.I.M.E.*, **221**, 344, (1961).

55. M. Hillert, in "Lectures on the Theory of Phase Transformations", (ed. H.I. Aaronson), American Institute of Mining, Metallurgical and Petroleum Engineers

Inc., New York, p.1, (1975).

56. R.Hultgren, P.D. Desai, D.T. Hawkins, M.Gleiser, and K.K. Kelley, "Selected Values of Thermodynamic Properties of Binary Alloys", ASM, Metals Park, OH., (1973).

57. B.D. Cullity, "Elements of X-Ray Diffraction - Second Edition", Addison-Wesley Publishing Company, p.506, (1978).

58. C.J. Smithells, "Smithells Metals Reference Book", Butterworths, London, (1983).

59. C. Gault, P. Boch, and A. Dauger, *Phys. Stat. Solidi*, **A43**, 625, (1977).

60. M.A. Meyes and K.K. Chaula, "Mechanical Metallurgy", Prentice-Hall, New Jersey, p.209, (1984).

61. P.E. Armstrong, 'Measurement of Elastic Constants', in "Techniques of Metals Research" Vol.V, (ed. R.F. Brushaw), Interscience, New York, (1971).

62. G.E. Dieter, "Mechanical Metallurgy", 2nd Edition, McGraw-Hill, New York, (1976).

63. P.M. Sutton, *Phys. Rev.*, **91**, 816, (1953).

64. M. Gündüz and J.D. Hunt, *Acta Metall.* **33**, 1651, (1985).

65. A.K. Roy and R.P. Chhabra, in "Handbook of Chemistry and Physics", 75th Edition, (ed. D.R. Lide), C.R.C. Press, Boca Raton, Florida, p.6-255, (1994).

66. T. Owadano, N. Ofuchi, and K. Yosa, *Kyushu Kogyo Krigaku Kenkyu Kugdu*, **22**, 45, (1971).

67. M.P. Watson and J.D. Hunt, *Metall. Trans.*, **8A**, 1793, (1977).

68. D.B. Butrymovicz, in "INCRA Monograph VIII - The Metallurgy of Copper. Diffusion Rate Data and Mass Transport Phenomena for Copper Systems - Part II", International Copper Research Association Inc., pp.184-185, (1981).

69. N.L. Peterson and S.J. Rothman, *Phys. Rev. B*, **1**, 3264, (1970).

70. I. Tuah-Poku, M. Dollar, and T.B. Massalski, *Metall. Trans A*, **19**, 675, (1988).

71. W.A. Tiller, K.A. Jackson, J.W.Rutter, and B. Chalmers, *Acta Metall.* **1**, 428,

(1953).

72. M. Hillert, in "The Mechanism of Phase Transformations in Crystalline Solids", p.231, Institute For Metals, London, (1968).

73. J.P. Hirth and J. Lothe, in "Theory of Dislocations", pp.513-519, McGraw-Hill Inc., London, (1958).

APPENDIX

A.1 ETCHANTS USED

Chromic Acid Cleaning Solution

16 g CrO_3
42.5 mL H_2SO_4
H_2O to make up 1 L of solution

1. Add H_2SO_4 to approximately 500 mL of the H_2O
2. Add the CrO_3
3. Add the remaining H_2O to make 1 L of solution
4. Heat the solution to a temperature in the range $43\,^\circ C < T < 82\,^\circ C$
5. Place sample in solution for approximately 30 minutes
6. Assemble the diffusion couple as soon as possible after removal

Poulton's Reagent

12 mL concentrated HCl
6 mL concentrated HNO_3
1 mL concentrated HF
1 mL distilled H_2O

All steps listed below must be performed in the fume hood wearing the recommended safety equipment:

1. Add the HCl slowly to the H_2O

2. Add the HF
3. Add the HNO_3 immediately before use
4. Etch by brief immersion or by swabbing the specimen surface
5. Rinse in cold H_2O
6. Do not allow the specimen or etchant to heat during the etching procedure

A.2 MAPLE PROGRAM

This program predicts liquid film morphology using the model developed in Chapters Five and Six. It uses empirical expressions for the free energies of both solid and liquid phases, to which the energies of coherency strain, curvature and misfit dislocations are added as appropriate. The analytical equivalent to the common tangent construction is then used to calculate solute concentrations in the liquid and the solid under local equilibrium conditions at both leading and trailing interfaces. From this, the concentration difference across the liquid film is obtained, and the migration characteristics are calculated as a function of time. This version of the program calculates liquid film morphology using the results of the previous loop as initial conditions for the current loop.

List of Variables:

fe_liquid	Free energy of the liquid phase as a function of temperature and composition
T	Experimental temperature [K]
c	Solute concentration [atom fraction]
fe_liquidT	Same as 'fe_liquid', evaluated at the experimental temperature (T) [J mol^{-1}]

fe_solid	Free energy of unstressed solid phase as a function of temperature and composition
fe_solidT	Same as 'fe_solid', evaluated at the experimental temperature (T) [J mol^{-1}]
fe_liqT	Same as 'fe_liquidT', replace 'c' with 'cl' [J mol^{-1}]
fe_solT	Same as 'fe_solidT', replace 'c' with 'cs' [J mol^{-1}]
cl	Solute concentration in the liquid phase
cs	Solute concentration in the solid phase
dfe_liqdc	Derivative of 'fe_liqT' with respect to 'cl'
dfe_soldc	Derivative of 'fe_solT' with respect to 'cs'
equil_cs	Equilibrium solid composition, calculated using the analytical equivalent of the common tangent construction
equil_cl	Equilibrium liquid composition, calculated using the analytical equivalent of the common tangent construction
youngmod_A	Young's modulus (E) of the dissolving grain [Pa]
youngmod_B	Young's modulus (E) of the growing grain - used in the early stages of migration only [Pa]
Y_A	Biaxial elastic constant of the dissolving grain ($= E/(1-\nu)$) [Pa]
Y_B	Biaxial elastic constant of the growing grain ($= E/(1-\nu)$) [Pa]
elastic_energy	Expression for the coherency strain energy ($=V_m Y \eta^2 (C_S-C_0)^2$) [J mol^{-1}]

elastic_energy_A	Coherency strain energy in the dissolving grain (function of 'cs') [J mol^{-1}]
elastic_energy_B	Coherency strain energy in the growing grain (function of 'cs') [J mol^{-1}]
Vm	Molar volume of the solid phase [m^3 mol^{-1}]
eta	Misfit parameter ($\eta = d\ln a/dc$)
co	Solute concentration in the parent α-phase
sigma	Solid-liquid interfacial energy (σ) [J m^{-2}]
zlead	Position of the leading interface as a function of time [μm]
ztrail	Position of the trailing interface as a function of time [μm]
delta	Liquid film thickness (δ) as a function of time [μm]
v	Velocity of the trailing solid-liquid interface [μm s^{-1}]
t	Array of time values [s]
DL	Diffusion coefficient of Cu in liquid Al-Cu (D_L) [μm^2 s^{-1}]
R	Gas constant (= 8.314 [J mol^{-1} K^{-1}])
K_equil	Equilibrium solute distribution coefficient (= equil_cs/equil_cl)
x1, x3	X-coordinates of pinned points [μm]
x2	X-coordinate of the central point - on the plane of symmetry [μm]
z1, z3	Z-coordinates of pinned points [μm]
k1, k2	Variables used in the calculation of radii of curvature

zclead	Z-coordinate of the center of radii of curvature for the leading interface [μm]
zctrail	Z-coordinate of the center of radii of curvature for the trailing interface [μm]
rlead	Radius of curvature of the leading interface [μm]
rtrail	Radius of curvature of the trailing interface [μm]
cl_lead	Solute concentration in the liquid phase at the leading interface
cs_lead	Solute concentration in the solid phase at the leading interface
cl_trail	Solute concentration in the liquid phase at the trailing interface
cs_trail	Solute concentration in the solid phase at the trailing interface
deltaC	Difference in solute concentration across the liquid film (ΔC)
leadcurvenergy	Energy due to curvature at the leading interface [J mol^{-1}]
trailcurvenergy	Energy due to curvature at the trailing interface [J mol^{-1}]
l1lead, m1lead, l1trail, m1trail	Variables used in the calculation of radii of curvature
fe_leadsol	Free energy of the solid phase at the leading interface [J mol^{-1}]
fe_leadliq	Free energy of the liquid phase at the leading interface [J mol^{-1}]
dfe_leadsoldc	Derivative of 'fe_leadsol' with respect to 'cs'
dfe_leadliqdc	Derivative of 'fe_leadliq' with respect to 'cl'
Ds	Diffusion coefficient of Cu in solid Al-Cu (D_S) [μm^2 s^{-1}]

pen_distance	**Penetration distance of solute into the growing grain [μm]**
critical_distance	**Penetration distance at which misfit dislocations are assumed to appear (L_C) [μm]**
E_disl_array	**Calculated energy of a wall of misfit dislocations that accommodates misfit strain [J mol^{-1}]**
R_cutoff	**Distance to which the strain field of the dislocation wall extends [μm]**
fe_trailliq	**Free energy of the liquid phase at the trailing interface [J mol^{-1}]**
fe_trailsol	**Free energy of the solid phase at the trailing interface [J mol^{-1}]**
dfe_trailliqdc	**Derivative of 'fe_trailliq' with respect to 'cl'**
dfe_trailsoldc	**Derivative of 'fe_trailsol' with respect to 'cs'**
regime	**Array to recognize which migration regime the program is in at any particular time (*e.g.* initiation, ztrail<0, ztrail>0, *etc.*)**
ztrail_at_coh_break	**Value of 'ztrail' when coherency is lost in the growing grain**
disl_effect_end	**Value of 'ztrail' when the strain field of the dislocation wall becomes negligible**
Leadsolutions	**Solutions to the local equilibrium calculation (common tangent) at the leading interface (*i.e.*, cl_lead, cs_lead)**
Trailsolutions	**Solutions to the local equilibrium calculation (common tangent) at the trailing interface (*i.e.*, cl_trail, cs_trail)**
K_dynamic	**Solute distribution coefficient (= cs_trail/cl_trail)**
delta_delta	**Amount by which the liquid film shrinks during the time interval, (t[i]-t[i-1]) [μm]**

vlead	Instantaneous velocity of the leading solid-liquid interface [μm s^{-1}]
Ds_over_v	Effective penetration distance of solute into the retreating grain (= D_S / vlead) [μm]
measured_zlead	Experimentally measured values for the position of the leading interface (microns) [μm]
measured_ztrail	Experimentally measured values for the position of the trailing interface (microns) [μm]
plot_measured_zlead	Name given to the plot of 'measured_zlead'
plot_measured_ztrail	Name given to the plot of 'measured_ztrail'
zlead_predictions, ztrail_predictions, fe_leadsol_pred, fe_leadliq_pred, fe_trailsol_pred, fe_trailliq_pred, leadcurvenergy_pred, trailcurvenergy_pred, Ds_over_v_pred, regime_pred	Arrays created to contain the predictions for several parameters along with the appropriate time values for later plots
plot_predicted_zlead	Plot of the predictions for the position of the leading solid-liquid interface as a function of time
plot_predicted_ztrail	Plot of the predictions for the position of the trailing solid-liquid interface as a function of time
zlead_error_3.... ....zlead_error_30	Plots created to represent the errors in the measured values for the leading interface
ztrail_error_3....	

....ztrail_error_30	Plots created to represent the errors in the measured values for the trailing interface
plot_fe_leadsol, plot_fe_leadliq, plot_fe_trailsol, plot_fe_trailliq	Plots of the free energies of the leading and trailing solids and liquids
predictions_excel	Array containing the 't', 'zlead', and 'ztrail' arrays for export to a spreadsheet program

Some important MAPLE commands

subs(variable=replacement, expression)	Substitutes a variable within a particular 'expression'
diff(expression, variable of differentiation)	Differentiates the 'expression' with respect to the 'variable of differentiation'
fsolve(set of equations, set of variables)	Solves sets of equations numerically. Used in this program to solve for the solid and liquid compositions using the analytical equivalent to the common tangent construction
evalf(expression)	Finds a numerical approximation to the 'expression'
assign(SolutionSet)	Assigns specified variables from the results of an 'fsolve' command
display([plot1, plot2, ..., plotn])	Displays previously 'suppressed' plots on a single set of axes

```
****************************************************************************
```

Input of free energy expressions for the liquid and solid phases

```
****************************************************************************
>fe_liquid:=(-804.7+174.134*T+31.7566*T*(1-ln(T)))*(1-c)+(-1607+184.689*T+32.63
5*T*(1-ln(T)))*c+8.314*T*(c*ln(c)+(1-c)*ln(1-c))+c*(1-c)*(-33255-16.5543*T+((1-2*c
)*(13308+6.603*T))+((6*c^2-6*c+1)*(2260-3.2823*T)));

> fe_liquidT:=subs(T=833,fe_liquid);

>fe_solid:=(-6531.4+122.71*T+21.1429*T*(1-ln(T))-(0.0075545*T^2)/2-0.47781*10^5/
(2*T)-0.59*10^(-5)*T^3/6)*(1-c)+(-6792.3+132.407*T+22.9847*T*(1-ln(T))-0.005676
*T^(2)/2)*c+8.314*T*(c*ln(c)+(1-c)*ln(1-c))+c*(1-c)*(-28353-13.578*T+((1-2*c)*(223
64+12.0517*T)));

> fe_solidT:=subs(T=833,fe_solid);

> fe_liqT:=subs(c=cl,fe_liquidT);

> fe_solT:=subs(c=cs,fe_solidT);
*************************************************************************
```

Calculation of strain free, planar equilibrium solid and liquid compositions using the analytical equivalent of the common tangent construction

```
*************************************************************************
> dfe_liqdc:=diff(fe_liqT,cl);

> dfe_soldc:=diff(fe_solT,cs);

> Digits:=10:

>Results:=fsolve({(fe_solT-fe_liqT)=dfe_soldc*(cs-cl),dfe_soldc=dfe_liqdc},{cl,cs},{cl=0
..0.5,cs=0..0.4});

> assign(Results);

> equil_cs:=cs;

> equil_cl:=cl;

> cl:='cl'; cs:='cs';
**********************************************************************
```

Calculation of the coherency strain energy.

'A' refers to the dissolving grain, and 'B' to the growing grain.
The strain energy in grain B is required only in the initiaton stages

```
**********************************************************************
> Y_A:=72.5*(10^9);

> Y_B:=66.7*(10^9);
```

```
> elastic_energy:=Y*Vm*(eta^2)*((cs-co)^2);
> elastic_energy_A:=subs(Y=Y_A , Vm=(10^(-5)) , eta=-.121 , co=.0063 , elastic_energy);
> elastic_energy_B:=subs(Y=Y_B , Vm=(10^(-5)) , eta=-.121 , co=.0063 , elastic_energy);
*******************************************************************
        Initialization of arrays and variables to be used in the calculations
                                   of migration kinetics
*******************************************************************
> sigma:=.18;
> zlead:= array(1..231):
> ztrail:=array(1..231):
> delta:=array(1..231):
> v:=array(1..231):
*******************************************************************
     Input of initial values for the position of the leading and trailing interfaces
*******************************************************************
> zlead[1]:=1.15;
> ztrail[1]:=-1.15;
> delta[1]:=zlead[1]-ztrail[1];
> v[1]:=0;
*******************************************************************
                              The time array is entered
*******************************************************************
> t:=array(1..231):
> for i from 1 to 231 do
>     if i <= 101 then
>         t[i]:=(i-1)*0.01;
>     fi;
>     if (i >101) and (i <= 191) then
>         t[i]:=(i-91)*0.1;
>     fi;
>     if i > 191 then
>         Digits:=4:
```

```
>         t[i]:=evalf(i/2)-85.5;
>      fi;
> od:
> Digits:=10:
**********************************************************************
            Input of some parameters to be used during modelling:
**********************************************************************
> DL:=3070;
> Ds:=.2206;
> critical_distance:=5*.029;
> R:=8.314;
> K_equil:=equil_cs/equil_cl;
**********************************************************************
   Values to be used in the calculation of the radii of curvature for the leading
   and trailing interfaces: (x1, z1) and (x3, z3) are the pinning points. (x2, zlead)
  and (x2, ztrail) are points of maximum displacement for the leading and trailing
                              interfaces respectively.
**********************************************************************
> x1:=-3.45;
> x2:=0;
> x3:=3.45;
> z1:=0;
> z3:=0;
> k1:=x2-x1;
> k2:=x3-x1;
> I:='i';
**********************************************************************
                          More arrays are initialized.
**********************************************************************
> zclead:=array(1..231):
> zctrail:=array(1..231):
```

```
> rlead:=array(1..231):
> rtrail:=array(1..231):
> cs_trail:=array(1..231):
> cs_lead:=array(1..231):
> cl_trail:=array(1..231):
> cl_lead:=array(1..231):
> deltaC:=array(1..231):
> fe_leadsol_v_t:=array(1..231):
> fe_leadliq_v_t:=array(1..231):
> fe_trailliq_v_t:=array(1..231):
> fe_trailsol_v_t:=array(1..231):
> leadcurvenergy:=array(1..231):
> trailcurvenergy:=array(1..231):
> Ds_over_v:=array(1..231):
> regime:=array(1..231):
****************************************************************
   The following loop calculates the position of the leading and trailing
                      interfaces as a function of time.
****************************************************************
> for i from 2 to 231 do
****************************************************************
 Calculation of the radii of curvature of the leading and trailing interfaces.
****************************************************************
>   l1lead:=zlead[i-1];
>   m1lead:=((zlead[i-1]^2)-(x1^2))/2;
>   l1trail:=ztrail[i-1];
>   m1trail:=((ztrail[i-1]^2)-(x1^2))/2;
>   zclead[i-1]:=m1lead/l1lead;
>   zctrail[i-1]:=m1trail/l1trail;
>   rlead[i-1]:=sqrt((x1^2)+(zclead[i-1]^2));
```

```
>  rtrail[i-1]:=sqrt((x1^2)+(zctrail[i-1]^2));
*****************************************************************
 Calculation of energy due to curvature of the leading and trailing interfaces.
*****************************************************************
>  leadcurvenergy[i-1]:=(1*(10^6))*(2*sigma*(10^(-5))/rlead[i-1]);
>  trailcurvenergy[i-1]:=(1*(10^6))*(2*sigma*(10^(-5))/rtrail[i-1]);
*****************************************************************
        Expressions for the free energies:
        F.E. of the leading solid = F.E. of strain free, planar solid + coherency
                                                    strain energy of grain 'A'
        F.E. of the leading liquid = F.E. of liquid + energy due to curvature for
                                                     the leading interface
*****************************************************************
>  fe_leadsol:=fe_solT+elastic_energy_A;
>  fe_leadliq:=fe_liqT+leadcurvenergy[i-1];
>  dfe_leadsoldc:=diff(fe_leadsol,cs);
>  dfe_leadliqdc:=diff(fe_leadliq,cl);

*****************************************************************
  The penetration distance of solute into the growing grain is estimated.
*****************************************************************
>  pen_distance:=(ztrail[i-1]-ztrail[1]) + sqrt(Ds*t[i-1]);
*****************************************************************
 The free energies of the trailing solid and trailing liquid are estimated:
*****************************************************************
  For negative values of ztrail:
     F.E. of the trailing liquid = F.E. of liquid + energy due to curvature for
                                                       the trailing interface
    Very early stages:
     F.E. of the trailing solid = F.E. of strain free, planar solid + coherency
                                             strain energy of grain 'B'.
    Once coherency is broken:
     F.E. of the trailing solid = F.E. of strain free, planar solid
```

```
*******************************************************************
  For positive values of ztrail:
    F.E. of the trailing liquid = F.E. of liquid (in equilibrium with a strain
                                                              free, planar solid)
    F.E. of the trailing solid = F.E. of strain free, planar solid + energy due
                                            to curvature for the trailing interface.
*******************************************************************
> if (ztrail[i-1] <= 0) then
>     fe_trailliq:=fe_liqT+trailcurvenergy[i-1];
>     fe_trailsol:=fe_solT;
>     regime[i]:=2;
>     if (pen_distance <= critical_distance) then
>         fe_trailsol:=fe_solT+elastic_energy_B;
>         regime[i]:=1;
>     fi;
> else
>     fe_trailliq:=fe_liqT;
>     fe_trailsol:=fe_solT+trailcurvenergy[i-1];
>     regime[i]:=3;
> fi;
> dfe_trailliqdc:=diff(fe_trailliq,cl);
> dfe_trailsoldc:=diff(fe_trailsol,cs);
*******************************************************************
    The solid and liquid solute concentrations in local equilibrium at the
  leading and trailing interfaces are calculated through use of the analytical
                   equivalent to the common tangent construction.
*******************************************************************
>Leadsolutions:=fsolve({(fe_leadsol-fe_leadliq)=dfe_leadsoldc*(cs-cl),dfe_leadsoldc=dfe_
leadliqdc},{cs,cl},{cs=0..0.3,cl=0..0.5});
> assign(Leadsolutions);
> cl_lead[i]:=cl;
> cs_lead[i]:=cs;
```

```
>   cl:='cl'; cs:='cs';
>Trailsolutions:=fsolve({(fe_trailsol-fe_trailliq)=dfe_trailsoldc*(cs-cl),dfe_trailsoldc=dfe_trailliqdc},{cs,  cl},{cs=0..0.3,cl=0..0.5});
>   assign(Trailsolutions);
>   cl_trail[i]:=cl;
>   cs_trail[i]:=cs;
>   cl:='cl'; cs:='cs';
**********************************************************************
     Calculation of the concentration difference across the liquid film, the
      dynamic solute distribution coefficient, and the liquid film thickness
**********************************************************************
>   deltaC[i]:=cl_trail[i]-cl_lead[i];
>   K_dynamic:=cs_trail[i]/cl_trail[i];
>   delta_delta:=2*K_dynamic*v[i-1]*(t[i]-t[i-1]);
>   delta[i]:=delta[i-1]-delta_delta;
**********************************************************************
        Calculation of the new 'zlead' and 'ztrail':
         If the liquid film thickness has become negative - migration ceases
**********************************************************************
>   if (delta[i] <= 0) then
>       zlead[i]:=zlead[i-1];
>       ztrail[i]:=ztrail[i-1];
>   else
>       v[i]:=(DL*deltaC[i])/((cl_trail[i]-cs_trail[i])*delta[i]);
>       ztrail[i]:=ztrail[i-1]+v[i]*(t[i]-t[i-1]);
>       zlead[i]:=ztrail[i]+delta[i];
>   fi;
**********************************************************************
 Calculation of the instantaneous velocity of the leading solid / liquid interface,
    and the effective penetration distance of solute into the retreating grain.
**********************************************************************
```

```
>   vlead:=(zlead[i]-zlead[i-1])/(t[i]-t[i-1]);
>   if vlead = 0 then
>       Ds_over_v[i]:=Ds_over_v[i-1];
>   else
>       Ds_over_v[i]:=Ds/vlead;
>   fi;
> od:
```

****

Plotting and tabulation of results.

****

The average experimentally measured values for the leading and trailing interface positions are entered:
(Note: t[106]=1.5 seconds from liquation, t[126]=3.5s, t[146]=5.5s, t[176]=8.5s,
t[198]=13.5s, t[208]=18.5s,
t[228]=28.5s).

****

```
> measured_zlead:=[ [t[106],2.36], [t[126],3.01], [t[146],3.27], [t[176],3.11], [t[198],3.48],
[t[208],3.32], [t[228],3.4] ]:

> measured_ztrail:=[ [t[106],.63], [t[126],1.12], [t[146],1.11], [t[176],.95], [t[198],1.15],
[t[208],1.21], [t[228],1.42] ]:

> with(plots):
```

****

The measured values are plotted (Note: the colon ':' suppresses the plot until required)

****

```
> plot_measured_zlead:=plot(measured_zlead, style=POINT, color=RED):

> plot_measured_ztrail:=plot(measured_ztrail, style=POINT, color=BLUE):

> i:='i';
```

****

Initialization of the 'prediction' arrays

****

```
> zlead_predictions:=array (1..230,1..2):

> ztrail_predictions:=array(1..230,1..2):
```

```
> fe_leadsol_pred:=array(1..230,1..2):
> fe_leadliq_pred:=array(1..230,1..2):
> fe_trailliq_pred:=array(1..230,1..2):
> fe_trailsol_pred:=array(1..230,1..2):
> leadcurvenergy_pred:=array(1..230,1..2):
> trailcurvenergy_pred:=array(1..230,1..2):
> deltaC_pred:=array(1..230,1..2):
> Ds_over_v_pred:=array(1..230,1..2):
> regime_pred:=array(1..230,1..2):
**************************************************************
      The following loop fills the 'prediction' arrays: The first column
      contains the time array, while the second column contains various
                                predictions
**************************************************************
> for i from 1 to 230 do
>    zlead_predictions[i,1]:=t[i];
>    zlead_predictions[i,2]:=zlead[i];
>    ztrail_predictions[i,1]:=t[i];
>    ztrail_predictions[i,2]:=ztrail[i];
>    fe_leadsol_pred[i,1]:=t[i];
>    fe_leadsol_pred[i,2]:=fe_leadsol_v_t[i];
>    fe_leadliq_pred[i,1]:=t[i];
>    fe_leadliq_pred[i,2]:=fe_leadliq_v_t[i];
>    fe_trailliq_pred[i,1]:=t[i];
>    fe_trailliq_pred[i,2]:=fe_trailliq_v_t[i];
>    fe_trailsol_pred[i,1]:=t[i];
>    fe_trailsol_pred[i,2]:=fe_trailsol_v_t[i];
>    leadcurvenergy_pred[i,1]:=t[i];
>    leadcurvenergy_pred[i,2]:=leadcurvenergy[i];
>    trailcurvenergy_pred[i,1]:=t[i];
```

```
>    trailcurvenergy_pred[i,2]:=trailcurvenergy[i];
>    deltaC_pred[i,1]:=t[i];
>    deltaC_pred[i,2]:=deltaC[i];
>    Ds_over_v_pred[i,1]:=t[i];
>    Ds_over_v_pred[i,2]:=Ds_over_v[i];
>    regime_pred[i,1]:=t[i];
>    regime_pred[i,2]:=regime[i];
> od:
> i:='i';
> Ds_over_v_pred[1,2]:=0:
> deltaC_pred[1,2]:=0:
> plot(Ds_over_v_pred, style=LINE, color=RED,view=[0..7,0..2]);
> plot(Ds_over_v_pred, style=LINE, color=RED,view=[0..20,0..20]);
> print(regime_pred);
*****************************************************************
      The predicted values for 'zlead' and 'ztrail' are plotted (suppressed)
*****************************************************************
> plot_predicted_zlead:=plot(zlead_predictions, style=LINE, color=RED):
> plot_predicted_ztrail:=plot(ztrail_predictions, style=LINE, color=BLUE):
*****************************************************************
       The error bars are created for the experimentally measured values
*****************************************************************
> zlead_error_3:=plot( [ [t[106],3.19], [t[106],1.53] ], style=LINE, color=RED):
> zlead_error_5:=plot( [ [t[126],3.84], [t[126],2.18] ], style=LINE, color=RED):
> zlead_error_7:=plot( [ [t[146],4.4], [t[146],2.14] ], style=LINE, color=RED):
> zlead_error_10:=plot( [ [t[176],4.17], [t[176],2.05] ], style=LINE, color=RED):
> zlead_error_15:=plot( [ [t[198],4.61], [t[198],2.35] ], style=LINE, color=RED):
> zlead_error_20:=plot( [ [t[208],4.52], [t[208],2.02] ], style=LINE, color=RED):
> zlead_error_30:=plot( [ [t[228],4.25], [t[228],2.55] ], style=LINE, color=RED):
```

```
> ztrail_error_3:=plot( [ [t[106],.95], [t[106],.31] ], style=LINE, color=BLUE):
> ztrail_error_5:=plot( [ [t[126],1.46], [t[126],.78] ], style=LINE, color=BLUE):
> ztrail_error_7:=plot( [ [t[146],1.4], [t[146],.82] ], style=LINE, color=BLUE):
> ztrail_error_10:=plot( [ [t[176],1.21], [t[176],.69] ], style=LINE, color=BLUE):
> ztrail_error_15:=plot( [ [t[198],1.61], [t[198],.69] ], style=LINE, color=BLUE):
> ztrail_error_20:=plot( [ [t[208],1.58], [t[208],.84] ], style=LINE, color=BLUE):
> ztrail_error_30:=plot( [ [t[228],1.61], [t[228],1.23] ], style=LINE, color=BLUE):
********************************************************************************
        The following 'display' command plots the previously suppressed plots in any
                                   combination required
********************************************************************************

> display([plot_measured_zlead, plot_predicted_zlead, zlead_error_3, zlead_error_5,
zlead_error_7,zlead_error_10, zlead_error_15, zlead_error_20, zlead_error_30,
plot_measured_ztrail, plot_predicted_ztrail, ztrail_error_3, ztrail_error_5, ztrail_error_7,
ztrail_error_10, ztrail_error_15, ztrail_error_20, ztrail_error_30], view=[0..30,-2..8]);
```